# Iron jarosite and zinc paratacamite as models of the classical and the quantum kagomé antiferromagnet.

Mark Alexander de Vries

A thesis submitted in fulfilment of requirements for the degree of

Doctor of Philosophy

to

CSEC and the School of Chemistry

The University of Edinburgh

July 2007

# Declaration

I hereby declare that this thesis is of my own composition, and that it contains no material previously submitted for the award of any other degree. The work reported in this thesis has been executed by myself, except where due acknowledgement is made in the text.

Mark Alexander de Vries

# Abstract

In this thesis two experimental antiferromagnets with the particularly interesting lattice resembling the kagomé basket-weaving pattern, are studied. The kagomé topology frustrates the classical antiferromagnetic Néel state, the commonly encountered magnetic ground state in transition-metal compounds. Extensive theoretical work has shown that in particular the $S = 1/2$ kagomé antiferromagnet should not show any symmetry-breaking transition to a classical long-range-ordered state. Hence, experimental realisations of this system should in theory allow a unique insight into properties of the symmetrical quantum-mechanical magnetic ground state.

Recently a viable experimental realisation of the $S = 1/2$ kagomé antiferromagnet has been discovered, the $x = 1$ phase of zinc paratacamite $Zn_xCu_{(4-x)}(OH)_6Cl_2$. Here samples of stoichiometry $0.15 \leq x \leq 1$ were synthesised and characterised. Using muon-spin relaxation spectroscopy on these samples, it was found that for $x > 0.6$ the spins do not freeze, even at 50 mK. From neutron powder diffraction for $x = 1$ and heat capacity measurements on zinc paratacamite with $0.5 \leq x \leq 1$, it was found that $\sim 6\%$ antisite disorder is present in the $x = 1$ phase, and that samples with Zn stoichiometry $0.8 \leq x \leq 1$ model the $S = 1/2$ kagomé antiferromagnet equally well. No quantum critical phase transition to a quantum spin liquid is found. Instead, the ground state of this model system is magnetic even for $x > 0.8$. The field dependence of the heat capacity provides additional evidence that the total magnetic quantum number $S_{\text{tot}}$ is

not a conserved quantity, despite the fact that no symmetry breaking transition occurs in the magnetic degrees of freedom.

In a polarised X-ray spectroscopy experiment on synthesised single crystals of the classical ($S = 5/2$) kagomé antiferromagnet iron jarosite ($KFe_3(SO_4)_2(OH)_6$), it is shown that the $Fe^{2+}$ ion with a $^6S$ free-ion configuration can acquire a large orbital angular momentum in the solid state. The high-resolution spectra are reproduced in excellent detail, using ligand-field multiplet calculations in which strong $\sigma$-type covalent bonding between the $Fe^{3+}$ ion and the oxygen ligands mixes in configurations of $Fe^{2+}$ character. The values found with this method for the orbital angular momentum $\langle L^2 \rangle = 1.9(2)$ and the easy-plane anisotropy energy of 0.4 meV are in excellent agreement with the values estimated from the high-temperature magnetic susceptibility and the results from spin-wave calculations. This is in support of a single-ion anisotropy as opposed to the Dzyaloshinsky-Moriya interaction, as the origin of the magnetic phase transition.

# Acknowledgements

It is my pleasure to thank the following people and institutions, without whom it would have been impossible to conclude this project in its present form. The first person I would like to thank is Andrew Harrison, my PhD supervisor at the University of Edinburgh, for introducing me to the physics and chemistry of geometrically frustrated magnetic materials - in particular iron jarosite and zinc paratacamite, and for all his advice and support during the experiments and during the write-up of results. Gerrit van der Laan at the SRS in Daresbury, Nicholas Harrison of the Centre for Materials Science and Chemistry of the CCLRC and Paolo Radaelli of the Rutherford Appleton Laboratory have been involved in this project from an early stage, and there is no doubt that the success of our grant and beam time applications was in part thanks to their involvement, input and interest in the project. By far the largest sub project of this PhD was the X-ray spectroscopy experiment on iron jarosite, spanning almost four years and several experiments at the SRS in Daresbury and the ESRF in Grenoble. Throughout this project I could count on Tarnjit Johal's support, as beamline responsible at 5U.1 at the SRS in Daresbury, but also during experiments at the ESRF and during the analysis of the data. Many thanks also to Peter Bencok of ID8 at the ESRF for his support during my experiments there. Thanks to Jill Claydon, Gøran Nilsen, Adam Freeman and Nicola Farley for their help during the X-ray experiments which often continued through the night. For the analysis of the spectra I have benefited from

discussions with Frank de Groot, Andrew Wills and finally Alessandro Mirone, whose computer program *Hilbert++* was instrumental in laying bare many of the secrets of iron jarosite, which were encrypted in the X-ray spectroscopy data. Thanks to Simon Parsons and Clivia Hejny for their help with the X-ray characterisation of the jarosite single crystals which were used in the spectroscopy experiments. A neutron experiment of natural single crystals was carried out in cooperation with Henrik Rønnow at the Paul Scherrer Institute in Switzerland. I would particularly like to thank him for his hospitality during my arrival in Lausanne, and for the many helpful discussions and advice he has given. In cooperation with Barry Searle, Nicholas Harrison and Adrian Wander electronic structure calculations have been carried out on iron jarosite. Though these calculations are not described here, this cooperation has been very beneficial to my understanding of magnetism in the theory of quantum chemistry.

The work on zinc paratacamite has been carried out in close cooperation with Philippe Mendels, Fabrice Bert and Aretha Olariu of the Muon/NMR group in Paris Orsay, in part with financial support from the European Science Foundation. It has been a pleasure to work with them over the last one and a half year. Winfried Kockelmann of the ISIS facility is gratefully acknowledged for the neutron diffraction measurements on zinc paratacamite which he carried out on Rotax at ISIS. Here I should thank my second supervisor Paul Attfield, for the discussions on the interpretation of the structural neutron data, but also for his general support and advice during my PhD. Thanks to Ross Stewart, Mark Telling, John Taylor and Pascual Manuel for their help and support with the neutron spectroscopy experiments at the ISIS facility. I should also thank Ross Stewart for carrying out measurements on zinc paratacamite at IN4 at the ILL facility in Grenoble. Many thanks also to Pascale Deen of the ILL for her support with the diffuse neutron scattering experiment at D7. Konstantin Kamenev has been a great help with the heat capacity measurements on zinc paratacamite. I would also like to thank him for his help during the write-up of the heat capacity results. Thanks furthermore to Javier Sanchez Benitez for his help with the numerous

heat capacity and magnetic susceptibility measurements on zinc paratacamite. On the theoretical side I have greatly benefited from a number of discussions with Philippe Monthoux and Claudine Lacroix. Many thanks also to Philip Camp for his help with Monte Carlo simulations, and for the many interesting discussions.

It was with the encouragement of Robert Donovan, Mike Stocks and Nina Moeller that I started applying for a PhD - many thanks! During most of my PhD I was based at the Centre for Science at Extreme Conditions in Edinburgh. This has been a great place to work where I have been made to feel "at home" thanks to the friendly atmosphere and help, whenever needed, from my office mates Anthony Williams, Jan-Willem Bos, Fiona Coomer, Gaetan Giriat, Simon Kimber, Adrian Hill, Marcela Pina Sandoval, Jennifer Rodgers, Luis Ortega San Martin, Ingo Loa and all the others in the open plan office. Thanks to Otti Croze and Iain McLeod for the enjoyable discussions about Quantum Mechanics. Other people around CSEC and the School of Chemistry who I should thank for their help with a number of projects are Neil Robertson, Nicola Meller and Christophe Guillaume. Thanks also to Stewart Mains and Stuart Johnstone for the numerous mechanical/glass-blowing services, and to Amanda Ewing for helping to fit me into my supervisor's tight schedule.

The School of Chemistry and Centre for Materials Physics and Chemistry of the CCLRC are gratefully acknowledged for providing me a PhD scholarship and the School of Chemistry also for providing funds which allowed me to travel to Japan, to attend the Highly Frustrated Magnetism conference in Osaka. Many thanks also go to the Highly Frustrated Magnetism network of the European Science Foundation, which has allowed me to participate in a $\mu$SR experiment at PSI, Switzerland, and to stay in Henrik Rønnow's group at the EPFL in Lausanne for the 6 months directly after my PhD.

On a personal note I am grateful for my parents, who supported me throughout my physics degree, and have always encouraged me to gain a deeper understanding of the world. Finally I thank Catherine Dickey, for being there.

# Preface

Two sources which have proved particularly valuable to me during my PhD were J.J. Sakurai's book "Modern Quantum Mechanics" [182], and "Lecture Notes on Electron Correlation and Magnetism" by P. Fazekas [70]. In particular in chapter 2, where established theory is discussed which in this thesis is not traced to the original researchers, these two textbooks could have been cited many times. Instead they are mentioned here.

Another indispensable resource I would like to mention is the open source software of the Debian Gnu/Linux operating system [1]. Where the use of particular software is not mentioned explicitly in the text I have totally depended on the multitude of software packaged with Debian, during my PhD, and while writing this thesis.

# Contents

# List of Tables

# List of Figures

Chapter 1

# Introduction

Central to this thesis is the physics of the kagomé antiferromagnet (figure 1.1 right). Most antiferromagnets have an ordered ground state, but the kagomé antiferromagnet is geometrically frustrated, and is not expected to undergo any phase transition, even at zero temperature. Geometric frustration arises when the lattice geometry of a magnetic system prevents the simultaneous satisfaction of all magnetic bonds (figure 1.1 left). The resulting underconstraint can lead to such a large ground state degeneracy that no symmetry breaking to a magnetically long-range ordered state occurs, even at $T = 0$. Due to the absence of symmetry-breaking for antiferromagnetically coupled spins on the kagomé lattice, the magnetic ground state - which can also be non-magnetic - should directly reveal the symmetry of the Hamiltonian.

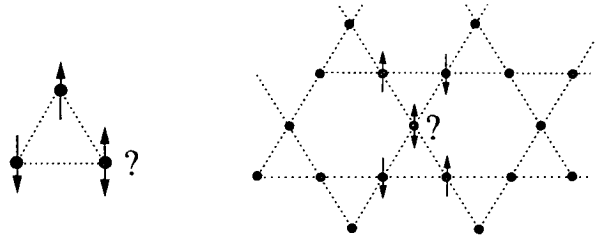


Figure 1.1: The principle of geometric frustration. There is no uniquely defined low-energy configuration for the antiferromagnetically coupled spins on a triangle (left) and on the kagomé lattice (right).

This summarises the strategy which will be employed here to study the magnetic Hamiltonian and its emergent properties in a class of materials which will soon be defined in detail. The importance of symmetry-breaking transitions is far-reaching. The classical world as it is familiar to us emerges from the underlying laws of quantum mechanics through a series of symmetry-breaking transitions, where step-by-step the system can be broken-up into components which in themselves are still described by quantum mechanics, but which behave in relation to each other in a more classical manner. It may at some point for example be possible to give judiciously defined sub-systems, as well as the system as a whole, definite coordinates and momentum, and abandon their description in terms of wave functions as the size of the system increases. In sections 2.1 to 2.2.5 some concrete examples of symmetry-breaking transitions are given, a combination of which describe the class of materials studied here; narrow-band magnetic insulators composed of first-row transition-metal (iron-group) ions which have a partially filled $3d$ shell, highly electronegative elements such as oxygen, sulphur and chlorine, and hydroxy groups. Large enough single crystals of such materials often have gemstone appeal [109], due to their deep and varied colours, transparency and often faceted shape revealing the symmetries of the crystal lattice.

On another level Landau and Anderson's theory of spontaneous symmetry breaking has inspired cosmological theories on the origin of the universe [6]. Though magnetic phase transitions have played an important role in the understanding of spontaneous symmetry breaking, many questions which date from the 1930's are still not answered satisfactorily [120]. Heisenberg [88] and Dirac first described a mechanism for the interaction between electron spins based on Pauli's exclusion principle, which was called the magnetic exchange interaction. As is elaborated in sections 2.2.3 and 2.2.6 it arises from the difference of the potential energy of the two electrons due to their Coulomb repulsion, when their spins are aligned parallel as compared to anti-parallel. Heisenberg and Dirac showed that the energy difference - the exchange energy - can be written as

a function of the spin operators,

$$\mathcal{H}_{12} = J_{12}\hat{S}_1 \cdot \hat{S}_2 \tag{1.1}$$

where $J_{12}$ is the exchange coupling between spins 1 and 2. Hence, on a lattice of spins such as for magnetic insulators

$$\mathcal{H}_{\mathrm{H}} = J_{\mathrm{nn}} \sum_{\langle i,j \rangle} \hat{S}_i \cdot \hat{S}_j, \tag{1.2}$$

where the sum is over all pairs of nearest-neighbour spins and $J_{\mathrm{nn}}$ is the nearest-neighbour exchange coupling. This is the Heisenberg Hamiltonian, due to Heisenberg and van Vleck. For a two-spin system, the ground state is a singlet (a closed shell or orbital) for antiferromagnetic exchange ($J > 0$) and a triplet for ferromagnetic exchange ($J < 0$). Néel suggested that for $J > 0$ the solution of equation 1.2 is a state where the spins are arranged in oppositely magnetised sub-lattices, as illustrated in figure 1.2.

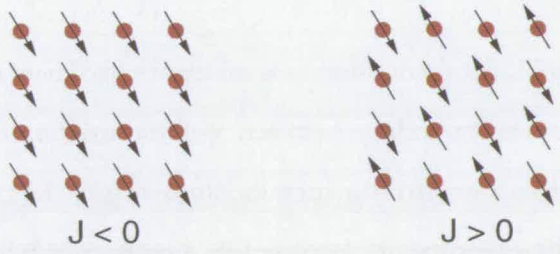


Figure 1.2: A ferromagnetic state (left) and an antiferromagnetic ground state (right) as proposed by Néel for magnetic insulators.

This idea was met with many objections, primarily because the state as proposed by Néel, the Néel state, is not an eigenstate of the Heisenberg Hamiltonian for any finite-sized system. However, using neutron diffraction Shull and Smart [189] were able to prove Néel's idea for a number of antiferromagnetic insulators. It is also understood theoretically that 3D and 2D square lattices in the thermodynamic limit have a Néel ground state [125]. The kagomé antiferromagnet is one of the few 2D systems which in theory should not order even at $T = 0$ [138].

The subject gained a renewed relevance in 1986, when a new class of superconductors was discovered [13, 233, 10]. These materials were superconducting at temperatures much higher than previously observed and a new theory was needed to understand them. In all cases the parent compounds of these new "high critical temperature" (high-$T_c$) superconductors are antiferromagnetic insulators with a very strong antiferromagnetic coupling. One such system is $La_2CuO_4$; when some $La^{3+}$ in this system is replaced with $Ba^{2+}$ the Cu ions become mixed-valence to balance the charge with the oxygen ions. The initially insulating system becomes superconducting when moderately doped, and with further doping the ground state becomes metallic. These are three qualitatively different phases of matter, which can be realised by tuning a single material parameter. The transitions between these different ground states, which are transitions between different kinds of broken symmetry, are called quantum phase transitions. They occur by definition at $T = 0$, as a function of some parameter other than temperature.

The story of the high-$T_c$ superconductors is an example of how entirely new phases of matter can emerge at the boundary between well-known phases. The symmetry-breaking transition, in this case from a metallic state with itinerant electrons to an insulating state where the electrons are localised, is a cross-over between quantum mechanical behaviour to classical behaviour. These are regions in the phase diagram of materials which are particularly rich in qualitatively new phenomena, hugely challenging to understand theoretically [112], let alone to predict a-priori. This inspires chemists, physicists and material scientists to keep searching for fundamentally new phases of matter in an empirical way. For example by studying the physics as a function of the system size, as is done in the fields of nano materials and molecular magnets [199], by chemical doping of existing materials and by the application of pressure. Figure 1.3 illustrates a quantum-critical phase transition as a function of an external magnetic field.

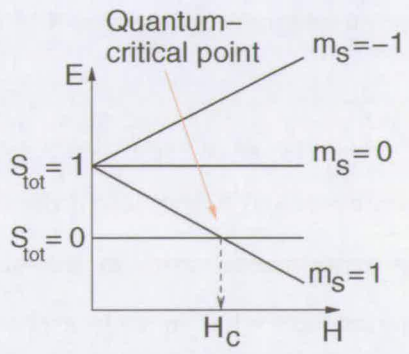


Figure 1.3: An example of a quantum critical phase transition of a two-spin system as a function of an external field. If in zero field the ground state is a singlet ($S_{\mathrm{tot}} = 0$) there will be a critical field $H_c$ at which the ground state changes from non-magnetic to ferro-magnetic.

This thesis builds on the efforts which have been made previously [85, 78] to tune to quantum critical phase transitions by synthesising antiferromagnetic materials with particular "frustrating" lattice topologies. Chapter 4 describes a study of potassium and hydronium iron jarosite ($A\mathrm{Fe_3(OH)_6(SO_4)_2}$ with $A =$ K or $\mathrm{H_3O}$), both $S = 5/2$ kagomé antiferromagnets which have been taken as model systems of the classical kagomé antiferromagnet. The main results in this chapter are single crystal and powder X-ray spectroscopy measurements of the Fe $\mathrm{L_{2,3}}$ edges carried out at the ESRF in Grenoble, France, and at the SRS in Daresbury, UK. In combination with ligand-field multiplet calculations they have yielded information on the local spins of unprecedented detail for an antiferromagnetic insulator. Chapter 5 describes a thorough experimental characterisation of the zinc paratacamites of general formula $\mathrm{Zn_xCu_{(4-x)}(OH)_6Cl_2}$ with $x \leq 1$. In August 2005 Shores *et al.* pointed out that the $x = 1$ phase is a perfect physical realisation of the $S = 1/2$ kagomé antiferromagnet [188]. In the field of highly-frustrated magnetism such a material represents the Holy Grail, and over the last few months a large number of publications on this exciting new material have appeared. Amongst these are two papers on the work discussed here [131, 57], including muon spin relaxation spectroscopy measurements also discussed in section 5.4, where it is shown that the spins in this system do not freeze even at 50 mK when $x > 0.6$. Other major results in this chapter come from neutron diffraction (section 5.2), the field-dependent

heat capacity for a range of zinc stoichiometries (section 5.5) and neutron spectroscopy measurements (section 5.7).

Experimental details have as much as possible been concentrated in chapter 3. Chapter 2 is an original representation and discussion of the theoretical concepts which motivate and complement the experimental work in this thesis. In chapter 6 some arguments are given which may explain what in some aspects is the rather surprising outcome of experiments on zinc paratacamite.

Chapter 2

# Theoretical background

## 2.1 The emergence of a solid state

One of the most intriguing aspects of condensed matter physics is that it covers the domain from strictly quantum mechanical phenomena to the classical physics we are familiar with from everyday experience. If parts of a system can be identified as behaving essentially *classical*, this allows important simplifications to be made to the description of the system. One of the underlying principles in this cross-over from quantum mechanics to classical mechanics is described in Philip Anderson's famous article "More is different" [6]. It describes how symmetries which are central in the solutions of the Schrödinger equation are broken when the size of the system is increased to macroscopic dimensions, giving rise to a new level of complexity requiring a new scientific approach. Anderson illustrated this idea by contrasting the inversion of the ammonia molecule $NH_3$, with the absence of such an inversion for the always right-handed spiral of sugar molecules made by living organisms. It goes against our intuitive concept of what is a particle that in the ground state the nitrogen atom is at both sides of the $H_3$ plane at the same time. In keeping with the laws of quantum mechanics the ammonia molecule has no dipole moment, when prepared in a stationary state. For the sugar molecule on the other hand, such a symmetric ground state does not exist. In the sugar molecule

the symmetry of the Hamiltonian has been broken, and it behaves in the way we would expect from our every-day intuitive and *classical* concept of a particle. Apparently, there is a qualitative change in the manner in which a (quantum mechanical) system behaves when the system size increases. The Landau theory of phase transitions is beyond the scope of this introduction. To provide a context for the experimental results which form the main body of this thesis, a number of concrete examples of strong symmetry breaking are given.

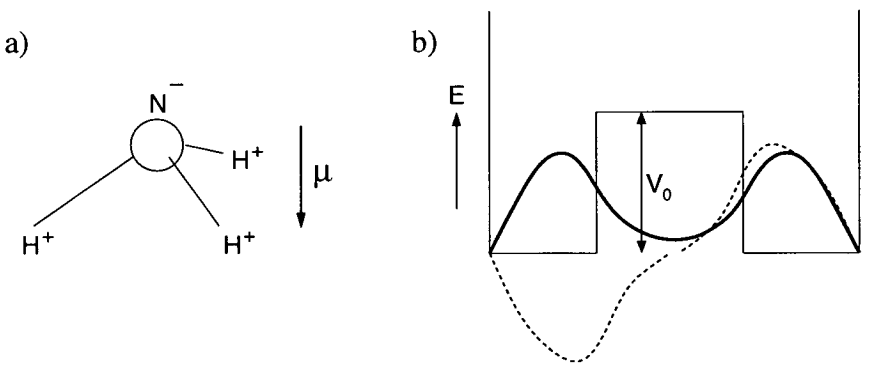


Figure 2.1: a) The "pyramidal" ammonia molecule with dipole moment $\mu$, and b) The symmetric double well potential, and the lowest energy symmetric $|S\rangle$ (thick line) and antisymmetric $|A\rangle$ (broken line) wave functions.

### 2.1.1 The symmetry of the ammonia molecule

The inversion symmetry of the ammonia molecule, a symmetry which is broken in larger systems with the same or a similar Hamiltonian is a good illustration of the emergence of a solid. The three hydrogen atoms form a plane, and the potential energy function for the nitrogen atom has minima above or below this plane. Hence the Hamiltonian $\mathcal{H}$ for the motion of the nitrogen atom has a two-fold up/down symmetry, i.e. $\pi^\dagger \mathcal{H} \pi = \mathcal{H}$ where $\pi$ is the parity operator $\pi^\dagger \mathbf{x} \pi = -\mathbf{x}$. If $|n\rangle$ are non-degenerate eigenfunctions of $\mathcal{H}$ so that $\mathcal{H}|n\rangle = E_n |n\rangle$, then all these $|n\rangle$ must possess the same symmetry as the Hamiltonian $\mathcal{H}$. This follows from $\pi^\dagger \mathcal{H} \pi = \mathcal{H}$, which can be rewritten as $[\pi, \mathcal{H}] = 0$, and hence $\pi \mathcal{H} |n\rangle = \mathcal{H} \pi |n\rangle$. The latter condition is only true when $|n\rangle$ is also an eigenfunction of $\pi$, i.e. $\pi |n\rangle = c |n\rangle$. In the present example of space-inversion

symmetry, the eigenvalues of $\pi$ are $\pm 1$. Let's define the lowest two energy eigenfunctions as $\pi |S\rangle = |S\rangle$ (symmetric) and $\pi |A\rangle = -|A\rangle$ (antisymmetric). Figure 2.1 shows the very approximate potential for the nitrogen atom in $NH_3$ where the central barrier is the $H_3$ plane, and approximate shapes for $|S\rangle$ and $|A\rangle$, $\psi_S(\mathbf{x}) = \langle \mathbf{x}|S\rangle$ and $\psi_A(\mathbf{x}) = \langle \mathbf{x}|A\rangle$ respectively.

This *proves* that quantum mechanics prescribes that for any non-degenerate eigenstate, as is the case for the lowest two energy levels of ammonia, the ammonia molecule has no dipole moment. Note that also in the case of $|A\rangle$ the probability of finding the nitrogen atom at either side of the barrier, given by $|\psi_A(\mathbf{x})|^2$, is equal. This proof is not specific to the ammonia molecule nor to parity symmetry. A much more general statement can be made using a group-theoretical argument [202].

Of course, it is always possible to "put" the nitrogen either in the left ($L$) or the right ($R$) well, by preparing the system in states $|L\rangle = \frac{1}{\sqrt{2}}(|S\rangle - |A\rangle)$ and $|R\rangle = \frac{1}{\sqrt{2}}(|S\rangle + |A\rangle)$ respectively. However, as long as $|S\rangle$ and $|A\rangle$ have different energy eigenvalues, $E_S$ and $E_A$ respectively, the states $|R\rangle$ and $|L\rangle$ are not eigenstates of the Hamiltonian, and therefore, they are not stationary. Apart from an arbitrary phase factor the time evolution of $|L\rangle$ is given by

$$|L;t\rangle = \frac{1}{\sqrt{2}}\left(|S\rangle - e^{-i(E_A - E_S)t/\hbar}|A\rangle\right). \tag{2.1}$$

Hence, we see that after a time $t_i = \frac{h}{2(E_A - E_S)}$ the nitrogen atom has tunnelled through the barrier, and $|L;t = t_i\rangle = |R\rangle$. The nitrogen atom is hopping from one side to the other with a frequency $\frac{h}{(E_A - E_S)} = 23.79$ GHz [46], so well defined and deterministic that it has been used for the first atomic clock.

It should be stressed that this oscillating state is very different from the ground state. In the ground state $|S\rangle$ (and also in $|A\rangle$) the nitrogen atom is at both sides of the barrier *at all times*, i.e. the atom, including its nucleus, is spread-out in space. Again different is the situation for the sugar molecule, which is asymmetric even in the ground state, and does not invert. According to quantum mechanics this situation

can only occur when the states $|A\rangle$ and $|S\rangle$ are degenerate, i.e. $E_A = E_S$, and hence $t_i = \frac{h}{2(E_A - E_S)} \rightarrow \infty$. By solving the Schrödinger equation for the double well, it can be seen that the energy difference $E_A - E_S \rightarrow 0$ when the mass of the tunnelling particle is increased, and when the height of the potential barrier is increased. The inversion will go slower and slower for heavier elements, and eventually cannot be observed anymore.

This shows how, in the presence of the right kind of degeneracy, the classical localised state can become a quantum-mechanically allowed solution. However, it would be a pointless exercise to try and prepare a sugar molecule which is symmetrical in $\pi$, i.e. left- and right-turning at the same time, despite the fact that this state would in theory still be a possible ground state. In practice a "symmetry breaking transition" happens before $E_A = E_S$ because the system is always coupled to the outside world in some way. If the system is in contact with a dissipative environment [1], the oscillations as described in equation 2.1 become (strongly) damped and the system will evolve towards a localised, i.e. *classical* state [117]. Even when the system is prepared in a state which at $t = 0$ reflects the symmetry of the Hamiltonian, like $|S\rangle$ in the case of the ammonia or sugar molecules, the symmetry will be broken in favour of a classical state [117, 214]. Spontaneous symmetry breaking is the mechanism by which for example a sugar molecule is always either left- or right-turning.

### 2.1.2 Symmetry breaking in a ferromagnet

Another instructive example of a symmetry breaking transition is the case of a ferromagnet. Take for example a cubic lattice of $N$ spins $\mathbf{S}_i$ with spin quantum number $S$, where nearest neighbour spins are coupled with a exchange interaction of strength $J_{\mathrm{nn}}$, so that the Hamiltonian is given by 1.2. The Heisenberg Hamiltonian is invariant upon the simultaneous rotation of all spins from one coordinate frame to another related by the Euler angles $\theta, \phi$ and $\psi$; $S_i' = R(\theta, \phi, \psi)S_i$. This is reflected in the degeneracy of the ferromagnetic ground state of $2S_{\mathrm{tot}} + 1 = 2NS + 1$, just like each individual free spin

[1] In this context, "the environment" can also mean additional internal degrees of freedom [213], such as nuclear moments in solids [177], etc.

has $2S+1$ states $m_S = -S, -S+1, \ldots S$. However, unlike a single free spin, a system consisting of a macroscopic number $N$ of spins will not fluctuate between the different states $|M_{S\text{tot}}\rangle$. These states are connected to each other via infinite-wavelength spin waves. Figure 2.2 shows a typical dispersion relation for spin-waves in a ferromagnet. In agreement with the spin-rotational symmetry of the Hamiltonian 1.2, the $q = 0$ spin-waves have zero energy. Nevertheless they do not occur, because their multiplicity is so low; of order $2NS+1$ compared to the total number of states $(2S+1)^N$. Hence,

> the time required for the total spin to drift around from one orientation to an essentially different one, in case we prepared the system originally in a state of definite spin orientation, is of order $N$ and thus extremely large. [5].

As in the previous example, the timescale of the symmetry restoring excitations goes to infinity because the energy spacing between the states goes to zero. Hence, this part of the spectrum is also called the *thin end* of the spectrum.

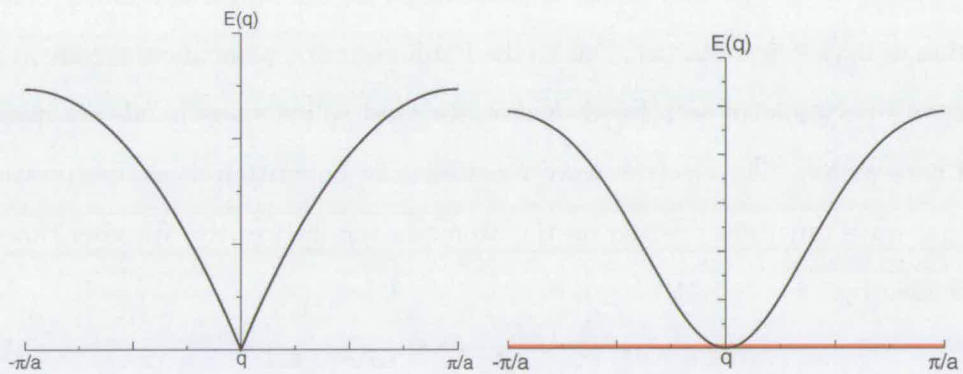


Figure 2.2: The spin-wave dispersion in a ferromagnet (left) and in a system in which global spin-rotational symmetry is not broken (right) [207]. The red line in the right panel, coinciding with the $x$ axis, gives the "dispersion" relation for the (zero-energy) collective spin modes on the kagomé lattice.

### 2.1.3 The solid state

As a last example; the symmetry-breaking transition to the solid state, a small wonder witnessed every time we opened our reaction vessel to find the shiny crystallites of

jarosite or paratacamite.

Cool a vessel with $^3$He or $^4$He to sufficiently low temperatures and it will become a Fermi or a Bose liquid respectively, which are normal (i.e. non symmetry broken) quantum states of matter [150]. However, Li which is only slightly heaver than He, condenses into a solid at a temperature as high as 298 K. In the solid the nuclei are classically localised particles, fixed in a periodic lattice. The lattices found in the solid state of matter in nature display a wide array of symmetries, but clearly the translational invariance of the underlying Hamiltonian has been broken. The symmetries which remain are always discrete symmetries, which are then the underlying symmetries of the Hamiltonian describing the electronic motion. This restricts the wave functions of electrons in solids to Bloch functions, of the form

$$\psi_{k,n}(\mathbf{x})(= \langle \mathbf{x}|\mathbf{k},\mathbf{n}\rangle) = e^{i\mathbf{k}\mathbf{x}} u_{k,n}(\mathbf{x}), \tag{2.2}$$

where $-\pi/a \leq k \leq \pi/a$ and $u_k(\mathbf{x})$ is periodic in $\mathbf{x}$, i.e. invariant under a lattice translation $\mathbf{g}$; $u_k(\mathbf{x}+\mathbf{g}) = u_k(\mathbf{x})$. Due to the Pauli exclusion principle there are at most two electrons per atom in each band. Hence, for most solids many bands are involved, labelled here with $n$. The electron wave functions can be written as a superposition of orthogonal wave functions centred on the atoms in the lattice, the Wannier functions $w_n$ as defined by

$$\psi_{k,n}(\mathbf{x}) = N^{-1/2} \sum_{i=0}^{N} e^{i\mathbf{k}\cdot\mathbf{g}_i} w_n(\mathbf{x}-\mathbf{g}_i), \tag{2.3}$$

The sum is here over all $N$ atoms in the lattice, labelled with $i$. In general the Wannier functions are not eigen functions because they are constructed from a superposition of Bloch states with different $k$. Neither are they the atomic wave functions $|n\rangle$, which in a solid are in general not orthogonal. The atomic wave functions will overlap in a solid so that the hopping of electrons from site $i$ to site $j$ is calculated with

$$t_{ij} = \langle n_i|\mathcal{H}|n_j\rangle\,. \tag{2.4}$$

In the tight-binding approximation $t = t_{i,i\pm1}$ is the only non-zero contribution apart from $t_{ii} = E_{k=0}$. In this case the dispersion of the band $n$ is given by [182]

$$E_n(k) = E_n(k = 0) - 2t\cos(ka). \tag{2.5}$$

When in the lattice the atomic wave functions do not overlap, such as is the case for the $n = 1$s, 2s and $2p$ levels in $3d$ transition metal compounds, the hopping $t = 0$ and the band is dispersionless. For these "bands" all wave vectors $\mathbf{k}$ have become degenerate, so that the maximally localised Wannier functions become eigenfunctions equal to the atomic wave functions $|n\rangle = |1s\rangle, |2s\rangle$ etc. In real systems the phase relations between the Wannier functions will then be lost, breaking the discrete translational symmetry of the lattice. This is also the case for the magnetic f shells in the rare-earth metals and their compounds. As a consequence the unpaired electrons in these systems form local moments, which only interact with each other indirectly via the itinerant electrons from the covalent bands in the system.

In "ab-initio" calculations of the electronic properties of crystals, this symmetry breaking allows for important simplifications of the numerical problem. First, the nuclei are assumed fixed, and are treated in the Born-Oppenheimer approximation [182]. Second, the atomic wave functions are taken for the core-level electrons. Not only does this constitute an enormous simplification of the calculation, it is actually a better representation of the physics, than could be achieved with a full basis of delocalised wave functions for each electron and each nucleus. Only the valence electrons need to be described as Bloch waves. For the transition metals, this includes in principle the magnetic shells/bands of unpaired electrons.

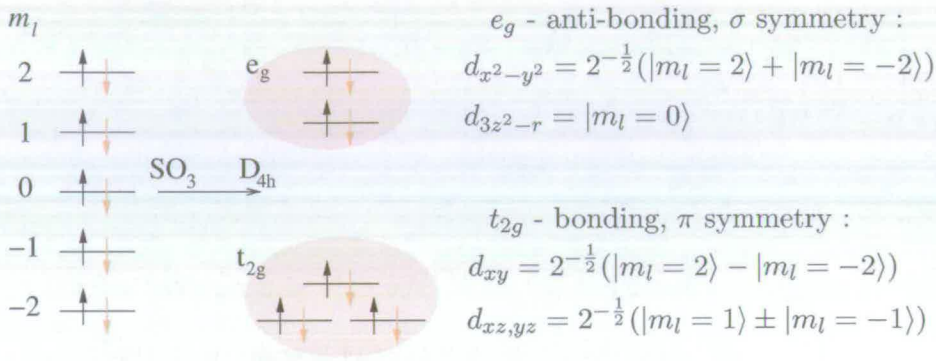


Figure 2.3: **Left:** Illustration of the quenching of the orbital angular momentum in the presence of a $D_{4h}$ crystal field. **Right:** The eigenstates of the $3d$ shell. In a cubic or octahedral ($O_h$) crystal field the $e_g$ levels and the $t_{2g}$ levels are still degenerate amongst each-other. They split in the way illustrated here due to a trigonal distortion, like the Jahn-Teller distortion.

## 2.2 Magnetism in transition-metal compounds

### 2.2.1 Crystal fields

So far the energy bands have been labelled with $n$ the quantum number of the corresponding atomic wave function. This is correct as far as the principal quantum number is concerned, but due to the crystal field surrounding every atom in a solid, the orbital angular momentum is no longer a conserved quantity. In the transition-metal compounds these are the cation $3d$ orbitals which for free ions all have an angular momentum quantum number $L = 2$. For both zinc paratacamite and iron jarosite the crystal field is approximately a trigonally distorted octahedron of symmetry $D_{4h}$. In $D_{4h}$ symmetry the eigenstates can still be written using a basis set of the states $|L = 2, m_L\rangle$. The five new states, all with $\langle L\rangle = 0$, pair into 3 bonding and 2 anti-bonding states, with the largest electron density pointing away from the ligands and towards the ligands respectively.

The energy difference between the $e_g$ and the $t_{2g}$ levels, which in an octahedral crystal field ($O_h$) are doubly and triply degenerate respectively, is called $10Dq$. A partial occupation of either the $e_g$ or the $t_{2g}$ levels will give rise to an orbital degeneracy. For example, in the case of $Cu^{2+}$ ($3d^9$) in a $O_h$ crystal field the unpaired electron in the

$e_g$ levels can occupy both the $d_{x^2-y^2}$ and the $d_{3z^2-r}$ orbital. For $Cu^{2+}$ this degeneracy is often lifted by a trigonal distortion of the $O_h$ crystal field, called a Jahn-Teller distortion [101]. Since only the lowest energy orbital will be occupied this minimises the total energy of the ion. However, there are examples where this degeneracy is not lifted, giving rise to an additional degree of freedom which often couples to the spin-degrees of freedom [110, 133, 215].

In most of the first-row transition-metal oxides the energy splittings between these crystal-field-split levels are larger than the $3d$ band-width and hence they will all have their own bands. Often the crystal-field splittings lie in the region of the optical spectrum, so that many compounds have colours characteristic of the crystal field of the transition metal ions. We will distinguish between $t_\sigma$ and $t_\pi$ hopping, reflecting the large difference in overlap of the bonding $t_{2g}$ and antibonding $e_g$ orbitals with the ligand orbitals. Systems with a higher electron density, such as metals, and many compounds of 2nd and 3rd row transition metals and also $La_2CuO_4$, the overlap between the atomic orbitals is larger. Hence, $t$ is larger and the electron band-with exceeds the crystal-field splitting. These materials are shiny or very dark coloured, depending on whether they are conducting or not.

### 2.2.2 The Pauli exclusion principle

Another symmetry of fundamental importance in the rest of this thesis is the permutation symmetry between indistinguishable particles [182]. "Indistinguishable" means that the particles must not only be of the same kind, but also that it is impossible to keep track of the individual trajectories of the particles in a classical way, because their wave functions overlap in space, i.e.

$$\int d\mathbf{r} |\omega_a(\mathbf{r})|^2 |\omega_b(\mathbf{r})|^2 \neq 0, \tag{2.6}$$

In this case the Hamiltonian should not change on application of permutation of the labels $P_{12}$ in the total wave function

$$\Psi(\mathbf{r}_1, \mathbf{r}_2, \mathbf{r}_3, \ldots) = \langle \mathbf{r} | \left( |n_1\rangle \, |n_2\rangle \, |n_3\rangle \ldots \right) \tag{2.7}$$

between any two overlapping electrons, i.e. $[\mathcal{H}, P_{12}] = 0$. All elementary building blocks in materials, and even their composite particles, split up into two classes. Bosons, for which

$$P_{12} \, |n_1\rangle \, |n_2\rangle \, |n_3\rangle \ldots = |n_2\rangle \, |n_1\rangle \, |n_3\rangle \ldots = + \, |n_1\rangle \, |n_2\rangle \, |n_3\rangle \ldots, \tag{2.8}$$

and fermions, for which

$$P_{12} \, |n_1\rangle \, |n_2\rangle \, |n_3\rangle \ldots = |n_2\rangle \, |n_1\rangle \, |n_3\rangle \ldots = - \, |n_1\rangle \, |n_2\rangle \, |n_3\rangle \ldots \tag{2.9}$$

Bosons always have zero or integer spins, and fermions always have half-odd-integer spin quantum numbers. Electrons are fermions with $S = 1/2$ and hence $m_S = \pm 1/2$. The two spin states are often labelled $\alpha$ and $\beta$, for up and down spin respectively. A "particle" consisting of two electrons has integer spin, and is a boson. An example are Cooper pairs which are a quasi-particle excitation involving two electrons and a phonon, which can form a Bose condensate giving rise to superconductivity [40]. The permutation of the coordinates of the composite bosonic particle requires a double permutation of the constituent electrons, and $-1 \times -1 = 1$.

The general Hamiltonian of the electrons in a material is given by

$$\mathcal{H} = h(\mathbf{r}_1) + h(\mathbf{r}_2) + \ldots h(\mathbf{r}_N) + \sum_{\langle i,j \rangle} \frac{e^2}{|\mathbf{r}_i - \mathbf{r}_j|} + \sum_i \lambda_i \hat{L}_i \cdot \hat{S}_i. \tag{2.10}$$

where $h(\mathbf{r}_i)$ are the single-electron Hamiltonians. To simplify the problem consider first a two-electron system with a Hamiltonian which does not contain any terms which are both a function of spin $m_S$ and of position $\mathbf{r}$, i.e. the spin-orbit term $\sum_i \lambda_i \hat{L}_i \cdot \hat{S}_i$. In

that case the total wave function can be written as a product of the space and the spin part

$$\Psi = \Phi(\mathbf{r}_1, \mathbf{r}_2)\chi \tag{2.11}$$

and the permutation operator can be written as $P_{12} = P_{12}^{\text{space}} P_{12}^{\text{spin}}$. Let's as a starting point define $\omega_{a,b\ldots}(\mathbf{r})$ as the eigenstates of the one electron Hamiltonians $h(r_1), h(r_2)\ldots$ [2] The total ground state wave function $\Phi(\mathbf{r}_1, \mathbf{r}_2)$ of $\mathcal{H}'$ defined as

$$\mathcal{H}'(\mathbf{r}_1, \mathbf{r}_2) = h(\mathbf{r}_1) + h(\mathbf{r}_2). \tag{2.12}$$

can now be constructed from the product of $\omega_a(\mathbf{r}_1)$ and $\omega_b(\mathbf{r}_2)$ so that $\Phi(\mathbf{r}_1, \mathbf{r}_2)$ is an eigenfunction of $P_{12}^{\text{space}}$ with eigenvalues $p_{\mathbf{r}} = \pm 1$. In the same way $\chi$ must be an eigenfunction of $P_{12}^{\text{spin}}$ with eigenvalues $p_{\mathbf{S}} = \pm 1$. To satisfy condition 2.9 only combinations of the space and spin parts of the wave function are allowed where $p_{\mathbf{r}} p_{\mathbf{S}} = -1$.

$$\chi \begin{cases} 2^{-\frac{1}{2}}(\alpha\beta - \beta\alpha) & S_{\text{tot}} = 0 \text{ (spin-singlet)} \quad p_S = \text{-1} \\ \alpha\alpha & \\ 2^{-\frac{1}{2}}(\alpha\beta + \beta\alpha) & S_{\text{tot}} = 1 \text{ (triplet)} \quad p_S = +1 \\ \beta\beta & \end{cases}$$

$$\Phi(\mathbf{r}_1, \mathbf{r}_2) \begin{cases} 2^{-\frac{1}{2}}[\omega_a(\mathbf{r}_1)\omega_b(\mathbf{r}_2) - w_b(\mathbf{r}_1)w_a(\mathbf{r}_2)] & p_{\mathbf{r}} = \text{-1} \\ \omega_a(\mathbf{r}_1)\omega_a(\mathbf{r}_2) & \text{closed shell} \\ 2^{-\frac{1}{2}}[\omega_a(\mathbf{r}_1)\omega_b(\mathbf{r}_2) + \omega_b(\mathbf{r}_1)\omega_a(\mathbf{r}_2)] & \text{valence bond} \quad p_{\mathbf{r}} = +1 \\ \omega_b(\mathbf{r}_1)\omega_b(\mathbf{r}_2) & \text{closed shell} \end{cases} \tag{2.13}$$

All these states are eigenstates of $\mathcal{H}'$, now correctly symmetrised. It should be clear that the total wave function can only be antisymmetric on permutation of any pair of

[2] One could start from a situation where the one-electron orbitals are a closer approximation of the actual solution of the total Hamiltonian $\mathcal{H}$, by adding to each $\langle(\mathbf{r}_i)$ a term $v(i)$ which is the average potential seen by electron $i$ due to the averaged Coulomb interactions with all other electrons in the system [196]. This is the Hartree-Fock approximation.

electrons, if each electron occupies a different state. This includes a different spin state, and therefore two electrons with opposite spin can occupy one spatial orbital. That is the Pauli exclusion principle.

An easy way to construct the antisymmetric wave function from the one-particle eigenfunction in the case when many electrons are involved, is with a Slater determinant. For example, the even-numbered $N$ electron $S_{\text{tot}} = 0$ configuration can be constructed from the available orbitals all occupied with an $\alpha$ and a $\beta$ electron;

$$\Psi(S_{\text{tot}} = 0, M_{S_{\text{tot}}} = 0; \mathbf{r}_1, \mathbf{r}_2, \mathbf{r}_3, \ldots \mathbf{r}_N) = \tag{2.14}$$

$$(N!)^{-\frac{1}{2}} \begin{vmatrix} \omega_a\alpha(\mathbf{r}_1) & \omega_a\beta(\mathbf{r}_1) & \omega_b\alpha(\mathbf{r}_1) & \omega_b\beta(\mathbf{r}_1) & \omega_c\alpha(\mathbf{r}_1) & \ldots \\ \omega_a\alpha(\mathbf{r}_2) & \omega_a\beta(\mathbf{r}_2) & \omega_b\alpha(\mathbf{r}_1) & \omega_b\beta(\mathbf{r}_2) & \omega_c\alpha(\mathbf{r}_2) & \ldots \\ \vdots & & & & & \\ \omega_a\alpha(\mathbf{r}_N) & \omega_a\beta(\mathbf{r}_N) & \omega_b\alpha(\mathbf{r}_N) & \omega_b\beta(\mathbf{r}_N) & \omega_c\alpha(\mathbf{r}_N) & \ldots \end{vmatrix}$$

Ferromagnetic states with total spin up to $S_{\text{tot}} = N/2$ can be obtained by using more $\alpha$ then $\beta$ spins, or the other way around, which will leave part of the orbitals half-filled. In this case higher energy orbitals must become occupied, and hence we can conclude that in the absence of electron-electron interactions, the ground state is non-magnetic.

### 2.2.3 Coulomb interactions

The properly antisymmetrised total wavefunctions can now be used as a basis set for calculations where the Coulomb interactions between the electrons are treated as a perturbation. Of course, the Coulomb energy depends on the overlap between the electrons. From equations 2.13 it is immediately clear that the doubly occupied orbitals have the largest Coulomb energy. In most transition metal compounds, to first order this energy

$$U_{aa(bb)} = e^2 \int d\mathbf{r}_1 \int d\mathbf{r}_2 \frac{|\omega_{a(b)}(\mathbf{r}_1)|^2 |\omega_{a(b)}(\mathbf{r}_2)|^2}{|\mathbf{r}_1 - \mathbf{r}_2|} \tag{2.15}$$

is much larger than the splitting of the $3d$ levels due to the crystal field as discussed in the previous section. Note that this is *not* the explanation that the transition metals and their compounds are magnetic. In the case of half-filled orbitals the magnetic configuration can still be triplet or singlet, i.e. ferromagnetic or non-magnetic.

Let's label the configurations of half-filled orbitals in 2.13 as $\Phi^+$ and $\Phi^-$ where the "$\pm$" refers to the sign of the $P_{12}^{\text{space}}$ eigenvalues $p_{\mathbf{r}}$. For these states, the probability $\rho(\mathbf{x}_1, \mathbf{x}_2)$ that electrons are simultaneously found at $\mathbf{x}_1$ and $\mathbf{x}_2$ respectively is given by

$$\rho^{\pm}(\mathbf{x}_1, \mathbf{x}_2) = |\Phi^{\pm}(\mathbf{x}_1, \mathbf{x}_2)|^2 = 2^{-\frac{1}{2}}\{|\omega_a(\mathbf{x}_1)|^2|\omega_b(\mathbf{x}_2)|^2 + |\omega_a(\mathbf{x}_2)|^2|\omega_b(\mathbf{x}_1)|^2 \pm 2\mathrm{Re}\left[\omega_a(\mathbf{x}_1)\omega_b(\mathbf{x}_2)\omega_a^*(\mathbf{x}_2)\omega_b^*(\mathbf{x}_1)\right]\}d\mathbf{x}_1 d\mathbf{x}_2. \tag{2.16}$$

The last term is the exchange density which arises from the symmetrisation of the orbitals. It is important to note that this term can be non-zero even if $\omega_a$ and $\omega_b$ are orthogonal. For $\psi^-$ which must be a spin-triplet, it can be seen that the exchange term should be subtracted, and cancels out the first term so that $\rho^-(\mathbf{x}_1, \mathbf{x}_2) = 0$ for $\mathbf{x}_1 = \mathbf{x}_2$. The probability to find the two electrons at the same point in space vanishes. On the other hand, for $\psi^+$ we see that in general it is now possible to find the two electrons at the same point in space; in fact, both electrons occupy the same wave function, as was the case for the closed shells [3].


Figure 2.4: Antisymmetric (left) and symmetric (right) superposition of two different orbitals. A darker shade signifies a higher electron density.

Figure 2.4 is a schematic depiction of the electron density for the configurations consisting of two half filled shells in equation 2.13. There is an obvious difference in

[3] The interpretation of the antisymmetric spin-singlet is in this case no different to the case of closed shells; it does not correspond to an antiferromagnetic state but to a non-magnetic state, as denoted by the total magnetic quantum number $S_{\text{tot}} = 0$, with no internal magnetic structure.

overlap between the singlet $\Phi^+$ and triplet $\Phi^-$, and hence the Coulomb energy of these states $U_{ab}^{\pm}$ is different too, so that either the magnetic or the non-magnetic state is chosen as the ground state. To first order perturbation theory,

$$U_{ab}^{\pm} = \int d\mathbf{r}_1 \int d\mathbf{r}_2 \rho^{\pm}(\mathbf{r}_1, \mathbf{r}_2) \frac{e^2}{|\mathbf{r}_1 - \mathbf{r}_2|} = C_{ab} \pm J_{ab} \tag{2.17}$$
$$= C_{ab} + J_{ab} \langle \chi | P_{12}^{spin} | \chi \rangle .$$

Both spin states have the Coulomb integral in common,

$$C_{ab} = e^2 \int d\mathbf{r}_1 \int d\mathbf{r}_2 \frac{|\omega_a(\mathbf{r}_1)|^2 |\omega_b(\mathbf{r}_2)|^2}{|\mathbf{r}_1 - \mathbf{r}_2|} \tag{2.18}$$

while their energy difference is determined by the exchange integral, which directly arises from the exchange density 2.16

$$J_{ab} = e^2 \int d\mathbf{r}_1 \int d\mathbf{r}_2 \frac{2\mathrm{Re}\left[\omega_a(\mathbf{x}_1)\omega_b(\mathbf{x}_2)\omega_a^*(\mathbf{x}_2)\omega_b^*(\mathbf{x}_1)\right]}{|\mathbf{r}_1 - \mathbf{r}_2|}. \tag{2.19}$$

It can be shown that the integral $J_{ab}$ is positive [70], and hence the ground state is a triplet. This is the direct exchange mechanism, which is responsible for the ferromagnetic alignment of spins within for example the transition metal $3d$ shell, as long as there are free $3d$ levels. We shall see that the energy difference can be expressed in terms of spin operators, and takes the form of the Heisenberg Hamiltonian

$$\mathcal{H}_{mag} = -2J_{ab}\hat{S}_1 \cdot \hat{S}_2. \tag{2.20}$$

Figure 2.2.3 illustrates this situation for a $Cr^{3+}$ ion in a $D_{4h}$ crystal field.

### 2.2.4 The valence bond

When $\omega_a$ and $\omega_b$ correspond to orbitals centered on different ions the singlet becomes the ground state. The electron density is the highest in between the two protons,

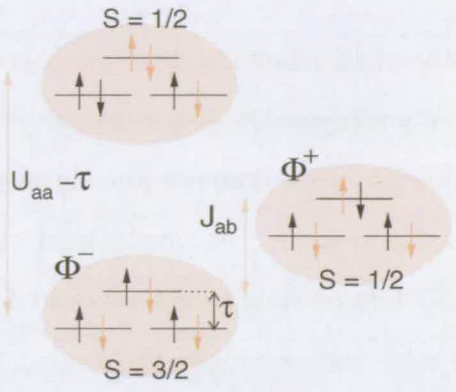


Figure 2.5: Illustration of the direct exchange mechanism. The energies of the different configurations for a $3d$ shell in a $D_{4h}$ crystal field occupied by electrons. For clarity only the $t_{2g}$ levels are shown. The $3d_{xy}$ level is $\tau$ higher in energy than the $3d_{xz}$ and $3d_{yz}$ orbitals due to the trigonal distortion of the octahedral (cubic) crystal field. The red arrows are unoccupied spin orbitals and $J_{ab}$ is the direct exchange integral.

creating a valence bond. The situation as illustrated in the right panel of figure 2.4 can in this case be taken more literally to resemble the actual charge density. In the case of molecular hydrogen the total Hamiltonian is

$$\begin{aligned}\mathcal{H} =&\mathcal{H}_{at}(\mathbf{r}_1 - \mathbf{R}_a) + \mathcal{H}_{at}(\mathbf{r}_1 - \mathbf{R}_a) - \\ &\frac{e^2}{|\mathbf{r}_1 - \mathbf{R}_b|} - \frac{e^2}{|\mathbf{r}_2 - \mathbf{R}_a|} + \frac{e^2}{|\mathbf{r}_1 - \mathbf{r}_2|} + \frac{e^2}{|\mathbf{R}_a - \mathbf{R}_b|},\end{aligned} \tag{2.21}$$

and $\omega_{a(b)}$ are eigenfunctions of $H_{at}(\mathbf{r} - \mathbf{R}_{a(b)})$. The energy difference between the two levels is now given by

$$E^{S_{\text{tot}}=1} - E^{S_{\text{tot}}=0} = 2\frac{l^2 C'_{ab} - I_{ab}}{1 - l^4} \tag{2.22}$$

where

$$C'_{ab} = C_{ab} - e^2 \int d\mathbf{r}_1 \frac{|\omega_a(\mathbf{r}_1)|^2}{|\mathbf{r}_1 - \mathbf{R}_b|} - e^2 \int d\mathbf{r}_2 \frac{|\omega_b(\mathbf{r}_2)|^2}{|\mathbf{r}_2 - \mathbf{R}_a|} \tag{2.23}$$

and

$$I_{ab} = J_{ab} - e^2 l \int d\mathbf{r}_2 \frac{\omega_a^*(\mathbf{r}_1)\omega_b(\mathbf{r}_1)}{|\mathbf{r}_2 - \mathbf{R}_a|} - e^2 l \int d\mathbf{r}_2 \frac{\omega_b^*(\mathbf{r}_2)\omega_a(\mathbf{r}_2)}{|\mathbf{r}_2 - \mathbf{R}_a|}.$$

where $l = \langle \omega_a | \omega_b \rangle$. This is the Heitler-London description of the valence bond. It illustrates how the formation of a spin-singlet gives rise to an effective attractive force between the nuclei. However, on its own it does not provide an accurate description of the ground state even in molecular hydrogen. At smaller inter-nuclear distances charge fluctuations start to play a role. Ionised state configurations (the closed shells in 2.13) start to mix into the ground state and eventually the ground state is best described by symmetric and antisymmetric molecular orbitals. This costs a lot of energy due to the electron-electron interaction, but happens due to the Coulomb attraction of the electron centred initially on proton $a$, with proton $b$;

$$t = e^2 \int d\mathbf{r} \frac{\omega_a^*(\mathbf{r})\omega_b(\mathbf{r})}{|\mathbf{r} - \mathbf{R}_b|} \tag{2.24}$$

The total matrix element which mixes the neutral singlet state with the two ionised configurations is $-2t$. It can be shown that as a result the ground state of the singlet is lowered by a further $\frac{4t^2}{U_{aa}}$ with respect to the triplet state [4]. This exchange mechanism is called kinetic exchange [4]. The total magnetic interaction for the hydrogen molecule is now

$$J_{ab} \approx J_{\text{dir}} + J_{\text{kin}} = 2\frac{l^2 C'_{ab} - I_{ab}}{1 - l^4} + \frac{4t^2}{U_{aa}}. \tag{2.25}$$

As mentioned earlier, in solid state systems the eigenstates of the valence electrons are Bloch waves, with a band for each corresponding atomic level. The Bloch waves are analogous to the molecular orbitals in molecular hydrogen, and hence, kinetic exchange is thought to be the dominant form of exchange in transition metal compounds. The treatment in terms of Coulomb and exchange integrals given here for molecular hydrogen, can also be given in the case of solid state systems, see for example Zeiger and Pratt [237] or Szabo and Ostlund [196]. However, the energy $U_{aa}$ is not always the relevant energy gap for doubly occupied states. In particular in transition-metal oxides with more than 4 or 5 $3d$ electrons, often the top of the filled oxygen $2p$ band

[4] Note that in this case $U_{aa} = U_{bb}$

has a higher energy than the top of the filled transition metal $3d$ band [235]. In that case there is a net charge transfer from the oxygen ligands to the transition-metal ions, giving rise to non-integer valences. These systems are called charge-transfer insulators [235] as opposed to Mott insulators. The relevant energy gap is in this case often denoted as $\Delta_{pd}$, as opposed to $U$ for the Mott insulators. In both cases the Hubbard model as discussed next, in section 2.2.5 is thought to apply.

### 2.2.5 The Hubbard model

The problem as sketched above can be formulated in second-quantisation language, which has the advantage that the antisymmetrisation of the electron wave function is automatically taken care of. This is the Hubbard model, defined by the Hamiltonian [94, 70, 128],

$$\mathcal{H} = -t \sum_{<\mathbf{j},\mathbf{l}>} \sum_{\sigma} (c^{\dagger}_{\mathbf{j}\sigma} c_{\mathbf{l}\sigma} + c^{\dagger}_{\mathbf{l}\sigma} c_{\mathbf{j}\sigma}) + U \sum_{j} \hat{n}_{j\uparrow} \hat{n}_{j\downarrow} \tag{2.26}$$

where $t$ is the hopping integral of the charge-carriers, the operator $c_{\mathbf{i}\sigma}$ creates an electron with spin $\sigma$ in an orbital centred at site $i$, $c^{\dagger}_{\mathbf{i}\sigma}$ is the corresponding annihilation operator removing an electron at site $i$, $\hat{n}_{\mathbf{j}\sigma}$ is the electron occupation number at site $j$, and $U = U_{aa}$ as given in equation 2.15. Here only the valence electrons are considered, and they are assumed to be delocalised into Bloch waves. Hubbard argued [94] that the energy contribution from the Coulomb interaction between electrons residing on neighbouring sites is small compared to the charge fluctuations with energy cost $U$ [94]. This on-site Coulomb interaction splits the $3d$ conduction band in two, a lower band corresponding to singly occupied $3d$ orbitals and an upper band corresponding to doubly occupied $3d$ orbitals. Figure 2.6 illustrates how in the case of perfect half-filling the electrical conductivity of the material depends on the band width $4t$ as determined by equations 2.4 and 2.5.

In general even this simplified model is difficult to solve. However, many transition metal compounds are thought to represent the limiting case of $U/t \rightarrow \infty$. In this case

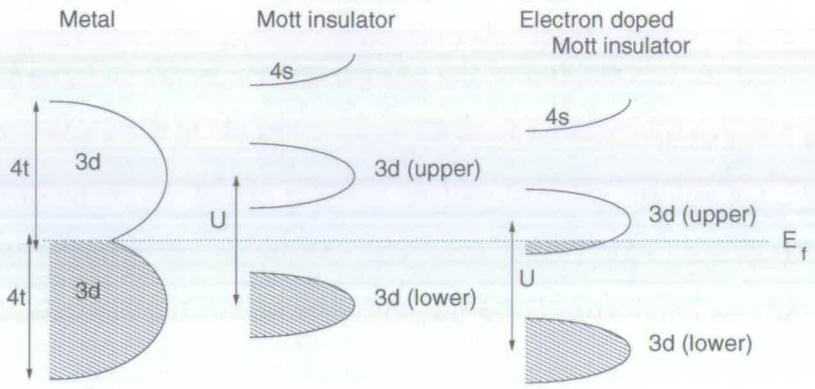


Figure 2.6: In metals the half-filled $3d$ band of the transition metals gives rise to a conducting state, because the density of states at the Fermi level ,$E_f$, is non zero. Most transition metal compounds are narrow-band systems with $U \gg t$, so that the $3d$ bands splits into two Hubbard sub-bands. The density of states at the Fermi level is now zero, and hence most transition metal compounds are insulators, termed Mott insulators. These materials can in general be made conducting by doping them with ions with a different valence.

it is thought [70] that the subspace of low-energy fluctuations can be described by the effective Hamiltonian

$$\mathcal{H}_{\mathrm{tJ}} = -t \sum_{<i,j>} \sum_{\sigma} [(1 - \hat{n}_{i-\sigma}) c^{\dagger}_{i\sigma} c_{j\sigma} (1 - \hat{n}_{j-\sigma}) + \mathrm{c.c.}] + \frac{4t^2}{U} \sum_{<i,j>} \left[ \vec{S}_i \cdot \vec{S}_j - \frac{\hat{n}_i \hat{n}_j}{4} \right] + \text{higher-order exchange terms} \tag{2.27}$$

where the sum is over nearest-neighbour pairs of spins. This is the Hamiltonian of the $t - J$ model, which has been the subject of intense investigation in order to decide whether it includes the essential physics to support super-conducting states up to high temperatures. An important parameter here is the degree of filling of the band; super-conditivity should appear away from half-filling, while when each site has exactly one electron, the system should be a Mott insulator with strong antiferromagnetic correlations [125]. In the case of half-filling the effective Hamiltonian can be further simplified to yield the effective magnetic Hamiltonian

$$\mathcal{H}_{\mathrm{H}} = J_{\mathrm{nn}} \sum_{<i,j>} \hat{S}_i \cdot \hat{S}_j \text{ where } J_{\mathrm{nn}} = 4t^2/U \tag{2.28}$$

where the sum is over all pairs of nearest-neighbour spins $i, j$ and $J_{\rm nn}$ is the nearest-neighbour exchange interaction. This is the kinetic exchange which arises, just like in the treatment in section 2.2.4, from the mixing-in of doubly occupied shells to the ground state singlet, which can be interpreted as charge fluctuations. Superexchange [5] is the counterpart of kinetic exchange in charge-transfer insulators [235].

The Mott metal-insulator transition is thought to coincide with the point where the valence electrons become localised [8]. In the limit of a narrow band, the Wannier functions become eigenstates and the electrons and their spins become *distinguishable* so that a magnetic structure emerges at the atomic scale. This is clearly a symmetry-broken regime of the Hubbard model in the sense that for the unpaired $3d$ electrons the discrete lattice symmetry is broken. That the $3d$ electrons have become distinguishable also means that in general the total electronic wave function does not need to be antisymmetric on permutation of electrons located at different sites! From the discussion in section 2.2.6 it will be clear that this is a necessary condition for the existence of Néel like magnetic order. The remaining hopping $t$ is still thought to give rise antiferromagnetic exchange in the form of the Heisenberg Hamiltonian [8], which it could be argued gives rise to a paradox; if the electrons interact through exchange, how can they be distinguishable? The materials studied in this thesis are narrow-band charge-transfer insulators, and the paradox outlined here is the central problem of this thesis.

### 2.2.6 The Heisenberg Hamiltonian

As already stated in equation 2.17, we can associate the operator $J_{ab}P_{12}^{\rm spin}$ with the energy difference of the two lowest-energy spin states. $P_{12}^{\rm spin}$ can also be written in terms of the spin operators $\hat{S}_1 \cdot \hat{S}_2$ because they have the same eigenstates, the singlet and the triplet, which can be seen from

$$\mathcal{H}_{\rm H} = J_{12}\hat{S}_1 \cdot \hat{S}_2 = \frac{1}{2}J_{12}[(\hat{S}_1 + \hat{S}_2)^2 - \hat{S}_1^2 - \hat{S}_2^2] = \frac{1}{2}J_{12}(S_{tot}^2 - \frac{1}{2}). \qquad (2.29)$$

First of all we see that $\mathcal{H}_{\rm H}$ commutes with $S_{\rm tot}$, the total spin operator. For two spins it can take the values 0 and 1, and hence, the eigen energies of $\mathcal{H}_{\rm H}$ can be calculated from $S^2_{\rm tot} = S(S+1) = 0$ or 2. The eigenstates are given by the symmetric and anti symmetric combinations of the spin states $\alpha$ and/or $\beta$.

$$\begin{array}{lll} S_{tot}=0 & 2^{-\frac{1}{2}}(|\alpha\beta\rangle - |\beta\alpha\rangle) & \text{NM} \qquad E=-\frac{1}{4}J_{12} \\ S_{tot}=1, m_S=1 & |\alpha\alpha\rangle & \left.\begin{array}{l}\\ \\ \\ \end{array}\right\} \\ S_{tot}=1, m_S=0 & 2^{-\frac{1}{2}}(|\alpha\beta\rangle + |\beta\alpha\rangle) & \left.\begin{array}{l}\\ \\ \\ \end{array}\right\} \text{FM} \qquad E=\frac{3}{4}J_{12} \\ S_{tot}=1, m_S=-1 & |\beta\beta\rangle & \left.\begin{array}{l}\\ \\ \\ \end{array}\right\} \end{array} \tag{2.30}$$

FM stand for ferromagnetic and NM for non magnetic, as opposed to antiferromagnetic. The AF state is a superposition of the singlet with the $|S_{\rm tot}=1, M_S=0\rangle$ state;

$$|\text{AF}\rangle = |\alpha\beta\rangle = |S_{\rm tot}=0\rangle + |S_{\rm tot}=1, M_S=0\rangle \tag{2.31}$$

For both the AF state and the singlet state the total magnetisation is zero. The difference between the two is that in the spin-singlet state there are no unpaired spins. The two electrons paired into a spin-singlet state share the same spatial wave function, given by $2^{-\frac{1}{2}}[\omega_a(\mathbf{r}_1)\omega_b(\mathbf{r}_2)+\omega_b(\mathbf{r}_1)\omega_a(\mathbf{r}_2)]$ where $\omega_{a,b}$ are the localised $3d$ orbitals of the ions involved in the pairing [5]. That there are no spins for a magnetic field to align, to measure for example a finite magnetisation using a SQUID magnetometer, can be seen by calculating the expectation value of the spin centred on site $a$,

$$\langle S_a\rangle = \frac{1}{2}(\langle\alpha\beta| - \langle\beta\alpha|)S_a(|\alpha\beta\rangle - |\beta\alpha\rangle) =$$
$$\frac{1}{2}(\langle\alpha\beta|S_a|\alpha\beta\rangle + \langle\beta\alpha|S_a|\beta\alpha\rangle - \langle\alpha\beta|S_a|\beta\alpha\rangle - \langle\beta\alpha|S_a|\alpha\beta\rangle) =$$
$$\frac{1}{2}(\frac{1}{2} - \frac{1}{2}) = 0.$$

[5] In the case ionised configurations are involved, the super-exchange term $\omega_a(\mathbf{r}_1)\omega_a(\mathbf{r}_2)+\omega_b(\mathbf{r}_1)\omega_b(\mathbf{r}_2)$ mixes in.

This is not a classical average of many actually realised spin orientations, the expectation value has been calculated for a single well-defined state.

It is also instructive to actually solve the eigenvalue problem $\mathcal{H}_{\mathrm{H}}|\chi\rangle = E|\chi\rangle$ by exact diagonalisation, because this method can be extended to larger systems. The spin operators $\hat{S}$ can be decomposed into their $x, y$ and $z$ components;

$$\hat{S}_1 \cdot \hat{S}_2 = S_1^x S_2^x + S_1^y S_2^y + S_1^z S_2^z \tag{2.32}$$

and if we take the following basis of spin states $\beta = \{\alpha\alpha, \alpha\beta, \beta\alpha, \beta\beta\}$, then the spin operator matrices $S_{1,2}^{x,y,z}$ can be set-up by letting the operators work on each of these basis elements. This requires the knowledge of the eigenstates of $S^x$ and $S^y$; $|S^x;\pm\rangle = 2^{-\frac{1}{2}}(|\beta\rangle \pm |\alpha\rangle)$ and $|S^y;\pm\rangle = 2^{-\frac{1}{2}}(|\alpha\rangle \pm i|\beta\rangle)$ or the Pauli spin matrices (see for example [26] page 9). The resulting matrix for $\hat{S}_1 \cdot \hat{S}_2$ for a two-spin system on the basis $\beta = \{\alpha\alpha, \alpha\beta, \beta\alpha, \beta\beta\}$ is

$$\hat{S}_1 \cdot \hat{S}_2 = \frac{1}{4}\begin{pmatrix} 1 & 0 & 0 & 0 \\ 0 & -1 & 2 & 0 \\ 0 & 2 & -1 & 0 \\ 0 & 0 & 0 & 1 \end{pmatrix} \tag{2.33}$$

It is now clear that only the two antiferromagnetic states $\alpha\beta$ and $\beta\alpha$ mix to form a singlet with eigenvalue $-\frac{1}{4}$, and the $M_S = 0$ level of the triplets with eigen value $\frac{3}{4}$.

This shows how the lowest-energy electronic configurations as found in sections 2.2.3, 2.2.4 and 2.2.5 can all be written in terms of spin states, with a Hamiltonian given by the Heisenberg Hamiltonian $\mathcal{H}_{\mathrm{H}} = J_{ab}\hat{S}_i \cdot \hat{S}_j$. At first sight it is therefore not a surprise that the same Hamiltonian was derived from the Hubbard model. However, in the treatments of sections 2.2.3 and 2.2.4 $\mathcal{H}_{\mathrm{H}}$ arises in first order perturbation theory from the Coulomb interactions. This can only be assumed to be correct for small $U$. In

the derivation of $\mathcal{H}_{\mathrm{H}}$ from the Hubbard model on the other hand, it was assumed that $U \gg t$.

It is also clear that the AF state is not an eigenstate of the Heisenberg Hamiltonian. This situation does not change for slightly larger systems [120]; regardless of the lattice structure $\mathcal{H}_{\mathrm{H}}$ commutes with $S_{\mathrm{tot}}$. This means that the spectrum of eigenvalues of $\mathcal{H}_{\mathrm{H}}$ can be ordered according to their total spin quantum number $S_{\mathrm{tot}}$. Quantum-mechanical spin-lattice calculations [125, 120] have shown that for most lattices the energy difference between the singlet and the triplet states vanishes in the thermodynamic limit ($N \rightarrow \infty$). In that case a symmetry breaking transition to a classical Néel long range ordered state occurs [5, 6, 120], in which $S_{\mathrm{tot}}$ is not conserved. In the same way as discussed in sections 2.1.1 and 2.1.2 a classical state is selected. Another problem with the AF state is that it is not an eigenstate of $P_{12}^{\mathrm{spin}}$. As mentioned in the previous section, a necessary condition for the presence of localised moments is that the electrons are distinguishable. In other words, the integral of equation 2.16 must be zero. Hence the wave function describing $3d$ electrons localised on different sites no longer needs to be antisymmetric on permutation of the two electrons.

### 2.2.7 Classical vs. Quantum spins

The classical analog of the quantum mechanical Heisenberg Hamiltonian operator 1.2 is defined by

$$E = \langle \mathcal{H}_{\mathrm{H}} \rangle \approx \sum_{\langle i,j \rangle} J_{ij} \vec{S}_i \cdot \vec{S}_j \tag{2.34}$$

The spin operators $\hat{S}$ are replaced with the classical spin vector $\vec{S}$ of magnitude $|S| = \sqrt{S(S+1)}$. The difference between $\hat{S}$ and $\vec{S}$ is the most clear for $S = \frac{1}{2}$ spins. The Hilbert space for $S = \frac{1}{2}$ spins is two dimensional, with basis vectors $|\alpha\rangle = |S = \frac{1}{2}, m_s = \frac{1}{2}\rangle$ and $|\beta\rangle = |S = \frac{1}{2}, m_S = -\frac{1}{2}\rangle$, as opposed to the classical vector $\vec{S}$ with a basis $\hat{x}, \hat{y}, \hat{z}$ the unit vectors along the three dimensions in Euclidian space. The

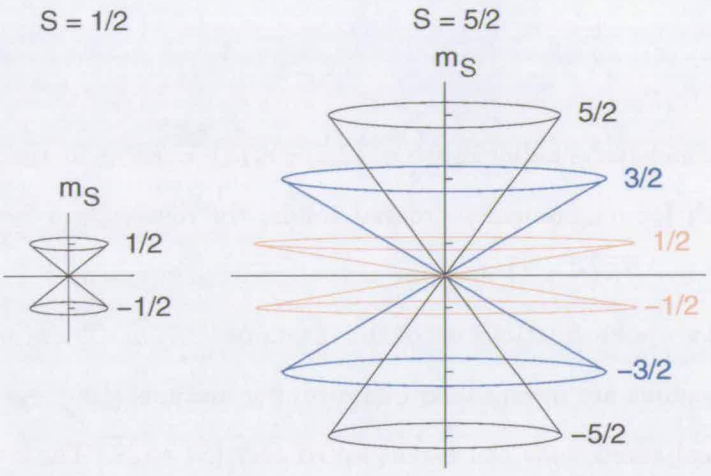


Figure 2.7: The classical representation of the up/down states of a $S = 1/2$ spin, and the 6 states of a $S = 5/2$ spin to scale.

corresponding quantum mechanical spin expectation value is

$$\langle \hat{S} \rangle = \hat{x} \langle S, m_S | \hat{S}_x | S, m_S \rangle + \hat{y} \langle S, m_S | \hat{S}_y | S, m_S \rangle + \hat{z} \langle S, m_S | \hat{S}_z | S, m_S \rangle . \tag{2.35}$$

In the case of $|S = \frac{1}{2}, m_S = \frac{1}{2}\rangle$ this gives $\langle \hat{S} \rangle = \frac{1}{2}\hat{z}$. However, the total spin moment is

$$\langle \alpha | \sqrt{\hat{S}^2} | \alpha \rangle = \langle \alpha | \sqrt{\hat{S}(\hat{S}+1)} | \alpha \rangle = \sqrt{\frac{3}{4}} \approx 0.8660. \tag{2.36}$$

The difference between $|\vec{S}|$ and $|\langle \hat{S} \rangle|$ can be explained in a classical picture as due to the precession of the spin moment around the $\hat{z}$ axis with an angle $\phi = \cos\left(\frac{0.5}{0.866}\right) = 48°$, as shown in figure 2.7. In reality there is no actual precession, the spin direction is simply no longer defined accurately. This is reflected in the expectation values $\langle S_x^2 \rangle$ and $\langle S_y^2 \rangle$ when the spin is maximally aligned along the $\hat{z}$ axis, in the state $|\alpha\rangle$,

$$\langle \alpha | S_x^2 | \alpha \rangle = \frac{1}{2} \left( \langle S_x; + | - \langle S_x; - | \right) S_x^2 \left( | S_x; + \rangle - | S_x; - \rangle \right) = \frac{1}{4} \tag{2.37}$$

where $|S_x; +\rangle$ and $|S_x; -\rangle$ are the eigenstates of $\hat{S}_x$.

As the spin quantum number $S$ increases, the description of the spin by a classical vector $\vec{S}$ becomes increasingly accurate. For $S = 5/2$ for example, the precession

angle is already somewhat smaller $\phi = \cos\left(2.5/\sqrt{8.75}\right) = 38°$. In the semi-classical spin-wave approach for magnetically ordered solids, the discrepancy between the total moment given by $\sqrt{S(S+1)}$ and the actual ordered moment $S$ can be entirely accounted for by zero-point fluctuations of the magnons [107, 5]. These zero-point fluctuations of the magnons are often called quantum fluctuations [120]. As $S \to \infty$ these quantum-mechanical corrections can be neglected and $\langle \hat{S} \rangle \to \vec{S}$. The term "quantum fluctuations" is also used in the context as described in section 2.1.2, as symmetry-restoring fluctuations or Goldstone modes, which in case of long-range order occur for $q \to 2\pi/V^{\frac{1}{3}}$ where $V$ is the volume of the system. In the case of antiferromagnetism it is not immediately clear whether the Goldstone modes appear at all $q$ in addition to zero-point magnons [175, 206] and [70].

From a classical point of view the electron spin of $S = 1/2$ is not sharply defined. From the quantum mechanical point of view on the other hand, it could be considered surprising that the spin of an electron is *always* in a symmetry-broken state. For a single electron it is not possible to construct a state where there is no net spin moment.

### 2.2.8 Spin-orbit coupling

So far the spin-orbit coupling, of the form

$$\mathcal{H}_{LS} = \sum_i \lambda_i \hat{L}_i \cdot \hat{S}_i = \sum_i \frac{2\mu_0^2}{e} \frac{1}{r_i} \left( \frac{\partial V(r_i)}{\partial r_i} \right) \hat{L}_i \cdot \hat{S}_i, \tag{2.38}$$

has been neglected. There are few treatments where this term is included in the derivation of a magnetic exchange Hamiltonian, because $L$ is generally assumed quenched. In transition metal compounds the term is relatively weak compared to the direct-exchange terms, so that when several unpaired electrons are present in each $3d$ shell, the individual $\hat{L}_i$ and $\hat{S}_i$ add up to $\hat{L}$ and $\hat{S}$ before they couple together, so that for

each $3d$ ion $\mathcal{H}_{LS} = \lambda \hat{L} \cdot \hat{S}$ where [237]

$$\lambda = \sum_i \frac{\langle LS|\lambda_i \hat{L}_i \cdot \hat{L}|LS\rangle}{L(L+1)} \frac{\langle LS|\hat{S}_i \cdot S|LS\rangle}{S(S+1)}. \tag{2.39}$$

This is called Russell-Saunders coupling. The other kind of coupling being $jj$ coupling, where each $\hat{S}_i$ and $\hat{L}_i$ first add to $\hat{J}_i$ before they add to a total angular momentum $J$. The latter situation arises in rare earth metals where the spin-orbit coupling is much stronger. For the $3d$ metals it can also be shown [237] that $\lambda$ is positive for less than half-filled 3 shells, and negative for more then half filled $3d$ shells.

In section 2.2.1 it was shown that the $3d$ orbitals split into states with $\langle L \rangle = 0$ in the presence of a crystal field. In the presence of $\mathcal{H}_{LS}$ the situation becomes a bit more complicated, and in general some of the orbital angular momentum will be reinstated [6]. In free ions with non-zero orbital angular momentum quantum number $L$, the spin and orbital angular momentum combine to a total angular momentum with possible values $J = L-S, L-S+1, L-S+2, \ldots, L+S-1, L+S$ [7]. In the presence of $\mathcal{H}_{LS}$ the degeneracy between these levels is lifted to form a group of levels called a multiplet. In TM compounds only $J = L-S$ and $J = L+S$ are encountered, for less than half-filled shells and more than half-filled shells respectively, depending on the sign of $\lambda$.

The total magnetic dipole moments are determined by $\mu_L = -\mu_B\sqrt{L(L+1)}$ and $\mu_S = -g_e\mu_B\sqrt{S(S+1)}$ with $g \simeq 2$. An external magnetic field couples to $\hat{L} + 2\hat{S}$. The total magnetic moment is therefore given by $\mu_J = g_J \mu_B J$ where

$$g_J = \frac{3}{2} + \frac{S(S+1) - L(L+1)}{2J(J+1)}. \tag{2.40}$$

and the Zeeman term is $\mathcal{H}_Z = \mu_B g_J \hat{J} \cdot \mathbf{H}$. In the case of $Cu^{2+}$ ($3d^9$) $g_J$ can be calculated by treating the spin-orbit coupling as a perturbation to the crystal-field-split $3d$ states.

[6] An exception are perfectly half-filled $3d$ shells, for which $\lambda = 0$ which follows from the fact that $\lambda$ changes sign at this point. More rigorous arguments have been given, see for example [237, 220]. However, in many $3d^5$ TM compounds the total orbital angular momentum does not seem to be zero. In chapter 4 this is for the first time fully explained.

[7] This $J$ should not be confused with the super-exchange constant, which carries two indices corresponding to the ions or shells between which the exchange interaction acts

$g_J$ relates the induced orbital angular momentum by the spin moment and external fields with the crystal field. In ions with $S > 1/2$ the difference in orbital angular momentum induced along different directions with respect to the crystal field can give rise to energy splittings between the levels $|M_S|$. This is the single-ion anisotropy term

$$\mathcal{H}_{\text{SI}} = D_{zz}\hat{S}_z^2 + E_{xy}(\hat{S}_x^2 - \hat{S}_y^2) \tag{2.41}$$

For $S = 5/2$ systems there is even such a term in a $O_\text{h}$ crystal field ([237] p. 155),

$$\mathcal{H}_{\text{cubic}} = \frac{1}{6}a(S_x^4 + S_y^4 + S_z^4) \tag{2.42}$$

with many more terms in the presence of an external field.

The spin-orbit coupling can also give rise to an anisotropic super-exchange interaction, which arises in first order of both super exchange $J$ and $H_{LS}$,

$$\mathcal{H}_{\text{DM}} = \mathbf{D}_{ab} \cdot (\hat{S}_a \times \hat{S}_b), \tag{2.43}$$

where $\mathbf{D}_{ab} = \eta_a - \eta_b$ and

$$\eta_a = -\frac{\lambda_a}{i} \sum_{\mu_a} \frac{\langle 0_a 0_b | \hat{L}_a | \mu_a 0_b \rangle \, J_{ab}(\mu_a 0_b, 0_a 0_b)}{E_{\mu_a}^{(0)} - E^{(0)}}, \tag{2.44}$$

with an analogous expression for $\eta_b$ [237]. The $\mu_{a(b)}$ denotes excited states of ion $a(b)$ which mix into the ground state due to the presence of the hopping matrix element $t$, and $|0_a 0_b\rangle$ denotes the zero'th order ground state configuration. Note that because $\hat{S}_a \times \hat{S}_b = -\hat{S}_b \times \hat{S}_a$ this term can only be present when $\mathbf{D}_{ab} = -\mathbf{D}_{ba}$. Hence, if the magnetic bond between ion $a$ and ion $b$ possesses inversion symmetry, then necessarily $\mathbf{D}_{ab} = 0$. This is the Dzyaloshinsky-Moriya interaction. It was postulated by Dzyaloshinsky [61] to explain the weak ferromagnetic moment in hematite, and later given a formal basis by Moriya [144].

The only other term in the total Hamiltonian which couples the spatial and spin degrees of freedom is the magnetic dipole-dipole interaction. It is given by [100]

$$\mathcal{H}_{\mathrm{dd}} = \frac{1}{2}(g\mu_{\mathrm{B}}\mu_0)^2 \frac{\sum_{ij}\left[\hat{S}_i \cdot \hat{S}_j - 3(\hat{r}_{ij} \cdot \hat{S}_i)(\hat{r}_{ij} \cdot \hat{S}_j)\right]}{|\vec{r}_{ij}|^{-3}}. \tag{2.45}$$

Here $\hat{r} = \frac{\mathbf{r}}{|r|}$, and is not an operator. In transition-metal compounds this interaction is very weak, but because it is long ranged it can give rise to a shape anisotropy. This holds in particular in materials with a long-range ordered magnetic structure and with a net magnetic moment.

### 2.2.9 Magnetic susceptibility

The magnetisation $\langle \mathbf{M} \rangle$ and $\chi = \langle \mathbf{M} \rangle / \mathbf{H}$ of $N$ free ions in a magnetic field can be calculated starting from

$$\langle M_z \rangle = -N \frac{\sum_{m_J=-J}^{J} g_J m_J \mu_{\mathrm{B}} e^{-g_J m_J \mu_{\mathrm{B}} H_z / k_{\mathrm{B}} T}}{e^{-g_J m_J \mu_{\mathrm{B}} H_z / k_{\mathrm{B}} T}}. \tag{2.46}$$

It can be shown that $\langle M_z \rangle = N g \mu_{\mathrm{B}} \hat{J} B_J(\hat{y})$ where $B_J(y)$ is the Brillouin function given by

$$B_J(y) = \frac{2J+1}{2J} \coth\left(\frac{2J+1}{2J} y\right) - \frac{1}{2J} \coth\left(\frac{y}{2J}\right) \tag{2.47}$$

where $y = g_J M_J \mu_{\mathrm{B}} J H_z / k_{\mathrm{b}} T$. For $S = 1/2$ this simplifies to

$$\langle M_{S=1/2}(T) \rangle = \mu_{\mathrm{B}} \tanh\left(\frac{\mu_{\mathrm{B}} H}{k_{\mathrm{B}} T}\right), \tag{2.48}$$

and in small fields/high temperatures the magnetic susceptibility can be approximated with

$$\chi = \frac{g_J^2 \mu_{\mathrm{B}}^2 J(J+1)}{3 k_{\mathrm{B}} T} = \frac{C_{\mathrm{curie}}}{T}. \tag{2.49}$$

In addition to the temperature dependent Curie susceptibility there are temperature independent contributions, the Van Vleck paramagnetic susceptibility and diamagnetic susceptibility [26].

Using mean field theory [22] it can be shown that 2.49 is also applicable to the magnetic susceptibility in the paramagnetic phase of magnetic insulators. In that case the energy scale of the magnetic interactions ($\theta_w$) must be added to the temperature $T$ in the denominator. This is the Weiss temperature given by $\theta_w = \frac{2}{3}zS(S+1)k_B J_{ij}$, where $z$ is the number of spins which couple to each site with strength $J_{ij}$. Hence, the expression

$$\chi = \frac{C_{\text{Curie}}}{T + \theta_w} \tag{2.50}$$

can be used to deduce the effective magnetic moment of the spins

$$\mu_{\text{eff}} = g_J \mu_B \sqrt{J(J+1)} \tag{2.51}$$

and the magnetic super-exchange constant $J_{ij}$, from the paramagnetic susceptibility of magnetic materials measured in a small applied field (of the order of 100 G) [8]. The Weiss temperature immediately indicates whether a material is ferromagnetic ($\theta_w > 0$) or antiferromagnetic ($\theta_w < 0$). The results in chapter 4 reconfirm that this method is a reliable way to obtain two essential parameters of the system - the effective magnetic moment, and the energy scale of the exchange interactions - in a model independent way.

## 2.3 Geometric frustration

There are lattices for which a spontaneous symmetry breaking to a classical Néel ordered state is not expected, such as the 1D chain and lattices on which the antiferromagnetic Néel order is frustrated, such as the kagomé and the pyrochlore lattices,

[8] The magnetic fields in magnetic susceptibility measurements are often stated in CGS units. In this unit system $\mu_B = 9.27 \cdot 10^{-21}$ erg/G, $\mu_0 = 1$ and $k_B = 1.3807e-16$ erg/K and $\mu_{\text{eff}} \simeq \sqrt{8C_{\text{Curie}}}$.

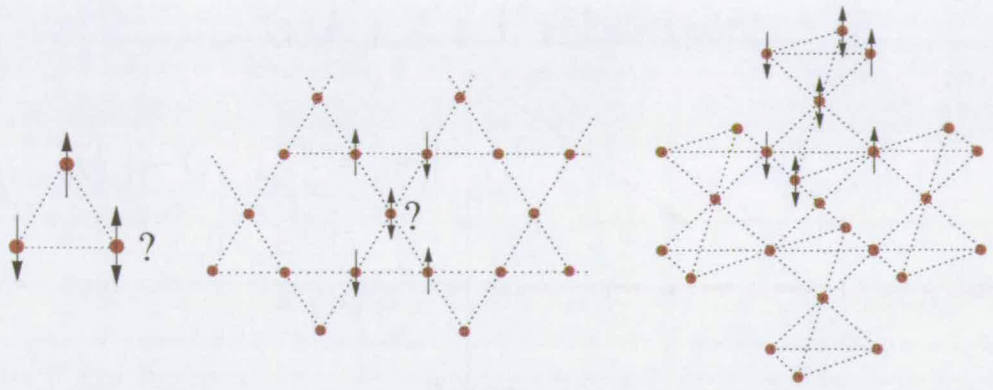


Figure 2.8: The principle of geometric frustration on a triangle (left), for the kagomé lattice (centre) and for the pyrochlore lattice (right).

as shown in figure 2.8. Geometric frustration can cause the ground state to become underconstrained, so that the magnetic ground state is not uniquely defined, giving rise to a finite ground state entropy [85, 78, 161, 120, 59]. This situation is illustrated in figure 2.8. Hence, for antiferromagnets with $S = 1/2$ spins on a kagomé or pyrochlore lattice no symmetry-breaking is expected, and the ground state should be the symmetrical quantum-mechanical ground state with $S_{\text{tot}} = 0$. Already in 1931 it was shown that the $S = 1/2$ linear chain has such an $S_{\text{tot}} = 0$ ground state [21].

Philip Anderson [7] provided a physical picture of the singlet ground state in the Mott insulating phase as a linear superposition of valence bond singlets between all (nearest neighbour) electron pairs, as illustrated in figure 2.9. This new kind of Mott insulating state was called a resonating valence bond (RVB) state. As was shown in section 2.2.4 the Heisenberg Hamiltonian as derived from the Hubbard model is identical to the effective Hamiltonian for the low-energy subspace describing the valence bond. Hence, in the original paper [7] it was suggested that the term valence bond should be taken literally, as described by Pauling [156]. Another argument was that materials such as $VO_2$ and $Ti_2O_3$ were known to undergo a static pairing of pairs of ions into singlet valence bonds. Since then many more valence bond crystals have been found. For example *bis-cis-* (1,2-perfluoromethylethylene-1,2-dithiolato)-copper (TTFCuBDT) [35], $CuGeO_3$ [91], and the spinels $CuIr_2S_4$ [160] and $MgTi_2O_4$ [186].

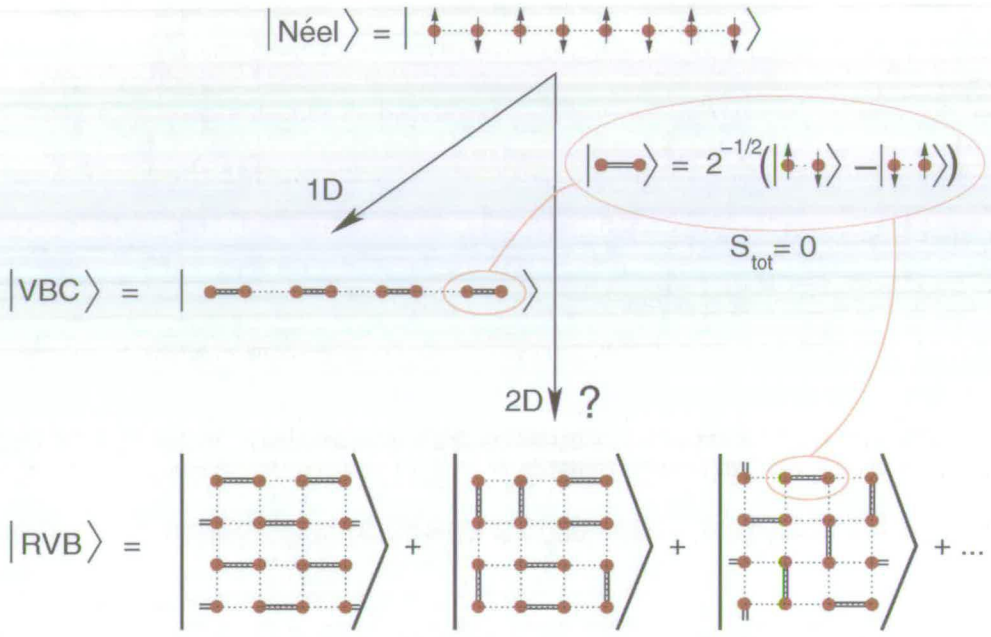


Figure 2.9: The Néel state (top) compared with the statically dimerised state of $S_{\text{tot}} = 0$ pairs - a valence bond crystal (VBC) - as is often found in $S = 1/2$ linear chain antiferromagnets, and the resonating valence bond (RVB) state (bottom). This state is a superposition of all possible dimerisations. It should be emphasised that this a quantum-mechanical superposition, which means that in the ground state never any of these particular dimerisation patterns is realised, not even for an infinitesimally short moment.

It was suggested that for the triangular lattice $S = 1/2$ antiferromagnet these valence bonds would no longer be pinned to particular locations (or "self trapped") [7, 71].

The idea of a resonating valence bond ground state gained renewed relevance with the discovery of an entirely new class of super conductors, the so-called high critical temperature - or high $T_c$ - superconductors [13, 233]. The common factor in these ceramic insulators is that they have non-orbitally degenerate $Cu^{2+}$ ions on well separated 2D square lattices. They are Mott insulators with relatively wide bands, and strong in-plane antiferromagnetic exchange. Anderson suggested [10] that in the stoichiometric insulating phase of for example $La_2CuO_4$, pre-formed singlet pairs are present in the magnetic ground state. He suggested that when these Mott insulators are hole doped by replacing some of the La with Ba or Sr, these spin singlets would be the bosonic charge carriers responsible for the superconducting properties of materials like $BaLa_4Cu_5O_{5(3-\delta)}$ [13] and $(Y_{0.6}Ba_{0.4})_2CuO_{(4-\delta)}$ [233]. The pairing mechanism was

therefore thought to be mainly a magnetic interaction. This has spurred the interest in geometrically frustrated systems, which are considered the most likely to have a RVB or quantum spin-liquid ground state. It has since been shown that the $S = 1/2$ triangular antiferromagnet has a three sub-lattice Néel state [17, 11]. Presently the most important candidates are the kagomé and pyrochlore antiferromagnets. The kagomé antiferromagnet is the subject of this thesis. First the classical case of $S \to \infty$ will be discussed because many semi-classical approaches for finite spin start out from a classical picture, for example [45]. It is also assumed that the systems of which the classical analogue does not freeze are more likely to have a quantum spin liquid ground state.

### 2.3.1 The classical kagomé antiferromagnet

The classical kagomé antiferromagnet does not show conventional symmetry breaking even at $T = 0$. It has been shown analytically [168] that the ground state of the classical Hamiltonian has a macroscopically large degeneracy. The only condition for a spin configuration to be a ground state is that the sum of the spins in each elementary triangle is zero [45]. Using linear spin-wave analysis starting from $q = 0$ and $q = \sqrt{3}\times\sqrt{3}$ ground states (two of the many possible ground states) shows that there is a whole band of dispersionless zero-energy modes. This means that collective spin re-arrangements are possible with no cost in energy, and for arbitrarily small clusters of spins [84]. Figure 2.10 illustrates examples of the open and closed lines of collective spin zero-energy modes in the $q = 0$ and the $q = \sqrt{3} \times \sqrt{3}$ respectively.

As is clear from figure 2.2 the ground state degeneracy of the classical kagomé antiferromagnet is much larger than needed to prevent symmetry breaking. It is has been shown that in this situation quantum and thermal fluctuations can select a subset within the ground state manifold [216] for which the entropy of the system is maximised. Using linear spin-wave theory and classical Monte Carlo simulations it has been shown that due to this "order from disorder" effect a spin-nematic order appears [43, 167]

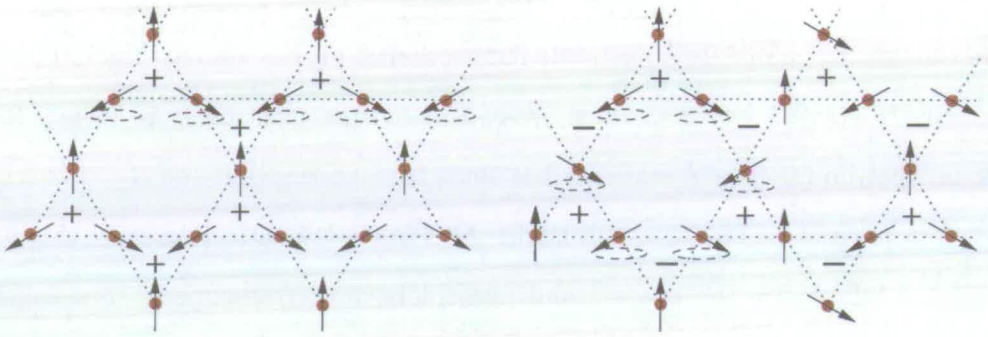

Figure 2.10: The zero-energy collective spin modes in the $q = 0$ unit-cell spin structure with positive chirality (left), and in a structure with a larger unit cell ($q = \sqrt{3} \times \sqrt{3}$) and a staggered chirality. In $q = 0$ the collective modes are open lines, which lends this structure a certain rigidity. The $q = \sqrt{3} \times \sqrt{3}$ structure is much softer because closed loops of collective spin reorientations exist. Hence, the short-ranged correlations in the ground state are mainly of the $q = \sqrt{3} \times \sqrt{3}$ type [84, 43]. The chirality of each triangle is defined in equation 2.53.

for the classical kagomé antiferromagnet. In the spin-nematic state all spin vectors lie in a common plane. This order can be mapped to a co-planar spin arrangement where all the spins lie within the 2D (kagomé) plane, by a global spin rotation. The leading quantum corrections to the spin-wave spectra also induce nematic correlations as $T \rightarrow 0$ [45]. This picture was confirmed by a large $N$ expansion specifically suited for frustrated systems in which the behaviour of the kagomé antiferromagnet was studied as a function of the spin quantum number [179].

It can however not be ruled out that at $T = 0$ in addition to the nematic order the ground state shows long range spin-spin correlations, most likely of a $\sqrt{3} \times \sqrt{3}$ structure [179]. This order as $T \rightarrow 0$ does not indicate a symmetry breaking transition; the dispersionless zero-energy modes guarantee that no symmetries are broken. Any time-averaged observable of the system such as the magnetic susceptibility will be isotropic. The situation can be compared with that in a high-spin single molecule magnet (SMM). All the spins within the SMM are aligned ferromagnetically, but as long as the SMM is small enough [199] the total spin orientation $m_S$ will not be fixed. As an illustration, figure 2.11 gives the nematic correlation function $g_n(r_{\alpha\beta})$ and the spin-spin correlation function $g(r_{ij})$ at $T/J = 0.0001$ for a system with 432 spins.

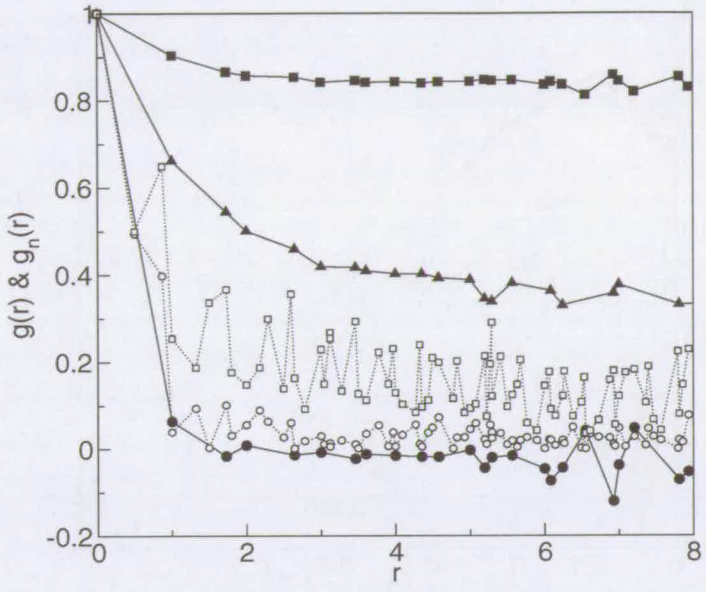


Figure 2.11: The spin-nematic order $g_n(r_{\alpha\beta})$ at $T/J = 0.01$ (filled circles), 0.001 (filled triangles) and at 0.0001 (filled squares). The spin-spin correlation function at $T = 0.01$ and $T = 0.001$ are the open circles and open squares respectively. This data was obtained in a simulation on 432 spins using *Spinner* [56], to reproduce [43].

$g_n(r_{\alpha\beta})$ defined as [43]

$$g(r_{\alpha\beta})_n = \frac{2}{3}\langle(\vec{n}_\alpha \cdot \vec{n}_\beta)^2\rangle - 1/2 \tag{2.52}$$

where $\vec{n}_\alpha$ is the chirality vector defined as

$$\vec{n}_\alpha = \frac{2}{3}\sqrt{3}\left(\vec{S}_1 \times \vec{S}_2 + \vec{S}_2 \times \vec{S}_3 + \vec{S}_3 \times \vec{S}_1\right). \tag{2.53}$$

where the subscripts index the spins in unit cell $\alpha$ in a clockwise order. $g(r_{\alpha\beta})$ is non-zero for $\alpha \neq \beta$ only because the average is taken over a scalar. The low-temperature susceptibility along all three crystallographic axes is identical, even as $T \to 0$, as is evident from figure 2.12.

This order from disorder effect does mean that an infinitesimally small $XY$ anisotropy is sufficient to turn the nematically ordered state into a symmetry-broken state with an associated second order phase transition [171]. In addition to a global spin-rotation, below the transition temperature the spins are free to align in three orientations making an angle of 120° with each other. The dynamics are thought to be glassy with a $T^2$

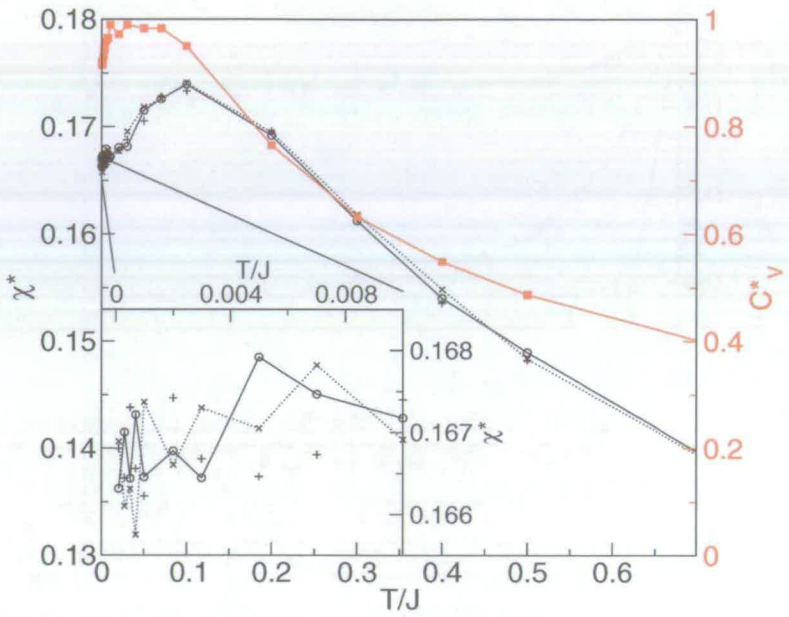


Figure 2.12: The magnetic susceptibility (black) along the $a$ axis (open circles), $b$ axis ($\times$) and $c$ axis ($+$). The heat capacity is given in red, and corresponds to the right-hand axis. The magnetic susceptibility and heat capacity are given in reduced dimensionless units.

temperature dependence of the specific heat [171, 44]. When the $XY$ anisotropy plane becomes locally canted as would be the case for the jarosites, it is expected that this kind of anisotropy induces long range order [147].

Further-neighbour interactions have been shown to induce long-range ordered ground states of the $q = 0$ type for $J_2 > J_3$ and $q = \sqrt{3} \times \sqrt{3}$ for $J_2 < J_3$ [84]. A Dzyaloshinsky-Moriya term in the Hamiltonian has been shown to induce $q = 0$ long-range order [63]. In this case the sign of $D_\perp$ determines the sign of the chirality vectors $\vec{n}_\alpha$; if the cross products in the DMI term are evaluated in a clockwise manner around each hexagon then $\text{sign}(D_\perp) = \text{sign}(n_\perp)$. An easy-axis anisotropy leads to a phase transition to a weakly ferromagnetic state, with critical exponents of the Ising universality class [33, 76], but the ground state remains degenerate, as was the case for the $XY$ system.

The magnetic structure factor $\langle \hat{S}_i \cdot \hat{S}_j \rangle_\beta$ of the kagomé antiferromagnet with only nearest neighbour exchange has been calculated using a high-temperature series expansion [84]. The corresponding Padé approximant of the uniform magnetic susceptibility

$\chi_0(T) = \frac{1}{T}\sum_r \langle \hat{S}_0 \cdot \hat{S}_r \rangle$ is given by [84, 143]

$$\chi_0(T) = \frac{C}{T}\frac{\sum_{n=0}^{M} b_n y^n}{\sum_{n=0}^{M} c_n y^n} \text{ where } y = \frac{JS(S+1)}{3T}. \tag{2.54}$$

and the coefficients up to order $M = 4$ are $b_0 = 1$, $b_1 = -10.282$, $b_2 = 8.18025$, $b_3 = -19.8368$, $b_4 = 9.19475$, $c_0 = 1$, $c_1 = -6.08282$, $b_2 = 28.151$, $b_3 = -29.8471$, and $c_4 = -18.8328$.

### 2.3.2 The $S = 1/2$ kagomé antiferromagnet

The theoretical search for the properties of the $S = 1/2$ kagomé antiferromagnet started with Elser's paper [64] on the interpretation of heat capacity measurements of $^3$He atoms physisorbed on graphite [73, 79]. Elser suggested that only part of the spins in this system would form dimers (pair into spin-singlets) and that at $T = 0$ this dimer pairing would be static. Over the last 18 years a large number of different theoretical approaches have been applied to the problem of the $S = 1/2$ kagomé antiferromagnet, and all of them confirm that this system cannot have a Néel type long range ordered state. Finite-size scaling analysis of exact diagonalisation results on small clusters [218, 238, 42, 119, 113] suggest that even in the thermodynamic limit the triplet ($S_{\text{tot}} = 1$) states are gapped, with an energy of the order $J/20$. This means that physical realisations should have a non-magnetic quantum spin liquid ground state [98]. A puzzling aspect of the exact diagonalisation results is the quasi-continuous spectrum of singlet states above the ground state. These singlet states are found to fill the singlet-triplet gap with non-magnetic excitations [218].

Finite temperature series expansions for the $S = 1/2$ kagomé antiferromagnet for $N \to \infty$ do not yield information on the ground state, but for finite temperatures these results [191, 65] confirm the correct convergence [190, 18, 137] of the finite size scaling of exact diagonalisation results. Using a hybrid approach combining the two techniques [137] a larger singlet-triplet gap was found, of order $J/10$. This evidence in favour of a $S_{\text{tot}} = 0$ ground state consisting pairs of spins coupled into valence bonds

has motivated a number of investigations which focus on the $S_{\text{tot}} = 0$ subspace alone, using quantum dimer models [132, 140, 141, 139].

Even quantum liquids can have broken symmetries. In the case of superfluid $^4$He and superconductors for example, this is the quantum mechanical phase of the wave function [9] which becomes uniform for all particles involved, while the Hamiltonian is of course invariant on such a phase. Similar symmetry breakings (Gauge symmetry breaking) are thought to occur in the quantum spin liquid ground state of frustrated spin systems [222, 179, 141, 139]. Due to interference effects of the uniform phase of the wave function, the properties of such systems are dependent on the surface on which the lattice is defined, i.e. the periodic boundary conditions. Hence, these systems are called topologically ordered phases [139]. A concrete example of this interference due to the topology of the system is the superconducting quantum-interference device, or SQUID ring [9] (see also section 3.4). In this state the elementary excitations are thought to be de-confined spinons. Spinons are pairs of $S = 1/2$ quasi-particles [179] which appear as a $S = 1$ excitation when a singlet bond is broken. In the quantum disordered phase these spinons are not bound together in the way they are in for example a valence bond crystal. They can independently travel through the lattice as defects in the dimerisation pattern. This is why they are called "*deconfined* spinons".

A large number of papers discuss the heat capacity of the $S = 1/2$ kagomé antiferromagnet [218, 190, 16, 241, 137, 139, 142, 166]. It is generally agreed that the heat capacity follows a power law as the temperature approaches zero; $C_V = \gamma T^{\alpha}$ where $1 \leq \alpha \leq 2$, although it has been said that even $\alpha < 1$ cannot be excluded on theoretical grounds [142]. It is also clear that a singlet-triplet gap should be evident as a shoulder in the heat capacity at $\approx J/10$ [137] corresponding to a peak in $dS/dT = C_V/T$. The application of an external field is expected to have a negligible effect on the heat capacity [190].

This is the theoretical evidence in favour of a quantum spin-liquid ground state. However, many questions remain open. For example whether or not the quantum

mechanical $S_{\text{tot}} = 0$ ground state is degenerate. Furthermore, no general consensus has been reached on the conclusiveness of the above results [142]. Some researchers suggest the ground state is a valence bond crystal, i.e. statically ordered dimers [126, 87, 146, 39] or a critical non-gapped spin liquid with gap-less spinons [87, 166]. In the light of the observations in chapter 5 some studies on the effects of decoherence effects in frustrated lattices should also be mentioned [217, 181, 130].

### 2.3.3 Experimental realisations

The first and the most well-known Mott insulator modelling the low-spin kagomé antiferromagnet is $SrCr_{9p}Ga_{12-9p}O_{19}$ (SCGO) [151, 163]. In this system $S = 3/2$ $Cr^{3+}$ ions are located in [111] slabs of the spinel structure, consisting of two kagomé layers sandwiching a layer with a triangular lattice [163]. The Weiss temperature ($\theta_{\text{w}}$) of this system is between -500 and -200 K depending on the Cr concentration [163, 185] - the Cr sites on the kagomé lattice are prone to substitutions with $Ga^{3+}$. An indication of the large degree of frustration in this system is that it does not freeze down to $T_g = 4.5(1.5)$ K [151, 163, 185]. At $T_g$ the magnetic susceptibility peaks, and develops a splitting in the field-cooled zero-field cooled susceptibility [185]. $\mu$SR measurements have shown that below $T_g$ the $Cr^{2+}$ spin fluctuations gradually slow down, but even at 1 K no long-range order is found and the ground state remains mainly dynamic [36, 37, 114, 27]. For this reason SCGO was long considered the most likely material to have a spin-liquid ground state. However, no sign of a singlet-triplet gap has been found [121], and using Ga NMR Limot *et al.* [121] have shown that the glassy characteristics are intrinsic to the system, rather than a consequence of $Ga^{3+}$ substitutions of the $Cr^{3+}$ ions on the kagomé lattice. This was confirmed by a comparative study of SCGO with the isostructural compound $Ba_2Sn_2ZnCr_{7p}Ga_{12-7p}O_{22}$ [28] which shows a spin-glass ordering at even lower temperatures, but again does not show any signature of a singlet-triplet splitting.

It may be that SCGO is a topological spin glass [171] due to the presence of a small magnetic anisotropy which is evidenced by an anisotropy in the magnetic susceptibility [185]. This is in agreement with the heat capacity [164] which follows the power law $C_V \propto T^2$ for low temperatures [171]. The heat capacity was found to be almost completely independent of external magnetic fields up to 10 T [164].

Better physical realisations of the kagomé antiferromagnet are the jarosite compounds, $AM_3(OH)_6(SO_4)_2$, where $A$ is typically a monovalent cation and $M$ trivalent Al, Ga, Fe, Cr or V. In chapter 4 iron jarosite is discussed. In this system the kagomé sites are occupied by $Fe^{3+}$ ions with strongly antiferromagnetically coupled $S = 5/2$ spins. The Weiss temperature is $\approx$ 750 K, and consistent with strong geometric frustration, the system only freezes at 65 K. The ground state is long-range ordered, with a $q = 0$ magnetic unit cell. A small number of studies exists on the chromium and vanadium analogues of iron jarosite, with $S = 3/2$ and $S = 1$ respectively. Chromium jarosite has a Weiss temperature of -60(10) K. This system orders into a long-range ordered structure with a $q = 0$ unit cell below $\sim$ 1.7 K [105, 115]. The ordered local moment $|\langle\hat{S}\rangle|$ at $T = 0.4$ K was found to be only $0.4(1)S$ [115, 96] with $S = 3/2$.

Vanadium jarosite ($S = 1$) has a Weiss temperature of $\sim$ 50 K [82, 155, 80], indicative of ferromagnetic exchange within the kagomé layers. Due to weaker antiferromagnetic interplane interactions the material still acts like an antiferromagnet. The effective magnetic moment as found from the high temperature magnetic susceptibility is significantly lower than that of $S = 1$ spins, which suggests that there is significant orbital angular momentum. The ferromagnetic exchange in vanadium jarosite is explained by the fact that for $V^{3+}$ only the $3d_{xz}$ and $3d_{yz}$ orbitals are occupied, and these orbitals can only form $\pi$ symmetry bonds with the connecting oxygen ligands [80].

The recently discovered compounds Nd- and Pr-langasites ($R_3Ga_5SiO_{14}$ with R = Nd or Pr) [29] improve on iron jarosite as models of the classical kagomé antiferromagnet with magnetic moments of $J = 9/2$ and $J = 4$ respectively. In these lanthanide magnets the magnetic shell is the 4f shell which retains almost all the orbital angular momentum

of the free ion. The large orbital angular momentum is also shown to give rise to a large magneto crystalline anisotropy. The Weiss temperature of Nd-langasite is $\theta_W = 52$ K, while the system remains strongly fluctuating down to 2 K. Diffuse neutron-scattering experiments have revealed short-ranged spin-spin correlations at 2 K, which is direct evidence that Nd-langasite is a cooperative paramagnet [172].

Another recently discovered compound is $Y_{0.5}Ba_{0.5}CaCo_4O_7$ [187]. This material is a very beautiful example of a $S = 3/2$ kagomé antiferromagnet. The $S = 3/2$ $Co^{2+}$ spins are located on well separated kagomé layers. The Weiss temperature in this system is -2200 K, indicative of strong antiferromagnetic exchange. This has allowed the experimental characterisation of the ground state down to very low $T/J$, revealing very strong dynamical spin-spin correlations with a periodicity of to two times the $\sqrt{3} \times \sqrt{3}$ unit cell below 40 K [187]. It was shown that the diffuse neutron magnetic scattering is in excellent agreement with classical Monte Carlo simulations.

A number of compounds have so far been considered as model systems of the $S = 1/2$ kagomé antiferromagnet. Of these materials volborthite ($Cu_2V_3O_7(OH)_2 2H_2O$) probably comes closest to the ideal. Using NMR it has been shown that the vanadium ions are in a non-magnetic state [90], resulting in well separated kagomé layers of antiferromagnetically coupled $S = 1/2$ spins. However, not all nearest neighbour bonds on the kagomé lattice are symmetry equivalent, and it is therefore possible that the system is governed by two different in-plane exchange constants. The magnetisation, heat capacity and NMR measurements do not show any sign of a magnetic freezing, but EPR results suggest the onset of short-range correlations below 5 K [153]. $\mu$USR measurements [19, 74] have shown that below 5 K the spin fluctuations slow down. At 1 K the muon spin relaxation rate due to the slowly fluctuating electronic $S = 1/2$ moments peaks with $\lambda = 0.37\ \mu s^{-1}$. On dilution of the magnetic structure with Zn [74] the muon relaxation rate decreases until at 60% $Cu^{2+}$ coverage of the kagomé lattice, well past the percolation limit, $\lambda \approx 0$ at 50 mK [74].

Other systems which should be mentioned are

- The copper coordination compound $[Cu_3(titmb)_2(OCOCH_3)_6]\cdot 6H_2O$, which has been found to be ferromagnetic [93, 145].
- $\beta$-$Cu_3V_2O_2$ on which the kagomé lattice is folded into a buckled staircase with different nearest-neighbour exchange interactions [174]. This compound orders magnetically at 75 K, while the Weiss constant is $-135$ K, which is an indication that the anisotropic exchange has lifted the geometric frustration [174].
- $Cs_2Cu_3ZrF_12$ has $Cu^{2+}$ ions on perfect kagomé layers. However, below 210 K a structural transition occurs leading to a distorted kagomé lattice below this temperature [198], and at 30 K a weak ferro-magnetic moment develops.

In August 2005 Shores *et al.* identified the $x = 1$ phase of zinc paratacamite of general stoichiometry $Zn_xCu_{4-x}(OH)_6Cl_2$ as a perfect realisation of the $S = 1/2$ kagomé antiferromagnet. This material will be discussed in chapter 5.

Chapter 3

# Experimental

Diffraction methods have been instrumental in revealing the structure of condensed matter. A sample is illuminated with a beam of light or particles with a wavelength smaller than the structure which is to be revealed. The intensity of the waves projected onto a large sphere around the sample equals the power spectrum (the Fourier transform times its complex conjugate) of the wave field at the sample surface. In the single scattering limit, i.e. when the mean scattering length in the sample is larger than the sample thickness, the diffraction pattern can be taken as the power spectrum of the spatial structure of the sample. To reveal the atomic structure of crystals, waves with a wavelength of the order of 1 to 2 Å are needed. This means either X-rays with an energy of at least 2 KeV or thermal neutrons, with an energy of 20 to 81 meV. The first three sections in this chapter will deal with X-ray and neutron diffraction, and a general derivation of the above statement will be given. In principle any particle with the right wavelength could be used. However, charged particles such as electrons and muons interact much more strongly. Hence, electrons are generally used to study surfaces or very thin samples. Muons of the energy as typically generated from neutron collisions, stop in the sample within a mm from the sample surface. Once in the sample, they can act as local probes for the magnetic fields and fluctuations in magnetic fields in their direct environment. This technique was used to prove that the spins do not freeze even

at 50 mK in the $x = 1$ phase of zinc paratacamite. The experimental details will be discussed in section 3.2.

## 3.1 Diffraction methods

The Huygens-Fresnel principle [30] states that a wave $\Psi(\mathbf{r}, t)$ emanating from a single point source $\delta(\mathbf{r} - \mathbf{r}_0)$ will be perfectly spherical[1], and the wave field from any source can be described by the interference of the spherical waves from all the point sources in the sample together. Let's consider the sample as a collection of point "sources" $g(\mathbf{r})$ illuminated by an incoming wave $f(\mathbf{r})$, which in general is given by

$$f(\mathbf{r}) = \int d\vec{\kappa}\, \tilde{f}(\vec{\kappa}) e^{i(\vec{\kappa}\mathbf{r} - \kappa ct)} \tag{3.1}$$

where $c$ is the propagation speed of the wave and $\kappa = |\vec{\kappa}|$. In the case that no energy transfer occurs between the incoming wave and the sample, the wave field at the sample surface $\Psi_0(\mathbf{r})$ of structure $g(\mathbf{r})$ can now be written as

$$\Psi_0(\mathbf{r}, t) = g(\mathbf{r}) \int d\vec{\kappa}\, \tilde{f}(\vec{\kappa}) e^{i(\vec{\kappa}\mathbf{r} - \kappa ct)}, \tag{3.2}$$

and the interference of all sources $g(\mathbf{r})$ at $\mathbf{r}, t$ is given by

$$\Psi(\mathbf{r}, t) = \int d\mathbf{r}' \frac{\Psi_0(\mathbf{r}', t - l/c)}{l} \tag{3.3}$$

where $l = |\mathbf{r} - \mathbf{r}'|$. Inserting 3.2 into 3.3 yields

$$\begin{aligned} \Psi(\mathbf{r}, t) = & \quad \int d\vec{\kappa}\, \tilde{f}(\vec{\kappa}) \int d\mathbf{r}'\, g(\mathbf{r}) l^{-1} e^{i(\vec{\kappa}\mathbf{r}' + \kappa(l - ct))} \\ \approx & \quad \tfrac{1}{r} \int d\vec{\kappa}\, \tilde{f}(\vec{\kappa}) \int d\mathbf{r}'\, g(\mathbf{r}) e^{i(\vec{\kappa}\mathbf{r}' + k(r - \hat{\mathbf{r}}\mathbf{r}') - \kappa ct)} \\ = & \quad \tfrac{1}{r} \int d\vec{\kappa}\, \tilde{f}(\vec{\kappa}) e^{ik(r - \kappa ct)} \int d\mathbf{r}'\, g(\mathbf{r}) e^{i(\vec{\kappa} - \kappa\hat{\mathbf{r}})\mathbf{r}'} \end{aligned} \tag{3.4}$$

[1] It is a Green's function $\frac{e^{ikr}}{r}$, the solution of the wave-equation for a point-source.

where we used that $l \approx r - \hat{\mathbf{r}} \cdot \mathbf{r}'$ for $r \gg r'$ [2]. For a monochromatic incoming wave $\tilde{f}(\mathbf{k}) = \delta(\mathbf{k} - \vec{\kappa})$ the momentum transfer $\mathbf{q}$ by the sample is given by $\mathbf{q} = \mathbf{k} - k\hat{\mathbf{r}}$, where it should be noted that $k\hat{\mathbf{r}}$ is the outgoing wave vector ($\mathbf{k}'$). Using these definitions, the wave field on a sphere of radius $r \gg r'$ around the sample is given by

$$\Psi_r(\mathbf{q}, t) = \frac{e^{ik(r-ct)}}{r} \tilde{g}(\mathbf{q}) \tag{3.5}$$

where $\tilde{g}(\mathbf{q})$ is the Fourier transform of $g(\mathbf{r}')$. The angle corresponding to $\mathbf{q}$ is given by Bragg's law; in the case of powder diffraction the diffraction angle $\theta$ is given by $q = 2k\sin(\theta)$, as can be deduced from diagram 3.1.

Hence, a one to one linear transformation relates the microscopic structure of the sample to the wave field of the diffracted waves over a large sphere around the sample. However, it is not straightforwards to measure the phase of the wave field, and most of the time the quantity of interest is the time-averaged intensity

$$I(\mathbf{q}) = \langle |\Psi_r(\mathbf{q}, t)|^2 \rangle \propto \tilde{g}^*(q)\tilde{g}(q), \tag{3.6}$$

where $\tilde{g}^*$ is the complex conjugate of $\tilde{g}(q)$. In the case of powder samples this reduces to $I(q)$. Hence, some information is lost, but both $I(\mathbf{q})$ and $I(q)$ do have a physical meaning. With the use of the convolution theorem;

$$\begin{aligned} I(q) \propto \tilde{g}^*(q)\tilde{g}(q) &= \int dr \left[ \int dx\, g(x)g(x+r) \right] e^{-iqr} dr \\ &= \int dr \langle g(x)g(x+r) \rangle e^{-iqr}. \end{aligned} \tag{3.7}$$

This demonstrates that $I(q)$ is the Fourier transform of the spatial correlation function $G(r) = \langle g(x)g(x+r) \rangle$ [3], also called the Patterson function.

[2] In the case of Fraunhofer diffraction as discussed here, only the first order term of the Taylor series expansion of $l = |\mathbf{r} - \mathbf{r}'| = \sqrt{\mathbf{r}^2 - 2\mathbf{r}\mathbf{r}' + \mathbf{r}'^2}$ in $\mathbf{r}'$ is taken into account.

[3] In principle the inner integral over $dx$ should be carried out of the area of the sample which is illuminated by the incoming wave. Hence, to obtain an accurate measurement of $G(r)$, the footprint of the beam on the sample, or the sample itself, must be much larger than the average correlation length. For smaller samples, spiky random variations on top of $\tilde{G}(q)$ are observed. These are called *speckle*,

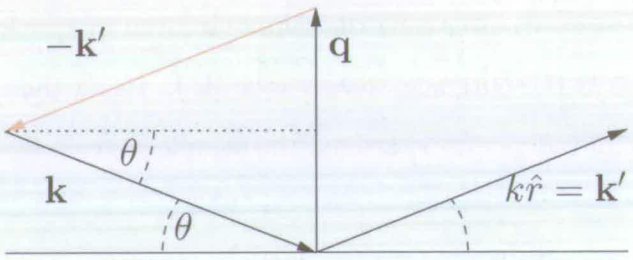


Figure 3.1: The Ewald construction illustrating Bragg's law. $\mathbf{q}$ is a lattice vector of the reciprocal lattice $\tilde{g}(\mathbf{q})$, $\mathbf{k}$ the incoming wave vector and $\mathbf{k}'$ the outgoing wave vector.

The formulation in terms of Fourier transforms as given above is equivalent to the quantum mechanical formulation, using Fermi's Golden Rule,

$$\tilde{g}(\mathbf{q}) = \int d\mathbf{r}\, g(\mathbf{r}) e^{i(\mathbf{k}-\mathbf{k}')\cdot\mathbf{r}} = \int d\mathbf{r}\, \left(e^{i\mathbf{k}'\mathbf{r}}\right)^{\dagger} g(\mathbf{r}) e^{i\mathbf{k}\mathbf{r}} = \langle \mathbf{k}' | g(\mathbf{r}) | \mathbf{k} \rangle \,. \tag{3.8}$$

where $g(\mathbf{r})$ is now the scattering potential.

### 3.1.1 X-ray diffraction and Rietveld refinement

The powder samples used in the experiments described here were characterised using the Centre for Science at Extreme Conditions (CSEC) Bruker AXS D8 powder diffractometer. Samples were mounted in a flat plate geometry and irradiated with Cu $K_\alpha$ radiation (8.0 KeV). The powder diffraction patterns were Rietveld analysed using the general structure analysis package (GSAS) [111] and the EXPGUI graphical interface [203]. The Rietveld refinement method [169] is a least squares algorithm which optimises the calculated diffraction pattern from a trial crystallographic structure to the measured diffraction pattern. This method can also deal with (partially) overlapping diffraction peaks ($y_i$) all assigned a weight $w_i$. The quality of the fit between the

and can for example be seen when a laser beam reflects from a piece of white paper. Such a pattern is never observed for neutrons because the time and spatial averages are much larger, and thermal neutrons are only correlated with themselves, not with other neutrons.

data and the model crystal structure is expressed in the $\chi^2$ and $R_{\mathrm{wp}}$, which is defined as

$$R_{\mathrm{wp}} = \left\{ \frac{\sum w_i \left[ y_i(obs) - y_i(calc) \right]^2}{\sum w_i (y_i(obs))^2} \right\}^{\frac{1}{2}}. \tag{3.9}$$

The analysis of the diffraction pattern is helped by the fact that the unit cell, spanned by the three vectors $\hat{a}, \hat{b}$ and $\hat{c}$, as parametrised by $a, b, c, \alpha, \beta$ and $\gamma$, is defined by the positions of the diffraction peaks - the structure factor. The positions and shapes of the atoms within the unit cell determine the intensities of these peaks - the form factor. The width of the diffraction peaks is determined by factors such as the quality of the crystal, i.e. the stoichiometry, the crystallinity, vacancies and dislocations, but also by the scattering geometry and the convergence and size of the incoming X-ray beam. The program GSAS [111] takes all these factors into account. The X-ray non-resonant atomic scattering cross section increases more or less linearly with the number of electrons per atom. In some situations this provided insufficient scattering contrast to allow a complete characterisation of our samples. When this was the case, neutron powder diffraction measurements were carried out.

### 3.1.2 Neutron diffraction

The nuclear neutron scattering cross section varies more or less randomly with the atomic number. This allows the determination of the positions of hydrogen (deuterium) atoms, or the distinction between copper and zinc. The diffracted neutron intensity $I(\mathbf{q}, E)$ at a detector covering the solid angle $\Delta\Omega$ with energy resolution $\Delta E$ is written in terms of the partial differential neutron scattering cross-section

$$I(\mathbf{q}, E) = \Phi \frac{d^2\sigma}{d\Omega dE}(\mathbf{q}, E) \Delta\Omega \Delta E, \tag{3.10}$$

where $\Phi$ is the total incoming neutron flux. The interactions between neutrons and the nuclear structure is weak and, in general, samples of a few grammes are required. As long as powder diffraction provides enough information this is an advantage. The

neutron flight path does not need to be high-vacuum such as is the case for soft X-rays, and the sample can easily be cooled to very low temperatures, because the neutrons easily pass through the walls of a cryostat.

The average thermal neutron (corresponding to a neutron reactor moderator temperature of 293 K) has a wavelength $\lambda = 1.798$ Å and an energy of $E = 81.81/\lambda^2 = 25.3$ meV. This is the wavelength typically needed to probe the atomic structure of materials. The corresponding energy is at the same time of the order of the energy of elementary excitations in the solid state. Hence, in addition to spatial correlations, time correlations within the sample can be studied using inelastic neutron diffraction - there is energy transfer between the sample and the incoming and outgoing neutrons, as well as momentum transfer. The energy transfer between the neutrons and the sample is often expressed as $E = \hbar\omega$, where $\omega$ is the oscillation frequency of the state composed of the superposition of the ground state and the excited state accessed in the transition.

In addition neutrons have a spin moment of $S = 1$. Hence neutrons also probe the magnetic structure (unpaired electrons). The cross sections for nuclear and magnetic scattering are of a similar order. For this reason neutrons have played a very important role in the study of magnetism. For example, using neutron diffraction Shull and Smart [189] were able to prove Néel's idea that the unpaired spins in insulating antiferromagnets ordered in two oppositely aligned magnetic sub-lattices.

The magnetic interaction between the neutron and a single unpaired electron is

$$-\hat{\mu}_{\mathrm{n}} \cdot \mathbf{H}_{\mathrm{el}}(\mathbf{R}) = -\gamma\mu_{\mathrm{n}} 2\mu_{\mathrm{B}} \hat{\sigma} \cdot \left[\nabla \times \left(\frac{\hat{s} \times \mathbf{R}}{R^3}\right) + \frac{1}{\hbar}\frac{\hat{p} \times \mathbf{R}}{R^3}\right], \tag{3.11}$$

the dipole-dipole interactions and the magnetic force due to the motion of the neutron. The Fourier transform of the term between brackets yields $\frac{2m}{\hbar^2}(\hat{\mathbf{q}} \times (\hat{s} \times \hat{\mathbf{q}}) - \frac{i}{q\hbar}\hat{\mathbf{q}} \times \hat{p})$ where $\mathbf{q} = \mathbf{k}' - \mathbf{k}$.

In systems with classically localised electrons (indexed as $i$), such as the Mott insulators, the magnetic differential scattering cross-section for the potential 3.11 is

given by [123]

$$\left[\frac{d^2\sigma_{\rm mag}}{d\Omega dE}(\mathbf{q},\omega)\right]_{\sigma\to\sigma'} = (\gamma r_0)^2\,\frac{k'}{k}S_{\rm mag}(\mathbf{q},\omega) =$$
$$(2\gamma\mu_{\rm N}\mu_{\rm B})^2\frac{k'}{k}\left|\langle\mathbf{k}'\lambda'\sigma'|\hat{\sigma}\cdot\sum_i\left[\nabla\times\left(\frac{\hat{s}_i\times\mathbf{R}}{R^3}\right)-\frac{1}{\hbar}\sigma\cdot\frac{\hat{p}_i\times\mathbf{R}}{R^3}\right]|\mathbf{k}\lambda\sigma\rangle\right|^2 =$$
$$(\frac{4m\gamma\mu_{\rm N}\mu_{\rm B}}{\hbar^2})^2\frac{k'}{k}\left|\langle\lambda'\sigma'|\hat{\sigma}\cdot\sum_i e^{i\mathbf{q}\mathbf{r}_i}\left[\hat{\mathbf{q}}\times(\hat{s}_i\times\hat{\mathbf{q}})-\frac{i}{q\hbar}\hat{\mathbf{q}}\times\hat{p}_i\right]|\lambda\sigma\rangle\right|^2 =$$
$$(\frac{2m\gamma\mu_{\rm N}}{\hbar^2})^2\frac{k'}{k}\left|\langle\lambda'\sigma'|-\hat{\sigma}\cdot\left[M_\perp^S(\mathbf{q},t)+M_\perp^L(\mathbf{q},t)\right]|\lambda\sigma\rangle\right|^2 =$$
$$(\frac{2m\gamma\mu_{\rm N}}{\hbar^2})^2\frac{k'}{k}\left|\langle\sigma'|-\hat{\sigma}\cdot\tilde{M}_\perp(\mathbf{q},\omega)|\sigma\rangle\right|^2 \qquad (3.12)$$

where $M_\perp^{S(L)}(\mathbf{q}) = \hat{\mathbf{q}}\times\left[\mathbf{M}^{S(L)}(\mathbf{q})\times\hat{\mathbf{q}}\right]$ and $\mathbf{M}(\mathbf{r}) = \mathbf{M}^S(\mathbf{r}) + \mathbf{M}^L(\mathbf{r})$ is the total magnetisation density.

Within an ion the spin and orbital magnetic moment are of course 100% correlated. Even in covalent systems the spin and orbital magnetic moment distribution per magnetic species is usually approximated using Hartree-Fock Slater-type wave functions. These ionic moment densities have been calculated by Clementi and Roetti [47], and Brown [38] has tabulated the magnetic form factors $f(q)$, which are the Fourier transform of the calculated ionic moment densities. The only variable is the degree to which the orbital angular momentum contributes to the total moment $J = 2S + L$;

$$f(q) = \langle j_0\rangle(q) + (1-\frac{2}{g})\langle j_2\rangle(q) \qquad (3.13)$$

where $g$ is the effective gyromagnetic ratio and $\langle j_0\rangle$ and $\langle j_2\rangle$ are the form factors from the spin-moment and and orbital-moment distributions. It is now possible to deal with the correlations of discrete localised moments

$$G_i(t) = \frac{\langle S_0(t)S_i(t)\rangle}{S(S+1)}. \qquad (3.14)$$

In the case of powder diffraction the scattering plane can be chosen to be the $x-y$ plane, so that $S_\perp = S_z$. In the absence of an external magnetic field, the magnetic scattering cross-section for powder samples with antiferromagnetic correlations can now be written as

$$\frac{d^2\sigma_{\rm mag}}{d\Omega dE} = (\gamma r_0)^2 \frac{k'}{k} \left(\frac{1}{2}\mu_{\rm B} g_J \hat{J} f(\mathbf{q})\right)^2 \sum_i \int dt \, \frac{\langle S_0(0) S_i(t)\rangle}{S(S+1)} e^{i(qr_i - \omega t)}. \tag{3.15}$$

This part of the neutron scattering cross section can be isolated from the nuclear and nuclear spin incoherent neutron scattering signals with the aid of neutron polarisation analysis. When the spin-flip [4] (SF) and non spin-flip (NSF) neutron diffraction patterns are measured for neutrons polarised initially along the positive $x, y$ and $z$ directions, the magnetic neutron scattering signal can be extracted using [183]

$$\begin{aligned}
\left(\frac{d^2\sigma_{\rm mag}}{d\Omega dE}\right)_{\rm NSF} &= 2\left[2\left(\frac{d^2\sigma_{\rm z}}{d\Omega dE}\right)_{\rm NSF} - \left(\frac{d^2\sigma_{\rm x}}{d\Omega dE}\right)_{\rm NSF} - \left(\frac{d^2\sigma_{\rm y}}{d\Omega dE}\right)_{\rm NSF}\right] \\
\left(\frac{d^2\sigma_{\rm mag}}{d\Omega dE}\right)_{\rm SF} &= 2\left[2\left(\frac{d^2\sigma_{\rm z}}{d\Omega dE}\right)_{\rm SF} + \left(\frac{d^2\sigma_{\rm x}}{d\Omega dE}\right)_{\rm SF} - 2\left(\frac{d^2\sigma_{\rm y}}{d\Omega dE}\right)_{\rm SF}\right]
\end{aligned} \tag{3.16}$$

and

$$\frac{d^2\sigma_{\rm mag}}{d\Omega dE} = \left(\frac{d^2\sigma_{\rm mag}}{d\Omega dE}\right)_{\rm NSF} + \left(\frac{d^2\sigma_{\rm mag}}{d\Omega dE}\right)_{\rm SF}. \tag{3.17}$$

Neutron polarisation analysis is particularly useful for the measurement of magnetic structures with only short ranged correlations.

### 3.1.3 Neutron instrumentation

Neutrons are generated from either a nuclear reactor such as at the Institut Laue Langevin (ILL) in Grenoble, France, or in a collision of high-energy protons on a heavy-metal target (spallation) ISIS in the United Kingdom and SINQ at the Paul Scherrer Institute (PSI) in Switzerland are spallation sources. Most often tungsten is

[4] With "spin-flip" a 180° rotation of the neutron spin is meant, i.e. the spin of a neutron polarised along the positive $x$ (or $y$ or $z$) axis can be rotated due to the interaction with the magnetic structure to point along the negative $x$ (or $y$ or $z$) axis.

used as a spallation target, but other heavy metals such as tantalum and mercury can be used too. The high-energy protons required for spallation sources are generated using a proton synchrotron [5]. For either method of neutron generation the energy of the neutron beam is attenuated with the use of moderators, typically a water tank at room temperature. ISIS is a pulsed neutron source operating at 50 Hz, while SINQ is a continuous source.

### DMC, PSI - powder diffraction

The DMC powder diffractometer at PSI was used to study the temperature dependence of a number of magnetic Bragg reflections in natural jarosite single crystals 4.4.2. This is a cold-neutron 2-axis powder diffractometer, with one axis for the monochromator and one for the sample. The monochromator is a pyrolytic graphite single crystal. Figure 3.2 illustrates the typical set-up of a 2-axis powder diffractometer.

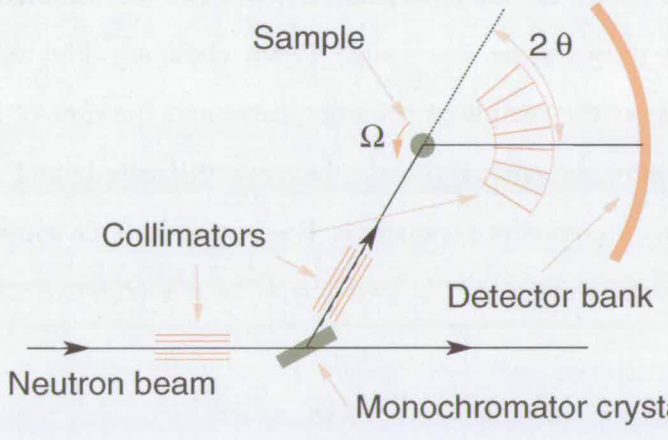


Figure 3.2: A schematic layout of the DMC 2-axis cold-neutron powder diffractometer at PSI. $2\theta$ is the scattering angle, and $\Omega$ is the sample rotation in the scattering plane.

### Rotax, ISIS - diffraction

The instrument Rotax at ISIS, which was used for the measurement of antisite disorder between $Cu^{2+}$ and $Zn^{2+}$ ions in zinc paratacamite, is a time-of-flight neutron

[5]The protons are obtained by the hydrolysis of water.

diffractometer [108]. Due to the pulsed nature of the neutron beam at ISIS, the energy (speed) of the a neutron can be deduced from its time-of-flight; $\hbar\omega = \frac{1}{2}m_n v^2 = 5.227 \cdot 10^{-6}(l/t_{TOF})^2$ eV where $l$ is the flight path of 15 m, and $t_{TOF}$ is the time between the creation of the neutron and its detection. The energy resolution is in this case limited by the pulse duration of the neutron source, for Rotax this is 30 ms. Due to the large range of neutron energies generated, each detector over a range of $\theta/2\theta$ angles measures a large section of the diffraction pattern by recording the time of each count, and a very wide range of $d$ spacings can be accessed $0.2 \leq d \leq 50$ Å.

### IN4, ILL - spectroscopy

The spectrometer IN4 at the ILL carries out time of flight analysis, but this time to measure the energy of inelastically scattered neutrons [195]. The neutron source of ILL is continuous, and a single neutron energy is selected with a focussing crystal monochromator. Just before the monochromated neutrons enter the sample the beam is chopped into short pulses using a so called *Fermi* chopper. The monochromated neutrons will all arrive at the sample at the same time, and the time-of-flight analysis is carried out to measure the energy transfer between the sample and the diffracted neutrons as a function of momentum transfer $q$. Due to the variable length of $k'$, which in the case of an energy transfer $\Delta E$ is given by $k' = k \pm (\Delta E/2.072)^{\frac{1}{2}}$, the Bragg condition changes to

$$\mathbf{q}^2 = \mathbf{k}^2 + \mathbf{k'}^2 - 2kk'\cos(2\theta) \tag{3.18}$$

where $2\theta$ marks the position of individual detectors.

### D7, ILL - polarisation analysis

D7 is a cold-neutron (long wavelength) diffractometer which allows for neutron polarisation analysis [58]. By measuring the spin flipped and non spin flipped neutrons diffracted at each $q$ for incoming neutrons subsequently polarised along the positive $x, y$ and $z$ axis, the short-ranged magnetic correlations in disordered magnetic phases can

be separated from diffuse scattering due to nuclear disorder and due to nuclear-spin incoherent scattering using equations 3.16 and 3.17. Because within each magnetic ion the magnetic structure will be 100% correlated, only the first and sometimes also the second Brillouin zones are of interest. Hence, low-energy neutrons can be used, with a wavelength of typically 3 to 6 Å. Figure 3.3 illustrates the layout of D7. The incoming neutrons are monochromated using a pyrolytic graphite focussing monochromator. By passing the neutrons through a gas chamber filled with polarised $^3$He the neutron beam is polarised [173]. The neutron polarisation is then rotated to the desired direction using a Mezei flipper [118] and electromagnetic coils around the sample. The polarisation analysis of the diffracted beam is done using polarising super mirrors which only reflect neutrons of a particular polarisation onto the detectors. Optionally a Fermi-chopper can be inserted in the beam before the sample, in order to allow for neutron time-of-flight analysis to measure the energy transfer of the diffracted neutrons. This goes at the cost of a factor 50 in neutron intensity.

#### Neutron detectors

The collision of thermal neutrons with nuclei can cause the nuclei to fragment, with the release of a large number of electrons in the case of $^3$He gas detectors, and release of photons in the case of a Li-glass scintillation detector. Electrons are easily detected using a cathode and anode in the compressed $^3$He gas chamber, and the photons produced in scintillation detectors are counted using photo-multiplier tubes.

## 3.2 Muon-spin relaxation spectroscopy ($\mu$SR)

Muons are generated by passing a high energy proton beam, readily available in neutron spallation sources such as ISIS and PSI, through a sheet of carbon. When a high energy ($\sim$ 800 MeV) proton collides with a light nucleus, a free pion is created. This particle, which is a boson which glues the nuclei within a nucleus together, has a half life of only 26 ns. On decay of positively and negative charged pions, muons of the same charge

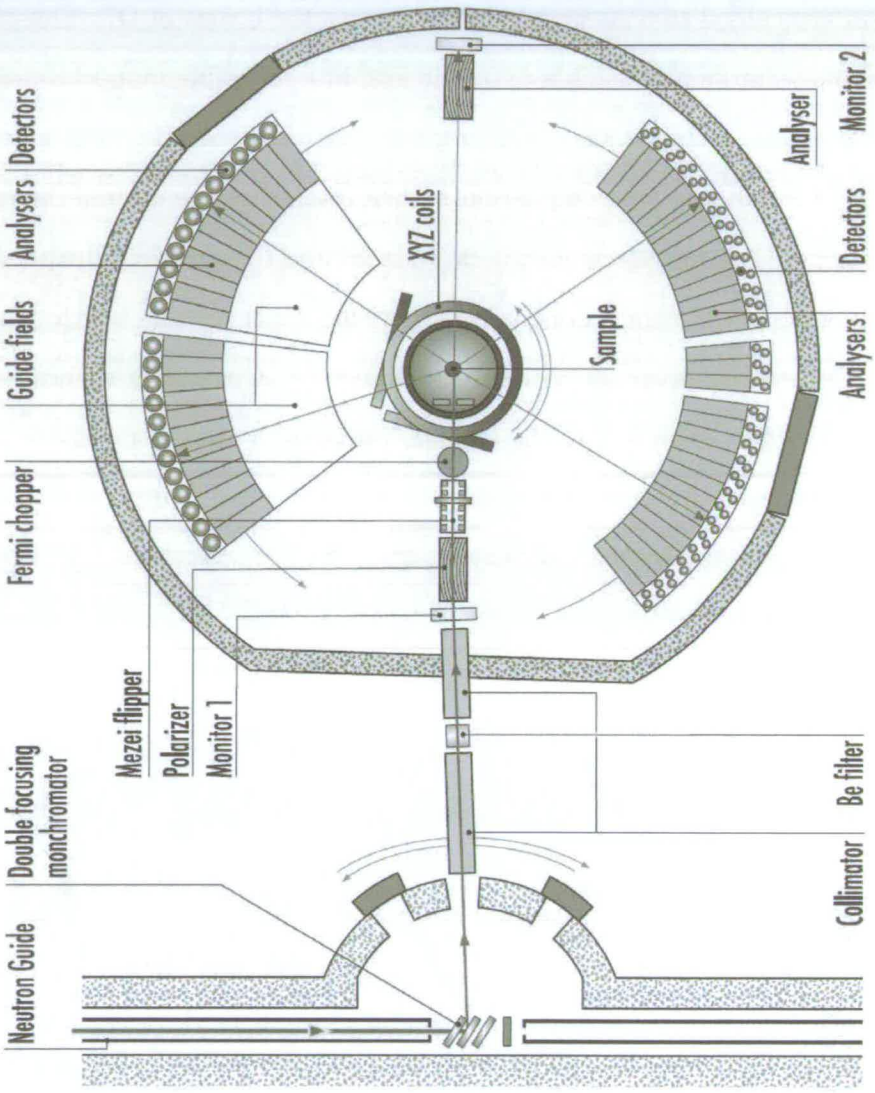


Figure 3.3: An illustration of the layout of D7 at ILL, from [58].

are produced, in addition to a neutrino. A typical reaction leading to a positive muon ($\mu^+$) is [62]

$$\begin{aligned} \mathrm{p} + \mathrm{p} &\longrightarrow \mathrm{p} + \mathrm{n} + \pi^+ \\ \pi^+ &\longrightarrow \mu^+ + \nu_\mu \end{aligned} \tag{3.19}$$

The pion is normally brought to rest in the so-called production target so that it decays when at rest in the laboratory reference frame and creates a muon of well-defined energy. The muon is a $S = 1/2$ particle with a mass of 139.6 MeV $\sim 200\times$ the electron mass. In process 3.19 the spin moment of the muon is aligned along the propagation direction of the muon.

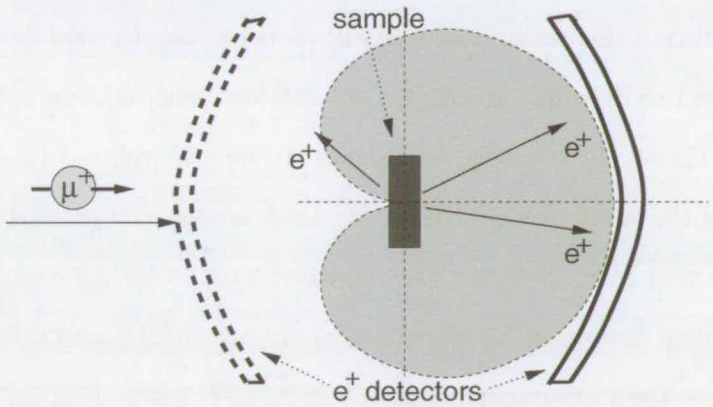


Figure 3.4: An illustration of the muon spin relaxation ($\mu$SR) spectroscopy technique. The grey area illustrates the angular distribution of positron decay in the case of a forwards polarised muon.

In a muon-spin relaxation ($\mu$SR) experiment positive muons are made incident on the sample, where they stop most often near a negative ion within 2 mm from the surface. Once at rest, each muon will precess in the local magnetic fields, until it decays into a positron and two neutrinos after on average 2.2 $\mu$s. The decay process is

$$\mu^+ \longrightarrow \mathrm{e}^+ + \nu_\mathrm{e} + \overline{\nu}_\mu \tag{3.20}$$

and the positron momentum is preferentially along the magnetic orientation of the muon spin at the time of decay. This situation is illustrated in figure 3.4. The asymmetry between forwards and backwards emitted positrons as a function of time is given by

$$A(t) = \frac{B(t) - \alpha F(t)}{B(t) + \alpha F(t)}, \tag{3.21}$$

where $\alpha$ is a calibration constant, correcting for misalignments of the sample and differences in detector efficiencies. $A(t)$ can be recorded over a time window of typically 10 $\mu$s and the distribution of precession frequencies obtained from $A(t)$ is a direct measure of the distribution of magnetic fields at the muon sites. In [205] an outline of the relaxation functions encountered in different situations is given.

The sample environment is surrounded by electromagnets which can generate magnetic fields transverse and longitudinal to the initial muon polarisation. A transverse field is used to calibrate the instrument and obtain $\alpha$. A longitudinal field of the order of 100 Gauss is used to decouple the dipole interactions with nuclear spins, which are of the order of 10 Gauss. In this way the muons can only be relaxed by electronic moments which are of the order of 2000 Gauss. Samples are usually pressed into pellets of $\approx$ 2 mm thickness and 2 cm diameter and attached to a Cu or Ag sample plate. The experiments described in section 5.4 were carried out at the LTF and GPS instruments at PSI, and later at the instrument MUSR at ISIS. LTF has a dilution-fridge sample environment which can be used to cool the sample to 20 mK. $\mu$SR can also be equipped with a dilution fridge, with a minimum temperature of 40 mK. Further characteristics of these instruments are discussed in section 5.4.

## 3.3 X-ray spectroscopy

In non-resonant X-ray diffraction all electrons are probed. This can be beneficial but it is very exceptional that the obtained electron density has a resolution of one or less electrons. A solution can be to tune to particular X-ray absorption lines involving

the atomic shells or bands of interest. In this way the X-ray scattering cross-section for the shells of interest can be increased by orders of magnitude. For the first-row transition-metal compounds the shell of most importance for the determination of the electronic structure is the $3d$ shell. Unfortunately, the highest-energy dipole-allowed transition $2p \rightarrow 3d$ lies at an energy ranging from 452.2 eV for Ti to 1011.7 eV for Zn. The corresponding wavelengths are well above 10 Å, too long to resolve atomic and antiferromagnetic structures. X-rays within this energy range are called soft X-rays, which is probably because even in air the absorption length is of the order of a few millimetre. As a consequence an ultra-high-vacuum (UHV) beamline and experimental set-up is required, and at most the top 100 nm of the sample surface are probed.

This means that the application of X-rays for the magnetic characterisation of transition-metal compounds is mostly restricted to spectroscopy. This turns out to be a very powerful technique, since it is possible to obtain detailed information on the magnetic state of the ions and their anisotropy, in particular when the X-ray polarisation dependent spectra are measured on single crystals. Where neutrons are often ideal for finding out *what* happens at the atomic scale, X-ray absorption spectroscopy of the $2p \rightarrow 3d$ absorption edges can help to find out *why* something is happening. This is exemplified by amongst many other experiments the X-ray absorption study described in section 4.5. The details of the interpretation of the absorption spectra will be described in the following paragraph, and the subjects of Hartree-Fock calculations and determinants was briefly touched in section 2.2.2.

### 3.3.1 The interpretation of X-ray spectra

The $2p$ core hole created by the promotion of a $2p$ electron to the $3d$ shell by the absorption of an X-ray photon modifies the $3d$ wave-functions in the final state. This is the reason why in the $2p^6d^n \rightarrow 2p^5d^{n+1}$ dipole transition the absorption cross-section $I(\hbar\omega)$ cannot be interpreted as the square of the density of states of unoccupied $3d$ levels in the ground state. For ferromagnets and magnetically soft materials, in which

all the magnetic moments can be aligned with the application of an external field, the X-ray magnetic circular dichroism (XMCD) and X-ray magnetic linear dichroism (XMLD) sum-rules can be applied to obtain expectation values for the orbital angular momentum and the magneto-crystalline anisotropy respectively. In the case of the jarosites it is not possible to align the magnetic moments using an external field, because the large energy scale of the antiferromagnetic interactions ($\theta_{\mathrm{w}} \approx 800\mathrm{K}$). Hence, the only way to obtain accurate information about the relevant expectation values is by explicitly calculating

$$f(E_{\hbar\omega}, \mathbf{q}) \approx \frac{\langle\psi_g|\,\hat{\mathbf{r}}_{\mathbf{q}}\,|\psi_e\rangle\,\langle\psi_e|\,\hat{\mathbf{r}}_{\mathbf{q}}\,|\psi_g\rangle}{E_{\hbar\omega} - \Delta E - i\Gamma/2},$$

where $f$ is the resonance amplitude between the ground state $\psi_g$ and the excited state $\psi_e$, $\hat{\mathbf{r}}_{\mathbf{q}}$ is the electric dipole operator for X-rays with polarisation state $\mathbf{q}$ and $\Gamma$ is the life-time broadening which is treated as a fitting parameter. Experimentally obtained X-ray spectra can now be used to find good approximations for $\psi_g$ (and $\psi_e$). The Hilbert space for $|\psi_g\rangle$ ($|\psi_e\rangle$) is spanned by determinants of the lowest atomic $JLS$ configurations of $|2\mathrm{p}^6 3\mathrm{d}^{\mathrm{n}}\rangle$ ($|2\mathrm{p}^5 3\mathrm{d}^{\mathrm{n}+1}\rangle$). If needed, also $|2\mathrm{p}^6 3\mathrm{d}^{\mathrm{n}+1}\underline{\mathrm{L}}\rangle$ ($|2\mathrm{p}^5 3\mathrm{d}^{\mathrm{n}+2}\underline{\mathrm{L}}\rangle$) configurations are included, where $\underline{L}$ denotes a ligand hole. The fitting procedure consists of finding the correct perturbations to the $3d$ valence shell of the free ion arising from crystal- and ligand-field effects, which split the degenerate orbital angular momentum states into the irreducible representations of the symmetry group of the local crystal field. In addition the spin-orbit coupling between single-electron states is taken into account, in the otherwise non-relativistic calculation. Comparison between experiment and theory has also shown that the Slater integrals for the Coulomb interactions and spin-orbit couplings need to be reduced to 70 - 80 % of the free ion values to account for solid-state effects.

This approach is of course of very general applicability. The power of core-level spectroscopies is that the energy and orbital angular momentum states of the core-levels are very well defined, and hence well known. In optical experiments only $3p \rightarrow 3d$ transitions can be probed. To treat them it would be necessary to integrate over a

number of possible initial states arising from the widening of the 3p energy bands and the partial quenching of the orbital angular momentum due to crystal fields. This blurs the effect of the optical selection rules arising from the conservation of angular momentum. It is the strict applicability of the optical selection rules which make polarisation-resolved X-ray absorption spectroscopy such a powerful technique for the study of magnetic materials.

### 3.3.2 Soft X-ray beamlines

Soft X-rays are generated at synchrotron facilities such as the SRS in Daresbury and the ESRF in Grenoble in France. The electrons making their orbit through the synchrotron are passed through a straight section with an array of undulating magnets, called an *undulator*. The undulators make the electrons oscillate with the frequency needed for the generation of X-rays of a particular energy. For the generation of X-rays with a tunable polarisation, i.e. well defined orbital angular momentum, two undulators which make an angle of 90° degrees with each other are used. By shifting one undulator with half a phase with respect to the other, the X-ray polarisation can be tuned from horizontal, to left- or right-hand circular and to vertical. In this way the APPLE II undulator at ID08 at the ESRF achieves 100% X-ray polarisation of any orientation, with a negligible loss in beam alignment between polarisation changes.

The beamline consists of a spherical grating monochromator [6] with a pattern of 1200 lines per mm. The X-rays are incident on this grating in a grazing angle and reflect a "rainbow" of frequencies of which one is selected using a narrow slit. The resulting energy resolution is $\Delta E/E = 5 \cdot 10^{-4}$ at $E = 850$ eV. A vertical focussing mirror is used to focus the beam onto the sample, resulting in a spot size of $h \times v = 1$ mm$\times 40$ $\mu$m. The beamline to station 5U.1 in Daresbury is of a similar design.

[6] Note that a single crystal Bragg reflection monochromator does not work, because the wavelength of soft X-rays is too long.

### 3.3.3 Sample environment at ID8, ESRF

For experiments at ID8 at the ESRF the high-field magnet end-station was used. The sample chamber in this instrument has a vacuum of $10^{-10}$ mbar. This is achieved without bake-out which has the advantage that delicate samples are not damaged prior to the experiment. The samples can be mounted onto a cryostat via a load lock mechanism, and cooled down to below 10 K. The sample can also be rotated in order to align the correct crystal faces to the beam. Especially when measurements are done at temperatures below $\sim$ 100 K, it is important that the vacuum is in the $10^{-10}$ mbar range, because only a very thin layer of ice frozen to the sample surface will absorb X-rays. Even with this pressure, it turned out to be impossible to measure the oxygen $K$ edge at low temperatures, due to water ice freezing onto the sample.

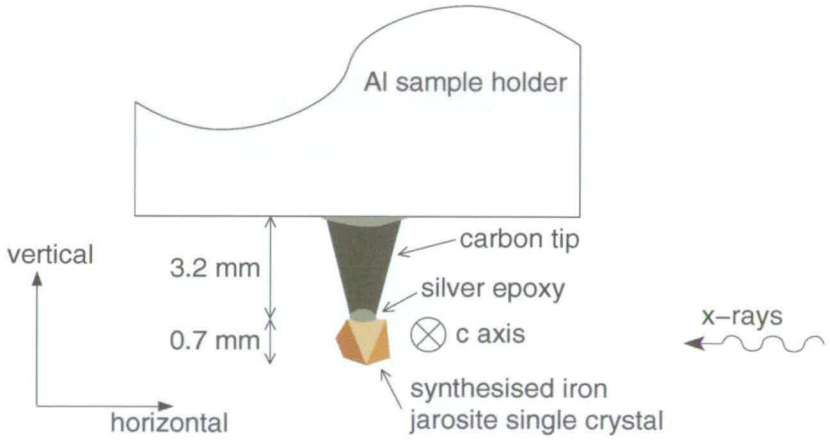


Figure 3.5: The oriented iron jarosite single crystal was suspended on a carbon tip below the standard ID8, ESRF sample plates, using silver epoxy. In this way good thermal and electrical contact was ensured, while the background noise from photo electron currents from the sample holder were minimised.

The experiments described in section 4.5 were carried out using synthesised potassium iron jarosite single crystals. The largest single crystals were 0.7 mm in diameter. The crystals were aligned using a Bruker APEX-II single-crystal X-ray diffractometer. A number of factors needed to be taken into consideration with mounting the samples. The X-ray absorption spectrum is obtained by measuring the photo-electron replacement current from the sample, hence it must be ensured that the sample makes good

electrical contact with the sample holder, as well as good thermal contact. This was achieved using a UHV compatible silver-filled epoxy and silver paint. An additional complication was that due to the strongly insulating nature of iron jarosite the signal from the sample was small compared to the signal from the metallic sample holder, even at the Fe $L_{2,3}$ edges, and in a normal set-up it was impossible to avoid X-rays hitting the sample holder because the beam was larger than the sample. Hence, the single crystal was suspended below the sample plate using a carbon tip glued to the bottom of the sample holder, as illustrated in figure 3.5. Carbon is a good thermal and electrical conductor, but does not give a large photo-electron current from incident X-rays. The samples were mounted with the $c$ axis perpendicular to the X-ray beam, so that the X-ray absorption spectra could be measured with the X-ray polarisation parallel to the $c$ axis and perpendicular to the $c$ axis by rotating the polarisation of the incoming X-ray beam.

Further measurements were carried out on a 16 mg single crystal from a natural source (Chihuahua, Mexico), as described in 4.4. Due to the shape of these crystals with large [001] and [00$\bar{1}$] surfaces they were mounted in a different geometry; a plate shaped crystal was glued on the sample plate with silver paint. The beam was incident on the [001] surface at a grazing angle of 30°. With horizontally polarised X-rays the polarisation made an angle of 60° with the [001] surface, measuring $I_{60°}$. $I_{ab}$ was measured using vertically polarised X-rays. The X-ray absorption spectrum with polarisation parallel to the $c$ axis was calculated using $I_c = \frac{4}{3}I_{60°} - \frac{1}{3}I_{ab}$, using $\hat{p}_{60°} = \cos(60)\hat{p}_{ab} + \sin(60)\hat{p}_c$ where $\hat{p}$ is the X-ray polarisation vector and hence $I \propto |\hat{p}|^2$. The isotropic spectrum ($I_{iso} = \frac{2}{3}I_{ab} + \frac{1}{3}I_c$) and the X-ray linear dichroism spectrum ($I_{xld} = I_c - I_{ab}$) can be calculated using respectively $I_{iso} = \frac{5}{9}I_{ab} + \frac{4}{9}I_{60°}$ and $I_{xld} = \frac{4}{3}(I_{60°} - I_{ab})$.

### 3.3.4 Sample environment at 5U.1 at the SRS

For the experiments at station 5U.1 at the SRS the instrument schematically illustrated in figure 3.6 (later called Mark I, before it being cannibalised for other experiments) was built. This instrument was designed to measure the isotropic soft X-ray absorption spectra of powder samples at temperatures down to $\sim$ 25 K. To minimise the number of vacuum bakes needed [7], several samples were mounted on a single sample plate at the end of the cold finger of a liquid He cryostat. The hydronium and potassium iron jarosite powder samples were either pressed into pellets mixed with carbon powder, or stuck onto carbon tape which is a vacuum compatible double-sided adhesive tape.

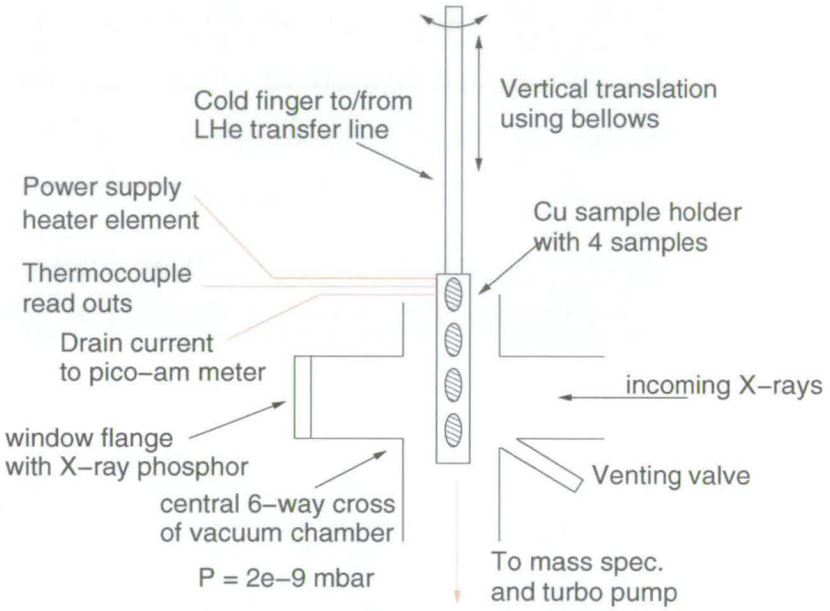


Figure 3.6: A schematic layout of the purpose built end-station for soft X-ray spectroscopy measurements at temperatures down to $\sim$ 25 K at station 5U.1 at the SRS in Daresbury.

At the top of figure 3.6 the liquid He transfer line is inserted into the cold finger. The tower in which the cold finger is inserted is topped with a differentially pumped rotary feed through, which allowed for rotation of the samples around the vertical axis. Using a vertical translation stage with vacuum bellows just below the rotary feed through, the

[7] When a UHV instrument is exposed to air, the instrument must be heated to approximately 160° Celsius for 12 hours while evacuated. In this way all water evaporates and a vacuum of better than $10^{-8}$ mbar can be achieved

samples could be moved to height of the incoming X-ray beam, at the 6-way cross at the centre of the figure. The vertical alignment of the samples was achieved by sliding a thick Al base plate (not shown), on which the 6-way cross was mounted, with respect to the instrument platform. The vacuum chamber is pumped with a turbo pump which is connected below the central 6-way cross, through a hole in the Al base plate. A mass spectrometer was inserted just above the turbo pump for diagnostics on the vacuum. A T-valve coming out of the central cross leading to a swagelock connection was used to vent the instrument with nitrogen before opening. The base pressure achieved after a vacuum bake was $2 \cdot 10^{-9}$ mbar. This was good enough to allow for the measurement of the absorption spectrum at the Fe $L_{2,3}$ edges at $\sim 25$ K. The oxygen $K$ edge was found to change with time when the cryostat was cold, which was interpreted as due to the increasing volume of water ice freezing onto the sample surface.

The sample plate at the end of the cold finger is electrically isolated from the cold finger by a sapphire disk, to allow for accurate measurement of the drain current from the sample. The drain current is measured using a pico-Ampère meter connected via the a well shielded co-axial cable connected to one of the electrical feed throughs at the top of the instrument. Other feed throughs were used for thermocouples and a heating element at the sample plate.

## 3.4 DC SQUID magnetometry

The magnetic susceptibility of a material $\chi$ is defined as $\chi = \frac{\partial M}{\partial H}|_{H=0} = \lim_{H \to 0} \frac{M}{H}$. The common way to measure the magnetic susceptibility as a function of temperature is with a Superconducting QUantum Interference Device (SQUID) magnetometer [178, 103], using fields of typically $H = 100$ Gauss. The measurements presented in chapter 5 and 4 have been measured using the Quantum Design Magnetic Properly Measurement System (QD-MPMS) [129] installed in CSEC.

In the QD-MPMS a uniform magnetic field $H$ is applied to the sample using a large superconducting magnet. The sample is normally contained in a gelatine capsule in a

plastic drinking straw, and suspended in that uniform magnetic field on a long rod. The material of the capsule and the straw is chosen for its negligible magnetic susceptibility. A superconducting pick-up coil is wound around the sample in the fashion illustrated in the left side of figure 3.7, with two clockwise and two anti-clockwise windings, so that any changes in the uniform applied magnetic field $H$ does not induce any current in it. When the sample, magnetised by the external field $H$, is moved up and down through the pick-up coils it will generate a magnetic induction current, because the field from the sample is only *local*, or at least, not uniform over the distance of the counter-wound pick-up coils.

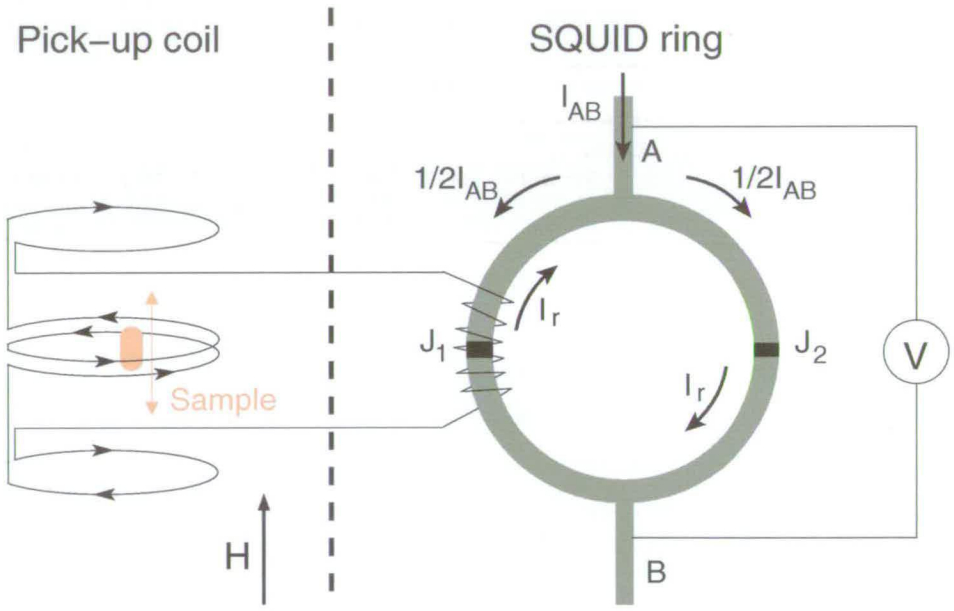


Figure 3.7: A schematic illustration of the principle of a operation of the QD-MPMS SQUID magnetometer. The actual measurement using the SQUID ring is separated from the sample environment. The field from the sample induces a current in the pick-up coil, which in turn produces a field at one of the Josephson junctions ($J_1$) in the superconducting ring.

This induction current is measured using a SQUID ring otherwise electromagnetically separated from the superconducting magnet. The SQUID ring [25] as illustrated on the right side of figure 3.7 is a superconducting loop with two weak links - Josephson junctions [102]. The Cooper pair wave function in the superconducting ring is a

standing wave with an integer number $n$ of phases fitting in the ring,

$$\Phi_n(x) = e^{ik_n x} \text{ with } k_n = \frac{2n}{d} \tag{3.22}$$

and $d$ is the diameter of the ring [8]. At the points of the weak links the wave function tunnels through the thin layer of insulating material giving rise to a phase lag in the wave function [102]. In zero applied field the phase lag of the junctions on both sides of the ring is equal. When a small magnetic field is applied to one of the junctions ($J_1$) due to a current from the pick-up coil, a current is induced in the SQUID ring, so that total wave function remains of the form 3.22.

When an additional current $I_{AB}$ is applied between the points A and B, the total current through the ring reaches the critical current at $I_c = \frac{1}{2}I_{AB} + I_r$, and a voltage will build up between A and B. At this point $I_r$ is given by $I_c - I_{AB}$. Hence, by measuring $I_r$ as a function of time, i.e. as a function of displacement of the magnetised sample through the pick-up coils, the magnetic moment of the sample can be deduced with a very high accuracy.

## 3.5 Heat capacity measurements

Heat capacity measurements were carried out on the Quantum Design Physical Property Measurement System (QD-PPMS) [159] available in CSEC. With this instrument the heat capacity can be measured in applied magnetic fields up to 9 T. With the use of the PPMS Helium-3 Refrigerator System temperatures down to 0.35 K could be reached. For each temperature scan the sample was first cooled in zero field, and data was taken from low to high temperatures. The system measures the temperature of the sample platform during the input of a well defined quantity of thermal energy, and

[8] Note that according to the theorem given in section 2.1.1 the periodic rotational symmetry of the ring restricts the wave functions to eigenfunctions which translate as $\Phi(x + \pi d) = e^{i\theta}\Phi(x)$ where $\theta$ is an arbitrary phase. The kind of order, or symmetry breaking exhibited in $\Phi_n(x)$ where $\theta$ can be set to zero for all cooper-pairs in the ring, is called topological order or gauge-symmetry breaking, which is characteristic for superconducting and superfluid phases.

during the release of this energy. Using this data, the system extracts both the sample's heat capacity and the thermal conductivity between the sample and the sample platform, by numerically solving the coupled differential equations for the heating/cooling curves of the platform and the sample.

Chapter 4

# Iron jarosite

The sulfates of the alunite group of minerals with general formula $AM_3(OH)_6(SO_4)_2$ provide the basis for a large number of compounds. The $A$ site can host a wide range of monovalent cations such as $K^+$, $Na^+$, $Rb^+$, $Ag^+$, $H_3O^+$ and $NH_4^+$, [224] and even divalent ions. This structure with $R\bar{3}m$ symmetry is the basis for a number of experimental kagomé antiferromagnets, this time with trivalent ions like $Fe^{3+}$ ($3d^5$) [105, 224, 81], $Cr^{3+}$ ($3d^3$) [204, 105, 96] and $V^{3+}$ ($3d^2$) [155, 80] at the $M$ site. All three ions have a high-spin ground state $S = 5/2$, $S = 3/2$ and $S = 1$ respectively, and they are antiferromagnetically coupled within the kagomé planes via shared oxygen atoms of hydroxy groups. The $M$ site resides at the centre of $O_6$ octahedra of $D_{4h}$ symmetry, forming kagomé nets as shown in figure 4.1a. The kagomé layers are stacked in an ABC manner and are well separated, with the shortest pathway being from one layer to the next via the sulfate group, shown as pyramids in figure 4.1b.

In nature the $A$- and $M$-site in $AM_3(OH)_6(SO_4)_2$ are most commonly occupied by potassium and trivalent iron respectively. This is the jarosite mineral, named after the location in which it was first found, the Barranco Jaroso in the Sierra de Almagrera, Spain. Single crystals of up to a few mm in diameter have been found with this composition. Now the entire group of minerals is commonly referred to as the jarosites. A large number of varieties of the jarosite mineral have been found as weathering

products in mines, and polluted sites where it takes up heavy metals. Iron jarosite has been found in places as far away as the planet Mars [66].

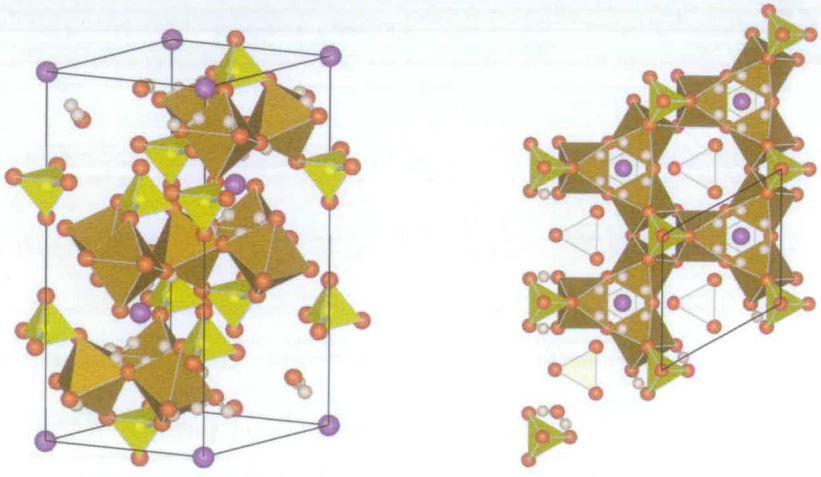

Figure 4.1: The jarosite structure viewed perpendicular to the $c$ axis (left picture) and along the $c$ axis (right picture). The $MO_6$ octahedra, forming the kagomé layers, are drawn in brown, $SO_4$ tetrahedra in yellow, with oxygen in red, the $A$ site in purple, and hydrogen in pink.

Here potassium iron jarosite ($KFe_3(OH)_6(SO_4)_2$) which can be seen as representative for the analogues with $A = Na^+$, $Rb^+$, $Ag^+$ and $NH_4^+$ and hydronium iron jarosite ($H_3OFe_3(OH)_6(SO_4)_2$) are studied. With their large $S = 5/2$ spin moment these systems were until very recently [172] the best physical realisations of the classical kagomé antiferromagnet. Despite their similarity and the fact that they appear such well-suited model systems, they have very different ground states. Potassium iron jarosite freezes into a long range ordered 120° spin structure at $\approx 65$ K, while hydronium iron jarosite becomes glassy below $\approx 17$ K, with only short-range 2D correlations. Frustration is often quoted as an essential ingredient for a glassy ground state. This raises the question whether for some reason one is a better realisation of the theoretical model than the other? It is also possible that because of the large ground state degeneracy of the Heisenberg Hamiltonians in frustrated geometries, additional terms in the magnetic Hamiltonians play a decisive role. Inevitably, these will vary from system to system.

For the iron jarosites this leaves us with an interesting question which will be addressed using a combination of experimental and numerical techniques.

This chapter describes the synthesis of single crystals, magnetic susceptibility measurements, a single crystal neutron diffraction measurement and an x-ray spectroscopy experiment which took up a large part of this PhD. In the next two sections the relevant literature is reviewed.

## 4.1 Potassium jarosite

### 4.1.1 The magnetic ground state

Based on Mössbauer measurements it was first suggested by Takano [197] that potassium iron jarosite orders in a triangular magnetic structure at low temperatures, which was confirmed by Townsend [204] using neutron diffraction at 4 K. Wills *et al.* [224, 225] have studied the whole series with $M$ = Fe and $A$ = K, Na, Rb, Ag, $H_3O$ and $NH_4$. Using neutron diffraction they found that all but the hydronium jarosite analogue, which will be discussed separately, order into a $q = 0$ structure with positive chirality around 50 K. This is a three sub-lattice ordering where the magnetic unit cell coincides with the crystallographic unit cell, as shown in figure 4.2.

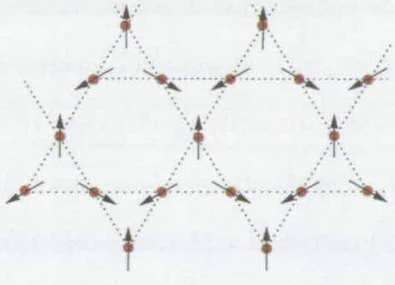

Figure 4.2: The three sub-lattice $q = 0$ structure with positive chirality.

Along the $c$ axis the crystallographic unit cell is doubled which could mean that the kagomé layers with a net moment are coupled antiferromagnetically. Such a situation could arise in a so-called umbrella structure where the spins are canted out of the kagomé planes, as was also suggested by Inami *et al.* [97, 147]. These experiments were

all carried out using powder samples synthesised using a solvothermal method [60]. A known problem with the solvothermal synthesis method is that a variable fraction of the $A$ site cations is substituted with $H_3O^+$ and the occupancy of the $M$ site is only around 90% [224, 148]. As a result the transition temperature found in these samples lies between 48 and 56 K. Recently a method to synthesise single crystals of potassium iron jarosite has been published [83] using a redox process. Samples grown using this redox method are stoichiometrically pure, and the phase transition occurs at a higher temperature, with 65(1) K quoted for the potassium analogue [83].

These synthetic single crystals have provided a wealth of information, mostly described in [83, 81] and [127]. The structural parameters of potassium jarosite crystals synthesised using this new method are listed in table 4.1. Neutron diffraction measurements on these single crystals have confirmed the $q = 0$ spin structure with a uniform positive chirality pointing along the $c$ axis [81]. The canting angle of the umbrella structure was found to be very small, only 0.65(6)° at 40 K. This is also been confirmed in a polarisation resolved neutron diffraction experiment on a large single crystal from a natural source, which shows that the ordered out-of-plane magnetic moment is less than $0.1\mu_B$ [86]. Surprisingly, on application of strong magnetic fields ($H > 5$ T) along the $c$ axis, a transition to a phase with staggered chirality occurs [81]. Furthermore, spin fluctuations were found to be primarily confined to the $xy$ plane coinciding with the kagomé layers even above $T_N$. Synthetic single crystals [81] as well as single crystals from a natural source ([157] and section 4.4.1) also reveal that at low temperatures the magnetic response is strongly anisotropic. At the transition temperature the susceptibility along the $c$ axis shows a sharp peak, while the susceptibility along the $ab$ axis has a rounded peak. This suggests that a magnetic anisotropy plays a role in the formation of the long range ordered ground state. The field-cooled and zero-field cooled susceptibilities are found to diverge at 53 K well below the transition temperature at 64 K. This has prompted speculations about a second transition [223], but further neutron

Table 4.1: Atomic coordinates of $KFe_3(OH)_6(SO_4)_2$. From Grohol *et al.* [81].

| atom | $x$ | $y$ | $z$ | $U_{iso}/Å^2$ |
|---|---|---|---|---|
| Fe | 0.3333 | 0.1667 | 0.1667 | 0.07(1) |
| S | 0 | 0 | 0.3087(2) | 0.07(1) |
| O1 | 0 | 0 | 0.3936(4) | 0.010(2) |
| O2 | 0.2203(7) | 0.1102(3) | 0.2795(2) | 0.011(1) |
| O3 | 0.1276(3) | 0.2553(7) | 0.1329(2) | 0.09(1) |
| K | 0 | 0 | 0 | 0.014(1) |

Space group $R\bar{3}m$, $a = 7.3044(7)$Å, $c = 17.185(2)$Å, $\alpha = 90°$, $\gamma = 120°$

diffraction measurements on natural single crystals (section 4.4) and powders has not revealed any further changes in the magnetic structure.

In table 4.3 a number of physical parameters, such as the Weiss temperature $\theta_w$, Curie constant $C$ and exchange interaction $J$ are given along with some crystallographic characteristics, for both the potassium and the hydronium analogs.

### 4.1.2 The role of a magnetic anisotropy in the transition

It has been shown [43] that due to an order from disorder effect [216], the classical kagomé antiferromagnet approaches a nematically ordered state with $T \to 0$. However, the Heisenberg Hamiltonian is invariant on the simultaneous local rotations of the spins, and hence the ground state of the classical system has a corresponding degeneracy. Even in the case of a symmetry-breaking transition to a spin-nematic, the nematic plane can be aligned in any direction, and does not need to coincide with the kagomé plane. This has been illustrated in section 2.3.1.

A magnetic anisotropy is needed to couple the spin-space to the lattice-space. This can happen in two ways; via the dipole-dipole interaction, which in transition metal compounds is much weaker than the super-exchange interaction, and via the spin-orbit ($LS$) couping, $\mathcal{H}_{LS} = \lambda LS$. The possibility that the former plays a role in the jarosites has been investigated, but this was found to be unlikely [55]. By elimination this leaves an anisotropy arising from the $LS$-coupling, despite the fact that there is no orbital momentum and $\lambda = 0$ in the half-filled shell ($3d^5$) of the $Fe^{3+}$ ion. Figure 4.3 illustrates

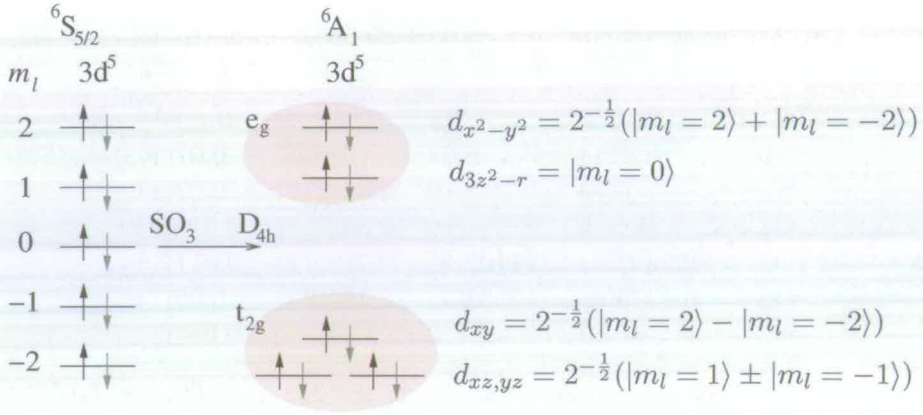


Figure 4.3: A half-filled $3d$ shell in the free ion (left) and in a tetragonal crystal field (right). The grey arrows are unoccupied states. The levels in the shaded areas are degenerate in an octahedral (cubic) crystal field.

the occupation of the angular-momentum states of the $3d$ shell in the case of half-filling. It should be clear from this diagram that as long as no low-spin or $3d^6$ configurations become occupied, there is no net orbital angular momentum, regardless of the way the orbital angular momentum states are re-arranged due to crystal fields and other terms.

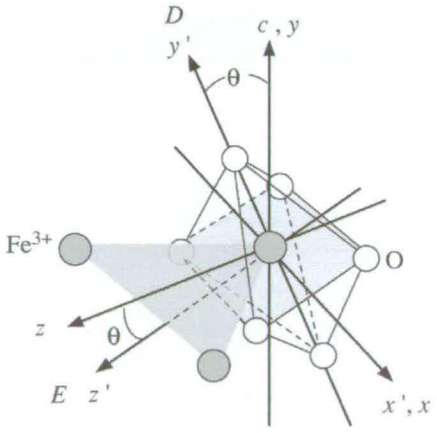


Figure 4.4: The orientation of the $FeO_6$ octahedra with local coordinates $x', y', z'$ with respect to the global coordinates $x, y, z$ where $x$ coincides with the $a$ axis and $z$ with the $c$ axis. $\theta$ is the canting angle of the octahedra with respect to the $c$ axis. Figure taken from [148].

Inami *et al.* [147] suggested that the $q = 0$ ground state is selected due to an easy-plane single-ion anisotropy due to the canting of the local anisotropy axis, the $z$ axis of the slightly trigonally distorted $FeO_6$ octahedra, as shown in figure 4.4. El-hajal *et al.* [63] suggested that the the Dzyaloshinsky-Moriya interaction (DMI) [144]

may play an important role in the jarosites, as it does in hematite [144] because it arises in first order of both $LS$-coupling and magnetic exchange $J$, while the single-ion anisotropy arises only in second order perturbation theory from the already weak $LS$-coupling. Moriya estimated that the strength of the DMI is of the order $\approx \delta g/g$, while the single-ion anisotropy is of the order $\lambda(g_{\|} - g_{\perp})$. The DMI is therefore much more likely to play a major role. Elhajal *et al.* have shown that this type of antisymmetric (and anisotropic) super-exchange is allowed in the geometry of the kagomé lattice, and that for the jarosites it can give rise to a $q = 0$ magnetic structure with positive chirality as defined with equation 2.53. Spin-wave measurements on single crystals can be fitted with both a combination of either DMI or single-ion anisotropy, with further neighbour interactions. The fit results from the literature [81, 127, 234, 48] are shown in table 4.1.2. Matan *et al.* also find that fits with DMI give a slightly better correspondence with the experimental data, and the general consensus in [63, 81, 127, 234, 48] is that the Dzyaloshinsky-Moriya provides the most plausible explanation of low temperature magnetic properties in most iron jarosites apart from the hydronium analog.

Table 4.2: Fit results of spin-wave analysis of inelastic neutron scattering data on potassium iron jarosite, using a model with single-ion anisotropy $\mathcal{H}_{\mathrm{CF}} = DS_{z'}^2 - E(S_{x'}^2 - S_{y'}^2)$ where $x', y'$ and $z'$ are the axes of the local $FeO_6$ crystal-field symmetry, and $\mathcal{H}_{\mathrm{DM}} = \vec{D}_{ij} \cdot \vec{S}_i \times \vec{S}_j$.

| | Coomer *et al.* [48] /meV | Matan *et al.* [127] /meV |
|---|---|---|
| $J_{\mathrm{nn}}$ | 3.50(3) | 3.34(9) |
| $J_{\mathrm{nnn}}$ | - | 0.12(2) |
| $D$ | 0.47(2) | 0.428(5) |
| $E$ | 0.038(2) | 0.0316(3) |
| $J_{\mathrm{nn}}$ | 3.33(5) | 3.18(5) |
| $J_{\mathrm{nnn}}$ | - | 0.11(1) |
| $D_{ij}^z$ | 0.21(1) | -0.196(4)[a] |
| $D_{ij}^y$ | 0.10(2) | 0.197(2) |

[a] The sign given in [127] and [48] is arbitrary, as long as the order in which the sum over all nearest-neighbour spin interactions is evaluated is not explicitly stated, since $\vec{S}_i \times \vec{S}_j = -\vec{S}_j \times \vec{S}_i$. This is the reason why the DMI contribution must be zero when the Fe-O-Fe bonds possess inversion symmetry.

The literature values for the magnetic moments as obtained from the paramagnetic susceptibility are listed in table 4.3. Both the values obtained using mean-field theory and from the Padé series expansion are larger than the free-ion $Fe^{3+}$ value of $5.85\mu_{\mathrm{B}}$,

which corresponds to $J = S = 5/2$. It is normally assumed that crystal fields quench the orbital angular momentum, while in the present case the opposite seems to happen. The presence of a DMI and a single-ion anisotropy are both consistent with the observation that $L > 0$ and hence $g > 2.01$, but how this orbital angular momentum arises still needs to be clarified. This question is not unique to iron jarosite either, it arises in other salts with $3d^5$ cations. An introduction to the present literature on this subject will be given at the beginning of 4.5, where an X-ray spectroscopy experiment is described, which has provided an explanation in both qualitative and quantitative terms.

Table 4.3: A comparison of structural and magnetic parameters.

| | potassium iron jarosite [a] | hydronium iron jarosite [b] | |
|---|---|---|---|
| formula | $KFe_3(OH)_6(SO_4)_2$ | $H_3OFe_3(OH)_6(SO_4)_2$ | |
| synthesis | Redox | Solvothermal | |
| $Fe^{3+}$ occ. | > 99% | 97% | |
| $R(Fe\text{-}O)_{eq/ap}$ | 0.964 | 0.977 | |
| $\angle$(Fe-O-Fe) | 133.6° | 133.6° | |
| $\theta$ [c] | 19.2° | 21.1° | |
| $\sqrt{8C}$ [d] | 6.7(2) | 6.2(1) | $\mu_B$ |
| $\theta_w$ [d] | -800(30) | -1200(200) | K |
| $\mu_{eff}$ [e] | 6.3(2) | 6.6(2) | $\mu_B$ |
| $J/k_B$ [e] | 44(2) | 40(2) | K |
| $T_N$,$T_g$ | 65(1) | 17(1) | K |
| $\xi$ | $\infty$ | 19(2) | Å |

[a] *Source:* Grohol and Nocera *et al.* [83, 149, 81].
[b] *Source:* Wills *et al.* [229, 228].
[c] $\theta$ is defined in figure 4.4.
[d] As obtained from the by fitting with the Curie-Weiss law.
[e] As obtained by fitting the Padé series expansion for the susceptibility of the kagomé lattice.

## 4.2 Hydronium iron jarosite

Hydronium iron jarosite is clearly a spin glass. Inelastic polarised neutron scattering experiments reveal increasing short-range spin-spin correlations between 140 K and 2 K in the magnetic scattering channel [231]. Susceptibility measurements also show the hallmark characteristics of a spin-glass [230, 228], with a large field-cooled- zero-field-cooled splitting below the spin-glass freezing transition at $\approx$ 18 K and a strong

frequency-dependent dissipative component in the ac-susceptibility. As in the geometrically frustrated $S = 3/2$ compound SCGO [165] the heat capacity approaches zero following a $T^2$ power law [229].

The central question is now whether the spin-glass magnetic ground state in hydronium iron jarosite arises due to disorder or if it is a ground state of a structurally perfectly ordered lattice topology which frustrates the magnetism [229, 230, 228, 231]. The classical kagomé antiferromagnet is expected to remain disordered even at $T = 0$. This does not mean that the magnetic properties in hydronium jarosite are closer to the theoretically expected behaviour, which is spin-liquid and not spin-glass. This can be seen as follows; A non-frustrated 2D system with 4 nearest neighbours is not expected to show long range order for any $T > 0$. Since in a frustrated system the ground state degeneracy is much higher than in a non-frustrated system it can only show less freezing. $XY$ spins on a 2D square lattice with $z = 4$ show a transition to a state with increased viscosity, the Kosterlitz-Thouless transition. For $XY$ spins in a frustrated geometry there is evidence of a Kosterlitz-Thouless like ground state [171, 43]. It also opens up the possibility of a more glassy ground state, and an easy-plane anisotropy has for this reason been suggested as the explanation for the glassy ground state in hydronium jarosite [228]. However, regarding a magnetic anisotropy the arguments as presented for potassium jarosite are of equal application in hydronium jarosite. No one has managed so far to grow hydronium jarosite crystals larger than 100 micron. Hence it is difficult to measure directly the extent to which magnetic anisotropy is present. Bisson and Wills [24] report of correlation between the trigonal distortion of the $FeO_6$ octahedra and the transition temperature. This cannot be taken as evidence of a causal relationship between the two. It is most likely that both effects have a common underlying cause, which could be the potassium/hydronium occupation of the $A$-site. The evidence presented later in this chapter is in support of the presence of a single ion anisotropy which varies with the strength of the trigonal distortion in the crystal field.

Table 4.4: Atomic coordinates of $H_3OFe_3(OH)_6(SO_4)_2$. From Wills *et al.* [229].

| atom | $x$ | $y$ | $z$ | $U_{iso}/Å^2$ | $f$ |
|---|---|---|---|---|---|
| Fe | 0.3333 | 0.1667 | 0.1667 | 0.0105(6) | 0.97 |
| S | 0 | 0 | 0.3055(3) | 0.09(1) | 1.00 |
| O1 | 0 | 0 | 0.3937(2) | 0.0162(5) | 1.00 |
| O2 | 0.2247(1) | -0.2247(1) | -0.0544(1) | 0.0162(5) | 1.00 |
| O3 | 0.12789(15) | -0.12789(15) | -0.1345(1) | 0.0162(5) | 1.00 |
| O4 | 0.0 | 0.0 | -0.0108(5) | 0.0047(14) | 0.50 |
| H1 | -0.07244 | 0.07244 | -0.0272(5) | 0.169(8) | 0.50 |
| H2 | 0.1934(3) | -0.1934(3) | 0.1075(2) | 0.0322(9) | 1.00 |

Space group $R\bar{3}m$, $a = 7.32457(12)$Å, $c = 16.9153(4)$Å, $\alpha = 90°$, $\gamma = 120°$

In section 4.5 the X-ray absorption spectra of powder samples of the two salts are compared, for evidence that the very small differences in the $Fe^{3+}$ ligand fields give rise to differences in the magnetic anisotropy or super-exchange interaction between adjacent iron sites.

Apart from the presence of an $H_3O^+$ ion instead of $K^+$, there is at first sight little difference in the structural parameters of the two analogues, as can be seen from comparison of tables 4.1 and 4.4. It should be noted that the O4 and H1 atoms belonging to the hydronium group have been refined with a fractional occupation of 0.5. From the refinement as stated in table 4.1 it may not be immediately clear that reason that the occupation $f$ must be 0.5 is that the site symmetry $\bar{3}m$ is not compatible with the symmetry of the hydronium ion. The central oxygen O4 of the hydronium group in table 4.4 will be copied to $-d_z$ when it is placed dz along the $z$ axis away from the unit cell origin. The same happens to the H1 which due to the $\bar{3}m$ symmetry operator will have a multiplicity of 6 instead of 3. The result is a (non-existent) $H_6O_2^{2+}$ group centred on the origin of the unit cell. With a fractional occupancy $f$ of 0.5 for these two sites the charge balance and the number of atoms is correct. Stricty speaking the symmetry is no longer $R\bar{3}m$ but $R3$ with twice as many atoms in the asymmetric cell as those presented in table 4.4, when the $K^+$ is substituted with $H_3O^+$. For the neutron refinement this is not thought to make a difference, but there is still uncertainly about

which $H_3O^+$ orientations are favoured. To address this issue a structure optimisation using ab-initio calculations has been attempted. The starting point of these calculations was the structure as shown in table 4.5. The atomic coordinates in this table are based on Wills' refinement [229], but the disorder arising from the structural degeneracy needed to be modelled in a slighlty different way. Clearly, strictly a-priori one can *not* say that hydronium jarosite is what has been termed "a topological spin glass" [228]; a system with a glassy ground state in the absence of structural disorder.

Grohol *et al.* [83] have suggested that the spin-glass behaviour arises due to proton transfer from the hydronium ($H_3O^+$) group to the hydroxy (OH) groups which mediate the super-exchange interaction. The altered charge balance on the hydroxy-turned water ligands would change the super-exchange coupling between neighbouring $Fe^{3+}$ ions, introducing a random-bond effect. Of course this can only lead to a glassy state if sufficiently strong further neighbour interactions are present, since a 2D system with up to 4 nearest neighbours orders at best at $T = 0$. A problem with this explanation is that the magnetic exchange coupling $J$ increases by up to 50% when the potassium is substituted for hydronium. Rather, it suggests that the $H_3O^+$ group mediates an inter-plane magnetic interaction, or increases the strength of further neighbour interactions. In that case it is a system in which the glassy magnetic ground state arises from an interplay between geometric frustration of two different kinds; a structural degeneracy and magnetic frustration.

## 4.3 Synthesis and single-crystal growth

### 4.3.1 Hydronium jarosite

The original solvothermal synthesis method [60, 223] for the jarosites was used for the preparation of $H_3OFe_3(OH)_6(SO_4)_2$. In this preparation 6.6 g (22 mmol) of $Fe_2(SO_4)_3{\cdot}5H_2O$ was dissolved in 50 mL water. This solution was transferred to a 125 mL PTFE liner of a stainless steel bomb. The solution was heated in the bomb to 140°C for 12 hours.

Table 4.5: Atomic coordinates in $R3$, of $H_3OFe_3(OH)_6(SO_4)_2$ based on Wills *et al.* [229].

| atom | $x$ | $y$ | $z$ | $U_{iso}/Å^2$ | $f$ |
|---|---|---|---|---|---|
| Fe | -0.16667 | -0.33333 | 0.16667 | 0.0105 | 1 |
| S | 0.33333 | -0.33333 | -0.27783 | 0.09 | 1 |
| S | -0.33333 | 0.33333 | 0.27783 | 0.09 | 1 |
| O1 | 0.33333 | -0.33333 | 0.60406 | 0.0162 | 1 |
| O1m | -0.33333 | 0.33333 | -0.60406 | 0.0162 | 1 |
| O2 | 0.22471 | -0.22471 | -0.54370 | 0.0162 | 1 |
| O2m | -0.22471 | 0.22471 | 0.54370 | 0.0162 | 1 |
| O3 | 0.12789 | -0.12789 | 0.13452 | 0.0162 | 1 |
| O3m | -0.12789 | 0.12789 | -0.13452 | 0.0162 | 1 |
| H1 | -0.19342 | 0.19342 | -0.10751 | 0.0322 | 1 |
| H1m | 0.19342 | -0.19342 | 0.10751 | 0.0322 | 1 |
| O4 | 0.0 | 0.0 | -0.10760 | 0.0047 | 0.5 |
| H2 | -0.72440 | 0.72440 | 0.27160 | 0.170 | 0.5 |
| O4m | 0.0 | 0.0 | 0.10760 | 0.0047 | 0.5 |
| H2m | 0.72440 | -0.72440 | -0.27160 | 0.170 | 0.5 |

Space group $R3$ (146), $a = 7.32457(12)$Å, $c = 16.9153(4)$Å, $\alpha = 90°$, $\gamma = 120°$

During the reaction hydronium jarosite precipitated. This precipitate was washed, filtered and dried in air, yielding $\approx 0.27$ g of product.

Only very small ($< 20$ $\mu$m) crystallites of hydronium jarosite were obtained in this way. The crystal size could be increased by using a pyrex liner inside the bomb, which provides fewer nucleation centres than the rough PTFE liner. Another source of nucleation centres is the surface area of the solution exposed to air in the reaction vessel. Hence, the shape of the glass liner was adapted to reduce this area to $\approx 0.8$ cm$^2$. The largest crystallites, perfect cubes of between 50 and 100 $\mu$m across were obtained when the oxygen content of the solution in the pyrex liner was reduced by bubbling dry nitrogen gas through the solution for a few minutes, and the bomb was sealed in a nitrogen filled glove bag. Though this was an improvement, the crystallites were still too small to use for oriented single crystal magnetic susceptibility measurements.

### 4.3.2 Potassium jarosite

$KFe_3(OH)_6(SO_4)_2$ can be obtained following a similar approach as described above for hydronium jarosite [157] but the best results are achieved with a reduction-oxidation method as described in [83]; 4.88 g (28.0 mmol) of $K_2SO_4$ and 2.2 mL (40 mmol) of $H_2SO_4$ were dissolved in 50 mL of distilled water, and transferred into a 125 mL PTFE liner of a stainless steel bomb. A 0.56 g length (10 mmol) of iron wire with a diameter of 2 mm diameter was added to the solution. The bomb was placed in an oven at 202°C for 4 days, and then cooled-down to room temperature at a rate of 0.3°C/min. The precipitate was washed, filtered and dried, yielding 0.37 g which is 22% based on Fe.

This reaction is reported to yield large single crystals with a volume of 1 $cm^3$ [83], but it is important that the surface area of the solution exposed to air inside the vessel is minimised. This was achieved using a glass container which fitted inside the PTFE liner, with only a small hole at the top. The temperature is also a very important parameter, and it must be accurate to one degree. The temperature of our precision box-furnace had to be calibrated using a mercury thermometer and a thermocouple. The largest crystals obtained in this way were approximately 1 $mm^3$ in size.

## 4.4 Jarosite crystals from a natural source

Even with the best crystal-growing efforts, our synthesised crystals are much smaller than potassium jarosite crystals from natural sources. Large crystals are needed for single-crystal neutron diffraction experiments, and with large crystals magnetic-susceptibility measurements can be carried out in lower fields, revealing field cooled zero-field cooled splittings. Large single crystals were also expected to simplify polarised X-ray spectroscopy experiments, which are discussed in section 4.5. A number of natural single crystals were carefully characterised using single crystal X-ray diffraction, optical polarisation analysis and susceptibility measurements.

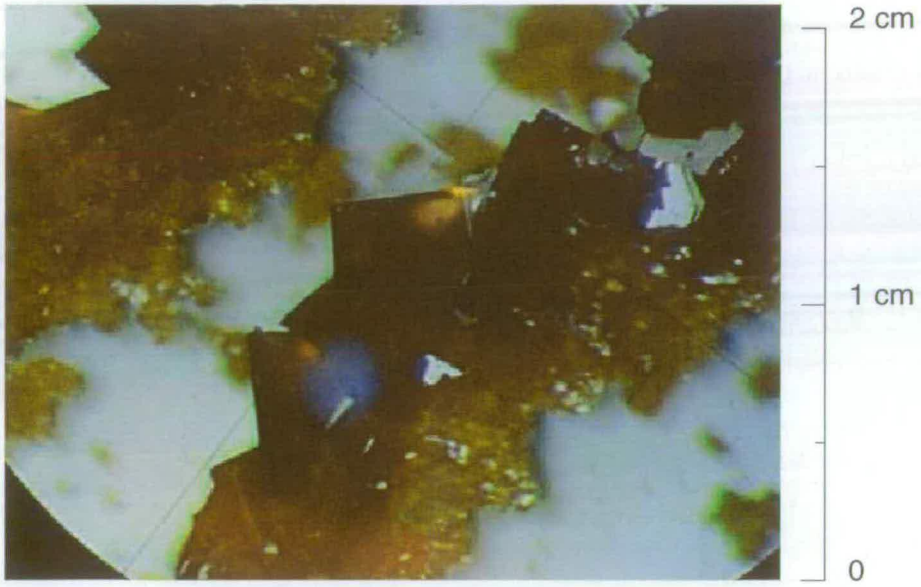


Figure 4.5: Clusters of synthesised potassium iron jarosite. The largest crystals in this picture are about 600 $\mu$m.

The crystals used in the following experiments were obtained by Keith Pettigrew [157] from Dr. P. Goodell of the University of Texas at El Paso and came from the Chihuahua region in Mexico. They were plate shaped, and the largest specimen, used for a neutron diffraction experiment, was 32 mg. Other experiments were carried out on an 8.2 mg sample. X-ray diffraction confirmed that these samples were reasonably single crystalline. The large area top and bottom surfaces of the plate-shaped crystals were indexed as the [001] and [00$\bar{1}$] faces.

### 4.4.1 Magnetic susceptibility

The magnetic susceptibility of a 8.2 mg single crystal of potassium jarosite was measured between 4.5 and 340 K on a Quantum Design MPMS magnetometer. The plate-shaped single crystal was oriented with the field in the *ab* plane, and along the *c* axis by clamping it between the walls of the gelatine capsule containing the sample. The results from measurements in a 200 Gauss field are shown in figure 4.6. The open and filled squares give the zero-field cooled susceptibility in the *ab* plane and along the *c* axis respectively. The circles give the field-cooled susceptibility. The cusp in the out-of-plane

susceptibility (along the $c$ axis) indicates that the transition temperature to long range order in this sample is 61.0(5) K. This is slightly lower than the reported transition temperature on the best synthesised single crystals of 64 K. Samples synthesised using the solvothermal method have an iron occupancy of around 90%, and their transition temperature lies around 50 K. We estimate that the iron occupancy in the natural single crystal used here is likely to be $> 95\%$. Comparison of data taken in 50, 100 and 200 G fields showed that the sample does have a remanent magnetic moment up to 340 K. This remanence, which is not present in synthesised powder samples, probably arises from spurious iron oxide phases present in the sample. Since above 150 K the magnetic response from potassium iron jarosite is purely paramagnetic, the remanence along each axis from the field-dependence of the susceptibility can be calculated and subtracted from our data.

Table 4.6: Fit results from oriented single crystal susceptibility

| Function | | $\parallel c$ | $\perp c$ | Lit. value | units |
|---|---|---|---|---|---|
| Curie-Weiss | $C$ | 5.65(10) | 5.55(10) | 5.6(2) | emu K mol$^{-1}$ |
| | $\sqrt{8C}$ | 6.72 | 6.66 | 6.7 | $\mu_B$ |
| | $\theta_w$ | 906(10) | 893(10) | 800(30) | K |
| Padé series- | $J$ | 42(2) | 42(2) | 45(2) | K |
| expansion | $\mu_{eff}$ | 5.5(1) | 5.4(1) | 6.3(2) | $\mu_B$ |

The corrected in-plane and out-of-plane susceptibilities are almost identical above 150 K, but the susceptibility along the $c$ axis diverges at the transition temperature at 61 K. Table 4.6 gives the results of the Curie-Weiss fit and the Padé series expansion (equation 2.54) for the kagomé lattice [84] along both axes. The errors given here are estimated from comparison of the results for different samples, and in the case of the Padé expansion, the results also depend on the temperature range fitted, increasing the error. It is clear however, that per sample the high-temperature susceptibility along the $c$ axis is larger. In principle this difference can be indicative of both an easy-axis along the $c$ axis, or an easy-plane anisotropy in the $ab$ plane. Since the ground state is almost perfectly co-planar, even above 150 K there is probably still a weak preference for the

spins to align in-plane, making it relatively easy for a field along the $c$ axis to pull the spins out of that plane. From fits with the Padé approximant the value found for $\mu_{\text{eff}}$ is considerably smaller than the spin-only value of $\mu_{\text{eff}} = 5.85\mu_{\text{B}}$, and also smaller than the value found in our Curie-Weiss fit. The latter corresponds well with the values reported by Grohol *et al.* [81]. Grohol used a Padé approximant which included further neighbour interactions, which we have omitted in our fit. This explains the different value obtained here, and it is a reminder that the values obtained with this kind of analysis strongly depend on the model the theory is based on. In this sense the most reliable fit is obtained with the mean-field theory result.

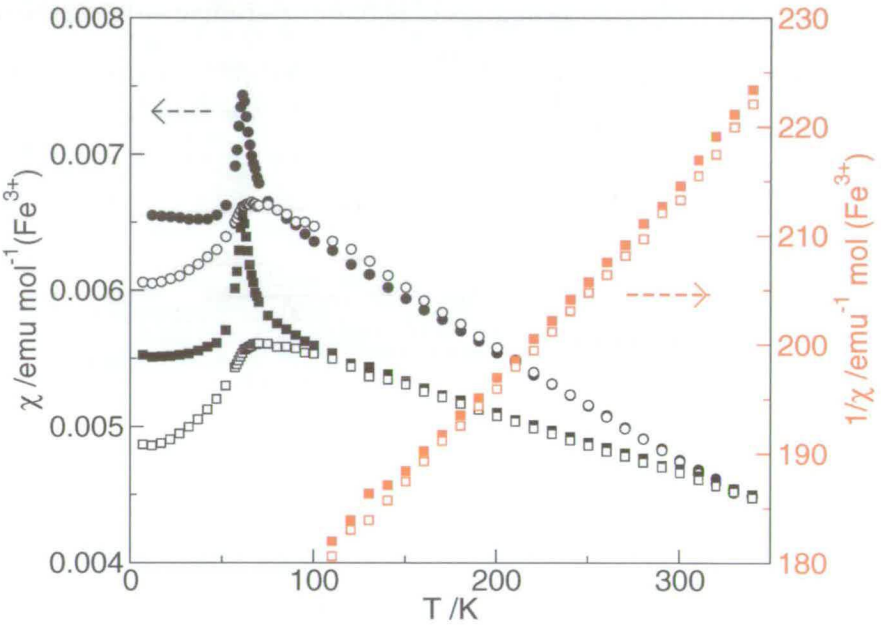


Figure 4.6: The magnetic susceptibility of a potassium iron jarosite single crystal from a natural source, in the $ab$ plane (open symbols) along the $c$ axis (filled symbols), in zero-field cooled (squares) and field cooled (circles). The right axis (red) gives the inverse susceptibility along the $c$ axis (filled symbols) and in the $ab$ plane (open symbols).

### 4.4.2 Neutron diffraction with a natural crystal

The divergence of the magnetic susceptibility at the transition temperature suggests that the transition to long-range order is a critical phase transition. In this neutron diffraction experiment, at the cold neutron powder diffractometer DMC at the Paul

Scherrer Institute, the initial aim was to measure the critical scattering at the phase transition. In a symmetry-breaking transition like the onset of Néel order in a conventional antiferromagnet, the spin-spin correlation length increases with temperature following a power law $\propto (T - T_c)^{-\eta}$ (where $\eta > 0$ is the critical exponent of the correlation length), as the system approaches the transition temperature $T_c$. However, no critical scattering could be observed, simply because of a lack in intensity from the sample used here. The experiment was started with a 46 mg single crystal, but during mounting the sample broke. Both pieces were used for the experiment, but the neutron diffraction pattern showed that the relative orientation within the $ab$ plane of the two crystal pieces was lost. Another limitation in this experiment was that a two axis powder diffractometer was used, missing the azimuthal rotation $\psi$ needed to optimally align the $c$ axis in the scattering plane.

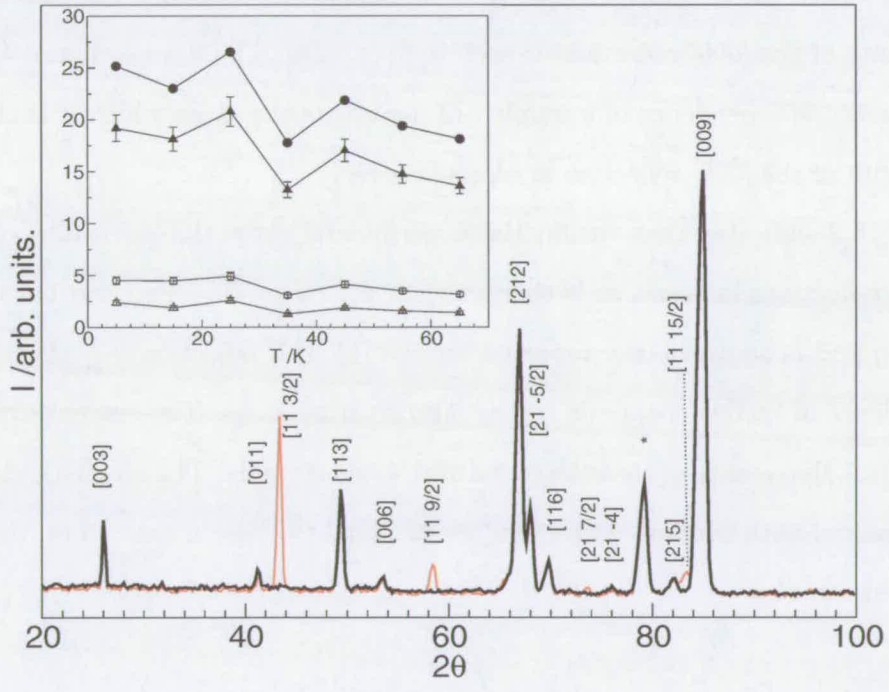


Figure 4.7: Indexed single-crystal neutron diffraction pattern integrated over all sample orientations with the [110] axis (which corresponded with the [210] axis for the second crystallite) perpendicular to the scattering plane, at 65 K (thick line) and at 15 K (red line). The pattern contains both [11$l$] peaks and [21$l$] peaks because the crystal broke in two before mounting, and the relative orientation within the $ab$ plane was lost. The asterisk indicates a powder peak from the Al sample holder. The inset shows the temperature dependence of some nuclear reflections; [003] (open circles), [009]/10 (filled circles, [21$\bar{2}$] (filled triangles) and [21$\bar{5}$] (open triangles).

Figure 4.7 shows the single-crystal diffraction patterns integrated over all sample orientations with the [110] axis ([210] axis for the second crystallite) perpendicular to the scattering plane, at 15 K and at 65 K measured with a neutron wavelength $\lambda = 2.568$ Å. The presence of [11$l$], [21$l$] reflections and a [011] reflections shows that the orientation of the $ab$ axes between the two crystal pieces was lost, one being aligned with the [11$l$] axis in the scattering plane, and one accidentally with the [21$l$] axis more or less aligned in the plane. From the positions of the most intense nuclear reflections the lattice parameters $a = 7.29(4)$ Å and $c = 17.10(2)$ Å are obtained. In addition to the nuclear reflections, new reflections appeared at [11$\frac{3}{2}$], [11$\frac{9}{2}$], [11$\frac{15}{2}$], [21$\frac{7}{2}$], [21$\frac{\overline{1}}{2}$] and [21$\frac{\overline{5}}{2}$] when the sample was cooled below 64 K. All these magnetic reflections are consistent with a $q = 0, 0, 3/2$ magnetic unit cell. The temperature dependence of these reflections was measured in steps of 10 K down to 5 K. The result is shown in figure 4.8, where the integrated intensity of the magnetic reflections was normalised to the intensity of the [009] reflection at each temperature. The inset in figure 4.7 shows the temperature dependence of a number of nuclear peaks, from which it is clear that the intensity of the [009] reflection is representative.

Figure 4.8 indicates that within the experimental error the intensities of all the magnetic reflections increase, as is characteristic for magnetic reflections below a Néel transition, and is as previously reported for the [11 3/2] reflection [81]. Hence, there is no evidence of further magnetic (or structural) transitions. The current experiment also confirms the quality of these large natural single crystals. The magnetic characteristics measured with neutron diffraction are identical to those measured on the largest synthesised samples.

## 4.5 Polarised soft X-ray spectroscopy

The remaining issue which has yet to be addressed is the deviation of the magnetic moment and the $g$-factor from the free-ion values. It is well known that the fine-structure splittings in many paramagnetic salts with $Mn^{2+}$ and $Fe^{3+}$ are much larger

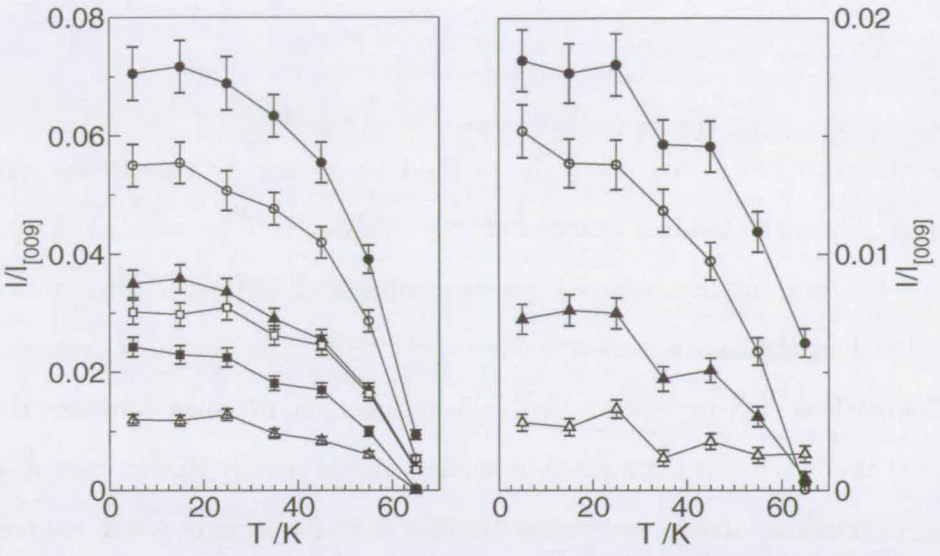


Figure 4.8: Temperature dependence of the magnetic reflections $[11\frac{3}{2}]$ (black circles), $[\bar{1}\,\bar{1}\,\frac{3}{2}]$ (white circles), $[11\frac{9}{2}]$ (white squares) $[\bar{1}\,\bar{1}\,\frac{9}{2}]$ (black squares), $[11\frac{15}{2}]$ (black triangles) and $[\bar{1}\,\bar{1}\,\frac{15}{2}]$ (white triangles) in the left panel, and $[\bar{2}\,\bar{1}\,\frac{7}{2}]$ (black circles), $[11\frac{9}{2}]$ (white squares) $[\bar{2}\,\bar{1}\,\frac{1}{2}]$ (white circles), $[\bar{2}\,\bar{1}\frac{5}{2}]$ (white triangles) and $[\bar{2}\,\bar{1}\frac{11}{2}]$ (white triangles) in the left panel. All intensities are normalised to the strongest non-magnetic reflection [009].

than expected [221, 3], even when admixtures of higher-energy configurations with the ground state are taken into account. Watanabe [220] has shown that only fourth-fifth- and sixth-order perturbations of crystal field, spin-orbit coupling and spin-spin interactions split the electronic levels and produce a $g$-factor deviation from its free electron value. For $Fe^{3+}$ he estimates that $\delta g = -0.0003$, and a spin-orbit coupling constant of $\lambda = 440$ cm$^{-1}$, much smaller than the values needed to account for the anisotropy in potassium jarosite with $\delta g \approx 0.12$ [127].

Using unrestricted Hartree-Fock (UHF) calculations on atomic Fe and Mn, Wood and Pratt [232] have shown that the large spin moment in the $3d$ shell can split the up-spin and down-spin levels in closed shells. These calculations are in good agreement with the experimentally observed hyperfine structure of atomic Mn arising from the resulting s symmetry net spin density at the nucleus and the Mn nuclear magnetic moment. This exchange polarisation effect will also affect p-symmetry core levels, and create a net orbital angular momentum in these levels. In theory this will give rise to a multiplet structure, but it is unlikely to cause a magneto crystalline anisotropy.

The fine structure calculated using the method for atomic Fe agreed less well with experiment. Since the binding energies of core-electrons will be affected, X-ray spectroscopy is the ideal method to investigate the importance of the exchange polarisation in Fe, which does not have a nuclear moment and hence does not show hyperfine splittings. Comparison of X-ray spectra with calculations [68, 67] show however, that this property of the free ion is diminished in solids. This is mainly due to crystal-field effects and/or covalent mixing- and charge-transfer from the ligands, which are crucial in the understanding of the core-level to $3d$ X-ray absorption spectra in transition metal compounds [53].

Transition metal $2p$- and oxygen $1s$ X-ray spectroscopy studies have played a key role in the understanding of electronic structure in transition metal compounds [235, 211, 51, 52]. It is now well established that many transition metal oxides are not ionic, but strongly covalent compounds. In one X-ray spectroscopy study it was found that covalency effects can even alter the orbital angular momentum states in a rare-earth ion [134]. In this section X-ray spectroscopy experiments to measure the degree and nature of the covalency in potassium and hydronium jarosite will be described. By comparison with accurate atomic multiplet calculations, taking into account ligand-field effects and multiple ionic configurations, we obtain estimates for the orbital angular momentum and magnetic anisotropy in both salts.

The X-ray magnetic circular dichroism (XMCD), i.e. the difference in absorption between left- and right circularly polarised X-rays, can be used to measure directly the expectation value for the orbital angular momentum in a solid, simply by integrating the circular dichroism spectrum [201]. However, jarosite is strongly antiferromagnetic, and hence does not exhibit any circular dichroism. What can be measured is the linear X-ray dichroism [210] which can be used as a direct measure of the in-plane out-of-plane charge anisotropy of the iron $3d$ shells.

### 4.5.1 XAS on hydronium- and potassium jarosite.

#### Experimental details

Powder samples of hydronium and potassium jarosite were synthesised following the method as described in section 4.3. The samples were mixed with graphite powder and pressed into pellets. Like many transition-metal oxides, jarosite is a strong insulator, which inhibits the replacement of photoelectrons emitted from the sample surface due to X-ray absorption. This can give rise to a charging of the sample surface which can potentially distort the peak shape. By mixing the finely powdered sample with graphite, sufficient electron transport is warranted. The X-ray absorption spectra around the iron $L_{2,3}$ edges and the oxygen $K$ edge on powder samples were measured at station 5U.1 at the SRS in Daresbury (for details on the beamline see 3.3.2). For the iron $L_{2,3}$ edges the total electron yield was recorded over the energy range from 690 to 750 eV, and for oxygen $K$ edge between 525 and 550 eV. A purpose-built UHV apparatus as described in section 3.3 was used as sample environment, with a base pressure of $\approx 2 \cdot 10^{-9}$ Torr. The samples were mounted on a cryostat and could be cooled down to approximately 30 K. The electron replacement current from the sample was recorded using a pico-ampère meter. The signal normalised for the incident X-ray intensity is proportional to the X-ray absorption cross section of the sample.

#### Discussion

Figure 4.9 shows energy scans around the Fe $2p^6 3d^5 \rightarrow 2p^5 3d^6$ transition for both potassium jarosite (black dots) and hydronium jarosite (crosses). Due to the $2p$-$3d$ spin-orbit coupling of the $2p$ core-hole in the $2p^5 3d^6$ final state the edge is split into two features. The transition around 710 eV (the $L_3$ edge) gives rise to a ${}^2p_{3/2}$ core-hole, while the transition around 722 eV (the $L_2$ edge) gives rise to a ${}^2p_{1/2}$ core-hole. In the inset the temperature dependence of the isotropic X-ray absorption at the $L_3$ edge in potassium jarosite is shown. There is some change in the peak shape with temperature, which is reproduced in the data taken at the ESRF on single crystals. On close examination

it is just apparent that the main $L_3$ peak consists of two closely spaced lines. In the data taken at the ESRF this feature is more clearly resolved, while otherwise the peak shape obtained at the two beamlines were practically identical.

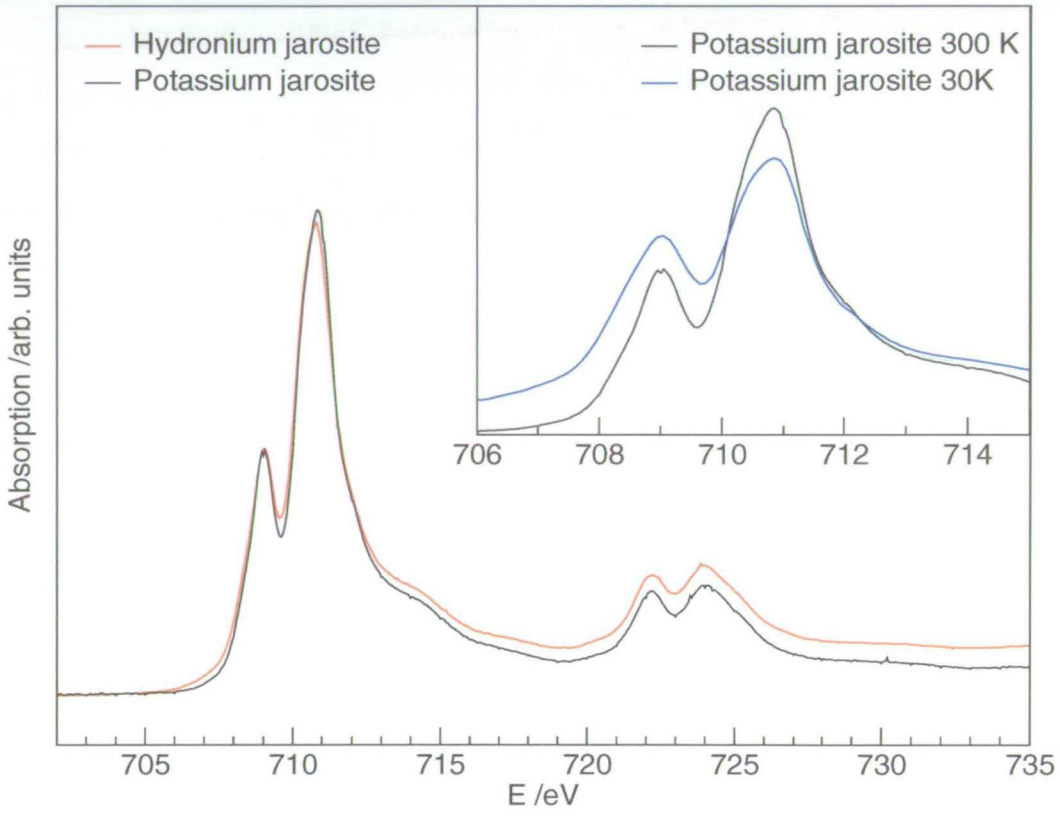


Figure 4.9: The isotropic XAS around the Fe $L_{2,3}$ edges of hydronium- (red) and potassium jarosite (black) at 300 K. The inset shows the $L_3$ edge in potassium jarosite at 300 K (black) and at $\approx 30$ K (blue).

It was also observed that the spectra from hydronium jarosite and potassium jarosite are identical. This implies that the ligand-field and covalency in both systems is identical, and that the slightly larger canting angle $\theta$ of the octahedra in hydronium jarosite (21° compared to 19° in potassium jarosite) has no effect on the degree of covalent mixing between the $Fe^{3+}$ ions and the $OH^-$ ligands. As mentioned earlier, the Weiss temperature of hydronium jarosite is $\approx 1200$ K, 50% larger than for potassium jarosite.

The data shown here rules out the possibility that the higher energy scale of the antiferromagnetic couplings can be attributed to stronger super-exchange between neighbouring $Fe^{3+}$ ions. A significant substitution of $OH^-$ with $H_2O$ as suggested by Grohol *et al.* [83] can also be expected to affect the Fe $2p$ absorption spectra. Unfortunately we do not have a low-temperature spectrum of hydronium jarosite. This sample did not survive the vacuum bake which is needed before the cryostat can be cooled down to 30 K without getting large amounts of ice freezing onto the sample surface.

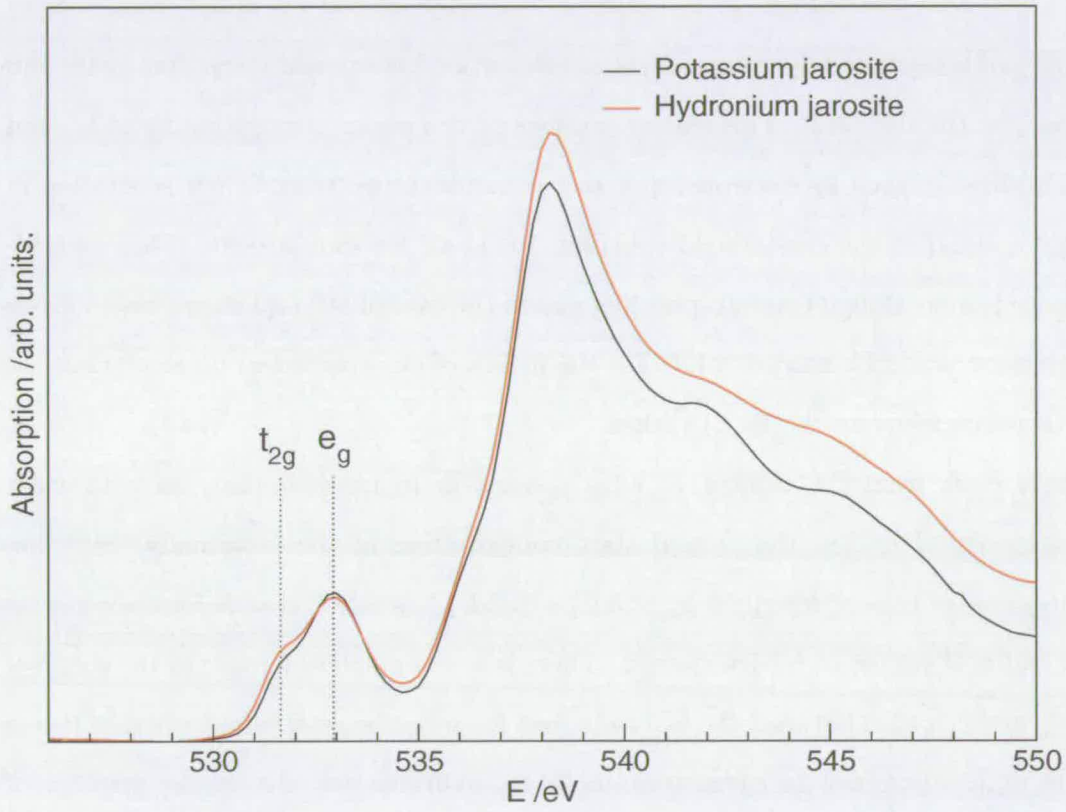


Figure 4.10: The isotropic oxygen K-edge absorption spectra taken at room temperature on hydronium jarosite (red) and potassium jarosite (black).

The oxygen $1s$ X-ray absorption spectra of both hydronium- and potassium jarosite are shown in figure 4.10. Here some differences are visible, but this will be at least in part due to the extra $H_3O^+$ group in hydronium jarosite. The spectra shown here have been taken at room temperature. Additional spectra were taken at 30 K, but despite the low base pressure of the chamber it was found that any change in peak shape at

this temperature could not be separated from the change due to the growth of ice on the sample surface.

Conservation of angular- and spin momenta requires that the electronic states involved in an X-ray absorption process have $\Delta L = \pm 1$ and $\Delta S = 0$. Hence, the edge structure in the oxygen $1s$ spectrum arises from transitions to states with oxygen $2p$ character. Systematic study of the oxygen edge in $3d$ transition metal compounds has shown [54] that the feature at the onset of the edge at 530 eV arises from "empty oxygen orbitals created by ground-state hybridisation between $3d$-transition-metal and oxygen $2p$ orbitals" [212]. This feature consists of two peaks, corresponding to $t_{2g}$ and $e_g$ hybridised oxygen $2p$ electrons, in $\pi$ and $\sigma$ bonds respectively. Their separation in energy is equal to the crystal-field splitting, 1.3(1) eV for iron jarosite. Their relative intensity is more difficult to interpret [54] and in the case of $3d^5$ and above large cluster calculations would be needed [212]. For the fitting of our spectra with calculations we will therefore focus on the Fe $L_{2,3}$ edges.

It is clear from the oxygen $K$ edge spectra in figure 4.10 that, as with most transition-metal oxides, the ground state configuration of the (nominally) $Fe^{3+}$ ion in the jarosites is best described by $\alpha\,|3d^5\rangle + \beta\,|3d^6\underline{\mathrm{L}}\rangle$, where $\underline{\mathrm{L}}$ stands for a oxygen $2p$ hole, and $\alpha, \beta$ are yet to be determined. There is a very small difference in the shape of the $t_{2g}$ and $e_g$ peaks between the two salts, but it cannot be established whether this is due to different oxygen $2p$ - transition metal $t_{2g}$ hybridisation, due to the presence of water, or due to the $H_3O^+$ ion. The higher energy structure arises from hybridisation of oxygen $2p$ states with metal $4s$ and $4p$ states. The $H_3O^+$ group in hydronium jarosite gives rise to a clear difference in the shape of this feature.

### 4.5.2 Polarised XAS on potassium jarosite single crystals

Polarised X-ray absorption spectra on potassium iron jarosite single crystals were measured at ID 8 at the European Synchrotron Radiation Facility (ESRF) in Grenoble.

ID 8 is a grazing angle grating monochromator beamline with helical undulators (section 3.3.2). This beamline can produce (coherent) circularly and linearly polarised X-rays over an energy range from 400 to 1500 eV. The high-field magnet end-station [15] was used.

The best spectra were obtained from a synthesised potassium jarosite single crystal with a diameter of 0.6 mm, mounted on a graphite tip as described in section 3.3.3. Figure 4.11 shows the resulting spectra with the X-ray polarisation parallel and perpendicular to the $c$ axis, at 290 K. The isotropic spectrum and linear dichroism were calculated from the spectra taken in these two orientations using $I_{\mathrm{iso}} = \frac{2}{3}I_{\mathrm{ab}} + \frac{1}{3}I_{\mathrm{c}}$ and $I_{\mathrm{xld}} = I_{\mathrm{ab}} - I_{\mathrm{c}}$. Scans were made with alternating horizontal and vertical polarisation, and for each polarisation averages were taken over at least 8 scans. A small number of scans were excluded because they would increase rather than reduce the total standard deviation to the average. In this manner spectra were taken at 290, 200, 80, 60 and 40 K. Figures 4.12 and 4.13 show the temperature dependence of the isotropic spectrum and the linear X-ray dichroism respectively. The spectra in figure 4.13 were also integrated in order to obtain the quadrupole moment of the $3d$ shell [210, 209, 208]. For the data taken at 290, 200 and 80 K, as shown in figure 4.13 the charge quadrupole moment of the $3d$ shell $(\rho_{\mathrm{ab}} - \rho_{\mathrm{c}})/\rho_{\mathrm{iso}} = 0.05(2)$, where $\rho_i$ is the integral of $I_i$. This may be interpreted as that the Fe $3d$ shell has between 3 and 7% net $x^2 - y^2$ or $xy$ character. For the linear dichroism spectrum taken at 40 K the integral is zero within the experimental error.

The linear dichroism spectrum only changes slightly at lower temperatures and gains in intensity as the temperature is lowered, as could be expected when the spins align. More clearly visible is the change in the isotropic line shape, in particular at the $L_3$ edge. Comparison with the powder-spectra discussed in the previous section suggests that this change is real, and not an artefact arising from misalignments or charging effects. To gain a better understanding of the cause for the change of shape of the isotropic spectrum figure 4.14 shows the unprocessed spectra, measured along

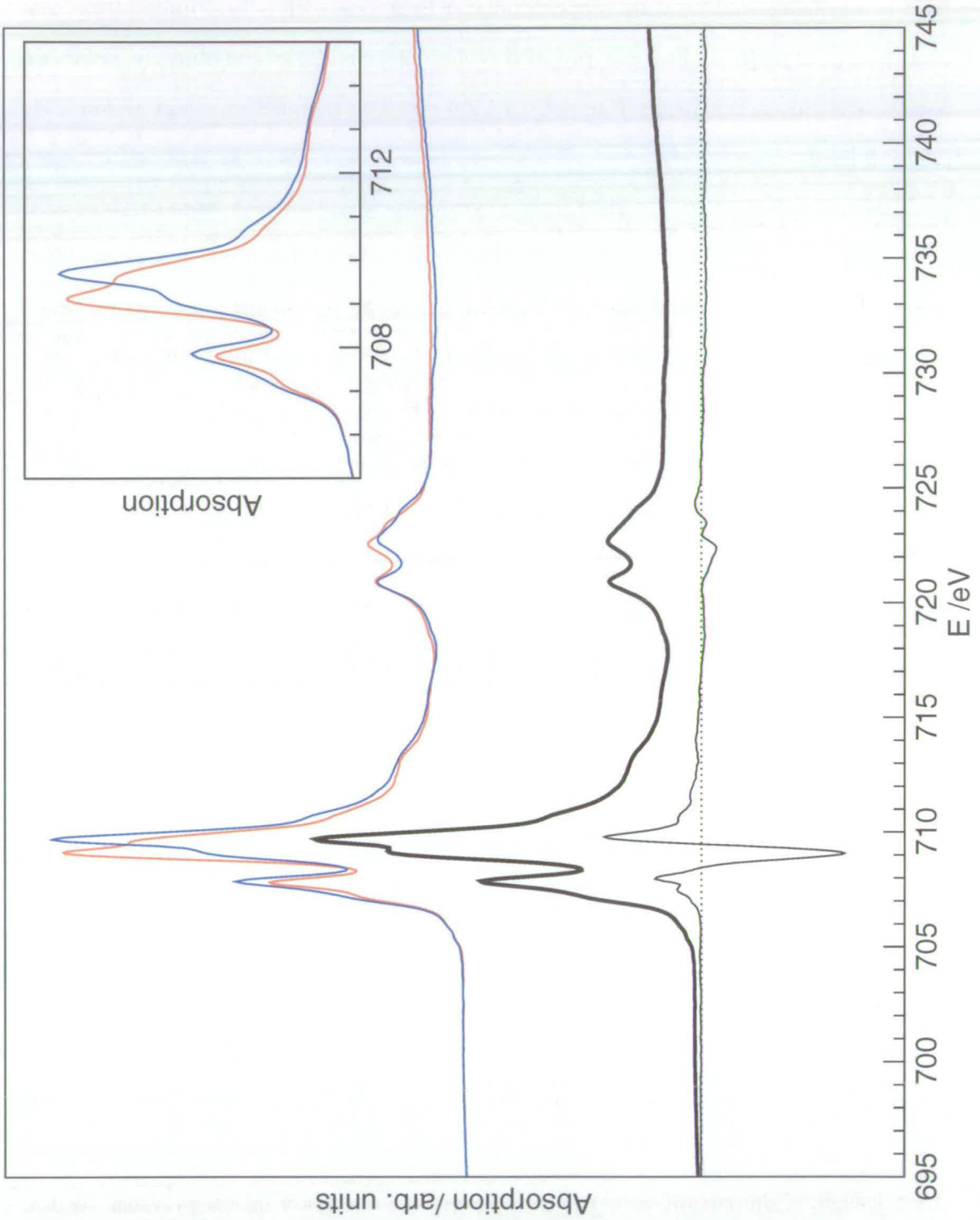


Figure 4.11: X-ray absorption spectra $I_c$ (red), $I_{ab}$ (blue), $I_{iso}$ (thick line) and $I_{xld}$ (thin line), from a synthesised potassium iron jarosite single crystal at 290 K.

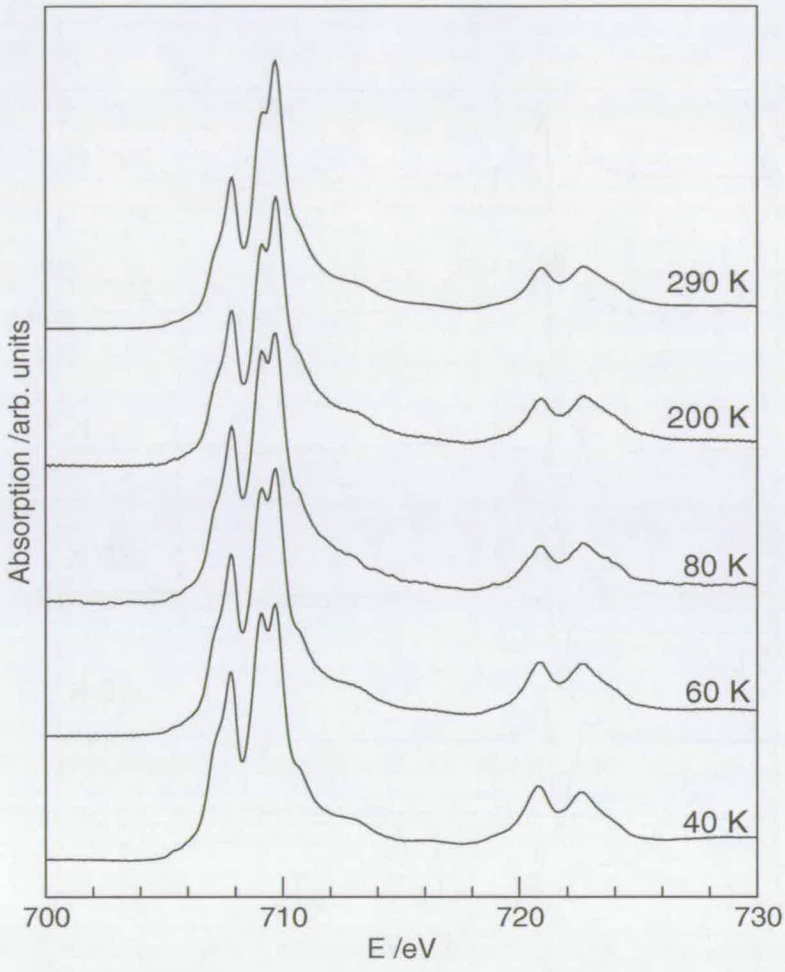


Figure 4.12: The temperature dependence of the isotropic X-ray absorption at the Fe $L_{2,3}$ edges, from a synthesised potassium iron jarosite single crystal.

the $c$ axis and perpendicular to the $c$ axis at 40 K and at 290 K. This figure reveals the remarkable detail with which this absorption spectrum has been obtained due to the continuous improvements in photon flux, X-ray polarisation, energy resolution and stability of the beam, realised at the facilities made available to us for this experiment. It is clear that the change in peak shape does not arise merely from a change in the relative intensities of the spectra obtained with different X-ray polarisation, but that the line shape of $I_{ab}$ and $I_c$ change individually. These features have turned out to be crucial in the interpretation of the spectra.

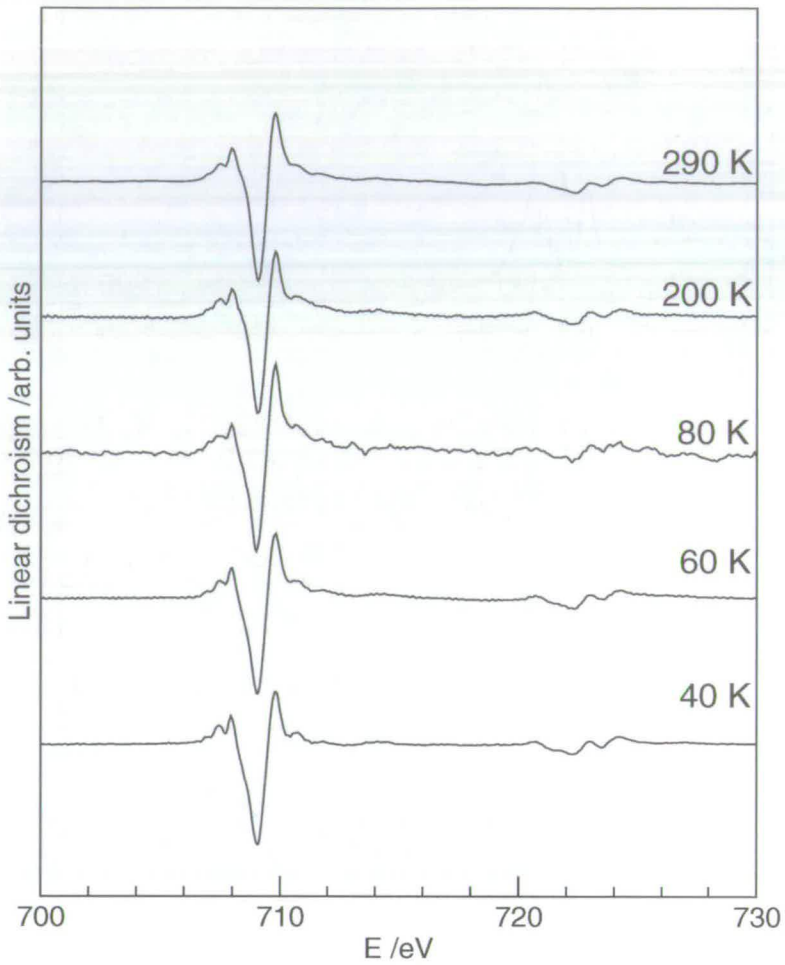


Figure 4.13: The temperature dependence of the X-ray linear dichroism spectrum ($I_{ab} - I_c$) to scale with 4.12, from a synthesised potassium iron jarosite single crystal.

We have long been suspicious of the change in the peak shape of the isotropic $L_3$ edge because in the data taken on natural crystals this feature is not well reproduced, as can be seen in figure 4.15. The linear dichroism spectra obtained from a single crystal from natural source are identical to those measured for the synthesised sample. However no temperature dependence was observed and will not be reproduced here. The isotropic spectra in one of the runs varied randomly with temperature (left panel in figure 4.15), while in another run (right panel in figure 4.15), possibly due a better alignment of the beam, the same effect is seen as in the isotropic spectra in figure 4.12, but much less clearly. We now believe that this is likely to be due to a lower quality of

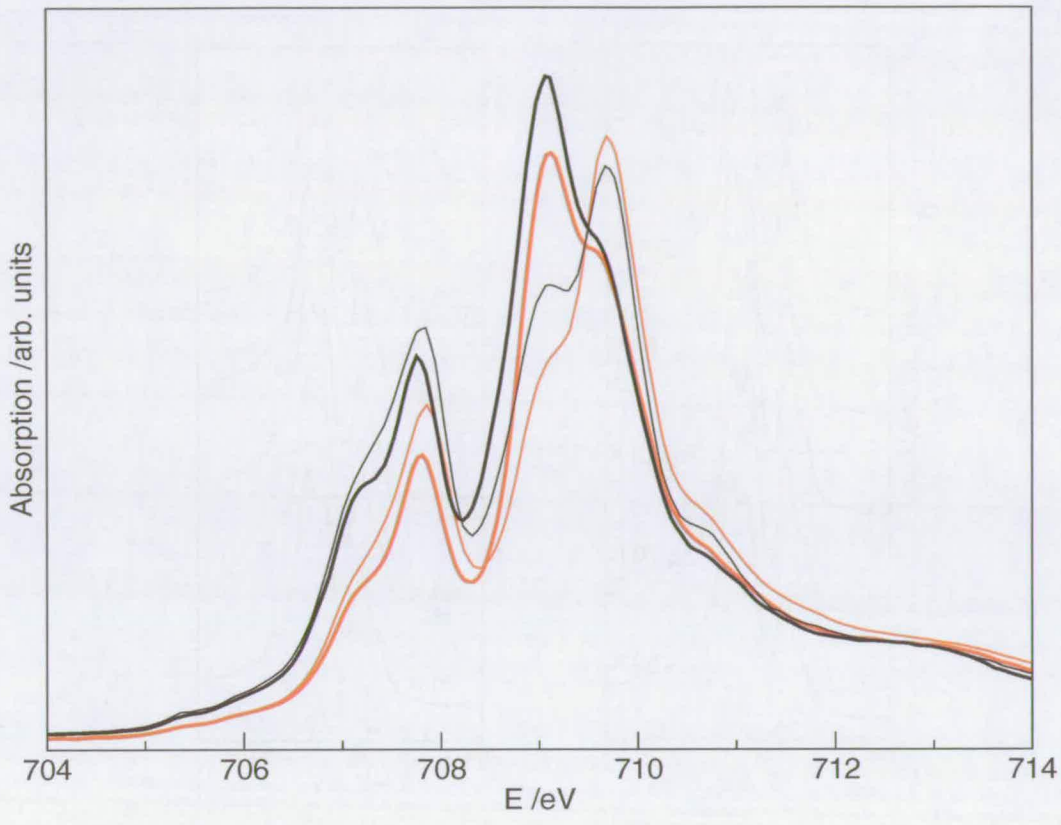


Figure 4.14: The unprocessed spectra with the X-ray polarisation along the $c$ axis (thick lines) and in the $ab$ plane (thin lines) at 290 K (red) and at 40 K (black).

the natural single crystal used. Soft X-rays probe only the first 100 nm of the sample surface, and very small volumes of impurity phases or crystal defects at the surface can therefore have a large effect on spectrum. The quality of the natural single crystal was thoroughly checked with single crystal X-ray diffraction, while the size of the natural specimen used here precludes accurate X-ray characterisation. In addition to this the geometry used for the measurements on natural crystals was more complicated and did not allow independent measurement of $I_c$. For these reasons we keep confidence in the data taken on the synthesised single crystal as shown in figures 4.12 and 4.13.

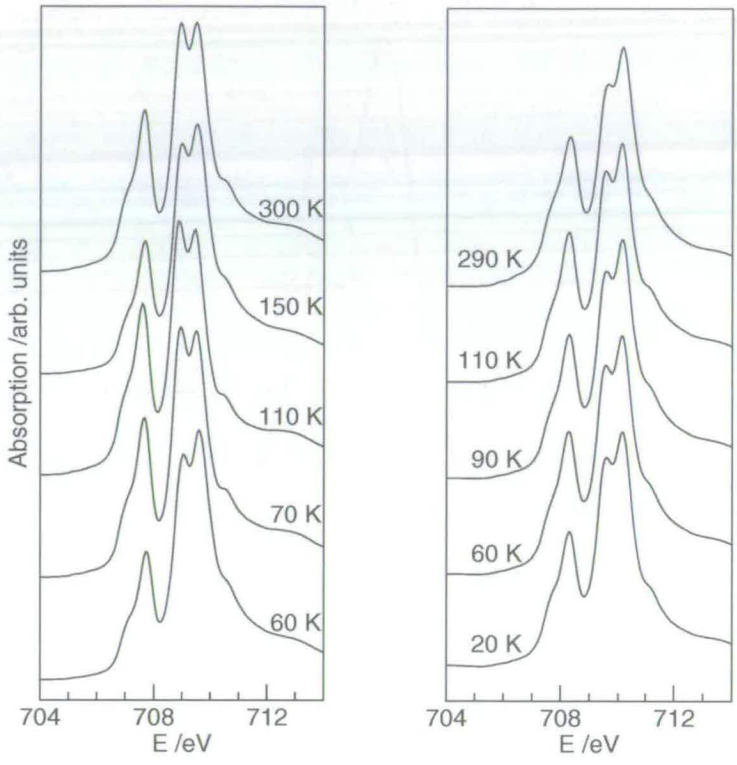


Figure 4.15: Comparison of the temperature dependence of the isotropic X-ray absorption at the $L_3$ edge measured in two different runs using a 16 mg potassium iron jarosite single crystal from the Chihuahua region in Mexico. In the left panel the peak shape varies randomly with temperature, while in the right panel there is behaviour reminiscent of the temperature dependence as shown in figure 4.12.

## 4.6 Ligand-field multiplet calculations

### Numerical procedure

The radial basis functions of the $2p^6 3d^5$ and $2p^5 3d^{n+1}$ configurations of the free $Fe^{3+}$ ion were calculated using R. D. Cowan's program [49]. The results were used as input for the program *Hilbert++* written by Alessandro Mirone [136, 135], which calculates the polarisation-dependent X-ray absorption spectra taking into account crystal- and ligand field effects and spin-orbit coupling. This program can deal with crystal fields of arbitrary geometry and returns spin- and orbital angular momentum expectation values. The lowest 15 $JLS$ configurations were used in the computations, and $3d$-$3d$

and $2p$-$3d$ Slater integrals were both reduced by a factor 0.8 as is common for this type of calculations.

### Results

First attempts were made to fit the spectra in the most conventional way, using only $Fe^{3+}$ states. A Boltzmann average was taken over all found configurations in order to simulate the paramagnetic state of the sample at 290 K. The first spectrum in figure 4.16 shows the calculated $L_{2,3}$ edges of the free $Fe^{3+}$ ion with reduced Slater-Koster integrals (dots). The second trace (broken line) shows the influence of an octahedral crystal field of 1.3 eV, as is consistent with the value obtained from the oxygen K-edge spectrum. In the third trace a trigonal distortion of 0.2 eV is introduced, amounting to an elongation of the octahedron along the $c$ axis. The Fe $L_{2,3}$ edges in hematite resemble the spectrum in the third trace. An important difference with the situation in hematite is that is has a long-range ordered ground state, which can be modelled by adding a Zeeman term to the Hamiltonian. In the present case a paramagnetic system with no particular alignment of the spins is simulated. It is clear however that a crystal-field alone cannot account for the spectra as observed experimentally. Even larger trigonal distortions will eventually split the main $L_3$ peak, but this does not improve the overall fit. In addition there is no motivation for such a large trigonal distortion in the electrostatic crystal field, given that in potassium jarosite the elongation of the octahedra along the $c$ axis is only $\sim 5\%$.

Much better results were obtained when $|2p^6 3d^{n+1}\underline{L}\rangle$ ($Fe^{2+}\underline{L}$) configurations were allowed to mix in, as shown in figure 4.17. Here different fitting parameters are used, and electrostatic crystal-field effects are deliberately left out. The system is now modelled as a charge-transfer compound where higher ionic states of the cation become occupied not as a result of electron hopping between cations, but due to charge transfer from the oxygen ligands' $2p$ shells to the cation. The relevant Coulomb repulsion energy in this case is the charge-transfer gap $\Delta_{pd}$. This energy is determined by the

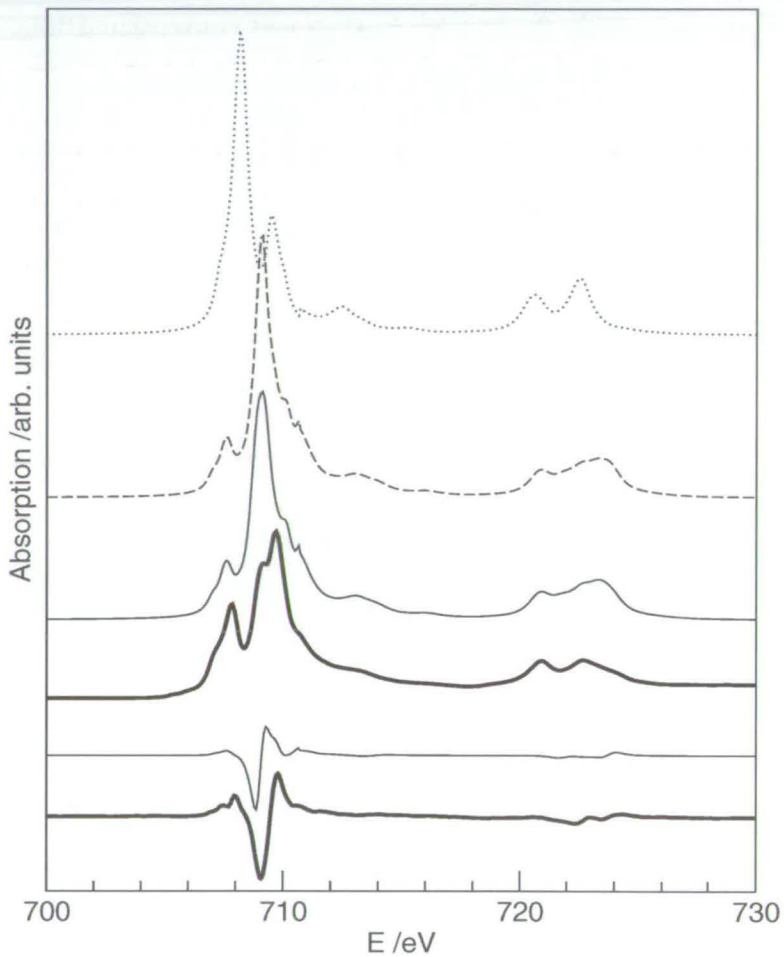


Figure 4.16: Calculated crystal field multiplet spectra for $Fe^{3+}$ with reduced Slater-Koster integrals (dots), in a $O_h$ crystal field with 10Dq = 1.3 eV (broken line), as previous with a trigonal distortion of 0.2 eV added (thin line) and the spectra measured at 290 K (thick line). The bottom two traces are the corresponding linear dichroism spectra, where present.

Hubbard $U$ and the energy of the oxygen $2p$ electrons relative to the valence electrons in the $Fe^{3+}$ ground state configuration $\Delta\underline{L}$ from $\Delta_{pd} = nU - \Delta\underline{L}$. In *Hilbert++* $\Delta\underline{L}$ can be varied, and in combination with the parameters for the degree of $\sigma$- and $\pi$- symmetry bonding (hopping) determines the spectral weight of $Fe^{2+}\underline{L}$ configurations. The best fit between experimentally obtained data as shown in figure 4.11 and the spectra calculated using *Hilbert++*, were obtained with $\Delta\underline{L} \approx 39$ eV, which corresponds to $\Delta_{pd} \approx 6$ eV, a common value in transition metal oxides [53, 52, 219]. The ligand field is now modelled by the positions of the oxygen atoms around the central cation. In the top trace of figure 4.17 (the dotted line) the oxygens along the (local) $c$ axis are moved 10% further from the cation ($R_{\mathrm{eq/ap}} = 0.91$), resulting in a trigonally distorted octahedron. Due to the trigonal distortion there is also a linear dichroism spectrum as shown in the third trace from below (another dotted line). Clearly this does not describe the situation well. The second trace (broken line) shows the spectrum calculated for $O_h$ symmetry but with a strongly anisotropic hybridisation between the oxygen $2p$ orbitals and the iron $3d$ orbitals, mainly of $\sigma$ character. The Slater-Koster transfer integrals for $\sigma$ and $\pi$ hopping ($V_\sigma$, $V_\pi$) were set to 3 and 0.3 respectively, compared to 2 for both of them for the spectrum in the top trace. The resulting spectrum starts to show some resemblance to the experimental spectra now. Because the Hamiltonian is in this case of $O_h$ symmetry no linear dichroism is present in the paramagnetic state. When in addition to the anisotropic hybridisation a trigonal distortion is introduced, the computed isotropic and linear dichroism spectra (thin lines) closely resemble the experimentally obtained spectra.

The main $L_3$ peak is now split in two, but the trigonal distortion is a bit too large here, giving rise to too large a splitting. The best results were obtained with $R_{\mathrm{eq/ap}} = 0.935$, an elongation of the octahedron along the local $c$ axis of 7% compared to 5% for the actual nuclear structure. The computed spectra obtained this way are shown in figure 4.18, along with the spectra measured at room temperature. The

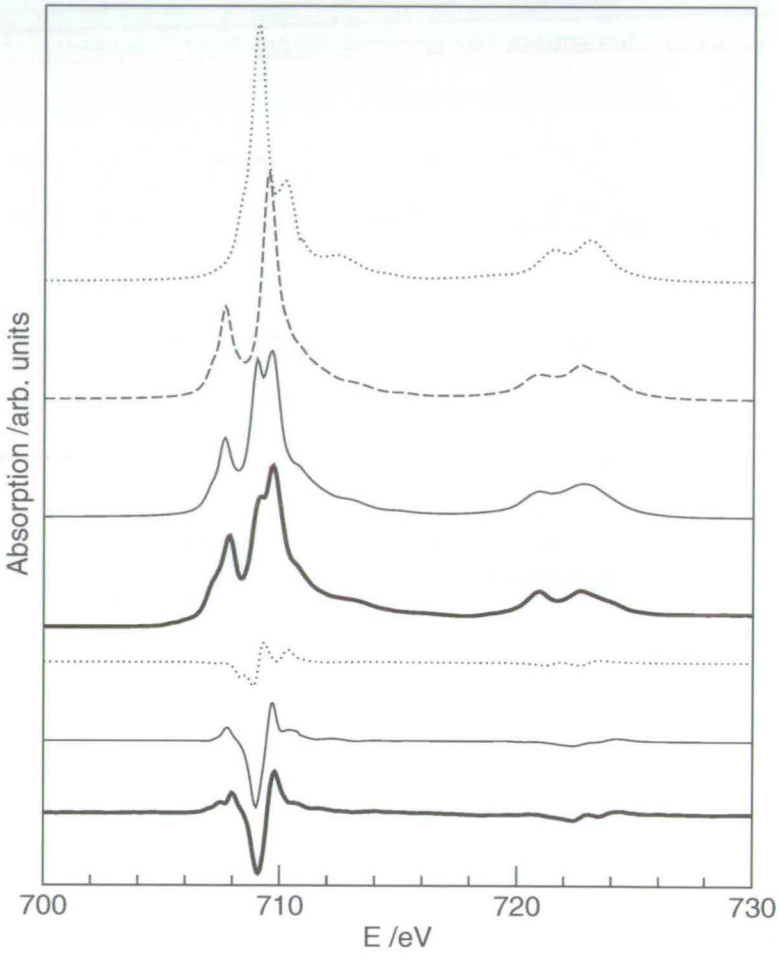


Figure 4.17: Calculated ligand field multiplet spectra. Isotropic hybridisation, i.e. equal $\sigma$- and $\pi$-type bonding in a trigonally distorted octahedron ($D_{4h}$) (dotted lines), in $O_h$ ligand field with strong $\sigma$-type bonding (broken lines), in $D_{4h}$ symmetry with strong $\sigma$-type bonding (thin line) and the measured spectra (thick lines). Where present the corresponding linear dichroism spectra are shown in the lowest three traces.

expectation values of $S^2$, $m_S$, $L^2$, $LS$ and the number of $3d$ electrons on the Fe ($n$) of the lowest energy levels are given in table 4.7.

Table 4.7: Some expectation values of interest for the lowest energy levels as obtained from the fit of experimental data with ligand-field multiplet calculations ($\Delta = 6.5$ eV, $V_\sigma = 3.0$ eV, $V_\pi = 0.3$ eV, with a 7% trigonal distortion from $O_h$ of the ligand field.). The first column gives the approximate corresponding free-ion configuration.

| | $E$ | $\langle S^2 \rangle$ | $\langle S_z \rangle$ | $\langle L^2 \rangle$ | $\langle LS \rangle$ | $\langle n \rangle$ |
|---|---|---|---|---|---|---|
| $^6S_{\frac{5}{2}}$ | 535.42439 | 7.85 | ±0.467 | 1.95 | 0.035 | 5.325 |
| | 535.42448 | 7.85 | ±1.40 | 1.95 | 0.034 | 5.324 |
| | 535.42468 | 7.85 | ±2.34 | 1.95 | 0.031 | 5.323 |
| $^8F_{\frac{1}{2}}$ | 537.11788 | 3.93 | ±0.26 | 12.1 | -0.0063 | 5.424 |
| $^8F_{\frac{1}{2}}$ | 537.11964 | 3.97 | ±0.35 | 11.9 | -0.073 | 5.425 |

Following the expectation values throughout the fitting process it can be seen that according to expectation no anisotropy nor orbital angular momentum arises in calculations where only the crystal-field is taken into account. With the moderate crystal-field as present in the jarosites, and iron oxides in general, the low-spin $Fe^{3+}$ configuration lies more than 2 eV higher in energy and does not mix into the ground state in any degree. Relatively strong trigonal distortions do not change this situation. When the energy of the $2p$ electrons at the oxygen ligands is increased to $\Delta \underline{L} = 39$ eV ($\Delta_{pd} = 6$ eV) approximately 30% $Fe^{2+}$ character mixes in as a result of the hybridisation of the Fe $3d$ orbitals with the oxygen $2p$ orbitals. Remarkably, the spin-orbit coupling induces nearly the maximum orbital angular momentum possible due to the additional $3d$ electron weight. Since the orbital angular momentum is induced by the spin-orbit coupling alone, it does not give rise to additional multiplet structure as it would in the free ion. Strong $\sigma$-type bonding further increases the spin-orbit coupling, and when a trigonal distortion is introduced the additional electron weight becomes mainly of $x^2 - y^2$ character, which is consistent with the result obtained using the XLD sum-rule. At this point the system also has an easy-plane anisotropy of 4 meV.

So far the spectra in the paramagnetic state have been compared by taking a Boltzmann average. This has resulted in excellent agreement between experimentally and

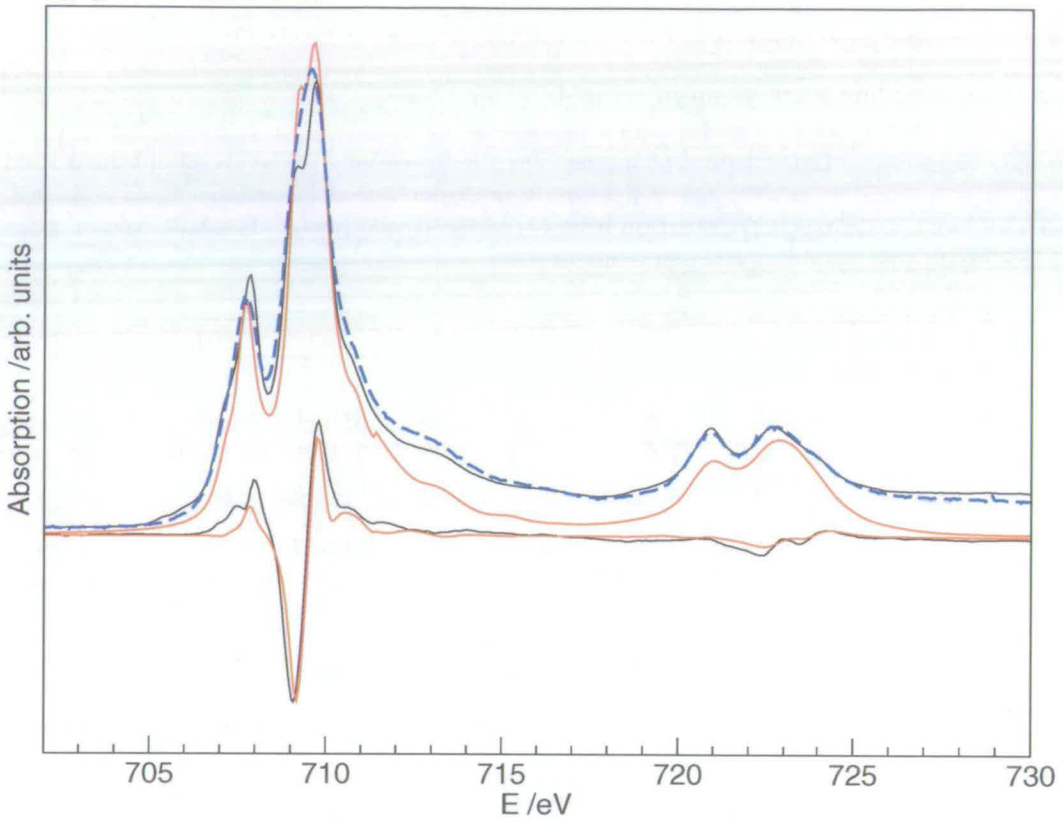


Figure 4.18: s

ample measured at the SRS.] The measured room temperature spectra from a powder sample measured at the SRS (broken blue line), and isotropic and linear dichroism spectra measured on a single crystal of potassium jarosite at the ESRF (black lines), compared with the best fitting calculated spectrum as detailed in table 4.7 (red line). The lifetime broadenings of the states at the $L_3$ and $L_2$ peaks were taken as 0.25 and 0.5 eV.

theoretically obtained spectra, and the advantage is that no assumptions needed to be made about the orientation of the magnetic moments, or how the magnetic super-exchange should be modelled in the calculation. This is an important advantage, because even the isotropic spectrum depends strongly on the strength of an additional Zeeman term, which is often used to model the magnetic super-exchange as well as external magnetic fields. In practise this means another fitting parameter. Figure 4.19 shows the calculated spectra where the single-ion ground state $|m_S \approx \pm\frac{1}{2}\rangle$ (the thick black line) is approached gradually from higher temperatures. As the temperature is lowered the left side of the main (split) peak in the $L_3$ edge increases relative to the

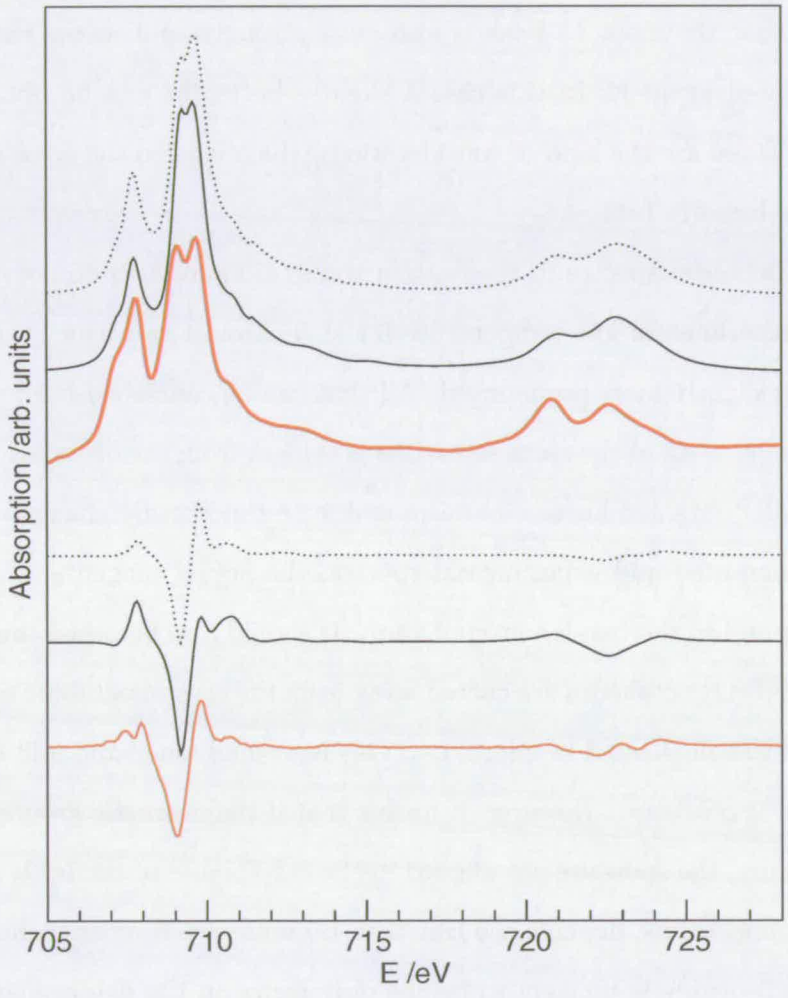


Figure 4.19: The temperature dependence of the calculated spectra. The two top traces correspond to the isotropic spectra simulated at 300 K and for the ground state ($T = 0$) compared with the experimentally obtained spectrum measured at 40 K, shown in red. The bottom traces give the corresponding linear dichroism spectra.

right side and the shoulders at either side of the $L_3$ edge become more pronounced, and the smaller peak before main peak also increases. All these effects are observed in the spectrum as measured at 40 K (red line), but it is clear that the experimentally obtained linear dichroism spectrum does not correspond to the single- ion ground state. It is also clear that the main $L_3$ peak is also more strongly split in the experimental spectrum measured at 40 K. In this case a slightly better fit can be obtained with $R_{\mathrm{eq/ap}} = 0.92$. These are the kind of considerations which lead to the error bars in the final solution as listed in table 4.8.

The linear dichroism spectra in the bottom traces of figure 4.19 do not correspond well with the experimental low temperature linear dichroism spectrum, though some features become slightly more pronounced. All that can be concluded from this is that although some alignment of the spins sets in, as is evident from the observed increase in the experimentally obtained linear dichroism and from the likewise change in isotropic line shape of computed and experimental spectra, the actual magnetic ground state does not correspond to the free-ion ground state. It should also be noted that the local $z$ axis ($z$') of the $FeO_6$ octahedra are canted away from the crystallographic $c$ axis by an angle of $20^\circ$ as was illustrated in figure 4.4. This is a small angle and still 96% of the linear dichroism is recovered. However, it means that if the magnetic ground state is a co-planar structure, the spins are not aligned in the easy-planes of the $FeO_6$ octahedra. The observed temperature dependence can then be interpreted as an indication that the single-ion anisotropy is unlikely to be the only factor in the determination of the magnetic ground state.

Table 4.8 lists the final solution, the best fit between experimental and theoretical spectra, obtained from comparison of a large number of combinations of the fitting parameters around the values listed in the caption of table 4.7. Fits were made between theoretical and experimental spectra in the paramagnetic state. In addition, their temperature dependence was taken into account. It was found that $J = L + S = 3.3(1)$ and that the effective magnetic moment $\mu_{\mathrm{eff}} = \mu_{\mathrm{B}} g_J \sqrt{J(J+1)} = 6.46(7)\mu_{\mathrm{B}}$, using

Table 4.8: The results from fits of the measured polarisation resolved Fe $L_{2,3}$ spectra of synthesised potassium iron jarosite single crystals, with ligand-field multiplet calculations using *Hilbert++* [135]. The left side of the table lists all fitting parameters which have varied in the fitting procedure. The right side gives the resulting expectation values.

| Fit parameters | | Expectation values | |
|---|---|---|---|
| $\Delta$ /eV | 6.5(10) | $D_z$ /meV | 0.4(1) |
| $R_{eq/ap}$ | 0.925(5) | $\langle S^2 \rangle$ | 7.85(15) |
| $V_\sigma$ | 3.0(1) | $\langle L^2 \rangle$ | 1.95(10) |
| $V_\pi$ | 0.3(1) | $\langle LS \rangle$ | 0.04(2) |
| | | $\langle n \rangle$ | 5.35(7) |
| | | $\mu_{\text{eff}}/\mu_{\text{B}}$ | 6.46(7) |

the expectation values of $S^2$ and $L^2$. This value is in good correspondence with the values obtained from analysis of the paramagnetic susceptibility, $6.7(2)\mu_{\text{B}}$ and $6.3(2)\mu_{\text{B}}$, from fits with the Curie-Weiss law (this work and [81]) and the Padé series expansion including further neighbour interactions [81] respectively. Furthermore, the energy of the easy-plane single-ion anisotropy, of $D_z = 0.4(1)$ meV, is in excellent agreement with the values found by Matan *et al.* [127] and Coomer *et al.* [48] in their spin-wave analysis of inelastic neutron data from single crystals, as shown in table 4.1.2. This is strong evidence that an easy-plane anisotropy, along with further neighbour interactions, are the explanation for the magnetic ground state in potassium iron jarosite, even though previously this option has be deemed unlikely by most researchers.

The Fe spectra from hydronium jarosite are similar to those of potassium jarosite. Considering the dependence of the orbital angular momentum and magnetic anisotropy on the ligand-field in our calculations, a similar amount of orbital angular momentum can be expected for hydronium jarosite as for potassium jarosite. Hence the DMI should be present to the same degree as in potassium jarosite. Because the trigonal distortion of the ligand-field in hydronium jarosite is slightly weaker, the easy-plane anisotropy will be slightly weaker, but still within the error bars as given in table 4.8, i.e. $\approx 0.3$ eV.

A last, and interesting, point is the interpretation of the additional electron weight on the $Fe^{3+}$ ions. A crucial step in the modelling of our cluster was to increase the energy of the oxygen $2p$ electrons to about 6 eV below the $Fe^{2+}$ state. This 6 eV is a common value for the charge-transfer gap ($\Delta_{pd}$), which in more than half-filled $3d$ shells takes the role of the Hubbard $U$. In the current case $\Delta_{pd}$ is small enough (and the $\sigma$ hopping large enough) for a partial spin-singlet to form; Some of the $Fe^{3+}$ spin moment is cancelled-out due to the more than half-filled $x^2 - y^2$ shell. Is this what is meant by a *quantum fluctuation* with which the classical spin must be renormalised [206, 176]? With its half-filled shell $Fe^{3+}$ lies at the boundary between what are called Mott insulators with direct hopping between the cations (with $3d^n$,$3d^n \leftrightarrow 3d^{n-1}$,$3d^{n+1}$ charge fluctuations), and charge-transfer insulators with $3d^n \leftrightarrow 3d^{n+1}\underline{\mathrm{L}}$ charge fluctuations. It seems there is fundamental difference between the two, in the way they are measured in an X-ray absorption measurement. The excitation of a core electron to probe the (albeit altered by the core-hole) empty density of states is a local measurement, upon which any singlet in the Mott-Hubbard sense will be destroyed. In the case of the charge-transfer insulators to which our system at least in part belongs, as can independently be verified from the oxygen K-edge spectrum, the question remains whether the renormalisation of the $Fe^{3+}$ spin is a result of the lattice topology as is widely assumed, or whether it only depends on $U$ (or in this case $\Delta_{pd}$) and $t$. A better experimental setting to develop these ideas would be a $3d^9$ system like a copper(II) salt, e.g. paratacamite, ideally in comparison with a $3d^1$ system.

## 4.7 Conclusion

Due to the technological advances in the generation of monochromatic polarised soft X-rays, it has been possible to measure the absorption spectra around the iron $L_{2,3}$- and oxygen K-edges in hydronium and potassium jarosite with an accuracy previously unseen for an iron oxide. Close reproduction of even the detailed features in the spectra is achieved with ligand-field multiplet calculations based on a minimum number of

fitting parameters; the charge-transfer gap $\Delta_{pd}$, the degree of $\sigma$ and $\pi$ hopping, and the trigonal distortion in the close to octahedral ligand-field. For potassium iron jarosite we find that an admixture of approximately 30% $Fe^{2+}$ character mixes into the ground state due to charge-transfer from the oxygen ligands. The resulting spin and orbital angular momenta arising from the admixture are listed in table 4.8 and are in excellent agreement with the literature values of the magnetic moment derived from the paramagnetic susceptibility. Having constructed an effective model of the $Fe^{3+}$ ion and its local environment it was also found that the single ion has an easy-plane anisotropy $D_z$ of the order of 0.4 meV. The temperature dependence of the spectra confirms that the actual magnetic ground state, arising from the cooperative behaviour of the system, does not coincide with the single-ion ground state. However, there is excellent agreement between the obtained value for $D_z$ and estimates from spin-wave analysis of inelastic neutron data ($D_z = 0.428(5)$ meV [127]). This is a strong indication that a locally canted easy-plane anisotropy, in combination with further neighbour exchange interactions, lie at the origin of the particular magnetic ground state observed in potassium iron jarosite. The additional presence of a DMI term cannot be excluded, but a DMI is not needed to explain the experimental observations.

For hydronium iron jarosite it is likely that the single-ion anisotropy is slightly weaker than for potassium iron jarosite, but we cannot say whether this explains the absence of a long range ordered ground state. Given the much larger Weiss constant of the hydronium analogue and the degeneracy in the orientation of the hydronium ions, the most likely explanation for the glassy magnetic ground state may be a random interplane exchange mediated by the hydronium ions.

Chapter 5

# Zinc paratacamite

Despite the fact that the mineral group of the paratacamites and the Zn-doped version, zinc paratacamite ($Zn_xCu_{(4-x)}(OH)_6Cl_2$ with $x \leq 1$) has been known for a while [72, 158, 31] it was only very recently pointed out that the $x = 1$ phase possesses a perfect kagomé lattice of antiferromagnetically coupled $Cu^{2+}$ ($S = 1/2$) ions [188]. The parent compound of this material, clinoatacamite, is polymorphous with two other naturally occurring phases with stoichiometry $Cu_2(OH)_3Cl$; atacamite which is orthorhombic and botallackite which is monoclinic. Clinoatacamite is also monoclinic, but has three symmetry inequivalent Cu sites, two of which are strongly Jahn-Teller distorted, while the third Cu site is only weakly angle distorted. The latter of these sites is particularly susceptible to substitutions with divalent ions such as $Ni^{2+}$, $Co^{2+}$, $Fe^{2+}$ and the diamagnetic ions $Zn^{2+}$, $Ca^{2+}$ and $Cd^{2+}$. One of the reasons Zn-doped clinoatacamite is so interesting, is that it allows us to move between different magnetic lattices with different connectivity and symmetries in a continuous manner, by replacing the magnetic ($S = 1/2$) $Cu^{2+}$ ions with diamagnetic $Zn^{2+}$ ions. For Zn concentrations $x > 0.3$ the angle distortion of the (partially) Zn-substituted site is lifted and a new phase with rhombohedral symmetry stabilises, called zinc paratacamite. In the resulting structure the remaining $Cu^{2+}$ sites become equivalent and form 2D kagomé planes. At the composition $x = 1.0$ the $Cu^{2+}$ to $Zn^{2+}$ replacement of the now undistorted ($O_h$)

inter-plane site (the "Zn-site" from now on) is complete, yielding well decoupled planes of $S = 1/2$ $Cu^{2+}$ ions at the vertices of a kagomé lattice (see figures 5.1 and 5.4). In 2004 $x = 1$ zinc paratacamite was also recognised as a mineral species of its own, called Herbertsmithite [31], based on the characteristic IR spectra of natural crystals.

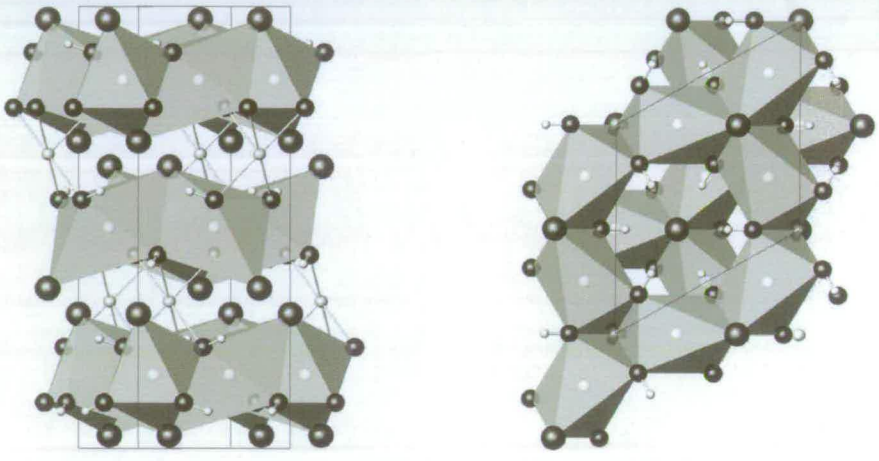

Figure 5.1: The structure of $x = 1$ zinc paratacamite, seen along the $ab$ axis (left panel) and along the $c$ axis (right panel). The $ClO_4$ octahedra ligating the $Cu^{2+}$ ions are drawn in grey. Three octahedra share a common Cl (large black). The oxygens (smaller black) are part of OH groups with hydrogen drawn in white. The left panel also illustrates the inter-plane Zn sites (grey), and in the right panel the stacked kagomé planes are visible.

Magnetic susceptibility measurements by Shores *et al.* [188] show no indication of freezing for the $x = 1$ phase down to 1.8 K. The response remains paramagnetic at least down to the lowest measured temperature and the field-cooled and zero-field-cooled susceptibilities are almost identical, both of which are promising indications that this material may be the best physical realisation of the $S = 1/2$ kagomé antiferromagnet known so far. The parent compound clinoatacamite undergoes two magnetic transitions on cooling. Below 18 K a splitting between the field-cooled and zero-field cooled susceptibility sets in, and at 6.5 K a weak ferromagnetic moment emerges. Muon spin relaxation spectroscopy measurements on clinoatacamite have shown that despite the weak ferromagnetic moment the ground state remains disordered and strong spin fluctuations persist [240, 239]. Shores' susceptibility results for intermediate Zn contents with $x = 0.3, 0.5, 0.66$ and 0.8 show that the transition at 18 K disappears between

$0 < x < 0.3$, while the formation of the weak ferromagnetic moment shifts to lower temperatures and gradually vanishes before $x = 1$. The reported Weiss temperature at $x = 1$ is $-300 \pm 40K$ indicative of reasonably strong antiferromagnetic super exchange between the $Cu^{2+}$ ions linked by hydroxy groups.

Theory predicts that the electronic ground state of the $S = 1/2$ kagomé antiferromagnet is non-magnetic. To check whether this is the case for the $x = 1$ phase, and if so, at which point $x$ a quantum critical phase transition occurs to the magnetic ground state as found for $x = 0$ [240], zinc paratacamite samples with Zn stoichiometry $x = 0.15$, 0.22, 0.5, 0.66, 0.8, 0.9, 1.0 have been synthesised and studied. In addition the synthesis of samples with $x > 1$ has been attempted. Details of the chemical synthesis are described in section 5.1. The magnetic susceptibility, muon spin relaxation spectroscopy and heat capacity of these samples are discussed in sections 5.3, 5.4 and 5.5 respectively. The muon spin relaxation spectroscopy measurements were carried out in collaboration with Philippe Mendels' group at the Université Paris Sud, Orsay. Winfried Kockelmann of the ISIS facility has taken accurate neutron powder diffraction data on an $x = 1$ sample at temperatures down to 10 K. The structure refinement of this data reveals the H positions, and the Cu/Zn partitioning is discussed in section 5.2. Inelastic neutron scattering measurements on the $x = 1$ phase of zinc paratacamite are discussed in section 5.7.

## 5.1 The chemical synthesis of zinc paratacamite

### 5.1.1 From clinoatacamite to Herbertsmithite ($x \leq 1$).

zinc paratacamite samples with Zn contents between $x = 0.15$ and $x = 1$ were synthesised using the method as described by Shores [188]. In this method a 23 mL PTFE bomb liner was filled with 10 mL distilled water, 0.662 g of $Cu_2(OH)_2CO_3$, anhydrous ZnCl and $CuCl{\cdot}2H_2O$ from Aldrich. The mass ratio of the amount of the two chlorides determines $x$ as shown in the upper panel of table 5.1. The liner was then sealed in a

Parr acid digestion bomb, heated to 210°C for 24 hours in a box furnace, and cooled down slowly, at a rate of 0.1°C/min. The precipitate was filtered and dried in air, yielding between 0.7 and 0.8 g of product, a hydrophobic blue/green powder.

Deuterated $x = 1$ samples for neutron diffraction experiments were prepared using 99% $D_2O$, and $Cu_2(OD)_2CO_3$ which was obtained by heating commercially bought basic copper(II)carbonate (Aldrich) in a bomb filled with $D_2O$ at 75°C overnight. The bombs were filled inside a nitrogen filled glove-bag, the precipitate was filtered in the glove-bag and the product was vacuum dried. Using this method we obtained deuteration levels of 98%. On exposure to air the deuteration level dropped to 92% in a few days.

The sample quality was verified with X-ray powder diffraction. Because the X-ray scattering cross sections of Cu and Zn are almost equal it is not possible to infer the Cu and Zn occupancies from X-ray diffraction. For this reason the Zn/Cu ratios of all samples were measured using Inductively Coupled Plasma Auger Electron Spectroscopy, with an accuracy of ±2% in Zn content. It should be noted that ICP-AES does not give an indication of the Cu/Zn partitioning (or antisite disorder) between the different sites. This issue will be addressed in section 5.2, where accurate neutron diffraction measurements on a deuterated $x = 1$ sample are discussed.

Historically a different method is used for the synthesis of zinc paratacamite [72, 158, 31]; $x = 1$ zinc paratacamite (or Herbertsmithite) can be obtained by boiling 1 g of basic copper(II)carbonate with 20 mL (excess) of 1 M aqueous zinc chloride for 24 hours [32]. This reaction can be carried out at temperatures as low as room temperature, but the reaction will take a few weeks to complete at such low a temperature. Unfortunately, powder X-ray diffraction showed that samples synthesised using this method had much broader diffraction peaks than samples made using the high temperature synthesis.

Table 5.1: The used mass in gram of all ingredients to be added to 10ml of water in a 23 ml bomb liner, to obtain zinc paratacamite with Zn content $x$. The values for $x \leq 1$ are interpolated from Shores' data [188]. The values for $x > 1$ (diluted kagomé) are as found in this study, using $2ZnCO_3{\cdot}3Zn(OH)_2 \cdot nH_2O$ (in the table noted as $ZnCO_3$...).

| $ZnCu_2$ | $CuCl{\cdot}2H_2O$ | $Cu_2(OH)_2CO_3$ | $ZnCO_3\ldots$ | $x(\pm 0.03)$ |
|---|---|---|---|---|
| 0.0 | 0.426 | 0.662 | 0.0 | 0.0 |
| 0.062 | 0.348 | 0.662 | 0.0 | 0.15 |
| 0.136 | 0.257 | 0.662 | 0.0 | 0.30 |
| 0.204 | 0.170 | 0.662 | 0.0 | 0.50 |
| 0.271 | 0.085 | 0.662 | 0.0 | 0.66 |
| 0.287 | 0.050 | 0.662 | 0.0 | 0.80 |
| 0.292 | 0.037 | 0.662 | 0.0 | 0.85 |
| 0.300 | 0.024 | 0.662 | 0.0 | 0.90 |
| 0.310 | 0.0 | 0.662 | 0.0 | 1.0 |
| 0.310 | 0.0 | 0.640 | 0.024 | 1.10 |
| 0.310 | 0.0 | 0.574 | 0.096 | 1.40 |

### 5.1.2 zinc paratacamite with $x > 1$, a diluted kagomé lattice.

As is clear from table 5.1 for $x < 1$ the Zn content is increased by adding less $CuCl{\cdot}2H_2O$ and more ZnCl to the reaction mixture. To get $x = 1$ zinc paratacamite no $CuCl{\cdot}2H_2O$ should be added. At that point the Zn content cannot be increased further by adding more ZnCl, this will only result in a lower yield. This is fortunate because as long as the ZnCl concentration is more or less right, and no $CuCl{\cdot}2H_2O$ is added to the reaction mixture, one can be confident that the Zn:Cu ratio is 1:3. However, to obtain samples with $x > 1$ clearly a different approach is needed. The approach of replacing some of the basic copper(II)carbonate with zinc(II)carbonate hydroxide hydrate with the same molar concentration in Zn has been explored[1]. For example, $x = 1.4$ zinc paratacamite was obtained by adding 0.31 g of ZnCl, 0.574 g of $Cu_2(OH)_2CO_3$ and 0.031 g of $2ZnCO_3{\cdot}3Zn(OH)_2 \cdot nH_2O$ to 10 mL water in a 23 mL bomb liner. The rest of the reaction is as described in the previous paragraph. The masses used in table 5.1 can be interpolated and extrapolated up to $x \sim 1.7$ but above $x = 1.4$ some impurity phases start to appear in the powder XRD patterns. In the resulting

[1]Though we chose here to replace a the Cu ions with the same number of Zn ions, the important parameter is probably the pH of the solution, which is determined by the molar ratio of $CO_3^{2-}$ and $OH^-$ ions added.

material the kagomé lattice of antiferromagnetically coupled $S = 1/2$ spins is doped with diamagnetic sites.

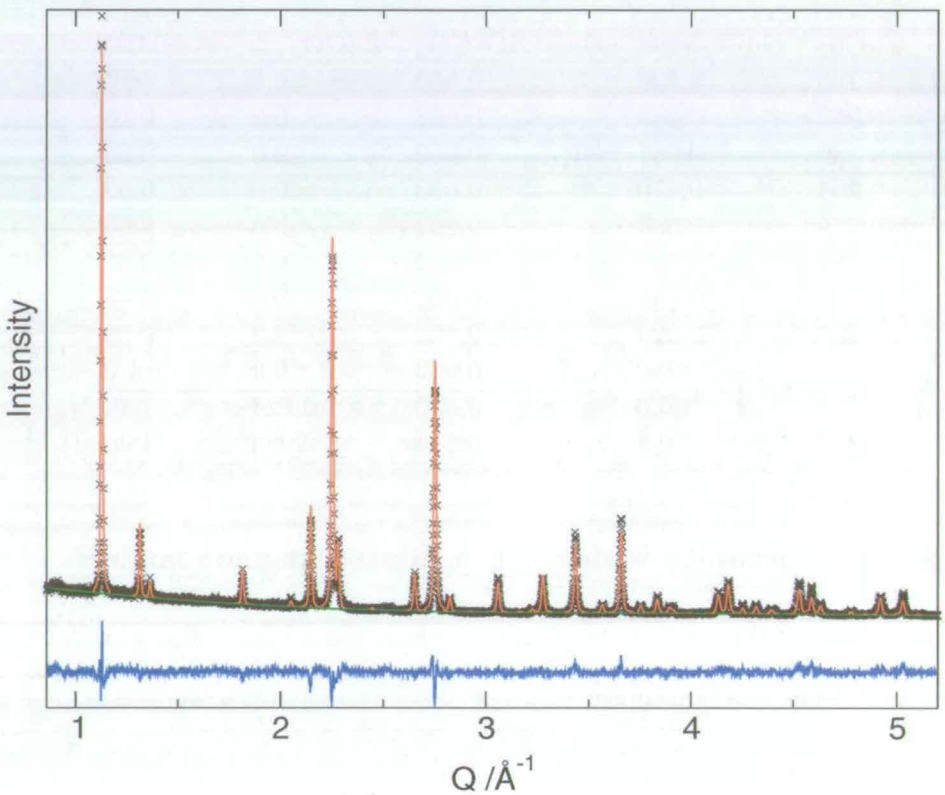


Figure 5.2: The X-ray diffraction pattern (black $\times$) for $x = 1.40 \pm 0.02$ zinc paratacamite, with structure refinement (red) and the difference (blue).

The diffraction pattern for an $x = 1.4$ sample is shown in figure 5.2. The pattern was Rietveld analysed using the General Structure Analysis Program [111], with residuals $\chi^2 = 2.6$, $R_{wp} = 13.32\%$ and $R_p = 10.28\%$. We found lattice parameters $a = 6.851(0)$Å and $c = 14.132(6)$Å compared to the reported values of $a = 6.8342(3)$Å and $c = 14.0320(12)$Å [188] respectively.

The refinement is clearly of poorer quality than the refinements of diffraction data of $x = 1$ samples (with typically $\chi^2 = 2.2$, $R_{wp} = 7.3\%$ and $R_p = 5.4\%$). It is likely that on substituting the Jahn-Teller distorted Cu sites in the $CuO_4Cl_2$ octahedra with Zn $3d^{10}$, which is not Jahn-Teller active, the distortion in these sites is at least partially lifted. For sufficient levels of doping this will give rise to disorder in the material.

A similar effect may play a role in $x < 1$ samples, in which part of the $O_h$ Zn sites are substituted with Cu and become weakly distorted away from $O_h$ symmetry. As mentioned earlier, for $x < 0.3$ this even gives rise to a structural transition.

## 5.2 Neutron powder diffraction

Neutron powder diffraction measurements were carried out on the ROTAX neutron time-of-flight diffractometer at the ISIS Facility, United Kingdom. A 4 g nominally $x = 1$ sample of $\approx 96\%$ deuterated zinc paratacamite was used. The exact Zn stoichiometry of this sample as measured with ICP-AES is $x = 0.98(2)$. Most of the data was collected at 10 K, and shorter scans were made at 150 K and 285 K. All powder diffraction patterns were Rietveld analysed using GSAS [111, 203]. Figure 5.3 and table 5.2 presents the data obtained at 10 K and the corresponding refinement results. Apart from an expansion of the lattice between 10 K and 285 K of 0.1% along the a,b axis and 0.3% along the c axis, the refinement results at 150 K and 285 K were in good agreement with the results shown in table 5.2. The residues were larger for the 150 K and 285 K data, $\chi^2 = 2.1$, $R_p = 3.9\%$, $R_{wp} = 3.2\%$ and $\chi^2 = 1.91$, $R_p = 3.7\%$, $R_{wp} = 3.1\%$ respectively, compared to $\chi^2 = 13.95$, $R_p = 2.83\%$, $R_{wp} = 2.73\%$ for the 10 K data.

Table 5.2: The results of the Rietveld refinement of neutron powder diffraction data taken at 10 K at ROTAX, ISIS on $ZnCu_3(OH)_6Cl_2$.

| atom | $x$ | $y$ | $z$ | $U_{iso}/Å^2$ | $f$ |
|---|---|---|---|---|---|
| Zn | 0.0000 | 0.0000 | 0.0000 | 0.0038(10) | 0.73(3) |
| Cu | 0.3333 | 0.1667 | 0.1667 | 0.0048(6) | 0.91(3) |
| O | 0.1278(2) | 0.2555(4) | 0.1052(16) | 0.0068(4) | 1 |
| D | 0.2023(2) | 0.4045(4) | 0.07598(15) | 0.011(4) | 0.948(2) |
| H | 0.2023(2) | 0.4045(4) | 0.07598(15) | 0.011(4) | 0.052(2) |
| Cl | 0.0000 | 0.0000 | 0.30427(15) | 0.011(4) | 1 |
| Cu | 0.0000 | 0.0000 | 0.0000 | 0.0038(10) | 0.27(3) |
| Zn | 0.3333 | 0.1667 | 0.1667 | 0.0048(6) | 0.09(3) |

Space group $R\bar{3}m$, $a = 6.83054(6)$ Å, $c = 14.0479(2)$ Å, $\alpha = 90°$, $\gamma = 120°$, $V = 567.613(9)$ Å$^3$, Residuals $\chi^2 = 13.95$, $R_p = 2.83\%$, $R_{wp} = 2.73\%$. The error bars are based on $2\sigma$ as returned by GSAS.

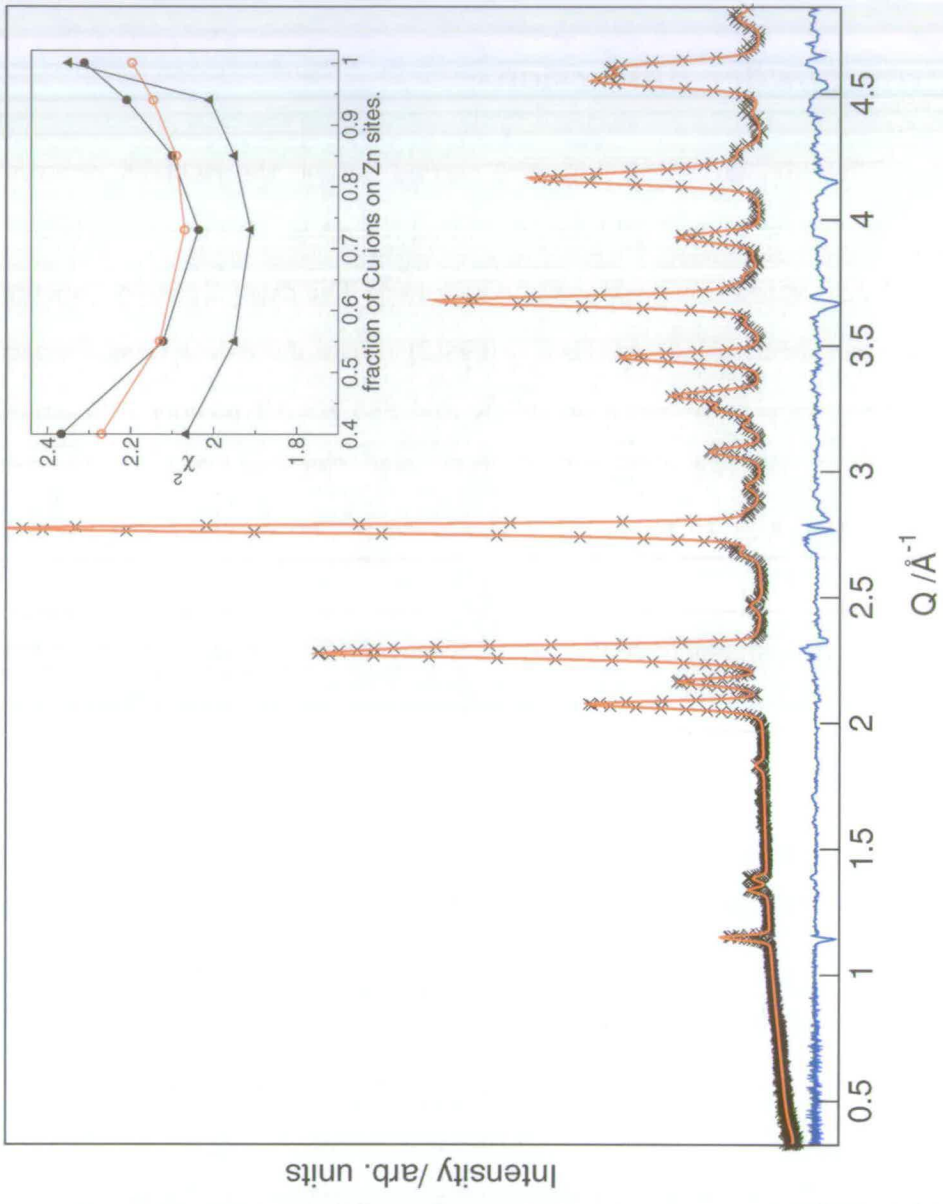


Figure 5.3: The 10K neutron diffraction pattern of $ZnCu_3(OD)_6Cl_2$, the Rietveld refinement (red) and the difference (blue). The inset gives the dependence of $\chi^2$ on the Zn stoichiometry $x$ for the data taken at 10 K ($\chi^2/6$ black filled circles), 150 K (red open circles) and 290 K (black filled triangles).

For all datasets the degree of antisite disorder refined to 9(3)% $Zn^{2+}$ ions on the Cu site, with a corresponding 27(3)% fraction of the Zn sites occupied by $Cu^{2+}$ ions. The inset in figure 5.3 shows the dependence of $\chi^2$ of the refinements at 10, 150 and 285 K, as a function of the antisite disorder. In all cases the minimum in $\chi^2$ lies around a 30% fraction of Zn sites occupied by $Cu^{2+}$ ions, and the minimum is the sharpest in the data taken at 10 K.

It is important to note that in these refinements the occupancies of the Cu and Zn sites with either $Cu^{2+}$ or $Zn^{2+}$ ions were fixed at 100%. A further constraint imposed on the refinement was that the Zn:Cu ratio should stay 1:3. The Zn:Cu ratio was measured independently using ICP-AES, and was later confirmed with muon spin-relaxation spectroscopy. This information had to be added to the refinement to obtain reproducible values for the antisite disorder. Subsequent relaxation of the constraints on the site occupancies and Zn:Cu ratio did not lead to large changes in the refinement; the Zn/Cu site occupancy went from 100% to 96(2)%, and there was only a very small further reduction of the residues. However, GSAS could no longer put error bars on the refinement because the obtained results were amongst a large manifold of possible solutions outside the subspace defined by the constraints discussed above. Given the high quality of the data and the refinement It appears reasonable to require that the structure solution is unique within the subspace of physically possible solutions. We believe that the relaxation of any of these constraints equates to ignoring relevant data on the one hand, and on the other hand to over-interpretation of the remaining data.

The large degree of antisite disorder is disappointing news for a material which has been heralded as the first perfect $S = 1/2$ kagomé antiferromagnet. it is not so surprising from a chemical point of view; in the previous section it was shown that even the strongly Jahn-Teller distorted Cu sites can host Zn ions, resulting in Zn stoichiometries of $x > 1$. The degree of antisite disorder found here corresponds to an energy of $\approx 1300$ K between a $Cu^{2+}$ ion on the Cu site and on the Zn site, given that the synthesis was carried out at $\approx 500$ K. The energy of the Jahn-Teller distortion is

probably larger than 1000 K, but it is likely that Zn sites hosting a $Cu^{2+}$ ion become locally weakly angle-distorted, which reduces the effective energy difference between the sites. Following through this line of thought a low-temperature synthesis would be preferential. Unfortunately the presently known low-temperature synthesis yields samples of a lower overall crystallinity. In the remainder of this chapter the importance of this imperfection will be assessed. From muon spin-relaxation spectroscopy [131] it is clear that despite this imperfection for $x = 1$ the spins do not freeze even at 50 mK, and there is no doubt that zinc paratacamite is still a material of outstanding interest.

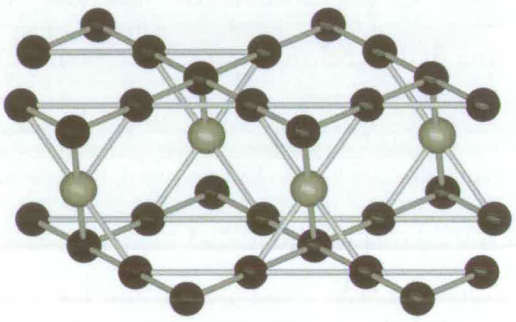

Figure 5.4: Two kagomé layers of $Cu^{2+}$ ions (black) sandwiching the interplane $Zn^{2+}$ sites (light grey) in $x = 1$ zinc paratacamite. The oxygen, chlorine and hydrogen atoms are omitted for clarity.

## 5.3 Magnetic susceptibility

The magnetic susceptibility of zinc paratacamite samples with $x = 0.15$, 0.22, 0.5, 0.66, 0.8, 0.9, 1.00, 1.1, 1.16, 1.4 and 1.5 has been measured with a Quantum Design MPMS magnetometer. The field cooled and zero-field cooled susceptibilities were measured in an applied field of 100 G between 1.8 and 340 K. Figures 5.5 and 5.6 show the field-cooled (open symbols) and zero-field cooled (filled symbols) susceptibilities for $x = 0.15$, 0.22, 0.5 and $x = 0.66$, 0.9, 1.0 respectively. It is clear from these figures that

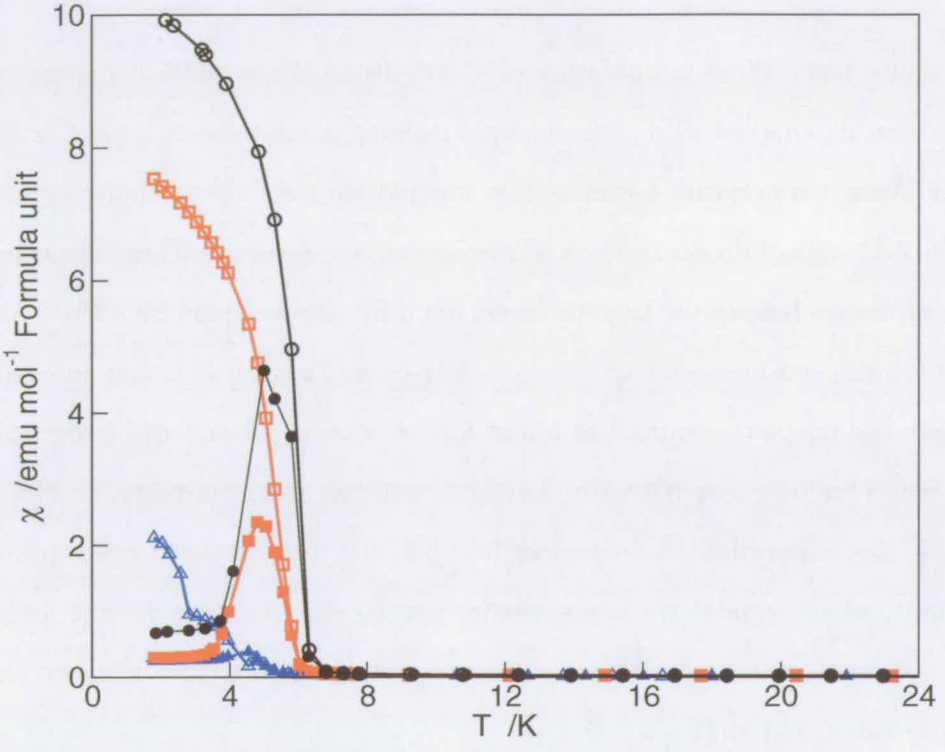


Figure 5.5: The low-temperature magnetic susceptibility for $x = 0.15$ (black circles), $x = 0.22$ (red squares) and $x = 0.5$ (blue triangles) phases. The open and filled symbols correspond to the zero-field cooled and field-cooled susceptibilities respectively.

the remanence which is present in clinoatacamite ($x = 0$) below 6.5 K vanishes with the $Cu^{2+}$ occupation of the $O_h$ Zn site.

Table 5.3 gives the Curie ($C$) and Weiss ($\theta_w$) constants against Zn stoichiometry $x$, obtained from the high temperature susceptibility $T > 150$ K. The Curie constant found for all concentrations, and those extracted manually from data published by Shores [188] is 0.58(8) emu K/mol. The analysis as presented in the chapter on the jarosites suggests that the mean-field estimate for the effective magnetic moment can be relied on. In this case it would be $2.1\mu_B$, which corresponds to $\langle L^2 \rangle = 0.70(7)$. It should be stressed that this orbital angular momentum is induced by the spin-orbit coupling alone, and hence does not induce multiplet effects. The total magnetic moment Hilbert space remains two dimensional, corresponding to the $S = 1/2$ spin. While the connectivity of the magnetic lattice goes down with increasing $x$, the Weiss temperature becomes more negative. The $x = 1$ phase, which should be the best approximation to the

kagomé lattice, has a Weiss temperature of $\sim 300(40)$ K. Hence the $Cu^{2+}$ spins on the kagomé lattice are coupled with a strong antiferromagnetic superexchange of $\sim 300$ K. The lower Weiss temperature found as $x$ is lowered suggests that populating the Zn sites with $Cu^{2+}$ spins introduces weak ferromagnetic interactions. These could be the exchange pathways linking the kagomé layers via a Zn site occupied by a $Cu^{2+}$ ion, or the direct interactions between $Cu^{2+}$ ions on inter-plane Zn sites. It is therefore natural to associate the magnetic remanence found for $0.6 < x < 1.0$ and the ferromagnetic moment found for $0 < x < 0.6$ with the $Cu^{2+}$ spins on the inter-plane Zn site. For this reason the susceptibilities in figures 5.5, 5.6, 5.7 and 5.8 have been given per formula unit, which equates the susceptibility per Zn site. In table 5.3 the magnetic remanence/ferromagnetic moment are given as a fraction of the $Cu^{2+}$ spins on the Zn site, naïvely calculated as $(1 - x)$.

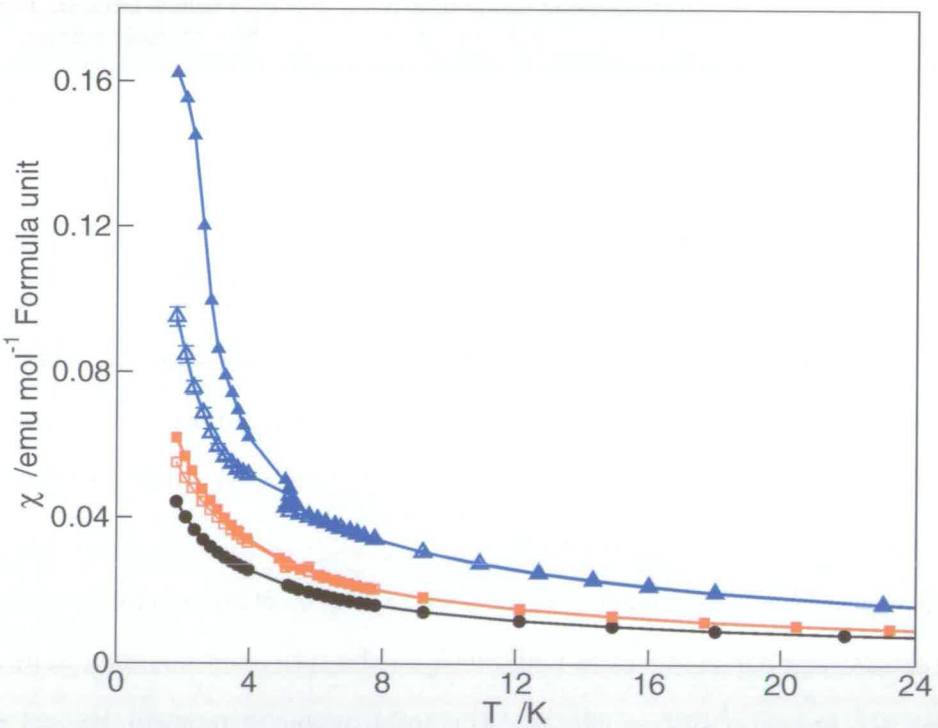


Figure 5.6: The low-temperature magnetic susceptibility for $x = 1$ (black circles), $x = 0.9$ (red squares) and $x = 0.66$ (blue triangles) phases. The open and filled symbols correspond to the zero-field cooled and field-cooled susceptibilities respectively.

Theory predicts that the magnetic ground state of the $S = 1/2$ kagomé antiferromagnet is non-magnetic, i.e. that its susceptibility vanishes for $T \to 0$. As is clear from figure 5.6 even for $x = 1$ this does not happen. In figure 5.7 and 5.8 the magnetic susceptilibity of samples with $0.8 \leq x \leq 1.4$ are plotted against the inverse temperature ($T^{-1}$). Figure 5.7 also shows the susceptibility from a fraction of 6% of the total number $Cu^{2+}$ spins per formula unit of free spins in a 100 G field, given by equation 2.49. The resemblance of the low-temperature susceptibility with the Curie susceptibility suggests that there is a contribution from weakly coupled (almost free) spins, which are likely to be the antisite spins making up a fraction of up to 9% of the total number of $Cu^{2+}$ spins. Most of the low-temperature magnetic susceptibility can thus be accounted for. It is however not possible to do this with such an accuracy as to *prove* that the contribution to the susceptibility from the $Cu^{2+}$ spins on the kagomé layer vanishes. The mean-field susceptibility at 1.8 K, $\chi(T = 1.8\text{ K}) = \text{C}/(1.8 - \theta_{\text{w}}) \approx \text{C}/-\theta_{\text{w}} \approx 0.005$ emu/mol formula unit, which is small compared to the total susceptibility measured at 1.8 K. Unfortunately it is exactly the matter of whether the $Cu^{2+}$ spins in the kagomé layers contribute to the magnetic susceptibility, or whether they are bound in a non-magnetic resonating valence bond-like ground state, that is a central question in this study.

The $x = 1$ sample shown in figure 5.7 is the deuterated sample for which the neutron powder diffraction data discussed in the previous section was taken. It seems that the splitting between the field-cooled and zero-field-cooled susceptibility is somewhat larger in deuterated samples than in hydrogenated samples. This should not be a cause of concern; muon spin relaxation measurements [131] confirm that the spin-dynamics in this sample are typical for $x = 1$ samples. This was further confirmed in specific heat measurements. One possible explanation for the observed variation in the magnetic susceptibility of samples with the same Zn stoichiometry $x$ is antisite disorder between the chlorine and oxygen ions. If such an antisite disorder is included in the refinement of the neutron powder data, it refines to $\approx 3\%$.

It could be questioned whether the magnetic lattice in zinc paratacamite can really be further diluted with diamagnetic Zn-ions. *Are the values found with ICP-AES unreliable because of the presence of a non-crystalline phase rich in Zn?*. The low-temperature magnetic susceptibilities as shown in figure 5.8 are an indication that dilution of the kagomé lattice has been successful. In all samples with $x > 1$ the magnetic remanence is zero. Again the susceptibility per formula unit is shown against $T^{-1}$. At first the susceptibility per formula unit decreases, and it even decreases per $Cu^{2+}$ unit up to $x = 1.16$. The susceptibility for $x = 1.4$ per $Cu^{2+}$ unit is much larger, while per formula unit it is again approximately equal to the $x = 1$ susceptibility. For $x = 1.5$ even the susceptibility per formula unit is much larger, despite a lower concentration of $Cu^{2+}$ spins. This trend can be explained as initially a reduction in antisite spins, which make-up the majority of the susceptibility at low-temperatures,

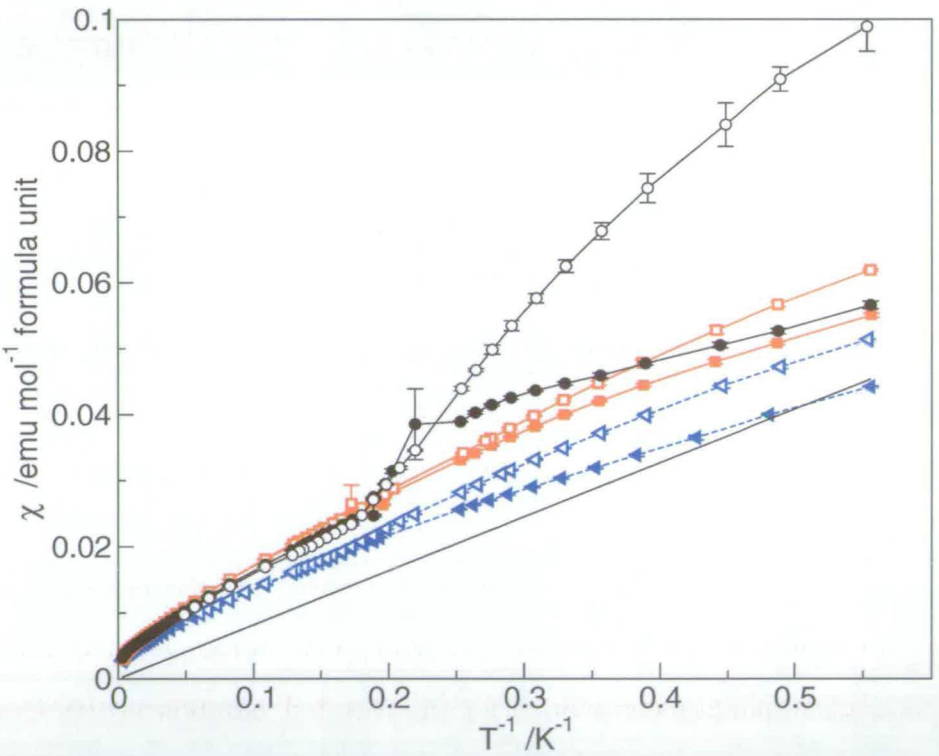


Figure 5.7: The magnetic susceptibility of $x = 0.8$ (black circles), 0.9 (red squares) and 1.0 (blue triangles) samples measured in 100 G, against $1/T$. The open and closed symbols correspond to the field-cooled and zero-field cooled susceptibilities respectively.

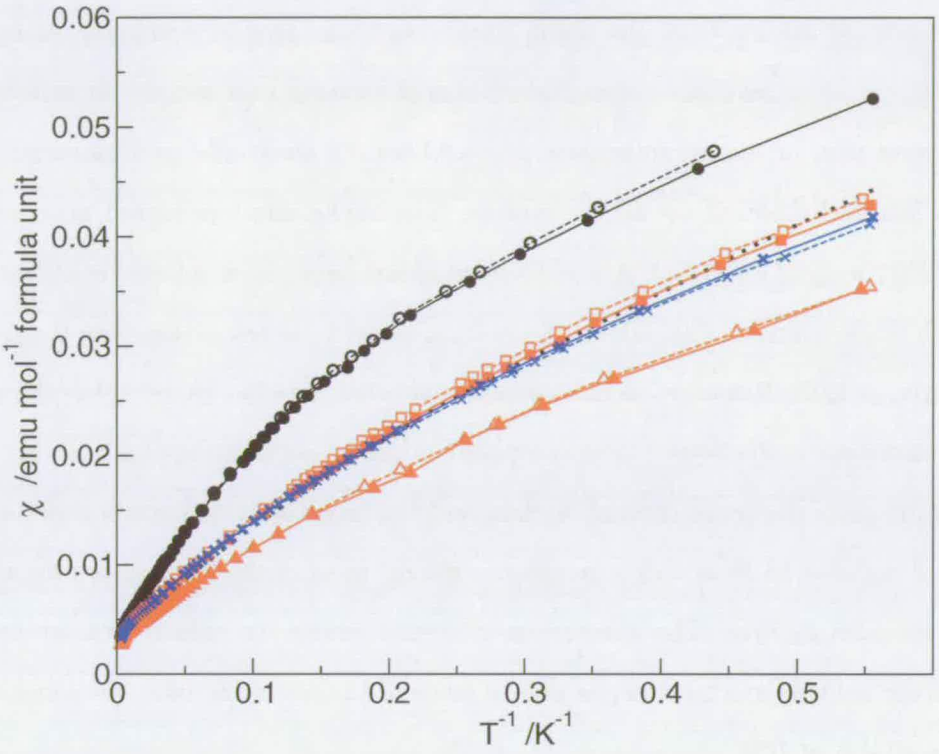


Figure 5.8: The magnetic susceptibility of $x = 1.5$ (black circles), 1.4 (red squares), 1.16 (red triangles), 1.1 (blue crosses) and 1.0 (black dotted line) samples measured in 100 G, against $1/T$. The open and closed symbols correspond to the field-cooled and zero-field cooled susceptibilities respectively.

and a general opening-up of the magnetic lattice for larger Zn concentrations, with $x > 1.4$. The Curie and Weiss constants obtained from the high-temperature susceptibility are very noisy, and do not give a clear trend. Even though the susceptibility data can be rationalised by assuming that dilution of the kagomé lattice has been successful, this issue will be revisited in the next two sections.

## 5.4 Muon spin relaxation spectroscopy

Muon spin rotation/relaxation spectroscopy was carried out at the GPS and LTF facilities at PSI, and at the $\mu$SR station at ISIS. A dilution refrigerator was used for measurements below 1.5 K on samples with $x > 0.6$. Positive muons were stopped in pellet-pressed samples of zinc paratacamite of $1 \sim 2$ mm thickness, with Zn stoichiometries $x = 0.15$, 0.33, 0.5, 0.66, 1.0 and 1.1. The asymmetry ($A$) in the forwards/backwards

emitted positrons arising from the muon decay were background corrected, using the characteristic nuclear relaxation signal which was observed for all samples at sufficiently high temperatures, in the paramagnetic phase where the electronic spin moments fluctuate too fast to be picked up by the muons. The background corrected polarisation given by $P(t) = (A(t) - \text{B.G.})/\text{A(t} = 0)$ is analysed here. The muon facility at PSI works with single-muon events, which allows for a better time resolution than the pulsed muon source at ISIS. However, in most samples studied here the muon spin-relaxation from the electronic spins is very slow compared to the muon lifetime of 2.2 $\mu$s. At $\mu$SR the muon intensity per pulse is much higher, and the muon spin relaxation signal could be followed up to $\approx$ 16 $\mu$s at this instrument. Hence, most of the data shown here were taken at the $\mu$SR facility. The spectra for $x = 0.33$ where the spin relaxation due to the electronic spins is much faster, as well as some of the $x = 0.66$ data, were measured at LTF and GPS at PSI.

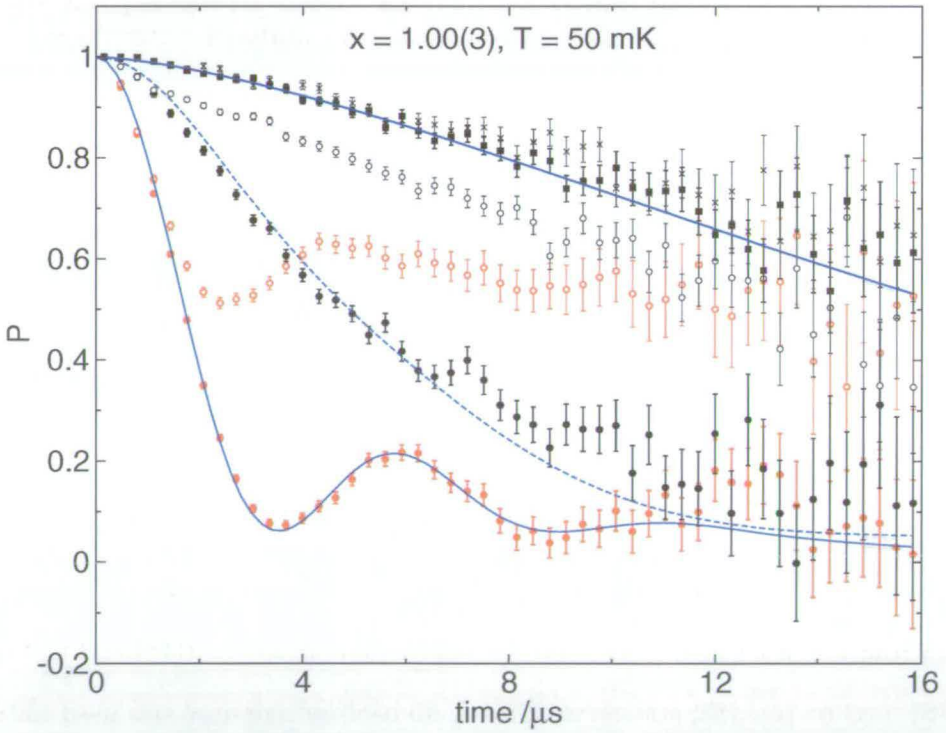


Figure 5.9: The muon polarisation in a hydrogenated sample (red) and a deuterated sample (black) at 50 mK, in zero field (filled circles) and longitudinal fields $H = 20$ G (open circles), 80 G (filled squares) and 160 G (open squares). The blue lines give fits to the data as discussed in the text.

Figure 5.9 gives the muon polarisation ($P$) in fields up to 160 G for an $x = 1$ sample at $\approx 50$ mK. The zero-field signals shown in red filled circles for hydrogenated zinc paratacamite and black filled circles for deuterated zinc paratacamite ($\approx 96\%$), are typical for what is observed in samples of all Zn stoichiometries in the paramagnetic state, i.e. $T > 20$ K. This oscillatory signal is explained by the formation of coherently-bound states between the muon and the OH groups in zinc paratacamite, forming muonium hydroxide ($OH\mu$) [122, 50]. To obtain accurate fits of the muon relaxation, an additional Gaussian Kubo-Toyabe term (KT) [205] accounting for muon relaxation from randomly oriented static nuclear spins at the Cl-site was included.

$$P(t) = (1 - f_{\mathrm{Cl}})P_{\mathrm{OH}}e^{-(\gamma_\mu \Delta_{\mathrm{OH}} t)^2/2} + f_{\mathrm{Cl}}\mathrm{KT_{Cl}(t)} \tag{5.1}$$

with $\gamma_\mu = 13.554 \times 2\pi$ kHz/G,

$$P_{\mathrm{OH}} = \frac{1}{6} + \frac{1}{3}\cos\left(\frac{\omega_{\mathrm{OH}} t}{2}\right) + \frac{1}{6}\cos(\omega_{\mathrm{OH}} t) + \frac{1}{3}\cos\left(\frac{\omega_{\mathrm{OH}} t}{2}\right)$$

and

$$\mathrm{KT_{Cl}(t)} = \frac{1}{3} + \frac{2}{3}(1 - \omega_{\mathrm{Cl}}^2 \mathrm{t}^2)\mathrm{e}^{-\omega_{\mathrm{Cl}}^2 \mathrm{t}^2/2}.$$

Excellent agreement was obtained for the relaxation in the hydrogenated sample. For the muonium site $H_{\mathrm{OH}} = 7.8(4)$ G with a field-distribution of $\Delta_{\mathrm{OH}} = 2.4(4)$ G. Approximately 15% of the signal can be attributed to the Cl site ($f_{\mathrm{Cl}} \approx 0.15$), with a field distribution of $\Delta \approx 1.8$ G. The deuterium nuclear moment is much smaller, with $\mu_{\mathrm{D}}/\mu_{\mathrm{H}} = 0.153$ resulting in a slower muon precession $\omega_{\mathrm{OD}} = \omega_{\mathrm{OH}}/0.153$. The broken blue curve in figure 5.9 is the muon relaxation expected for a deuterated sample, based on the parameters as found for hydrogenated samples, but with a larger value for the field distribution at the Cl site. It should be noted that for samples with $x \geq 1$ these signals are recorded even at 50mK and below. Apparently, the $x = 1$ sample remains

fully paramagnetic down to these very low temperatures, so that the only magnetic moments "seen" by the muons are the randomly distributed static nuclear moments.

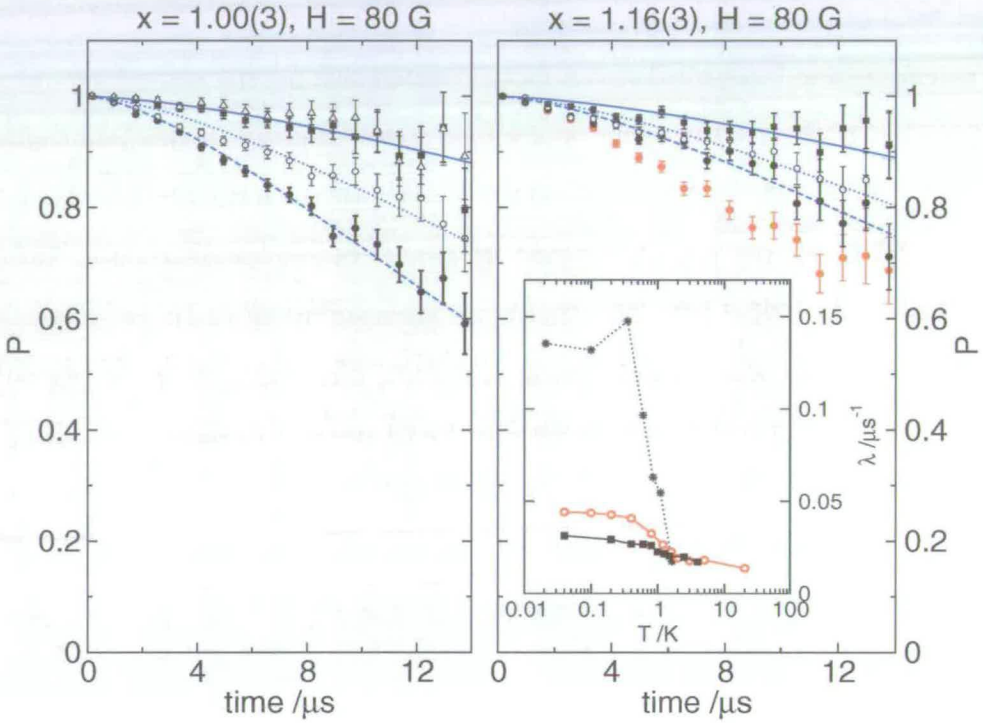


Figure 5.10: The muon polarisation in a longitudinal field of 80 G for $x = 1.00(3)$ (left panel), and $x = 1.15(3)$ (right panel) at $T = 40$ mK (filled circles), 800 mK (open circles), 5 K (filled squares) and 20 K (open triangle). The red dots in the right panel show the 100 mK data for $x = 1.00(3)$ for comparison. The lines through the data points give the fits with a compressed-exponential decay. The obtained relaxation rate ($\lambda$) is given in the inset as a function of temperature for 0.66(3) (stars), $x = 1.00(3)$ (open red circles) and $x = 1.15(3)$ (filled black squares).

A longitudinal field of 80 G (full black squares in figure 5.9) was sufficient to decouple the muons from the nuclear moments, which as we have just found, are up to $\simeq 8$ G. Much larger fields, up to 2500 G, were needed to decouple the muons from the electronic spins. Hence the muon relaxation in a longitudinal field of $\sim 80$ G is a measure of the remaining fast spin fluctuations which can be picked up by the muons. Figure 5.10 shows the muon polarisation in 80 G at different temperatures for an $x = 1.16(3)$ sample and for $x = 1$ at 40 mK in red. The slow relaxation from the fast fluctuating spins evident here can be fitted with a compressed-exponential decay $e^{-(\lambda t)^{\alpha}}$ with $\alpha = 1.4$.

In most cases $\alpha = 1$ and in the case of dilute-alloy spin glasses $\alpha = 0.5$ and even $\alpha = 1/3$ have been found [205, 41, 106]. Stretched exponential decay can be explained by rapid relaxation of muons close to magnetic sites, and slower relaxation from muons further away in dilute magnetic systems. It also occurs in glassy systems with a random energy landscape resulting in a wide distribution of relaxation times. That the muon relaxation is different in the present case may be evidence that the relaxation does not arise from "defects" in the lattice alone, and hence, that the time-correlations of the $Cu^{2+}$ spins in the kagomé lattice in a *magnetic* ground state are probed. Compressed exponential relaxations have been found for gel and sponge phases [12, 69, 75], and the implications of this particular muon decay in the case of a co-operative paramagnet may be the subject of future investigation. In the "classical" kagomé antiferromagnet iron jarosite there is also some evidence of compressed exponential muon relaxation [2] at higher temperatures.

For the moment the muon decay is treated phenomenologically. The relaxation is found to increase slightly below $T < 1 \sim 2$ K, indicative of some slowing down of the spins. This effect is more pronounced for samples with a higher $Cu^{2+}$ contents (lower $x$), and becomes very weak for samples with $x > 1$. In theory this compressed-exponential decay is also present in the zero-field muon spin relaxation as shown in figure 5.9. For samples with $x \geq 1$ the inclusion of the compressed-exponential in equation 5.1 does not affect the fit. For $x = 0.66$ on the other hand, the relaxation rate due to electronic spin fluctuations is much stronger, as is clear from figure 5.11. In this case equation 5.1 must be multiplied with the compressed-exponential decay to obtain a good agreement.

With increasing $Cu^{2+}$ contents the zero-field muon relaxation rate gradually increases, and for $x < 0.6$ the dynamics become more spin-glass like. The zero-field muon polarisation signals at $\sim$ 1.5 K are shown in figure 5.11. For samples with $x < 0.6$ there is a gradual transition from the slow precession indicative of muonium hydroxide formation, to a faster decay, in the case of $x = 0.33$ relaxing to almost 1/3, as is typical for a random distribution of static electronic spins. For all samples with

Table 5.3: Magnetic constants for $Zn_xCu_{(4-x)}(OH)_6Cl_2$, $0 \leq x \leq 1.5$

| $x$ (±0.02%) | $C$ /emu K | $\theta_w$ /K | $T_g$ /K | $R^{(c)}$ % |
|---|---|---|---|---|
| 0 [a] | | -194 | 6.5(2) | 20 |
| 0.15 | 0.52 | -190 | 6.4(2) | 20 |
| 0.22 | 0.56 | -230 | 6.0(2) | 16 |
| 0.5 | 0.53 | -230 | 5.5(2) | 8 |
| 0.5 [b] | 0.55 | -231 | 5.5(1) | |
| 0.66 | 0.5 | -180 | 5.5(2) | 0.8 |
| 0.66 [b] | 0.50 | -272 | 5.5(1) | |
| 0.81 | 0.76 | -285 | 4.0(6) | 0.5 |
| 0.90 | 0.53 | -236 | 4.0(6) | 0.1 |
| 1.00 | 0.58 | -330(80) | n/a | 0.00(7) |
| 1.11 | 0.88 | -450 | n/a | 0 |
| 1.16 | 0.52 | -340 | n/a | 0 |
| 1.40 | 1.4 | -770 | n/a | 0 |
| 1.56 | 0.89 | -320 | n/a | 0 |

[a] *Source:* Zheng *et al.* [239]. [b] *Source:* Shores *et al.* [188].
[c] We define the remanent moment here as the difference between the field-cooled and the zero-field cooled susceptibilies at 1.8 K. It is stated as a percentage of the minimum number of $Cu^{2+}$ spins on the Zn site, as given by $1 - x$.

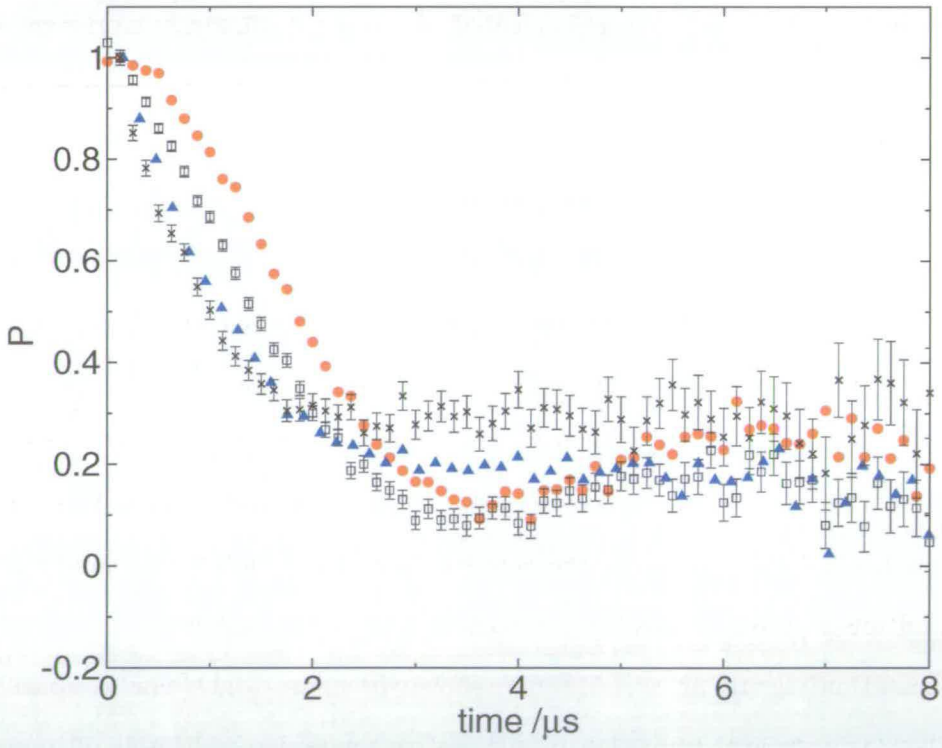


Figure 5.11: Muon spin relaxation at $\sim 1.5$ K for $x = 1.00(3)$ (filled red circles), $x = 0.65(2)$ (open black squares), $x = 0.51(2)$ (filled blue triangles) and $x = 0.33(2)$ (black crosses).

$x < 0.6$ this transition takes place between 3 and 6 K. For $x = 0.15$, (not shown here[2]) an oscillation indicative of a weak ordered moment emerges, reminiscent of the muon relaxation in the parent compound clinoatacamite [240].

Muons can also be used as local probes of the magnetic susceptibility, by measuring the muon Knight shift [184]. Ofer *et al.* [152] claim to have measured the bulk susceptibility this way, and conclude that the bulk of the system has a magnetic ground state. However, our data does not show any measurable shift in the Larmor frequency of the implanted muons away from $\omega_\mu = \gamma_\mu \mu_0 H_{\text{ext}}$. This issue still needs to be resolved.

In conclusion, the muon data shows that for $x \geq 0.66$ the magnetic ground state is dynamic, i.e. mainly paramagnetic. For $x < 0.66$ spin fluctuations are slower and more glass-like. No ordered moment is present until $x \approx 0.15$. A crucial question is now "Is the electronic ground state for $x = 1$ paramagnetic or *non*-magnetic, i.e. RVB-like?". On cooling the $x = 1$ sample no transitions are observed, but this does not exclude that at some temperature a transition occurs from paramagnetic to RVB. Exact diagonalisation studies of the Heisenberg Hamiltonian on the spin 1/2 kagomé antiferromagnet show that there is only a gradual onset of triplet states in a continuum of singlet states. This means that no discrete transition can be expected. The increasing relaxation rate at very low temperatures would suggest that rather than being bound into spin singlets, the spins are fluctuating. As was shown in previous sections, some disorder is present in the material. It is therefore possible that the material is inhomogeneous, containing regions of higher $Cu^{2+}$ concentration and connectivity. The muon relaxation could arise from a slowing down of the dynamics in these regions, while in other regions the spins are bound into singlet states and hence invisible to the muons. However, it could be argued that in this scenario an exponent $\alpha < 1$ could be expected. To resolve this issue the exponent found here, of $\alpha = 1.4$ should be explained. An inhomogeneous sample would also be the only explanation that no quantum phase

[2]Technically this is clinoatacamite because between $x = 0.15$ and $x = 0.3$ a structural transition occurs from rhombohedral to monoclinic symmetry, where the Zn site becomes angle distorted away from $O_h$.

transition is observed as a function of Zn stoichiometry $x$, while if we assume that the bulk of the spin in the $x = 1$ phase are bound in singlets, clearly one must have taken place somewhere between $x = 0$ and $x = 1$. So far the most straightforward explanation of the observed behaviour is that fluctuations remain throughout the system, and become gradually faster as the Zn stoichiometry and the temperature are increased. Some of this data was first analysed by Fabrice Bert and Philippe Mendels, and has been published in [131].

## 5.5 Heat capacity

Heat-capacity measurements were carried out using a Quantum Design PPMS system, on $\sim 5$ mg dye-pressed pellets of $Zn_xCu_{4-x}(OH)_6Cl_2$ powder samples with $x = 0.8$, 0.9, 1, 1.1 and 1.4 in 0 T and 9 T, and in 0 T only for $x = 0.5$. Temperatures down to 0.4 K were reached using the PPMS $He^3$ refrigerator. For one $x = 1.00(3)$ sample the heat capacity was in addition measured in 1,2,3,5 and 7 T. Here the low-temperature heat capacity, up to 30 K will be discussed. At higher temperatures there is no difference in heat capacity between fields up to 9 T, and the response is dominated by phonon contributions which could not be fitted well with the Debye heat capacity. This could be due to OH bending modes [23].

### 5.5.1 Zinc paratacamite with $0.5 \leq x \leq 1$.

Figure 5.12 presents the heat capacities of samples with $x = 0.8, 0.9$ and $x = 1$ in 0 and 9 T and for $x = 0.5$ in 0 T. The heat capacity of an $x = 1$ sample for intermediate fields is shown in figure 5.13. We could reproduce the heat capacity for $x = 1$ in 0, 1, 2, 3, 5, 7 and 9 T fields as reported by Helton *et al.* [89]. The shoulder gradually moves to higher temperatures while the total entropy below $\sim 24$ K remains constant.

In order to separate the field-dependent part of the heat capacity, for each Zn stoichiometry the difference was taken between the interpolated heat-capacity curves measured in different fields. The inset in figure 5.12 shows the difference between the

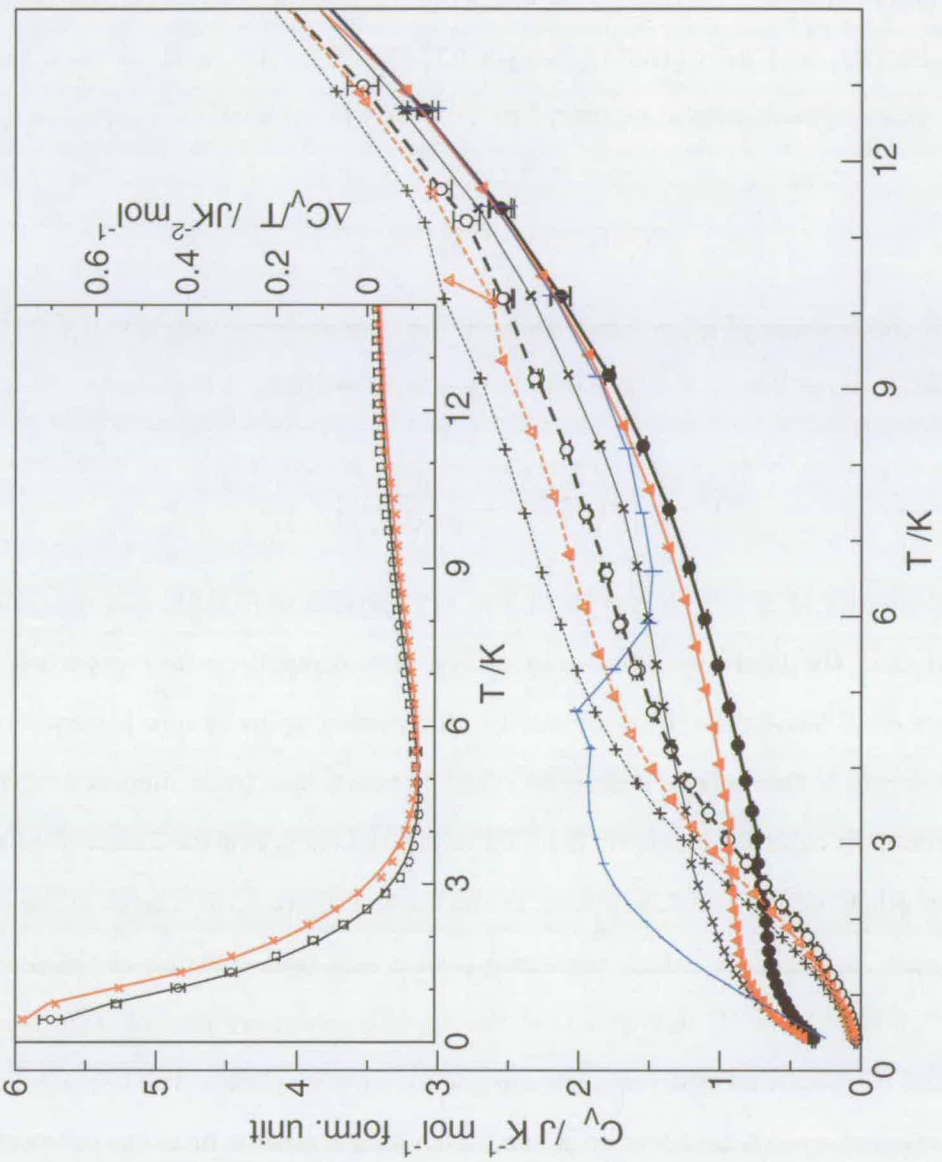


Figure 5.12: The heat capacity in 0 T ( lines and filled symbols) and 9 T (broken lines, open symbols) of samples with 0.5 (blue vertical lines), $x = 0.8$ ($\times$ and $+$), $x = 0.9$ (thick red $\triangle$) and $x = 1$ ($\circ$). The error bars are given for $x = 1$ only. The inset displays $\Delta C_V/T$ for the $x = 0.8$ (red $\times$) and $x = 1$ ($\circ$) and their respective fits, the red and black lines.

0 and 9 T heat capacity curves $\Delta C_V/T = [C_V(0\ \mathrm{T}) - C_V(9\ \mathrm{T})]/T$ for $x = 0.8$ (red crosses) and for $x = 1$ (black circles). To the eye, the field dependence of the heat capacity observed here is similar to the Schottky anomaly arising from defects in Zn-doped $Y_2BaNiO_5$ and $[Ni(C_2H_8N_2)_2(NO_2)]ClO_4$ (NENP) [162], and we have applied a similar analysis as described in [162]. $\Delta C_V/T$ was fitted with an expression of the form

$$f[C_V^S(\Delta E_1) - C_V^S(\Delta E_2)]/T, \tag{5.2}$$

where $f$ is the fraction of spins $S$ per unit cell (or their spectral weight). $C_V^{S=1/2}(\Delta E)$ is the heat capacity from a $S = 1/2$ spin with a level splitting $\Delta E$ given by

$$C_V^{S=1/2} = \left(\frac{\Delta E}{\tau}\right)^2 \frac{\exp(\Delta E/\tau)}{(\exp(\Delta E/\tau) + 1)^2}. \tag{5.3}$$

The heat capacity of $S = 1$ (triplet) and $S = 3/2$ systems were evaluated numerically. We found that the field-dependent part of the heat capacity is best modelled by a small number of zero-field split doublets, i.e. interacting spins or quasi particles with a spin $S = 1/2$. The energy difference ($\Delta E$) between the levels increases with the application of an external magnetic field, following the energy of the Zeeman splitting, $E_{\mathrm{Zeeman}} = g\mu_B H$ with $g = 2.2$, as shown in the inset of figure 5.16. The shoulder in the heat capacity in zero-field, which corresponds to a zero-field splitting of the doublets of $\Delta E \sim 1.7$ K (0.15 meV) indicates that the levels involved are part of an interacting system, and cannot be ascribed to a paramagnetic impurity phase. The best agreement with experiment was obtained when a small Gaussian spread $\sigma$ in level splittings $\Delta E$ was taken into account, indicated as the error bars in the inset of figure 5.14.

For the $x = 1$ sample all 21 combinations of magnetic fields were fitted using formula 5.2. For example, figure 5.14 shows the difference between the heat capacity in 1 T and in 3 T (circles), and 1 T and 9 T (squares) for an $x = 1$ sample. The lines through the data points are the fit results for $S = 1/2$ where equation 5.2 could be fitted with a single value for $f$ and for $\Delta E(H = 1\ \mathrm{T})$ for both curves. In the

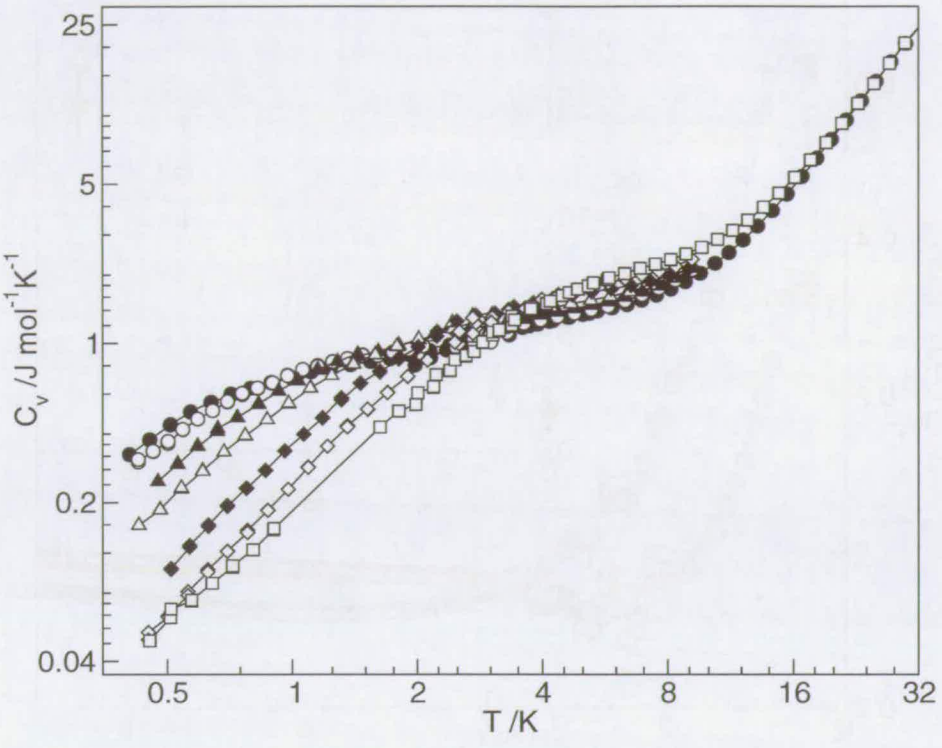


Figure 5.13: The heat capacity of $x = 1$ zinc paratacamite on a log-log scale fields of 0 T (filled circles), 1 T (open circles), 2 T (filled triangles), 3 T (open triangles), 5 T (filled diamonds), 7 T (open diamonds) and 9 T (open squares).

case of $S = 1$ the agreement was less good, and for $S = 3/2$ the fit results for the $C_V(H = 1\text{ T}) - C_V(H = 3\text{ T})$ curve (the fit is the broken line through this curve) for $f$ and $\Delta E(H = 1\text{ T})$ could not be used to fit the $C_V(H = 1\text{ T}) - C_V(H = 9\text{ T})$ curve. Even the best fit with $S = 3/2$ spins where all parameters except the spin were left free, shown in figure 5.14 as the broken line through the $C_V(H = 1\text{ T}) - C_V(H = 9\text{ T})$ data points, is poor. The lines through the data points in the inset of figures 5.12 and 5.14 are the fit results for $x = 0.8$ and $x = 1$ respectively. We find that $f = 0.21(1), 0.22(1)$ and $0.19(1)$ for $x = 0.8, 0.9$ and $1.0$ respectively. For $x = 1$, with three $Cu^{2+}$ ions per unit cell, this accounts on average for $6.3(3)\%$ of all $Cu^{2+}$.

As a result of the spin gap the heat capacity is expected to show a shoulder at $\sim J/10$ corresponding to the population of the lowest magnetic ($S_{\text{tot}} = 1$) levels [190, 16, 137]. In our data a shoulder is evident in zero field. However, a model with a triplet of $S = 1$ levels results in a slightly poorer fit with the data. That multiplets with $S_{\text{tot}} > 1$ are

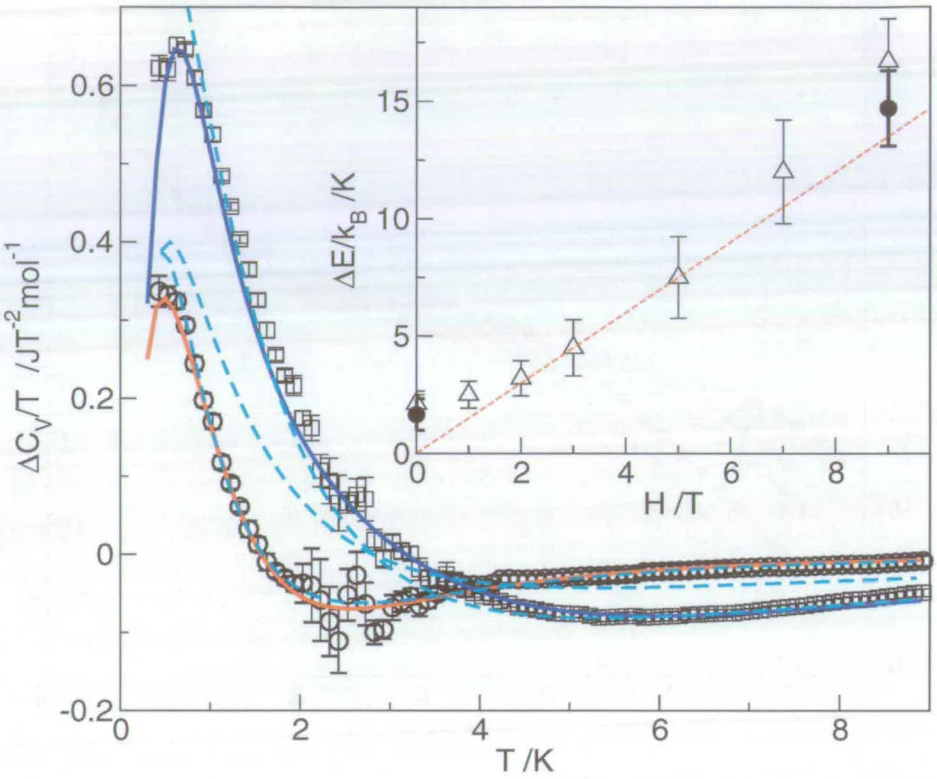


Figure 5.14: Two of the 21 heat-capacity differences, $[C_V(1\mathrm{T}) - C_V(3\mathrm{T})]/\mathrm{T}$ (circles) and $[C_V(1\mathrm{T}) - C_V(9\mathrm{T})]/\mathrm{T}$ (squares) on a $C_V/T$ scale. The red and blue lines through the data points are the mutually consistent fits with formula 5.2 using $S = 1/2$ spins, yielding $f \approx 0.19$. The broken lines give less successful fits with $S = 3/2$ multiplets. The inset shows the obtained $\Delta E$ against $H$ for two samples. The broken red line in the inset gives the Zeeman splitting with $g = 2.2$.

involved [190] can be ruled out from the fits with $S = 3/2$ heat capacities as shown in figure 5.14. From the field dependence of the shoulder in our data, it can also be ruled out that the corresponding zero-field splitting is a singlet-triplet gap; if the ground state were non-magnetic, then the application of a magnetic field should shift some magnetic levels to lower energies, until a quantum-critical phase transition to a magnetic ground state is reached. In the present data all the spectral weight shifts to higher energies with the application of a magnetic field, as is also evident in the inset of figure 5.16. Hence, we conclude that the lowest energy level of the system must correspond to a magnetic state, i.e. either $S_{\mathrm{tot}} > 0$ or $S_{\mathrm{tot}}$ is not a good quantum number. In samples with $x = 0.8$ and $x = 0.9$ no quantum-critical phase transition is observed, as would be indicated by a competition of phases or a down-shift of part of the spectral weight.

Rather, similar behaviour as in $x = 1$ is observed. Hence, the magnetic ground state in these samples is essentially identical to the ground state in the $x = 1$ phase, which is also reflected in the total entropy per spin recovered at 24 K, as shown in table 5.4. The only difference, as made evident by the muon results [131] and the appearance of a magnetic hysteresis, is that the spin fluctuations gradually slow down with increased connectivity of the magnetic lattice.

Table 5.4: The estimated number of antisite spins ($f$), the corresponding $Cu^{2+}$ occupancy of the kagomé lattice ($c = 4 - x - f$), the total entropy from the antisite spins ($\mathcal{S}_f$), the measured total entropy ($\mathcal{S}_{\text{tot}}$) up to 24 K, the percentage of the entropy recovered per spin and the percentage of the entropy recovered per spin in the kagomé lattice. The entropy is given in units of $R = N_a k_B = 8.314$ $JK^{-1}mole^{-1}$ formula unit.

| $x$ | $f$ | $c$ | $\mathcal{S}_f\ /R$ | $\mathcal{S}_{\text{tot}}\ /R$ | $\frac{\mathcal{S}_{\text{tot}}}{(4-x)\ln(2)}$ | $\frac{\mathcal{S}_{\text{tot}}-\mathcal{S}_f}{g\ln(2)}$ |
|---|---|---|---|---|---|---|
| $\pm 0.02$ | $\pm 0.010$ | $(4-x-f)$ | $(f\ln(2))$ | @$T = 24$ K | /% | /% |
| 0.51 | 0.51(2)[a] | 3.0 | 0.346(8) | 1.061(12) | 43.9(8) | 34.4(11) |
| 0.80 | 0.210 | 2.97(3) | 0.146(6) | 0.993(11) | 44.7(8) | 41.1(13) |
| 0.90 | 0.219 | 2.87(3) | 0.151(6) | 0.959(9) | 44.8(7) | 40.6(13) |
| 1.00 | 0.189 | 2.81(3) | 0.131(7) | 0.933(9) | 44.8(7) | 41.1(14) |
| 1.10[b] | 0.183 | 2.74(3) | 0.127(7) | 0.933(9) | 46.1(7) | 42.4(14) |
| 1.40[b] | 0.153 | 2.44(3) | 0.106(6) | 0.877(9) | 48.9(7) | 45.6(14) |

[a] Here $f$ was not measured experimentally, it was assumed that $c = 3.0$ (full occupancy) and hence $f = x$.
[b] This data is discussed in the next section.

From the magnetic susceptibility of samples with $0 \leq x \leq 1$ as published in [188] and also shown in table 5.3, it is clear that the exchange interaction between the $Cu^{2+}$ spins on the interplane Zn sites, and between the $Cu^{2+}$ spins on the Zn sites and the spins kagomé lattice is much weaker than the exchange interactions within the kagomé lattice. This suggest that the fraction $f$ of zero-field split doublets, which models the field-dependence in the heat capacity for $0.8 \leq x \leq 1$, are weakly-coupled $S = 1/2$ spins from $Cu^{2+}$ ions residing on inter-plane Zn sites (antisite spins) as also suggested in [166]. For $x = 1$ an identical fraction $f$ of $Zn^{2+}$ ions must occupy Cu sites on the kagomé lattice. Once $f$ is known for each $x$ ($f_x$) the $Cu^{2+}$ coverage $c$ of the three Cu sites per unit cell is given by $c = 4 - x - f_x$. An important assumption in our argument is that the heat capacity of a slightly diamagnetically doped kagomé lattice

is field independent, which is reasonable as long as $g\mu_B H \ll \theta_w$ [165, 190]. For the deuterated $x = 1$ sample of the neutron-diffraction measurements it follows that the antisite disorder is 6.3(3)% in $Cu^{2+}$ or 19.0(9)% in $Zn^{2+}$. By treating the zero-field splitting of the antisite spins as the Weiss temperature, an estimate for the susceptibility of the antisite spins $\chi_A \approx 0.58f/(T+1.7)$ for $T \gg 1.7$ K is obtained. If $\chi_A$ is subtracted from the total susceptibility for $x = 1$, the susceptibility corresponding to the kagomé layers levels out to $1.1(1) \cdot 10^{-3}$ emu $mol^{-1}$ $Cu^{2+}$ for $20 < T < 100$ K, as shown in figure 5.15. The correction of the susceptibility for contribution of the antisite spins also leads to a considerably larger estimate of the Weiss temperature for the kagomé lattice, of $\sim$ 500 to 600 K.

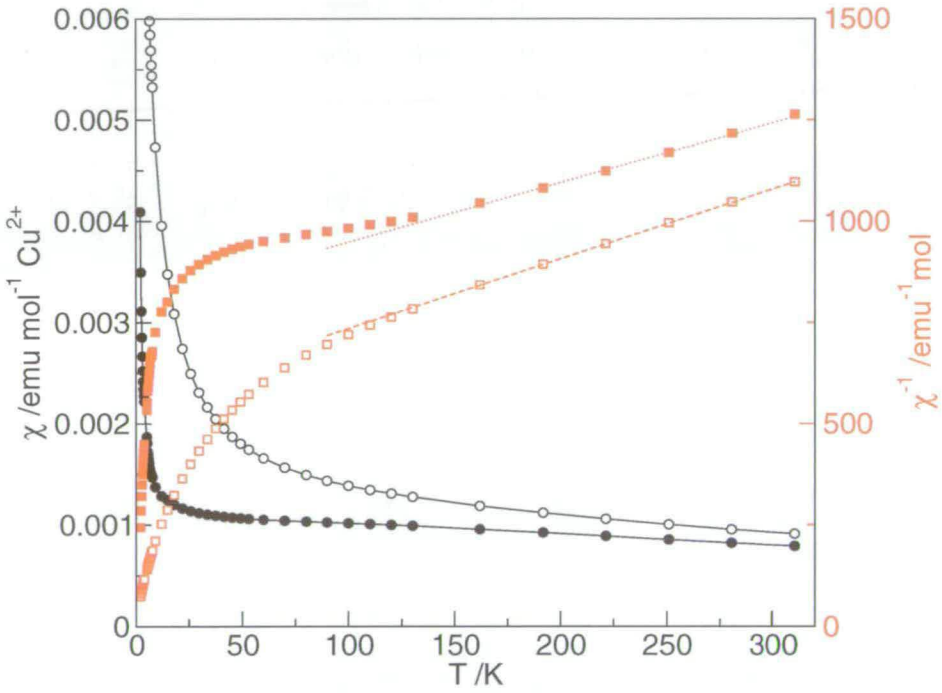


Figure 5.15: The magnetic susceptibility (open circles), the susceptibility corrected for the antisite spins (filled) circles and the corresponding inverse susceptibilities (red) against the right-hand axis.

Comparing the heat-capacity data of several $x = 1$ samples, all synthesised at a temperature of 484 K, an average antisite disorder of $\sim$ 6.0(6)% in $Cu^{2+}$ is derived. From a simple counting argument it can be seen that the chemical potential $\mu =$

$E(Zn^{2+}$ on Zn site$) - E(Cu^{2+}$ on Zn site$)$ behind the $Cu^{2+}/Zn^{2+}$ partitioning can be deduced using [3]

$$1 - \langle f \rangle = \frac{\exp(-\mu/k_B T)}{\exp(-\mu/k_B T) + 3}. \tag{5.4}$$

For samples synthesised at 484 K it was found that $f \simeq 0.18$, from which it can be estimated that $\mu \approx 1250$ K. This is a plausible value given that most likely the Zn site becomes locally slightly angle-distorted, if occupied by an otherwise orbitally degenerate $Cu^{2+}$ ion. This distortion will lower the energy difference between the Cu and the Zn sites. It would also introduce an additional energy scale for the orbital ordering of the $Cu^{2+}$ ions on the Zn site, which may explain the lattice fluctuations below 125 K observed in $^{63}Cu$ and $^{35}Cl$ NMR [95]. The results for $x = 0.8$ and $x = 0.9$ are given in table 5.4. The Cu sites on the kagomé lattice are energetically favoured by the $Cu^{2+}$ ions, and there is only a slow increase of the $Cu^{2+}$ occupancy on the Zn sites until the $Cu^{2+}$ occupancy of the kagomé lattice ($c$ in table 5.4) is almost complete. We observe that from a structural point of view samples with $0.8 \leq x \leq 1$ model the kagomé antiferromagnet equally well. This is consistent with our observation that no quantum-critical phase transition occurs within this range of Zn stoichiometries.

Table 5.4 also compares the total entropy $\mathcal{S}(T) = \int_{t=0}^{T} \frac{C_V(t)}{t} dt$ in all samples at $T = 24$ K. This temperature was chosen to be above the point where no relative changes in $\mathcal{S}(T)$ between samples were observed, and at a temperature where the contribution from structural degrees of freedom can still be expected to be small. On average 45% of the total magnetic entropy given by $(4-x)R\ln(2)$ is recovered at 24 K. This value goes down slowly as the $Cu^{2+}$ contents and the connectivity of the lattice increase. The last column in table 5.4 gives the entropy which remains when the total entropy from the antisite spins is subtracted, as a percentage of the remaining $Cu^{2+}$ spins which must reside on the kagomé lattice. The numbers in this column show a similar trend as the previous column.

[3] The entropy of the system is constant for a given $x$, hence it is not necessary to find the minimum of the Helmholtz free energy in the present situation.

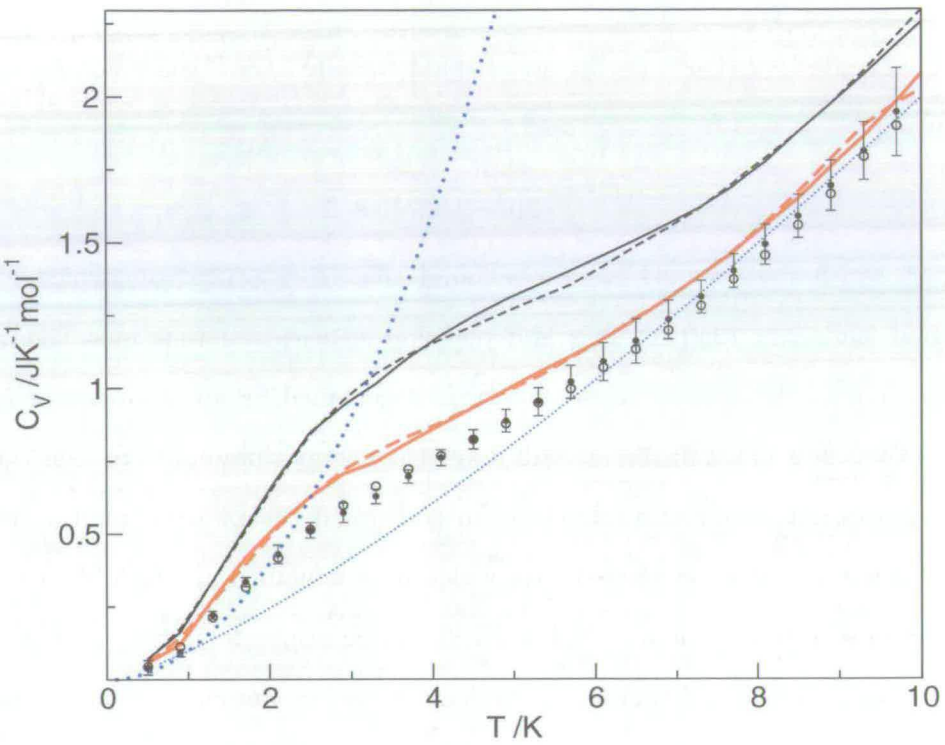


Figure 5.16: The field-independent part of the heat capacity as obtained from the 0 T (lines or filled circles) and 9 T (broken line or open circles) data of samples with $x = 0.8$ (black lines), $x = 0.9$ (thick red lines), $x = 1$ (black circles with error bars). The dotted blue lines give fits to the corrected heat capacity for $x = 1$ with $\gamma T^{\alpha}$ with $\alpha = 1.3$ and 1.7.

The heat capacity of the kagomé lattice can be estimated by subtracting the heat capacity from the $Cu^{2+}$ spins on the Zn sites. The result for the data with $0.8 \leq x \leq 1$ is shown in figure 5.16. For all $x$, the curves obtained from the 0 and 9 T data are identical within the experimental error. This is not an additional proof of the validity of our model, but follows from the quality of the fit as described in the previous paragraphs. This part of the heat capacity most likely corresponds to weakly-coupled kagomé layers. In particular the shoulder in the heat capacities as shown in figure 5.16, which corresponds to a peak in $C_V/T = d\mathcal{S}/dT$ around 2.5 K, is likely due to the entropy release when the fluctuations in neighbouring kagomé layers decouple. For larger $x$ this peak becomes smaller, and the remaining entropy approaches an exponential temperature dependence, $0.1T^{\alpha}$ $JK^{-1}mol^{-1}$ form. unit, with $\alpha = 1.3(1)$

up to 10 K. However, it cannot be ruled out that at 10 K phonon and OH-bending modes already play a role.

### 5.5.2 Zinc paratacamite with $1 < x < 1.4$.

In figure 5.17 the heat capacity divided by temperature ($C_V/T$) of samples with $x = 1.1$ and 1.4 is given, along with the $x = 1$ data for comparison. The $x = 1.1$ curve is identical to the $x = 1$ curve, while the $x = 1.4$ curve can be scaled to overlap with the other two curves. Nevertheless the analysis as carried out for $x < 1$ has been applied here too, and the results are given in table 5.4. Not surprisingly, the heat capacity which can not be accounted for by the antisite spins is also identical to the heat capacity remaining for $x = 1$. It could be expected that the further reduction of the $Cu^{2+}$ occupancy of the kagomé layers should result in a further reduction of the peak in $C_V/T$ at 2.5 K. This does not happen, which suggests that samples with $x > 1$ are not pure. Though some extra dilution of the lattice is likely, most of the extra zinc may be present as a non-crystalline impurity phase.

## 5.6 Transport properties and doping

In general first row transition metal compounds are insulators. As a rule of thumb it can be said that for those with a bright colour there is no need to measure the transport properties, since there will not be any significant conductivity. Compounds which are black or with a very dark shade on the other hand, often do have a significant conductivity. At the other end of the spectrum is the shine of metallic compounds, which can be attributed to the dielectric properties of good conductors. Zinc paratacamite is bright green/blue, regardless of the Zn stoichiometry. Nevertheless, the conductivity of a small pellet-pressed powder sample with $x = 1$ has been measured between 1.8 K and 300 K in a Quantum Design PPMS. This measurement confirmed that the resistivity $\rho > 10$ M$\Omega$cm. It would be interesting to see whether the material can be doped with ions which take another electron from the $Cu^{2+}$ ions, or donate an electron to the $Cu^{2+}$

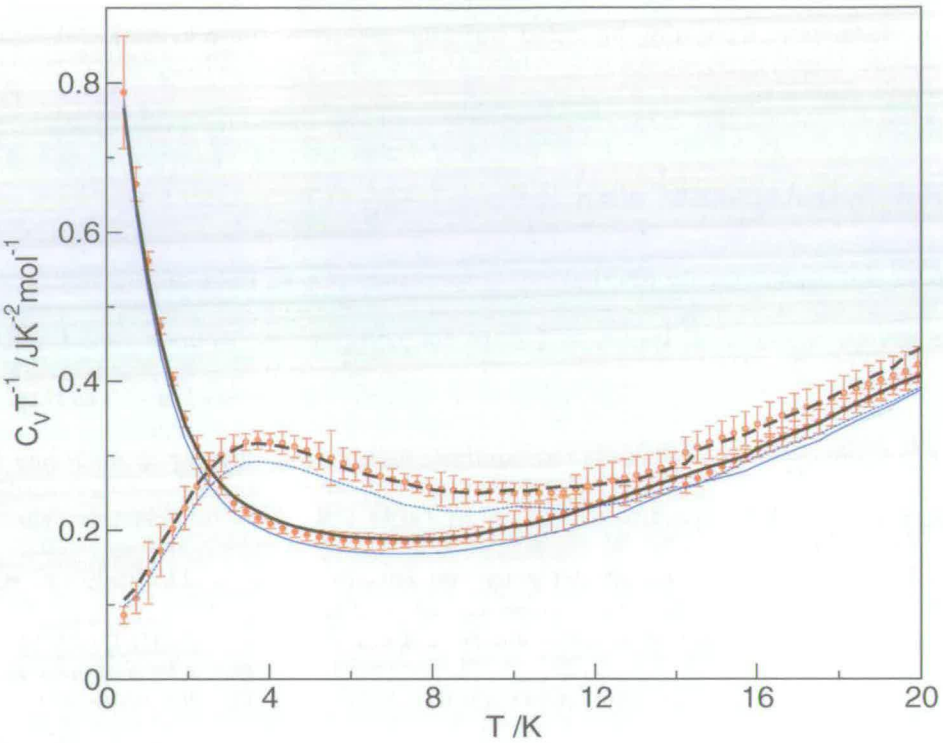


Figure 5.17: $C_V/T = dS/dT$ in 0 T (full lines and filled symbols) and 9 T (broken lines and open symbols) of samples with $x = 1$ (red circles), $x = 1.1$ (thick black lines) and $x = 1.4$ (thin blue lines).

band. In theory the sample should in that case become conducting, and it would be very interesting to study the magnetic ground state in this situation.

## 5.7 Inelastic and polarised neutron scattering

Inelastic neutron diffraction allows for a direct measurements of the time and $q$ dependent excitation spectrum $S(q, \omega)$, typically with $\omega > 5 \cdot 10^{11}$ s$^{-1}$. A singlet-triplet or spin gap should be evident as a gap in the magnetic part of the neutron excitation spectrum. The first inelastic neutron scattering measurements on the $x = 1$ phase of zinc paratacamite were carried out at the pulsed-neutron time-of-flight instrument MARI at the ISIS facility UK. 12 g of a deuterated powder sample was used and spectra were taken with incident neutron energies of 8 meV and 50 meV. Data were

collected for 24 hours at each energy, which proved to be too short to see any magnetic excitations. At OSIRIS, ISIS an inelastic neutron spectrum was measured with 3 meV neutrons probing excitations between 0.2 meV and 2 meV. Also in this region the inelastic neutron spectrum was featureless.

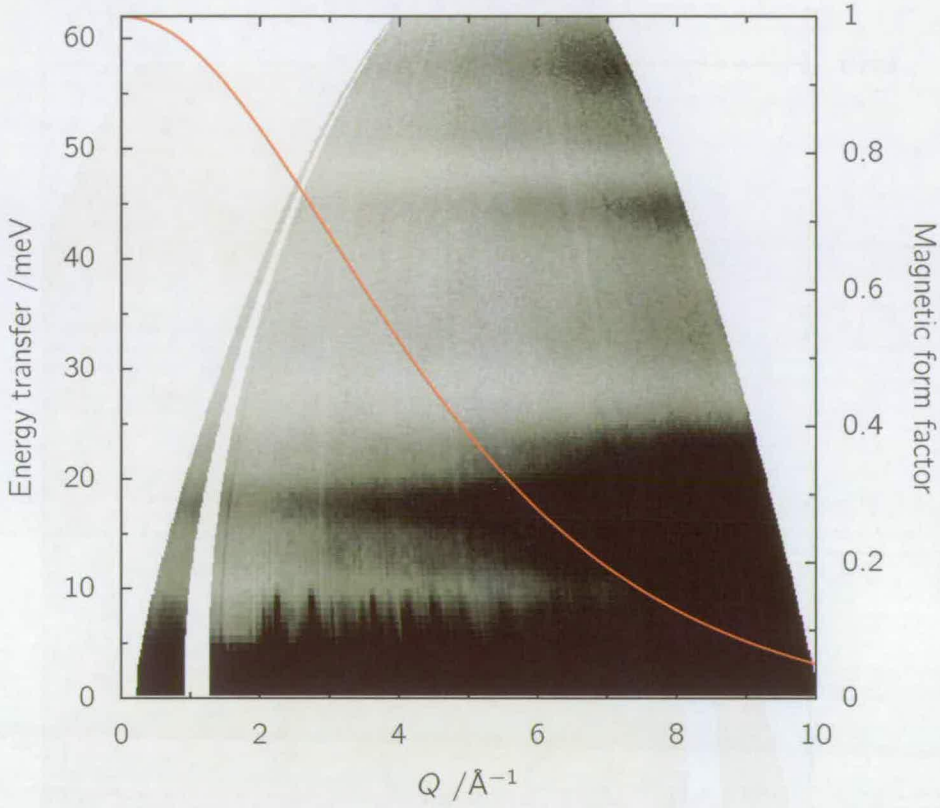


Figure 5.18: Inelastic neutron spectrum from a 20 g powder sample of $ZnCu_3(OD)_6Cl_2$ at the IN4 neutron spectrometer with 69.35 meV (1.086 Å) neutrons. The sample temperature is 2 K. The right axis corresponds to the red line, which gives the neutron magnetic form factor for $Cu^{2+}$, obtained using the constants from [38]. The upper marks the Brillouin zone boundaries along the a axis. The magnetic Brillouin zone is twice the crystallographic zone along this axis.

Further spectra were obtained by Ross Stewart, at the direct geometry time-of-flight spectrometer IN4 at the Institute Laue Langevin, France, using 20 g of deuterated sample. The spectra obtained with incident neutron energy $\hbar\omega = 69.35$ meV at a temperature of 2.2 K is shown in figure 5.18. The horizontal features observable here all get weaker for lower $q$ following the phonon form factor. No distinct features are visible at low wave-vector transfer, while the magnetic form factor for $Cu^{2+}$ ions (from [38])

which is also shown here, remains relatively large for most of the $q$ range probed with 69.35 meV neutrons.

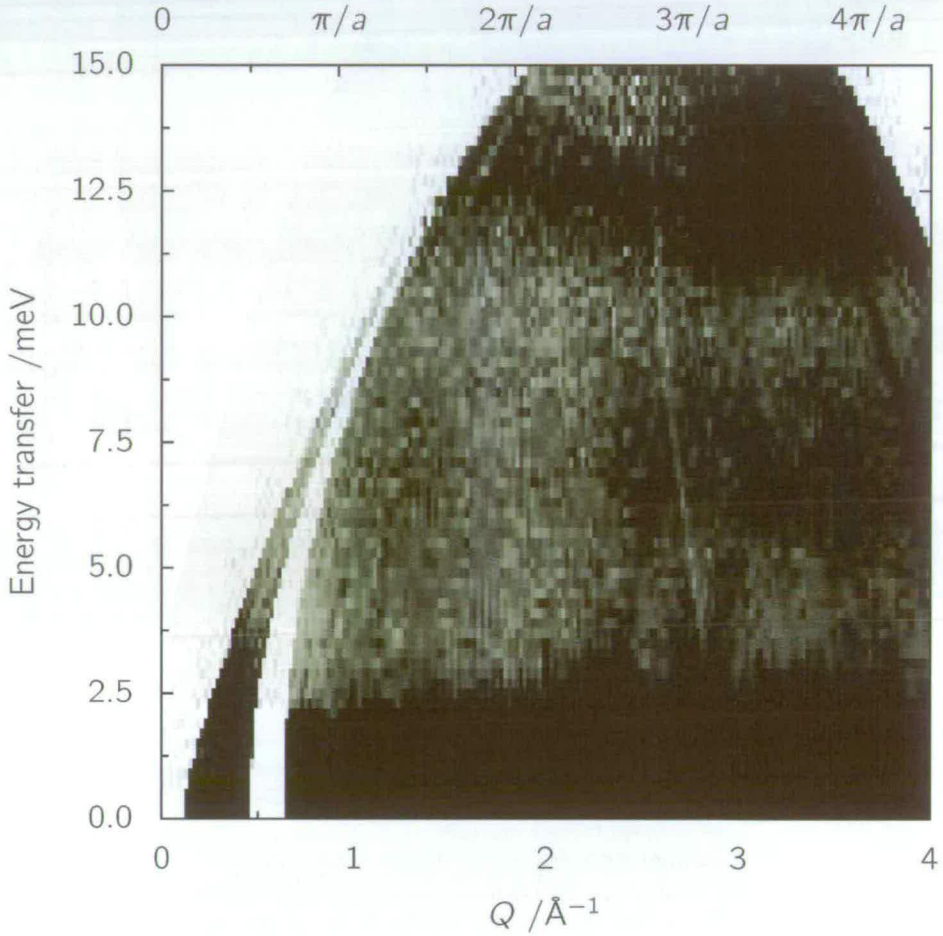


Figure 5.19: Inelastic neutron spectrum from a 20 g powder sample of $ZnCu_3(OD)_6Cl_2$ at the IN4 neutron spectrometer with 17.21 meV (2.18 Å) neutrons. The sample temperature is 2 K.

The spectra obtained with incident neutrons of 17.21 meV at 2 K (figure 5.19) and at 60 K (figure 5.20) show a very weak feature around $q = 1.2$ Å and $\hbar\omega = 7$ meV. The intensity of this feature does not change with temperature while the intensity of the phonon modes at higher $q$ clearly increases with temperature. From figure 5.21 it is can be seen that the feature around $q = 1.2$ Å$^{-1}$ becomes more distinguished at

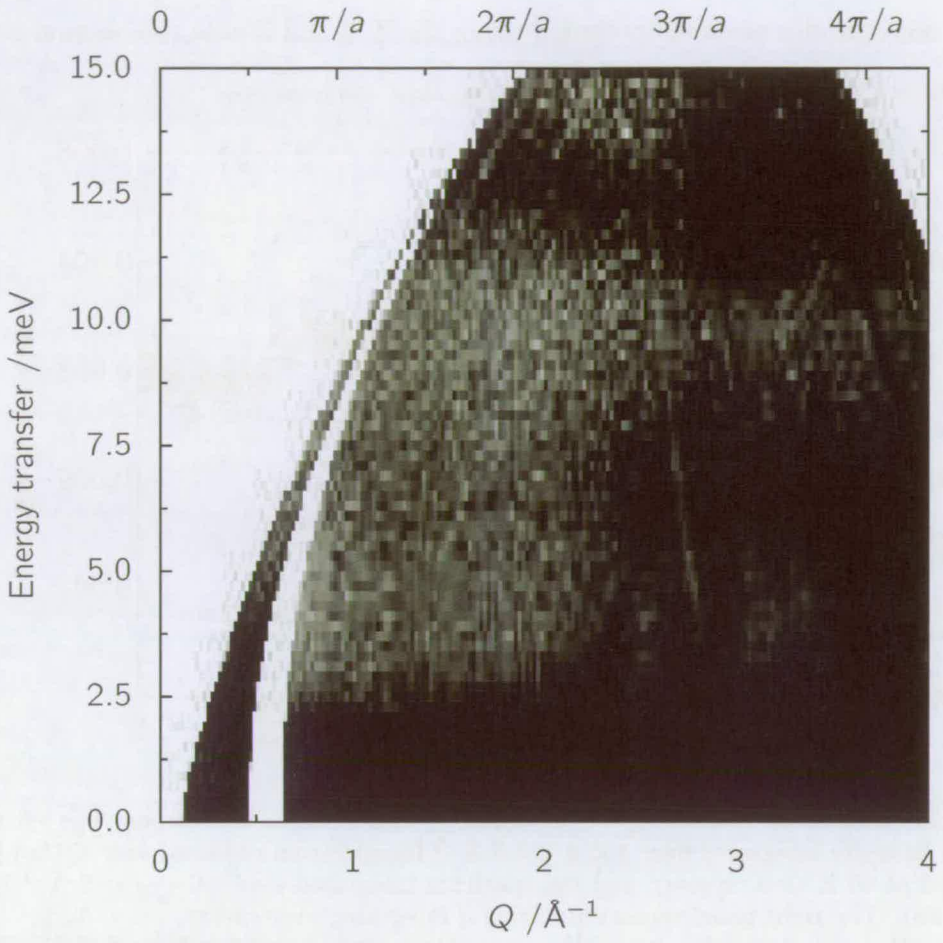


Figure 5.20: Inelastic neutron spectrum from a 20 g powder sample of $ZnCu_3(OD)_6Cl_2$ at the IN4 neutron spectrometer with 17.21 meV (2.18 Å) neutrons. The sample temperature is 60 K

low temperatures [4]. There is a maximum around 7 meV and the FWHM is at least 1.5 meV. However, below 4 meV the intensity is dominated by the inelastic line, and it is not immediately clear whether or not the spectrum is gapped.

That this feature corresponds to the magnetic density of states was confirmed in a polarisation-resolved diffuse neutron scattering experiment at the cold-neutron spectrometer D7, at the ILL. This instrument allows for $XYZ$-polarisation analysis of the scattered neutrons. The nuclear coherent, spin incoherent, isotope incoherent and magnetic scattering cross sections can then be separated from each other by analysing the

[4]The neutron scattering cross section has in this experiment not been calibrated. The intensity scale given in figure 5.21 was obtained by comparison of the energy integrated spectrum with the energy integrated spectra of the same sample obtained at D7. Hence, the values given in 5.21 are only approximate

spin flip/non spin flip neutrons polarised along the X,Y and Z axes (see section 3.1.3). This enables a quantitative analysis of the magnetic correlations.

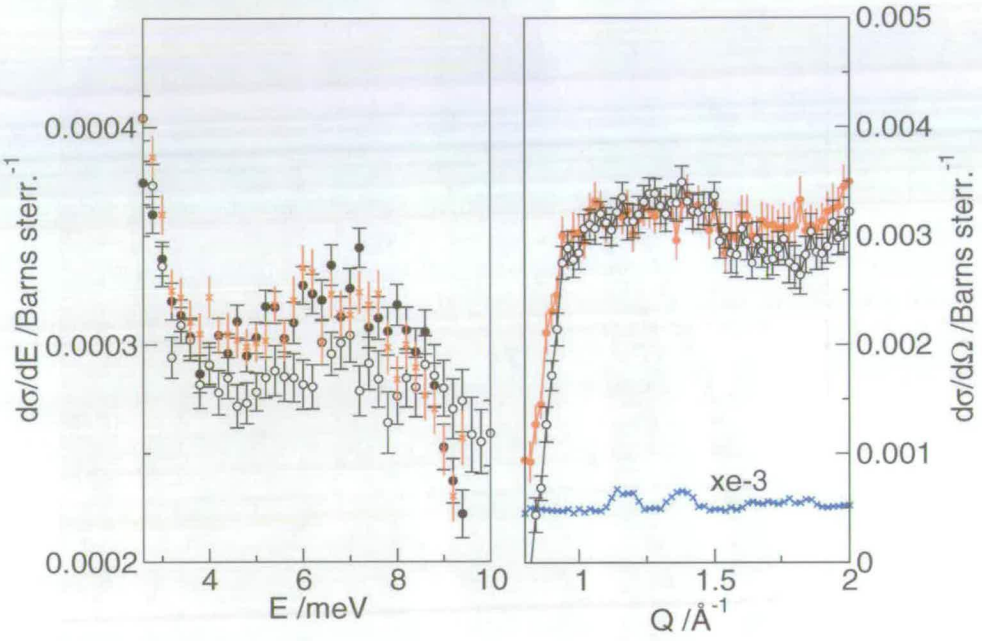


Figure 5.21: Cuts of the inelastic spectrum obtained with 17.21 meV neutrons. The left panel shows the intensity integrated over $1 < q < 1.5$ Å$^{-1}$ for spectrum obtained at 2 K (full black circles) and at 60 K (red crosses), and the spectrum integrated over $1.6 < q < 2$ Å$^{-1}$ (open black circles). The right panel shows cuts along $q$ integrated over energy, $-1 < \hbar\omega < 1$ meV (blue line with crosses), $6 < \hbar\omega < 8$ meV at 2 K (black circles) and $6 < \hbar\omega < 8$ meV at 60 K (full red circles).

A 20 g powder sample of $x = 1$ zinc paratacamite was mounted in an Al can inside a dilution refrigerator with a low pressure of $^4$He transfer gas to optimise thermal contact between the powder sample and the cryostat. Polarised neutrons with an energy of 8.51 meV were used. The diffracted intensity in the magnetic scattering channel was insufficient for time-of-flight analysis, and for this reason only the approximate [5] energy-integrated magnetic structure factor was obtained. Data was taken for 24 h at each of the temperatures 0.5, 2, 4, 10 and 60 K. Below 4 K the magnetic scattering signal seemed to vanish at all $q$, and even become slightly negative at low $q$, but this was due to condensation of the $^4$He transfer gas in the sample can below 4 K. There is no

[5] In principle the energy of the diffracted neutrons is required to calculate the actual wave-vector transfer $Q$ at a given diffraction angle. Hence, giving up in energy resolution comes with the additional cost of a (slight) loss in $q$ resolution.

observable change with temperature in the data taken at 4, 10 and 60 K. To improve the statistics the data taken at 4, 10 and 60 K have been combined. The result, shown in figure 5.22, corresponds well with the spectra obtained at IN4 with 17.21 meV neutrons, and confirms that the weak feature around 7 meV corresponds to magnetic excitations. From comparison of figures 5.21(right) and 5.22 it is clear that the magnetic signal at energy transfers above 4 meV make up only a very small part of the total magnetic scattering cross section. Hence, it can be ruled out that this feature corresponds with a singlet-triplet gap.

After [194, 123] and [193] the powder-averaged magnetic scattering cross section is given by

$$\left(\frac{d\sigma}{d\Omega}\right)_{\text{mag}} = \frac{2}{3}(\gamma r_0)^2 \int_0^\infty S(q,\omega) d(\hbar\omega) = \frac{2}{3}(\gamma r_0)^2 \left(\tfrac{1}{2} g_J \mu_B f(q)\right)^2 J(J+1) \sum_N \langle \hat{S}_0 \hat{S}_{R_N} \rangle e^{iqR_N}$$

where $\gamma r_0 = \frac{\gamma e^2}{m_e} = 5.39 \cdot 10^{-15}$ m is the strength of the dipolar interaction between the neutron and the electron, and $\langle \hat{S}_0 \hat{S}_{R_N} \rangle$ is the *normalised* instantaneous spin-spin correlation function. In the case of short-range correlations this can be made explicit following [194].

$$\left(\frac{d\sigma}{d\Omega}\right)_{\text{mag}} = 0.0496 \left(g_J f(q)\right)^2 J(J+1) \left[1 + \langle \hat{S}_0 \hat{S}_1 \rangle N_1 \frac{\sin(qR_1)}{qR_1} + \ldots\right] \tag{5.5}$$

where the sum is over near-neighbour shells with coordination number $N_n$ and distance $R_n$ from $S_0$. This function could be made to fit to the data approximately using only one shell of the nearest neighbour spins within the kagomé plane, at a distance of 3.415 Å, yielding a very small nearest-neighbour correlation coefficient $\langle \hat{S}_0 \hat{S}_1 \rangle = -0.025$. The result is shown as the thick line in figure 5.22. Inclusion of further neighbours did not improve the quality of the fit. The effective spin magnitude corresponding to the magnetic scattering cross section found here is $S = 0.1$, 20% of the $S = 1/2$ moment.

In conclusion, the magnetic diffuse scattering at temperatures $\ll \theta_w$ reveals only weak near-neighbour correlations, characteristic of a liquid.

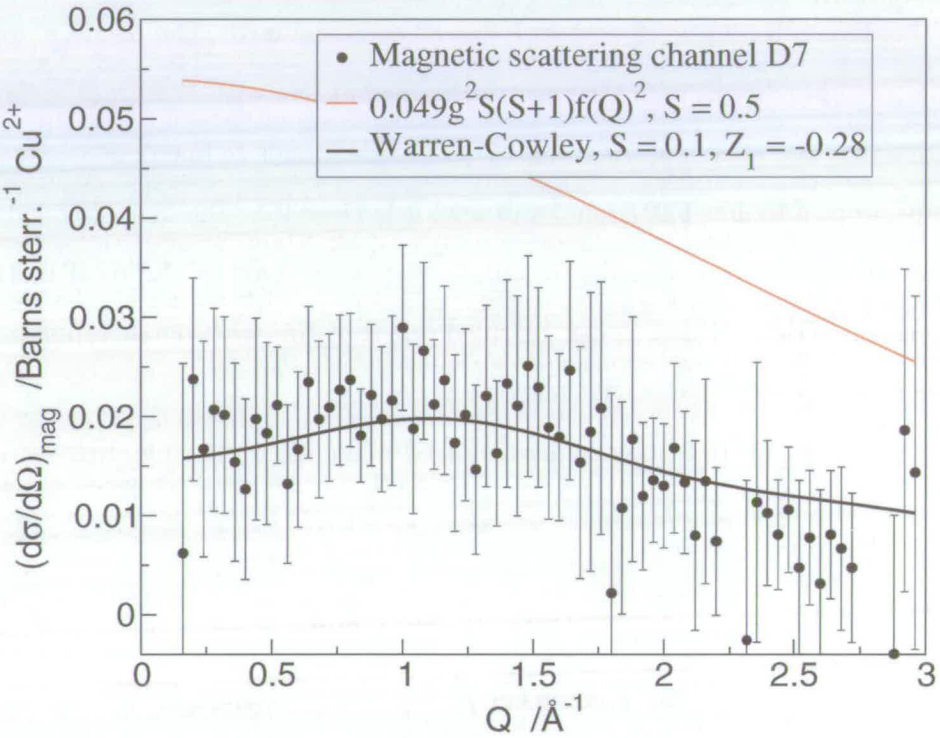


Figure 5.22: The instantaneous magnetic structure factor, averaged over data taken at 4, 10 and 60 K. The thin red line shows the total $Cu^{2+}$ magnetic form factor. The thick black line gives the fit with equation 5.5 as discussed in the text.

The inelastic neutron spectra measured at IN4 show that the magnetic scattering is not entirely semi elastic. From the energy profile with $1.0 < q < 1.5$ Å, as shown in figure 5.21, it is clear that at least part of the spatial correlations occur in a broad peak with an energy offset of $\sim 7$ meV. This excitation is not necessarily a singlet-triplet gap. In real liquids, broad phonon modes appear alongside the quasi-elastic scattering, and with increasing glassiness the quasi-elastic line becomes smaller [236]. For *classical* spin-liquids (i.e. cooperative paramagnets) and spin-glasses we could expect a similar behaviour. If the magnetic ground state in the $x = 1$ phase is cooperative paramagnetic, i.e. a collection of fast-fluctuating localised $S = 1/2$ spins, the quasi-elastically scattered neutron intensity in the magnetic channel should be strong, where the uniform magnetic susceptibility $\chi(T)$ can be calculated from $S_{q=0,\omega=0}(T)$ [123]. The other possibility is

that the magnetic form factor vanishes entirely at $\omega = 0$, corresponding with a bulk susceptibility $\chi_{\text{bulk}} = 0$. This would mean that the ground state is of spin-singlet character, a quantum spin liquid. The lowest elementary excitations probed by neutrons are in this case thought to be the formation of pairs of deconfined spinons [104]. These are two delocalised $S = 1/2$ excitations created at an energy corresponding to the singlet-triplet (or spin) gap. Another measurement at D7 would be needed, taking data over long periods of time at low temperature with time-of-flight analysis, to measure the quasi-elastic line shape as has previously done for $GeCuO_3$ [192]. However, the first priority in a future neutron experiment would be to measure the inelastic spectrum of an $x = 0.8$ sample. The heat capacity data suggests that such a sample would model the $S = 1/2$ kagomé antiferromagnet equally well above the energy scale where the $Cu^{2+}$ spins on the interplane Zn site start to play a role, which is, the entire energy range probed with neutrons in zero external magnetic field. The neutron data as shown here suggests that the inelastic features for an $x = 0.8$ sample are stronger, and therefore more easy to study.

Helton *et al.* [89] have measured the inelastic neutron spectrum at low energy/$Q$ in 0 and 13.5 Tesla. They find a single weakly-dispersive band at an energy corresponding to the Zeeman splitting, and with an intensity corresponding to $\sim$ 3% of the $Cu^{2+}$ spins. In zero field no band was observed but it could be hidden in the quasi elastic line. This field-dependent band in the neutron spectrum must be of the same origin as the field dependence of the heat capacity. Helton *et al.* interpret this feature as evidence of deconfined spinons, and point out that the dispersion of this band does not follow the neutron magnetic form factor for the $Cu^{2+}$ ion. We suggest that this band corresponds to the up/down level splitting of the $Cu^{2+}$ spins on the interplane Zn sites due to antisite disorder. In that case the dispersion arising from these $Cu^{2+}$ spins does not need to follow the neutron magnetic $Cu^{2+}$ form-factor, as it should for paramagnetic spins, since at low temperatures the $Cu^{2+}$ spins randomly distributed over the Zn sites are ferromagnetically ordered in a field of 13.5 Tesla.

## 5.8 Discussion

Remarkably, the inelastic neutron spectrum of clinoatacamite [226] shows a similar, but much more intense, feature around $q \sim 1.2$ Å$^{-1}$ and $\hbar\omega \sim 7$ meV as observed in figure 5.19 and 5.20. The neutron spectrum in clinoatacamite also shows a dispersionless line at 1.4 meV below the magnetic transition temperature at 6 K [227]. It seems likely that the low-energy feature corresponds to the $Cu^{2+}$ spins on the Zn sites, and the high-energy feature to the much more strongly coupled $Cu^{2+}$ spins on what is for clinoatacamite a distorted kagomé lattice, because of the different energy scales of the magnetic coupling on those sites. This is consistent with the picture which emerged from the analysis of the heat capacity data, where the contributions to the heat capacity from the weakly coupled $Cu^{2+}$ spins on the Zn sites can be separated from the heat capacity corresponding to the kagomé layers. Regardless of whether the different components of the system can be separated, it is clear that there is only a gradual change in the characteristics of the system, over the entire range of Zn stoichiometries from $x = 0$ to $x = 1$. This suggests that $x$ does not influence the characteristics of the system on a microscopic level, consisting of weakly-coupled spins (doublets) between the kagomé layers, and more strongly-coupled doublets within the kagomé lattice. A quantum spin liquid or resonating valence bond state is a qualitatively different state of matter from a spin-glass with magnetic remanence such as for zinc paratacamite with $0.3 < x < 0.66$, or a phase with a weak ferromagnetic moment such as for $x < 0.3$. Hence, if the $x = 1$ phase possessed a quantum spin liquid ground state, necessarily a quantum phase transition should occur at some $x$. This transition can be blurred by an inhomogeneous material composition. However, the heat capacity should still show a shift of some of the spectral weight to lower energies as the quantum critical point is approached. This is not observed. The neutron powder-diffraction data for $x = 1$ and the heat capacity of samples with $0.5 \leq x \leq 1$ shows that due to the antisite disorder, samples with Zn stoichiometries $0.8 \leq x \leq 1$ model the $S = 1/2$ kagomé antiferromagnet equally well. For $x = 0.8$ the magnetic hysteresis

is too large to be ascribed to impurities or local variations in Zn stoichiometry [188]. Since only approximately one in five inter-plane Zn sites is occupied for $x = 0.8$, this hysteresis is ascribed to the higher connectivity of the lattice. This is mainly due to a higher connectivity *within* the kagomé planes (see table 5.4). This is in support of a growing consensus [95, 170, 142] that the ground state of this model $S = 1/2$ kagomé antiferromagnet is magnetic. In the present situation, we see no reason why the $S = 1/2$ spins on the kagomé lattice should behave differently from the $Cu^{2+}$ spins on the Zn sites. The ground state may be best described as co-operatively paramagnetic, such as found in $Tb_2Ti_2O_7$ [77]. In other words, neither $S_{\rm tot}$ nor $J_{\rm tot}$ seem good quantum numbers. In the present theoretical framework [5] $S_{\rm tot}$ ceases to be conserved when a symmetry breaking transition to a Néel -like long-range ordered state occurs. The muon data presented in this chapter shows that according to expectation there is no symmetry-breaking transition to a magnetically ordered, or spin-glass state, for systems with $x > 0.6$. *Even before a symmetry breaking transition of the magnetic degrees of freedom has occurred the system has a magnetic ground state.*

One explanation for the absence of a quantum-critical phase transition to a non-magnetic, quantum spin liquid ground state is that the antisite spins are a source of quantum mechanical dissipation, causing the quantum mechanical ground state to decohere to a classical state. With *decoherence* is meant the loss of the phase relationship between the wave-functions of the constituents of the system. Once the phase relationship between the wave-functions is lost, the typically quantum mechanical interference effects disappear giving rise to classical behaviour. This is what happens if a system is strongly coupled to a heat bath [117, 177]. As the excitation spectrum of a system narrows with increasing system size, the system becomes increasingly susceptible to this kind of dissipation. This is what happens in a symmetry-breaking transition such as the onset of Néel order in antiferromagnets [6, 9], and it is also the reason the Born-Oppenheimer approximation can be used for many systems. What is so special about the kagomé antiferromagnet, is that theory predicts that even in the thermodynamic

limit, there is a large energy gap (of the order $J/10$ [137]) to the states ($S_{\text{tot}} = 1$ states) which need to mix with the ground state ($S_{\text{tot}} = 0$ states) to create a classical system of apparently localised spins as encountered in the Néel ground state of many antiferromagnets. The kagomé lattice antiferromagnet has been suggested to be *topologically* protected from quantum mechanical decoherence, making it of interest in the design of quantum computers [99, 139]. For zinc paratacamite the exchange interaction has been estimated at $J/k_{\text{B}} = 170$ K [89], and hence the singlet-triplet gap should be of the order of 10 K. Because of the many-body nature of the problem, it is difficult to say what is the effect of perturbations of an energy scale corresponding to $\sim 2$ K.

The observation of "weakly-coupled" $S = 1/2$ spins sounds like a paradox; if these spins are coupled to the sandwiching kagomé layers, they should form higher-level multiplets. As was shown in section 5.5 the antisite spins can be identified as as interacting two-level systems, or localised $S = 1/2$ spins. The presence of localised but nevertheless interacting spins without forming higher level multiplets has been observed directly in the heat capacity of other localised spin systems [162, 124]. Ran *et al.* [166] suggest it could happen in the case of the $Cu^{2+}$ spins on Zn sites in zinc paratacamite, where they speculate that "Kondo-like moments" are coupled to the deconfined spinons of the kagomé lattice. We believe this scenario is very unlikely since the exchange interaction strenght and the spectral weight of the doublets increase as the $Cu^{2+}$ concentration increases, and gives rise to hysteresis, a phenomenon which cannot co-exist with a non-magnetic ground state. The presence of a magnetic hysteresis suggests that at least for the antisite spins we have to do with a phase described by a local state-dependent Hamiltonian.It is clearly a symmetry-broken phase where $S_{\text{tot}}$ is no longer a good quantum number [6, 9, 120]. One could then ask whether this Hamiltonian describes only the antisite spins or all the spins in the system, including those of the kagomé layers.

## 5.9 Conclusion

Powder samples of zinc paratacamite with Zn stoichiometry $x = 0 \ldots 1$ have been prepared. Muon spin relaxation spectroscopy shows that for $0.6 < x \leq 1$ the spins do not freeze, not even at 50 mK. For the $x = 1$ phase there is even at 50 mK only a very slow muon relaxation, indicative of very fast fluctuating spins. For increasing Cu content the fluctuations gradually slow down, and for $x < 0.3$ the muon signal approaches the static relaxation as was found previously for clinoatacamite [240]. Also some samples for which $x > 1$ have been synthesised, and an even slower muon relaxation was found. However, there are indications that that samples with $x > 1$ are not sufficiently phase pure, and it cannot be said with certainty what is the actual Cu/Zn ratio in the crystalline phase.

On the basis of neutron powder-diffraction data for $x = 1$ and heat-capacity measurements in a range of magnetic fields on zinc paratacamite for $0.5 \leq x \leq 1$, it can be concluded that Cu/Zn antisite disorder is present, corresponding to 6.3(3)% in Cu or 18.9(10)% in Zn in the $x = 1$ phase. The Cu spins residing on a Zn interplane site are only weakly coupled to the lattice, which explains the upturn in the magnetic susceptibility as $T \rightarrow 0$, though it is not likely that all the low-temperature magnetic susceptibility can be accounted for in this way. The heat capacity of the antisite spins could be modelled with very high accuracy, where the only underlying assumption was that the heat capacity of the kagomé system is independent of a relatively small external field. In this way the heat capacity corresponding to the kagomé layers was derived, revealing a power law $C_V \propto T^{1.3}$ temperature dependence below 10 K.

It is also demonstrated that due to the antisite disorder samples with Zn stoichiometry $0.8 \leq x \leq 1$ model the $S = 1/2$ kagomé antiferromagnet equally well. However, within this range of stoichiometries a large magnetic hysteresis develops, betraying a *magnetic* ground state. This situation is quite unique for a $S = 1/2$ system: No symmetry breaking is observed in the magnetic degrees of freedom, and yet, the ground state is magnetic. Furthermore, it is clear from muon data, heat capacity data, and

neutron spectroscopy data that no quantum critical phase transition occurs within the range $x = 0 \ldots 1$. Hence, the $x = 1$ phase is at best close to a quantum-critical gap less spin-liquid, but evidently, it must be at the *classical* side of the quantum critical point. The disagreement with the existing theory not only of the $S = 1/2$ kagomé antiferromagnet, but of quantum antiferromagnetism in general becomes even more pressing when it is recalled that the antisite spins could be modelled as doublets, but not as higher-level multiplets. The antisite spins were found to be localised doublets ($S = 1/2$ spins) which nevertheless interact with the spins on the kagomé lattice. This means that the total spin quantum number $S_{\mathrm{tot}}$ is not a conserved quantity, while $S_{\mathrm{tot}}$ commutes with the Heisenberg Hamiltonian. Since no symmetry breaking transition has occurred in the magnetic degrees of freedom, the effective magnetic Hamiltonian must be of a lower symmetry than the Heisenberg Hamiltonian.

Chapter 6

# Discussion

The experiments on zinc paratacamite discussed in the previous chapter demonstrate that the observed magnetic properties at low temperature are not adequately described by the quantum mechanical solutions of the Heisenberg Hamiltonian. The ground state of the kagomé layers is not a macroscopic quantum state, and has a non-vanishing magnetic susceptibility. This has been confirmed independently using $^{17}$O NMR [154]. Low temperature magnetic susceptibility measurements in the presence of high fields [20] also confirm the interpretation of the heat capacity results given here, of weakly-coupled $S = 1/2$ spins arising from antisite disorder. Furthermore, the results on zinc paratacamite do not stand on themselves. A number of other low-spin antiferromagnets which model the kagomé antiferromagnet to some degree are known in the literature [115, 121, 19, 74, 187]. Most of these systems remain fluctuating at very low temperatures, and all of them seem to have a magnetic ground state. These systems, of which zinc paratacamite comes closest to the theoretical model, are all narrow-band charge-transfer insulators. All experimental evidence suggests that on a microscopic scale the magnetism in these systems is similar. What these materials have in common is that the $3d$ electrons have localised, they are Mott insulators. Though in the $x = 1$ phase of zinc paratacamite no symmetry breaking occurs in the spin rotational degrees

of freedom, for the system to be magnetic clearly some symmetry breaking must have occurred [70].

## 6.1 On macroscopic quantum phases in Mott insulators.

That a singlet magnetic ground state is theoretically expected should not be understood as an electronic state described by a single determinant where all available orbitals are doubly occupied. The localised unpaired electrons in the $3d$ shell are thought to be *entangled* in the same way as a pair of photons in the well-known Einstein-Podolsky-Rosen experiment [14, 180]. In that way the singlet states can even have a spatial structure, unlike a single determinant. It should be clear that such entangled states are very susceptible to decoherence effects which enter even in the case of the well-controlled experiments which are carried out to test the Bell-inequality using photons [34]. The presence of super conductivity in many metals and in some copper oxides tells us that such macroscopic quantum states can emerge in the symmetry-broken state of matter which is the solid state [1]. In the Mott insulating state even the valence electrons are said to be localised albeit obviously a finite hopping $t$ remains. Though this is currently not universally accepted, a natural interpretation of this localisation would be that the electrons are still hopping, but now in a classical sense rather than in the quantum mechanical "everywhere-at-once" sense. In such a picture the residual hopping is a Goldstone mode giving rise to (quantum) fluctuations which occur even at $T = 0$. In this symmetry-broken and strongly fluctuating electronic state one cannot expect a-priory a macroscopic quantum state for the electronic spins. On the other hand, one can probably not exclude that they do exist.

Very recently a paper was published in Nature Materials reporting inelastic neutron spectroscopy data on zinc paratacamite with $0 \leq x \leq 1$ [116]. A weakly dispersive

[1] The broken symmetry is in this case the translational symmetry of the nuclei, which in the solid are localised. In the case of the nuclei the localisation is so strong that in general the nuclear spins do not interact through super-exchange. Exceptions are 2D systems of condensed $^3$He [64] and Bose-Einstein condensates in general.

neutron excitation around $Q = 1.341$ Å$^{-1}$ and $E = 7$ meV is reported for $x = 0$, but not for $x = 1$ as reported here in section 5.7. In [116], the weakly dispersive mode at 7 meV is interpreted as a singlet-triplet excitation of a valence bond solid ground state. At first sight, the fact that the system is magnetic at all temperatures seems to be ignored, while at the time of publication this was already a well established experimental fact for $x = 0$ [240, 239]. It may be that the authors have assumed, without saying so, that one can not expect a macroscopic quantum (magnetic) state in a Mott insulator. i.e. the singlets are constantly broken due to decoherence, leading to antiferromagnetic correlations. Something similar has been observed in the 1D linear chain system $KCuF_3$ [200] in which the inelastic neutron spectrum reveals spinon excitations in agreement with exact solutions of the $S = 1/2$ Heisenberg Hamiltonian for the linear chain, despite the fact that the ground state also shows a Néel type correlations. Note however, the situation in the 1D chain is very different from the present case; The 1D chain does not have a spin gap, $S_{\text{tot}} = 0$ and $S_{\text{tot}} = 1$ states have become degenerate, which is thought to be required for a Néel -type ordering to be possible. In the interpretation of the neutron data as described in [116] the $S_{\text{tot}} = 0$ and $S_{\text{tot}} = 1$ states are not degenerate, the $S_{\text{tot}} = 1$ state lies 7 meV higher. In this case the effects of decoherence must be much stronger than in the case of the 1D linear chain to explain the magnetic ground state. The interpretation given by [116] may be correct, but even then we should be careful not to see the presence of a singlet-triplet gap in the neutron spectrum as a confirmation of the present theory. A successful theoretical description of the zinc paratacamites should rationalise all observables, including the magnetic susceptibility and any magnetic correlations in the ground state. Furthermore, it is, as mentioned earlier, presently by no means universally agreed that the Mott insulating state is a fluctuating symmetry-broken electronic state.

We believe that strong correlation, which should not be taken for strong exchange-correlation integrals in ab-initio calculations, gives rise to *classical* order and accompanying quantum fluctuations. This provides a natural explanation for the paradox

highlighted in section 2.2.5, as to what is the interpretation of the residual hopping $t$ when the electrons are localised - as a Goldstone mode. Super-exchange then arises naturally from these quantum fluctuations. In the case that there is disagreement on this point we strongly believe that the experiments on zinc paratacamite can add to this debate. The central point being that the phase with $x = 1$ has a finite magnetic susceptibility, even though no symmetry breaking occurs in the spin rotational degrees of freedom. There are two possible interpretations of the data, but in both interpretations the ground state should be described as a classical ensemble of pure quantum states, in a density matrix.

- The Mott insulating state is a symmetry broken state, in which the residual electron hopping $t$ is a Goldstone mode which is also the origin of super-exchange. In that case the excitation at 7 meV could be interpreted as a singlet-triplet gap while the majority of spins are not bound into singlets, as is done in [116].
- There are unpaired spins because the system has no spin-gap. i.e. the $S_{\text{tot}} = 0$ and $S_{\text{tot}} = 1$ states are degenerate, and the 7 meV feature in the neutron spectrum arises from some other effect. These two states becoming degenerate may be a symmetry breaking in itself. Then the emergence of a state dependent local Hamiltonian for $x < 1$ is also explained.

Chapter 7

# Conclusion & Outlook

The approach as outlined in the introduction has been successful. For both iron jarosite and zinc paratacamite the symmetry of the underlying Hamiltonian has been determined, in both cases with a surprising outcome.

Iron jarosite has a weak easy-plane anisotropy and freezes into a three sub-lattice Néel state at 65 K. Using polarised x-ray absorption spectroscopy of the $2p \rightarrow 3d$ Fe $L_{2,3}$-edges in combination with ligand-field multiplet calculations [135], an accurate model of the Fe spins and their local environment is constructed. This has yielded accurate values for the actual spin, orbital angular momentum, and single-ion anisotropy in the nominally $Fe^{3+}$ ions which do not possess any orbital angular momentum even as free ions. Hence we have explained the magnetic anisotropy, and the spin-wave spectrum in the frozen state as previously observed by several groups.

We assert that zinc paratacamite with Zn stoichiometry within $x = 0.8 \ldots 1.0$ represents the best physical realisation of the $S = 1/2$ kagomé antiferromagnet known at present, despite the Cu/Zn antisite disorder which was for $x = 1$ found to be 6.3(3)% in Cu or 18.9(1.0)% in Zn. It was found that in agreement with theoretical predictions the system does not freeze, not even at 50 mK. No qualitative change in the (very weak) muon relaxation at low temperatures is observed for samples with $0.6 \leq x \leq 1$,

and in the heat capacity for samples $0.8 \leq x \leq 1$, while these samples are clearly magnetic and for $x < 1$ develop a magnetic hysteresis. Even when we take into account that a considerable contribution to the magnetic susceptibility comes from the antisite spins, we do not need to say *how large* this contribution is to conclude on a strictly experimental basis that:

- The ground state is magnetic.
- No quantum critical phase transition occurs as a function of Zn stoichiometry between $x = 0$ and $x = 1$, nor as a function of magnetic field.
- The ground state can not be described by a single stationary wave function. It must be written as a classical ensemble of wave functions, as a density matrix.

From a detailed analysis of the field-dependence of the heat capacity for samples with $x = 0.8, 0.9$ and $1.0$, it is found that the antisite spins behave as weakly coupled doublets, which is surprising but not completely without precedent [92]. It seems that $S_{\text{tot}}$ is not a conserved quantity. Since $S_{\text{tot}}$ commutes with the Heisenberg Hamiltonian on the kagomé lattice, the actual effective magnetic Hamiltonians must be of a lower symmetry than the Heisenberg Hamiltonian.

From an experimental point of view it can not be ruled out that the ground state is magnetic simply because $S_{\text{tot}} = 0$ and $S_{\text{tot}} = 1$ states have become degenerate, though this would still leave open the question of what is the effective Hamiltonian in the case of the $S = 1/2$ kagomé antiferromagnet. However, we believe that a successful theory of the magnetism in transition metal compounds should embrace the idea that the Mott insulating state is a symmetry broken state; a localised electron is not described by a Bloch wave, and hence, the discrete translational symmetry of the lattice is broken. The residual hopping of the electrons is then a symmetry-restoring fluctuation, or Goldstone mode, responsible for super-exchange. In such a fluctuating system, a macroscopic quantum mechanical ground state for the electron spins cannot be taken for granted.

# References


[1] The Debian Gnu/Linux operating system. www.debian.org.

[2] Magnetic ordering in diluted kagomé antiferromagnets. *J. of Mat. Chem. 11* (2001), 179–185.

[3] ABRAGAM, A., AND PRYCE, M. Theory of the nuclear hyperfine structure of paramagnetic resonance spectra in crystals. *Proc. Roy. Soc. A 205*, 1080 (1951), 135–153.

[4] ANDERSON, P. W. Antiferromagnetism. theory of superexchange interaction. *Phys. Rev. 79*, 2 (Jul 1950), 350–356.

[5] ANDERSON, P. W. An approximate quantum theory of the antiferromagnetic ground state. *Phys. Rev. 86*, 5 (Jun 1952), 694–701.

[6] ANDERSON, P. W. More is different. *Science 177*, 4047 (1972), 393–396.

[7] ANDERSON, P. W. Resonating valence bonds: a new kind of insulator? *Mat. Res. Bull. 8* (1973), 153–160.

[8] ANDERSON, P. W. Local moments and localized states. *Science 201* (1978), 307–316.

[9] ANDERSON, P. W. *Basic Notions of Condensed Matter Physics.* Benjamin/Cummings, Menlo Park, 1984.

[10] ANDERSON, P. W. The resonating valence bond state in $La_2CuO_4$ and superconductivity. *Science 235* (1987), 1196–1198.

[11] AZARIA, P., DELAMOTTE, B., AND MOUHANNA, D. Spontaneous symmetry breaking in quantum frustrated antiferromagnets. *Phys. Rev. Lett. 70*, 16 (Apr 1993), 2483–2486.

[12] BANDYOPADHYAY, R., LIANG, D., YARDIMCI, H., SESSOMS, D. A., BORTHWICK, M. A., MOCHRIE, S. G. J., HARDEN, J. L., AND LEHENY, R. L. Evolution of particle-scale dynamics in an aging clay suspension. *Phys. Rev. Lett. 93*, 22 (2004), 228302.

[13] BEDNORZ, J. G., AND MÜLLER, K. A. Possible high $T_c$ superconductivity in the Ba-La-Cu-O system. *Z. Phys. B 64*, 2 (1986), 189–193.

[14] BELL, J. S. On the einstein-podolsky-rosen paradox. *Physics (U.S.) 1* (1964), 195–290.

[15] BENCOK, P., AND BROOKES, N. ID8 dragon beamline. Tech. rep., European Synchrotron Radiation Facility (ESRF), Grenoble, 2006. Last accessed at 7/06/07.

[16] BERNHARD, B. H., CANALS, B., AND LACROIX, C. Green's function approach to the magnetic properties of the kagomé antiferromagnet. *Phys. Rev. B 66*, 10 (Sep 2002), 104424.

[17] BERNU, B., LHUILLIER, C., AND PIERRE, L. Signature of Néel order in exact spectra of quantum antiferromagnets on finite lattices. *Phys. Rev. Lett. 69*, 17 (Oct 1992), 2590–2593.

[18] BERNU, B., AND MISGUICH, G. Specific heat and high-temperature series of lattice models: Interpolation scheme and examples on quantum spin systems in one and two dimensions. *Phys. Rev. B 63*, 13 (Mar 2001), 134409.

[19] BERT, F., BONO, D., MENDELS, P., LADIEU, F., DUC, F., TROMBE, J.-C., AND MILLET, P. Ground state of the kagomé-like $S = 1/2$ antiferromagnet volborthite $Cu_3V_2O_7(OH)_2{\cdot}2H_2O$. *Phys. Rev. Lett. 95*, 8 (2005), 087203.

[20] BERT, F., NAKAMAE, S., LADIEU, F., L'HOTE, D., BONVILLE, P., DUC, F., TROMBE, J. C., AND MENDELS, P. Low temperature magnetization of the $S = 1/2$ kagomé antiferromagnet $ZnCu_3(OH)_6Cl_2$, 2007.

[21] BETHE, H. On the theory of metals. 1. Eigenvalues and eigenfunctions for the linear atomic chain. *Z. Phys. 71* (1931), 205–226.

[22] BINNEY, J. J., DOWRICK, N. J., FISHER, A. J., AND NEWMAN, M. E. J. *The Theory of Critical Phenomena.* Oxford Science Publications, 1992.

[23] BISENGALIEVA, M., KISELEVA, I., MELCHAKOVA, L., OGORODOVA, L., AND GUREVICH, A. The molar heat capacity of hydrous copper chloride: atacamite $Cu_2Cl(OH)_3$. *The Journal of Chemical Thermodynamics 29* (1997), 345–352(8).

[24] BISSON, W., AND WILLS, A. S. Intermediate phase in the oxidative hydrothermal synthesis of potassium jarosite, a model kagomé antiferromagnet. arXiv.org:cond-mat/0610119.

[25] BLAND, J. *A Mössbauer spectroscopy and magnetometry study of magnetic multilayers and oxides.* PhD thesis, Department of Physics, University of Liverpool, 2002.

[26] BLUNDELL, S. *Magnetism in condensed matter.* Oxford Univeristy Press, 2001.

[27] BONNET, P., PAYEN, C., MUTKA, H., DANOT, M., FABRITCHNYI, P., STEWART, J. R., MELLERGARD, A., AND RITTER, C. Spin correlations in the pyrochlore slab compounds $Ba_2Sn_2Ga_{10-7p}ZnCr_{7p}O_{22}$. *J. Phys. Cond. Mat.*, 16 (2004), S835.

[28] BONO, D., MENDELS, P., COLLIN, G., BLANCHARD, N., BERT, F., AMATO, A., BAINES, C., AND HILLIER, A. D. $\mu$SR study of the quantum dynamics in the frustrated $S = 3/2$ kagomé bilayers. *Phys. Rev. Lett. 93*, 18 (2004), 187201.

[29] BORDET, P., GELARD, I., MARTY, K., IBANEZ, A., ROBERT, J., SIMONET, V., CANALS, B., BALLOU, R., AND LEJAY, P. Magnetic frustration on a kagomé lattice in $R_3Ga_5SiO_{14}$ langasites with R = Nd, Pr. *J. Phys.: Cond. Matt. 18*, 22 (2006), 5147–5153.

[30] BORN, M., AND WOLF, E. *Principles of Optics*, 7th ed. Cambridge University Press, 1999.

[31] BRAITHWAITE, R., MEREITER, K., PAAR, W., AND CLARK, A. Herbertsmithite, $Cu_3Zn(OH)_6Cl_2$, a new species, and the definition of paratacamite. *Min. Mag. 68* (2004), 527.

[32] BRAITHWAITE, R. S. W. A low temperature synthesis of herbertsmithite. Private communication.

[33] BRAMWELL, S., AND GINGRAS, M. Weak ferromagnetism in a kagomé lattice antiferromagnet. Unpublished, 1994.

[34] BRANCIARD, C., LING, A., GISIN, N., ANDÕ ANTIA LAMAS-LINARES, C. K., AND SCARANI, V. Experimental falsification of leggett's nonlocal variable model. *Physical Review Letters 99*, 21 (2007), 210407.

[35] BRAY, J. W., HART, H. R., INTERRANTE, L. V., JACOBS, I. S., KASPER, J. S., WATKINS, G. D., WEE, S. H., AND BONNER, J. C. Observation of a spin-peierls transition in a heisenberg antiferromagnetic linear-chain system. *Phys. Rev. Lett. 35*, 11 (Sep 1975), 744–747.

[36] BROHOLM, C., AEPPLI, G., ESPINOSA, G. P., AND COOPER, A. S. Antiferromagnetic fluctuations and short-range order in a kagomé lattice. *Phys. Rev. Lett. 65*, 25 (Dec 1990), 3173–3176.

[37] BROHOLM, C., AEPPLI, G., ESPINOSA, G. P., AND COOPER, A. S. A strongly fluctuating quasi-two-dimensional insulator (invited). vol. 69, AIP, pp. 4968–4973.

[38] BROWN, P. J. *International tables for chrystallography*, vol. C. Kluwer scientific, 1995, ch. 4.4.5, pp. 391–399.

[39] BUDNIK, R., AND AUERBACH, A. Low-energy singlets in the heisenberg antiferromagnet on the kagomé lattice. *Phys. Rev. Lett. 93*, 18 (2004), 187205.

[40] BURNS, G. *High-temperature superconductivity.* Academic Press, Boston, 1992.

[41] CAMPBELL, I. A., AMATO, A., GYGAX, F. N., HERLACH, D., SCHENCK, A., CYWINSKI, R., AND KILCOYNE, S. H. Dynamics in canonical spin glasses observed by muon spin depolarization. *Phys. Rev. Lett. 72*, 8 (Feb 1994), 1291–1294.

[42] CHALKER, J. T., AND EASTMOND, J. F. G. Ground-state disorder in the spin-1/2 kagomé heisenberg antiferromagnet. *Phys. Rev. B 46*, 21 (Dec 1992), 14201–14204.

[43] CHALKER, J. T., HOLDSWORTH, P. C. W., AND SHENDER, E. F. Hidden order in a frustrated system: Properties of the heisenberg kagomé antiferromagnet. *Phys. Rev. Lett. 68*, 6 (Feb 1992), 855–858.

[44] CHANDRA, P., COLEMAN, P., AND RITCHEY, I. The anisotropic kagomé antiferromagnet: a topological spin glass? *J. Phys. I France 3* (1993), 591–610.

[45] CHUBUKOV, A. Order from disorder in a kagomé antiferromagnet. *Phys. Rev. Lett. 69*, 5 (Aug 1992), 832–835.

[46] CLEETON, C. E., AND WILLIAMS, N. H. Electromagnetic waves of 1.1 cm wavelength and the absorption spectrum of ammonia. *Phys. Rev. 45*, 4 (Feb 1934), 234–237.

[47] CLEMENTI, E., AND ROETTI, C. *Atomic Data and Nuclear Data Tables*, vol. 14. Elsevier, 1974, ch. Roothaan Hartree-Fock Basis functions and their coefficients for ground and certain excited states of neutral and ionized atoms, $Z =< 54$, pp. 177–478.

[48] COOMER, F. C., HARRISON, A., OAKLEY, G. S., KULDA, J., STEWART, J. R., STRIDE, J. A., FÅK, B., TAYLOR, J. W., AND VISSER, D. Inelastic neutron scattering study of magnetic excitations in the kagomé antiferro magnet potassium jarosite. *J. of Phys.: Cond. Mat. 18*, 39 (2006), 8847–8858.

[49] COWAN, R. *The Theory of Atomic Structure and Spectra.* University of California Press, Berkeley, 1981.

[50] COX, S. Muonium states and dynamics. In *MUON SCIENCE. Muons in physics, chemistry and materials* (1998), S. Lee, S. Kilcoyne, and R. Cywinski, Eds.,

Scottish Universities Summer School in Physics & Institute of Physics Publishing, Briston and Philadelphia, pp. 239–286.

[51] DE GROOT, F. X-ray absorption and dichroism of transition metals and their compounds. *J. El. Spec. Rel. Phen. 67*, 4 (Aug 1994), 529–622.

[52] DE GROOT, F. Multiplet effects in X-ray spectroscopy. *Coordination Chemistry Reviews 249*, 31-63 (2005).

[53] DE GROOT, F., FONTAINE, A., KAO, C., AND KRISCH, M. Charge transfer multiplet calculations of the k$\beta$ X-ray emission spectra of divalent nickel compounds. *J. Phys.: Cond. Mat. 6* (1994), 6875–6884.

[54] DE GROOT, F. M. F., GRIONI, M., FUGGLE, J. C., GHIJSEN, J., SAWATZKY, G. A., AND PETERSEN, H. Oxygen 1s X-ray-absorption edges of transition-metal oxides. *Phys. Rev. B 40*, 8 (Sep 1989), 5715–5723.

[55] DE VRIES, M. A. Dipole dipole interactions in real kagomé antiferromagnets. unpublished, April 2007.

[56] DE VRIES, M. A. Spinner, a classical spin-lattice simulation program, using Markov-Chain Monte Carlo. http://www.ccp5.ac.uk/librar.shtml#Internal, August 8, 2007.

[57] DE VRIES, M. A., KAMENEV, K. V., KOCKELMANN, W. A., SANCHEZ-BENITEZ, J., AND HARRISON, A. Antisite disorder and the magnetic groundstate of an experimental $S = 1/2$ kagomé antiferromagnet. arXiv:cond-mat/0705.0654.

[58] DEEN, P., MURANI, A., AND FÖDINGER, L. Diffuse scattering spectrometer d7. www.ill.fr/YellowBook/D7, January 2007. last acessed at 4/06/07.

[59] DIEP, H. T., Ed. *Frustrated spin systems.* World Scientific, Singapore, 2004.

[60] DUTRIZAC, J. E., AND KAIMAN, S. Synthesis and properties of jarosite-type compounds. *Canadian Mineralogist 14*, 2 (1976), 151–58.

[61] DZYALOSHINSKY, I. A thermodynamic theory of "weak" ferromagnetism of antiferromagnetics. *J. Phys. Chem. Sol. 4* (1958), 241–255.

[62] EATON, G. H., AND KILCOYNE, S. H. Muon production: past, present and future. In *MUON SCIENCE. Muons in physics, chemistry and materials* (1998), S. Lee, S. Kilcoyne, and R. Cywinski, Eds., Scottish Universities Summer School in Physics & Institute of Physics Publishing, Briston and Philadelphia, pp. 11–37.

[63] ELHAJAL, M., CANALS, B., AND LACROIX, C. Symmetry breaking due to dzyaloshinsky-moriya interactions in the kagomé lattice. *Phys. Rev. B 66*, 1 (Jul 2002), 014422.

[64] ELSER, V. Nuclear antiferromagnetism in a registered $^3$He solid. *Phys. Rev. Lett. 62*, 20 (May 1989), 2405–2408.

[65] ELSTNER, N., AND YOUNG, A. P. Spin-1/2 heisenberg antiferromagnet on the kagomé lattice: High-temperature expansion and exact-diagonalization studies. *Phys. Rev. B 50*, 10 (Sep 1994), 6871–6876.

[66] ELWOOD-MADDEN, M. E., BODNAR, R. J., AND RIMSTIDT, J. D. Jarosite as an indicator of water-limited chemical weathering on mars. *Nature 431* (2004), 821.

[67] FADLEY, C. S., AND SHIRLEY, D. A. Multiplet splitting of metal-atom electron binding energies. *Phys. Rev. A 2*, 4 (Oct 1970), 1109–1120.

[68] FADLEY, C. S., SHIRLEY, D. A., FREEMAN, A. J., BAGUS, P. S., AND MALLOW, J. V. Multiplet splitting of core-electron binding energies in transition-metal ions. *Phys. Rev. Lett. 23*, 24 (Dec 1969), 1397–1401.

[69] FALUS, P., BORTHWICK, M. A., NARAYANAN, S., SANDY, A. R., AND MOCHRIE, S. G. J. Crossover from stretched to compressed exponential relaxations in a polymer-based sponge phase. *Phys. Rev. Lett. 97*, 6 (2006), 066102.

[70] FAZEKAS, P. *Lecture Notes on Electron Correlation and Magnetism.* Series in Modern Condensed Matter Physics 5. World Scientific (Singapore), 1999.

[71] FAZEKAS, P., AND ANDERSON, P. W. On the groundstate properties of the anisotropic triangular antiferromagnet. *Philosophical Magazine 30*, 2 (174), 423–440.

[72] FEITKNECHT, W., AND MAGET, K. Über doppolhydroxide und basische doppolsalze. Über basische doppelchloride des kupfers. *Helvetica Chim. Atca 32* (1949), 1653–1667.

[73] FRANCO, H., RAPP, R. E., AND GODFRIN, H. Nuclear ferromagnetism of two-dimensional $^3$He. *Phys. Rev. Lett. 57*, 9 (Sep 1986), 1161–1164.

[74] FUKAYA, A., FUDAMOTO, Y., GAT, I. M., ITO, T., LARKIN, M. I., SAVICI, A. T., UEMURA, Y. J., KYRIAKOU, P. P., LUKE, G. M., ROVERS, M. T., KOJIMA, K. M., KEREN, A., HANAWA, M., AND HIROI, Z. Muon spin relaxation and susceptibility studies of the pure and diluted spin $\frac{1}{2}$ kagomé-like lattice system $(Cu_xZn_{1-x})_3V_2O_7(OH_2)\cdot 2H_2O$. *Phys. Rev. Lett. 91*, 20 (Nov 2003), 207603.

[75] GADO, E. D., AND KOB, W. Length-scale-dependent relaxation in colloidal gels. *Phys. Rev. Lett. 98*, 2 (2007), 028303.

[76] GARCIA-ADEVA, A. J., AND HUBER, D. L. Critical behavior of two- and three-dimensional ferromagnetic and antiferromagnetic spin-ice systems using the effective-field renormalization group technique. *Phys. Rev. B 64*, 1 (Jun 2001), 014418.

[77] GARDNER, J. S., DUNSIGER, S. R., GAULIN, B. D., GINGRAS, M. J. P., GREEDAN, J. E., KIEFL, R. F., LUMSDEN, M. D., MACFARLANE, W. A., RAJU, N. P., SONIER, J. E., SWAINSON, I., AND TUN, Z. Cooperative paramagnetism in the geometrically frustrated pyrochlore antiferromagnet $Tb_2Ti_2O_7$. *Phys. Rev. Lett. 82*, 5 (Feb 1999), 1012–1015.

[78] GREEDAN, J. E. Geometrically frustrated magnetic materials. *J. of Mat. Chem. 11* (2001), 37–53.

[79] GREYWALL, D. S., AND BUSCH, P. A. Heat capacity of $^3He$ adsorbed on graphite at millikelvin temperatures and near third-layer promotion. *Phys. Rev. Lett. 62*, 16 (Apr 1989), 1868–1871.

[80] GROHOL, D., HUANG, Q., TOBY, B. H., LYNN, J. W., LEE, Y. S., AND NOCERA, D. G. Powder neutron diffraction analysis and magnetic structure of

kagomé-type vanadium jarosite $NaV_3(OD)_6(SO_4)_2$ . *Phys. Rev. B 68*, 9 (Sep 2003), 094404.

[81] GROHOL, D., MATAN, K., CHO, J. H., LEE, S. H., LYNN, J. W., NOCERA, D. G., AND LEE, Y. S. Spin chirality on a two-dimensional frustrated lattice. *Nature Materials 4* (2005), 323–328.

[82] GROHOL, D., AND NOCERA, D. Hydrothermal oxidation-reduction methods for the preparation of pure and single crystalline alunites: Synthesis and characterization of a new series of vanadium jarosites. *Journal of the American Chemical Society 124*, 11 (2002), 2640–2646.

[83] GROHOL, D., NOCERA, D. G., AND PAPOUTSAKIS, D. Magnetism of pure iron jarosites. *Phys. Rev. B 67*, 6 (2003), 064401.

[84] HARRIS, A. B., KALLIN, C., AND BERLINSKY, A. J. Possible Néel orderings of the kagomé antiferromagnet. *Phys. Rev. B 45*, 6 (Feb 1992), 2899–2919.

[85] HARRISON, A. First catch your hare: the design and synthesis of frustrated magnets. *J. of Phys.: Cond. Mat. 16*, 11 (2004), S553–S572.

[86] HARRISON, A., OAKLEY, G., PETTIGREW, K., DE VRIES, M., MCINTYRE, G., LELIÉVRE-BERNA, E., HARRIS, M., VISSER, D., AND WILLS, A. Neutron-diffraction study of magnetic ordering in a single crystal of the madel kagomé antiferromagnet potassium jarosite. To be published.

[87] HASTINGS, M. B. Dirac structure, rvb, and goldstone modes in the kagomé antiferromagnet. *Phys. Rev. B 63*, 1 (Dec 2000), 014413.

[88] HEISENBERG, W. *Zeits. f. Physik 49* (1928), 619.

[89] HELTON, J. S., MATAN, K., SHORES, M. P., NYTKO, E. A., BARTLETT, B. M., YOSHIDA, Y., TAKANO, Y., SUSLOV, A., QIU, Y., CHUNG, J.-H., NOCERA, D. G., AND LEE, Y. S. Spin dynamics of the spin-1/2 kagome lattice antiferromagnet $ZnCu_3(OH)_6Cl_2$. *Phys. Rev. Lett. 98*, 10 (2007), 107204.

[90] HIROI, Z., HANAWA, M., KOBAYASHI, N., NOHARA, M., TAKAGI, H., KATO, Y., AND TAKIGAWA, M. Spin-1/2 kagomé-like lattice in volborthite $Cu_3V_2O_7(OH)_2 \cdot 2H_2O$. *J. Phys. Soc. Jpn. 70* (2001), 3377–3384.

[91] HIROTA, K., COX, D. E., LORENZO, J. E., SHIRANE, G., TRANQUADA, J. M., HASE, M., UCHINOKURA, K., KOJIMA, H., SHIBUYA, Y., AND TANAKA, I. Dimerization of $CuGeO_3$ in the spin-peierls state. *Phys. Rev. Lett. 73*, 5 (Aug 1994), 736–739.

[92] HOGLUND, K. H., SANDVIK, A. W., AND SACHDEV, S. Impurity induced spin texture in quantum critical 2d antiferromagnets. *Phys. Rev. Lett. 98*, 8 (2007), 087203.

[93] HONDA, Z., KATSUMATA, K., AND YAMADA, K. The spin gap in a quantum antiferromagnet on the kagomé lattice. *J. Phys.: Cond. Matt. 14*, 38 (2002), L625–L629.

[94] HUBBARD, J. Electron correlations in narrow energy bands. *Proc. Roy. Soc. A 276*, 1365 (1963), 238–257.

[95] IMAI, T., NYTKO, E. A., BARTLETT, B. M., SHORES, M. P., AND NOCERA, D. G. $^{63}Cu$ and $^{35}Cl$ NMR investigation of the $S = 1/2$ kagomé lattice system $ZnCu_3(OH)_6Cl_2$. cond-mat/0703141.

[96] INAMI, T., MORIMOTO, T., NISHIYAMA, M., MAEGAWA, S., OKA, Y., AND OKUMURA, H. Magnetic ordering in the kagomé lattice antiferromagnet $KCr_3(OD)_6(SO_4)_2$. *Phys. Rev. B 64*, 5 (Jul 2001), 054421.

[97] INAMI, T., NISHIYAMA, M., MAEGAWA, S., AND OKA, Y. Magnetic structure of the kagomé lattice antiferromagnet potassium jarosite K $Fe_3(OH)_6(SO_4)_2$. *Phys. Rev. B 61*, 18 (May 2000), 12181–12186.

[98] IOFFE, L. B., AND FEIGEL'MAN, M. V. Possible realization of an ideal quantum computer in josephson junction array. *Phys. Rev. B 66*, 22 (Dec 2002), 224503.

[99] IOFFE, L. B., FEIGEL'MAN, M. V., IOSELEVICH, A., IVANOV, D., TROYER, M., AND BLATTER, G. Topologically protected quantum bits using josephson junction arrays. *Nature 415* (2002), 503–506.

[100] JACKSON, J. D. *Classical Electrodynamics*, 2nd ed. John Wiley & Sons, New York, 1962.

[101] JAHN, H. A., AND TELLER, E. Stability of polyatomic molecules in degenerate electronic states. i. orbital degeneracy,. *Proc. Roy. Soc. A 158* (1937), 220–235.

[102] JOSEPHSON, B. D. Possible new effects in superconductive tunneling. *Phys. Lett. 1* (1962), 251–253.

[103] JOSEPHSON, B. D. The discovery of tunneling supercurrents. *Rev. Mod. Phys. 46*, 2 (1974), 251–254.

[104] KALMEYER, V., AND LAUGHLIN, R. B. Equivalence of the resonating-valence-bond and fractional quantum hall states. *Phys. Rev. Lett. 59*, 18 (Nov 1987), 2095–2098.

[105] KEREN, A., KOJIMA, K., LE, L. P., LUKE, G. M., WU, W. D., UEMURA, Y. J., TAKANO, M., DABKOWSKA, H., AND GINGRAS, M. J. P. Muon-spin-rotation measurements in the kagomé lattice systems: Cr-jarosite and Fe-jarosite. *Phys. Rev. B 53*, 10 (Mar 1996), 6451–6454.

[106] KEREN, A., MENDELS, P., CAMPBELL, I. A., AND LORD, J. Probing the spin-spin dynamical autocorrelation function in a spin glass above $t_g$ via muon spin relaxation. *Phys. Rev. Lett. 77*, 7 (Aug 1996), 1386–1389.

[107] KLEIN, M. J., AND SMITH, R. S. A note on the classical spin-wave theory of heller and kramers. *Phys. Rev. 80*, 6 (Dec 1950), 1111.

[108] KOCKELMANN, W. Rotax: Multipurpose diffractometer. http://www.isis.rl.ac.uk/excitations/rotax/, May 2001. last accessed at 4/06/07.

[109] KORBEL, P., AND NOVAK, M. *Geillustreerde mineralen encyclopedie.* Rebo productions, Lisse, 2001.

[110] KUGEL, K. I., AND KHOMSKII, D. I. The jahn-teller effect and magnetism: transition metal compounds. *Sov. Phys. Uspekhi 25*, 4 (1982), 231–256.

[111] LARSON, A. C., AND DREELE, R. B. V. General structure analysis system (gsas). Tech. rep., Los Alamos National Laboratory, 2000.

[112] LAUGHLIN, R., LONZARICH, G. G., MONTHOUX, P., AND PINES, D. The quantum criticality conundrum. *Adv. Phys. 50* (2001), 361.

[113] LECHEMINANT, P., BERNU, B., LHUILLIER, C., PIERRE, L., AND SINDZINGRE, P. Order versus disorder in the quantum heisenberg antiferromagnet on the kagomé lattice using exact spectra analysis. *Phys. Rev. B 56*, 5 (Aug 1997), 2521–2529.

[114] LEE, S.-H., BROHOLM, C., AEPPLI, G., RAMIREZ, A. P., PERRING, T. G., CARLILE, C. J., ADAMS, M., JONES, T. J. L., AND HESSEN, B. Spin-glass and non-spin-glass features of a geometrically frustrated magnet. *Europhysics Letters (EPL) 35*, 2 (1996), 127–132.

[115] LEE, S.-H., BROHOLM, C., COLLINS, M. F., HELLER, L., RAMIREZ, A. P., KLOC, C., BUCHER, E., ERWIN, R. W., AND LACEVIC, N. Less than 50% sublattice polarization in an insulating $S = \frac{3}{2}$ kagomé antiferromagnet at $t \approx 0$. *Phys. Rev. B 56*, 13 (Oct 1997), 8091–8097.

[116] LEE, S.-H., KIKUCHI, H., QIU, Y., LAKE, B., HUANG, Q., HABICHT, K., AND KIEFER, K. Quantum-spin-liquid states in the two-dimensional kagomé antiferromagnets $Zn_xCu_{4-x}(OD)_6Cl_2$. *NMat. 6* (2007), 853–857.

[117] LEGGETT, A. J., CHAKRAVARTY, S., DORSEY, A. T., FISHER, M. P. A., GARG, A., AND ZWERGER, W. Dynamics of the dissipative two-state system. *Rev. Mod. Phys. 59*, 1 (Jan 1987), 1–85.

[118] LELIEVRE-BERNA, E. Novel polarized neutron tools. I. S. Anderson and B. Guýrard, Eds., vol. 4785, SPIE, pp. 112–125.

[119] LEUNG, P. W., AND ELSER, V. Numerical studies of a 36-site kagomé antiferromagnet. *Phys. Rev. B 47*, 9 (Mar 1993), 5459–5462.

[120] LHUILLIER, C. Frustrated quantum magnets. arXiv.org:cond-mat/0502464.

[121] LIMOT, L., MENDELS, P., COLLIN, G., MONDELLI, C., OULADDIAF, B., MUTKA, H., BLANCHARD, N., AND MEKATA, M. Susceptibility and dilution effects of the kagomé bilayer geometrically frustrated network: A Ga NMR study of $SrCr_{9p}Ga_{12-9p}O_{19}$. *Phys. Rev. B 65*, 14 (Apr 2002), 144447.

[122] LORD, J., COTTRELL, S., AND WILLIAMS, W. Muon spin relaxation in strongly coupled systems. *Physica B: Cond. Mat. 289-290* (2000), 495–498.

[123] LOVESEY, S. *Theory of neutron scattering from condensed matter*, vol. 2 of *International Series of Monographs on Physics*. Oxford Science Publications, 1984.

[124] MANABE, K., ISHIMOTO, H., KOIDE, N., SASAGO, Y., AND UCHINOKURA, K. Antiferromagnetic long-range order in $Cu_{1-x}Zn_xGeO_3$ with extremely low zn concentration. *Phys. Rev. B 58*, 2 (Jul 1998), R575–R578.

[125] MANOUSAKIS, E. The spin- 1/2 Heisenberg antiferromagnet on a square lattice and its application to the cuprous oxides. *Rev. Mod. Phys. 63* (Jan. 1991), 1–62.

[126] MARSTON, J. B., AND ZENG, C. Spin-peierls and spin-liquid phases of kagom[e-acute] quantum antiferromagnets. vol. 69, AIP, pp. 5962–5964.

[127] MATAN, K., GROHOL, D., NOCERA, D. G., YILDIRIM, T., HARRIS, A. B., LEE, S. H., NAGLER, S. E., AND LEE, Y. S. Spin waves in the frustrated kagomé lattice antiferromagnet $KFe_3(OH)_6(SO_4)_2$. *Phys. Rev. Lett. 96*, 24 (2006), 247201.

[128] MATATOSHI IMADA, A. F., AND TOKURA, Y. Metal-insulator transitions. *Rev. Mod. Phys. 70* (October 1998), 1039–1263.

[129] MCELFRESH, M. *Fundamentals of magnetism and magnetic measurements featuring Quantum Design's Magnetic Property Measurement System*. Quantum Design, San Diego, 1994.

[130] MELIKIDZE, A., DOBROVITSKI, V. V., RAEDT, H. A. D., KATSNELSON, M. I., AND HARMON, B. N. Parity effects in spin decoherence. *Phys. Rev. B 70*, 1 (2004), 014435.

[131] MENDELS, P., BERT, F., DE VRIES, M. A., OLARIU, A., HARRISON, A., DUC, F., TROMBE, J. C., LORD, J. S., AMATO, A., AND BAINES, C. Quantum magnetism in the paratacamite family: Towards an ideal kagomé lattice. *Phys. Rev. Lett. 98*, 7 (2007), 077204.

[132] MILA, F. Low-energy sector of the $S = 1/2$ kagome antiferromagnet. *Phys. Rev. Lett. 81*, 11 (Sep 1998), 2356–2359.

[133] MILA, F., SHIINA, R., ZHANG, F.-C., JOSHI, A., MA, M., ANISIMOV, V., AND RICE, T. M. Orbitally degenerate spin-1 model for insulating $V_2O_3$. *Phys. Rev. Lett. 85*, 8 (Aug 2000), 1714–1717.

[134] MIRONE, A. The magnetic moment reduction of fullerene encapsulated gadolinium. a combined effect of spin-orbit interaction and anisotropic hybridisation. *Eur. Phys. J. B 47* (2005), 509–515.

[135] MIRONE, A. Hilbert++ manual. arXiv:0706.4170v1, June 2007.

[136] MIRONE, A., SACCHI, M., AND GOTA, S. Ligand-field atomic-multiplet calculations for arbitrary symmetry. *Phys. Rev. B 61*, 20 (May 2000), 13540–13544.

[137] MISGUICH, G., AND BERNU, B. Specific heat of the $S = 1/2$ heisenberg model on the kagome lattice: High-temperature series expansion analysis. *Phys. Rev. B 71*, 1 (2005), 014417.

[138] MISGUICH, G., AND LHUILLIER, C. Frustrated spin systems. In *Two-dimensional quantum antiferromagnets* (2004), H.T.Diep, Ed., World Scientific Publishing, pp. 229–306.

[139] MISGUICH, G., PASQUIER, V., MILA, F., AND LHUILLIER, C. Quantum dimer model with $Z_2$ liquid ground state: Interpolation between cylinder and disk topologies and toy model for a topological quantum bit. *Phys. Rev. B 71*, 18 (2005), 184424.

[140] MISGUICH, G., SERBAN, D., AND PASQUIER, V. Quantum dimer model on the kagome lattice: Solvable dimer-liquid and ising gauge theory. *Phys. Rev. Lett. 89*, 13 (Sep 2002), 137202.

[141] MISGUICH, G., SERBAN, D., AND PASQUIER, V. Quantum dimer model with extensive ground-state entropy on the kagomé lattice. *Phys. Rev. B 67*, 21 (2003), 214413.

[142] MISGUICH, G., AND SINDZINGRE, P. Magnetic susceptibility and specific heat on the spin-$\frac{1}{2}$ heisenberg model on the kagomé lattice and experimental data on $ZnCu_3(OH)_6Cl_2$. cond-mat/0704.1017.

[143] MORIMOTO, T., NISHIYAMA, M., MAEGAWA, S., AND OKA, Y. Magnetization of new kagomé lattice antiferromagnets: Cr-Jarosites, $ACr_3(OH)_6(SO_4)_2$ [ $A$ =Na, K, Rb, $NH_4$]. *J. Phys. Soc. Japan 72*, 8 (2003), 2085–2090.

[144] MORIYA, T. Anisotropic superexchange interaction and weak ferromagnetism. *Phys. Rev. 120*, 1 (Oct 1960), 91–98.

[145] NARUMI, Y., KATSUMATA, K., HONDA, Z., DOMENGE, J.-C., SINDZINGRE, P., LHUILLIER, C., SHIMAOKA, Y., KOBAYASHI, T. C., AND KINDO, K. Observation of a transient magnetization plateau in a quantum antiferromagnet on the kagomé lattice. *Europhysics Letters (EPL) 65*, 5 (2004), 705–711.

[146] NIKOLIC, P., AND SENTHIL, T. Physics of low-energy singlet states of the kagome lattice quantum heisenberg antiferromagnet. *Phys. Rev. B 68*, 21 (Dec 2003), 214415.

[147] NISHIYAMA, M., MAEGAWA, S., INAMI, T., AND OKA, Y. Magnetic ordering and spin dynamics in potassium jarosite: A heisenberg kagomé lattice antiferromagnet. *Phys. Rev. B 67*, 22 (Jun 2003), 224435.

[148] NISHIYAMA, N., AND MAEGAWA, S. Heirarchical orderings in kagomé lattice antiferromagnets, jarosites. *Physica B 329-333* (2003), 1065–1066.

[149] NOCERA, D. G., BARTLETT, B. M., GROHOL, D., PAPOUTSAKIS, D., AND SHORES, M. P. Spin frustration in 2d kagomé lattices: A problem for inorganic synthetic chemistry. *Chem. Eur. J. 10* (2004), 3850–3859.

[150] NOZIÈRES, P., AND PINES, D. *The theory of quantum liquids.* Perseus books, Cambridge Massachusetts, 1999.

[151] OBRADORS, X., LABARTA, A., ISALGU, A., TEJADA, J., RODRIGUEZ, J., AND PERNET, M. Magnetic frustration and lattice dimensionality in $SrCr_8Ga_4O_19$. *Solid Sate Comm. 65*, 3 (Jan 1989), 189–192.

[152] OFER, O., KEREN, A., NYTKO, E., SHORES, M., BARTLETT, B., NOCERA, D., BAINES, C., AND AMATO, A. Ground state and excitation properties of the quantum kagomé system $ZnCu_3(OH)_6Cl_2$ investigated by local probes. *cond-mat 0610540* (2006).

[153] OKUBO, S., OHTA, H., HAZUKI, K., SAKURAI, T., KOBAYASHI, N., AND HIROI, Z. High-field ESR study of kagome-like substance $Cu_3V_2O_7(OH)_2{\cdot}2H_2O$. *Physica B 294B-295B* (2001), 75.

[154] OLARIU, A., MENDELS, P., BERT, F., DUC, F., TROMBE, J., DE VRIES, M. A., AND HARRISSON, A. $^{17}O$ NMR study of the intrinsic magnetic susceptibility and spin dynamics of the quantum kagome antiferromagnet $ZnCu_3(OH)_6Cl_2$. arXiv:cond-mat/0711.2459, 2007.

[155] PAPOUTSAKIS, D., GROHOL, D., AND NOCERA, D. Magnetic properties of a homologous series of vanadium jarosite compounds. *J. Am. Chem. Soc. 124*, 11 (2002), 2647–2656.

[156] PAULING, L. *The Nature of the Chemical Bond*, 3nd ed. Cornell University Press, Ithaca, New York, 1960.

[157] PETTIGREW, K. *Magnetic Properties of the Jarosites: Model Kagomé Antiferromagnets.* PhD thesis, The University of Edinburgh, 2002.

[158] POLLARD, A., THOMAS, R., AND WILLIAMS, P. Synthesis and stabilities of the basic copper(II) chlorides atacamite, paratacamite and botallackite. *Mineralogical Magazine 53* (1989), 557–563.

[159] QUANTUM DESIGN, SAN DIEGO. *PPMS Hardware and options manual*, 1999.

[160] RADAELLI, P. G., HORIBE, Y., GUTMANN, MATTHIAS J. ANDISHIBASHI, H., CHEN, C. H., IBBERSON, R. M., KOYAMA, Y., HOR, Y.-S., KIRYUKHIN, V., AND CHEONG, S.-W. Formation of isomorphic $Ir^{3+}$ and $Ir^{4+}$ octamers and spin dimerization in the spinel $CuIr_2S_4$. *Nature 416* (2002), 155–158.

[161] RAMIREZ, A. P. Geometric frustration: Magic moments. *Nature 421* (2003), 483.

[162] RAMIREZ, A. P., CHEONG, S.-W., AND KAPLAN, M. L. Specific heat of defects in haldane systems $Y_2BaNiO_5$ and NENP: Absence of free spin-1/2 excitations. *Phys. Rev. Lett. 72*, 19 (May 1994), 3108–3111.

[163] RAMIREZ, A. P., ESPINOSA, G. P., AND COOPER, A. S. Strong frustration and dilution-enhanced order in a quasi-2d spin glass. *Phys. Rev. Lett. 64*, 17 (Apr 1990), 2070–2073.

[164] RAMIREZ, A. P., HESSEN, B., AND WINKLEMANN, M. Entropy balance and evidence for local spin singlets in a kagomé-like magnet. *Phys. Rev. Lett. 84*, 13 (Mar 2000), 2957–2960.

[165] RAMIREZ, A. P., HESSEN, B., AND WINKLEMANN, M. Entropy balance and evidence for local spin singlets in a kagomé-like magnet. *Phys. Rev. Lett. 84*, 13 (Mar 2000), 2957–2960.

[166] RAN, Y., HERMELE, M., LEE, P. A., AND WEN, X.-G. Projected-wave-function study of the spin-1/2 heisenberg model on the kagomé lattice. *Phys. Rev. Lett. 98*, 11 (2007), 117205.

[167] REIMERS, J. N., AND BERLINSKY, A. J. Order by disorder in the classical heisenberg kagomé antiferromagnet. *Phys. Rev. B 48*, 13 (Oct 1993), 9539–9554.

[168] REIMERS, J. N., BERLINSKY, A. J., AND SHI, A.-C. Mean-field approach to magnetic ordering in highly frustrated pyrochlores. *Phys. Rev. B 43*, 1 (Jan 1991), 865–878.

[169] RIETVELD, H. M. A profile refinement method for nuclear and magnetic structures. *J. Appl. Cryst. 2* (1969), 65–71.

[170] RIGOL, M., AND SINGH, R. R. P. Magnetic susceptibility of the kagome antiferromagnet $ZnCu_3(OH)_6Cl_2$. *Phys. Rev. Lett. 98*, 20 (2007), 207204.

[171] RITCHEY, I., CHANDRA, P., AND COLEMAN, P. Spin folding in the two-dimensional heisenberg kagomé antiferromagnet. *Phys. Rev. B 47*, 22 (Jun 1993), 15342–15345.

[172] ROBERT, J., SIMONET, V., CANALS, B., BALLOU, R., BORDET, P., LEJAY, P., AND STUNAULT, A. Spin-liquid correlations in the Nd-Langasite anisotropic kagomé antiferromagnet. *Phys. Rev. Lett. 96*, 19 (2006), 197205.

[173] ROESSLI, B., AND BÖNI, P. Polarised neutron scattering. arXiv:cond-mat/0012180v1.

[174] ROGADO, N., HAAS, M. K., LAWES, G., HUSE, D. A., RAMIREZ, A. P., AND CAVA, R. J. $\beta$-$Cu_3V_2O_8$ : magnetic ordering in a spin-1/2 kagomé-staircase lattice. *J. Phys.: Cond. Matt. 15*, 6 (2003), 907–914.

[175] RØNNOW, H. M., MCMORROW, D. F., COLDEA, R., HARRISON, A., YOUNG SON, I. D., PERRING, T. G., AEPPLI, G., SYLJUÅSEN, O., LEFMANN, K., AND RI SCHEL, C. Spin dynamics of the 2d spin $\frac{1}{2}$ quantum antiferromagnet copper deutero formate tetradeuterate (CFTD). *Phys. Rev. Lett. 87*, 3 (Jun 2001), 037202.

[176] RØNNOW, H. M., MCMORROW, D. F., AND HARRISON, A. High-temperature magnetic correlation in the 2D $S = 1/2$ antiferromagnet copper formate tetradeuterate. *Phys. Rev. Lett. 82* (1999), 3152–3155.

[177] RØNNOW, H. M., PARTHASARATHY, R., JENSEN, J., AEPPLI, G., ROSENBAUM, T. F., AND MCMORROW, D. F. Quantum phase transition of a magnet in a spin bath. *Science 308* (2005), 5720.

[178] ROWELL, J. M. Magnetic field dependence of the josephson tunnel current. *Phys. Rev. Lett. 11*, 5 (Sep 1963), 200–202.

[179] SACHDEV, S. Kagomé- and triangular-lattice heisenberg antiferromagnets: Ordering from quantum fluctuations and quantum-disordered ground states with unconfined bosonic spinons. *Phys. Rev. B 45*, 21 (Jun 1992), 12377–12396.

[180] SACHDEV, S. Quantum magnetism and criticality, 2007.

[181] SACHDEV, S., SENTHIL, T., AND SHANKAR, R. Finite-temperature properties of quantum antiferromagnets in a uniform magnetic field in one and two dimensions. *Phys. Rev. B 50*, 1 (Jul 1994), 258–272.

[182] SAKURAI, J. J. *Modern Quantum Mechanics*, 2nd ed. Addison Wesley, 1994.

[183] SCHÄRPF, O., AND CAPELLMANN, H. The $XYZ$-difference method with polarized neutrons and the separation of coherent, spin incoherent, and magnetic scattering cross sections in a multidetector. *Phys. Stat. S. (a) 135*, 2 (1993), 359–379.

[184] SCHENCK, A. Static magnetic properties of metallic systems. In *MUON SCIENCE. Muons in physics, chemistry and materials* (1998), S. Lee, S. Kilcoyne, and R. Cywinski, Eds., Scottish Universities Summer School in Physics & Institute of Physics Publishing, Briston and Philadelphia, pp. 85–114.

[185] SCHIFFER, P., RAMIREZ, A. P., FRANKLIN, K. N., AND CHEONG, S.-W. Interaction-induced spin coplanarity in a kagomé magnet: $SrCr_{9p}Ga_{12-9p}O_{19}$. *Phys. Rev. Lett. 77*, 10 (Sep 1996), 2085–2088.

[186] SCHMIDT, M., RATCLIFF, W., RADAELLI, P. G., REFSON, K., HARRISON, N. M., AND CHEONG, S. W. Spin singlet formation in $MgTi_2O_4$: Evidence of a helical dimerization pattern. *Phys. Rev. Lett. 92*, 5 (2004), 056402.

[187] SCHWEIKA, W., VALLDOR, M., AND LEMMENS, P. Approaching the ground state of the kagomé antiferromagnet. *Phys. Rev. Lett. 98*, 6 (2007), 067201.

[188] SHORES, M. P., NYTKO, E. A., BARTLETT, B. M., AND NOCERA, D. G. A structurally perfect $S = 1/2$ kagomé antiferromagnet. *J. Am. Chem. Soc. 127*, 39 (2005), 13462.

[189] SHULL, C. G., AND SMART, J. S. Detection of antiferromagnetism by neutron diffraction. *Phys. Rev. 76*, 8 (Oct 1949), 1256–1257.

[190] SINDZINGRE, P., MISGUICH, G., LHUILLIER, C., BERNU, B., PIERRE, L., WALDTMANN, C., AND EVERTS, H.-U. Magnetothermodynamics of the spin- $\frac{1}{2}$ kagomé antiferromagnet. *Phys. Rev. Lett. 84*, 13 (Mar 2000), 2953–2956.

[191] SINGH, R. R. P., AND HUSE, D. A. Three-sublattice order in triangular- and kagomé-lattice spin-half antiferromagnets. *Phys. Rev. Lett. 68*, 11 (Mar 1992), 1766–1769.

[192] SMITH, T. J., CAPELLMANN, H., KREMER, R. K., NEUMANN, K.-U., AND ZIEBECK, K. R. A. A quantitative determination of magnetic fluctuations in $CuGeO_3$. *Eur. Phys. J. B - Cond. Matt. 21* (2001), 341–347.

[193] SQUIRES, G. *Introduction to the field of thermal neutron scattering.* Dover Publications, 1978.

[194] STEWART, J. R., ANDERSEN, K. H., CYWINSKI, R., AND MURANI, A. P. Magnetic diffuse scattering in disordered systems studied by neutron polarization analysis (invited). vol. 87, AIP, pp. 5425–5430.

[195] STEWART, R., ROLS, S., AND MARCHAL, F. Diffuse scattering spectrometer in4. www.ill.fr/YellowBook/IN4, January 2007. last accessed at 4/06/07.

[196] SZABO, A., AND OSTLUND, N. S. *Modern Quantum Chemistry.* Dover Publications, Mineola, New York, 1984.

[197] TAKANO, M., SHINJO, T., KIYAMA, M., AND TAKADA, T. Magnetic properties of jarosites, $R Fe_3(OH)_6(SO_4)_2$($R$=$NH_4$, Na or K),. *J. Phys. Soc. Jpn. 25* (1968), 902.

[198] TAKANORI SUTO, TOSHIO ONO, H. T., AND UEKUSA, H. Structural and magnetic properties of $s = 1/2$ kagomé antiferromagnet $Cs_2Cu_3ZrF_{12}$. *Progr. Th. Phys.*, 159 (2005), 67–71.

[199] TASIOPOULOS, A. J., VINSLAVA, A., WERNSDORFER, W., ABBOUD, K. A., AND CHRISTOU, G. Giant single-molecule magnets: A $Mn_{84}$ torus and its supramolecular nanotubes. *Angew. Chem. Int. Ed. 43* (2004), 2117.

[200] TENNANT, D. A., PERRING, T. G., COWLEY, R. A., AND NAGLER, S. E. Unbound spinons in the s=1/2 antiferromagnetic chain $KCuF_3$. *Phys. Rev. Lett. 70*, 25 (Jun 1993), 4003–4006.

[201] THOLE, B. T., CARRA, P., SETTE, F., AND VAN DER LAAN, G. X-ray circular dichroism as a probe of orbital magnetization. *Phys. Rev. Lett. 68*, 12 (Mar 1992), 1943–1946.

[202] TINKHAM, M. *Group theory and quantum mechanics.* McGraw-Hill, 1964.

[203] TOBY, B. H. Expgui, a graphical user interface for gsas. *J. Appl. Cryst. 34* (2001), 210–213.

[204] TOWNSEND, M. G., LONGWORTH, G., AND ROUDAUT, E. Triangular-spin, kagome plane in jarosites. *Phys. Rev. B 33*, 7 (Apr 1986), 4919–4926.

[205] UEMURA, Y. $\mu$sr relaxation functions in magnetic materials. In *MUON SCIENCE. Muons in physics, chemistry and materials* (1998), S. Lee, S. Kilcoyne, and R. Cywinski, Eds., Scottish Universities Summer School in Physics & Institute of Physics Publishing, Briston and Philadelphia, pp. 85–114.

[206] VAJK, O. P., MANG, P. K., GREVEN, M., GEHRING, P. M., AND LYNN, J. W. Quantum impurities in the two dimensional spin one-half heisenberg antiferromagnet. *Science 295* (2002), 1691–1695.

[207] VAN DEN BRINK, J. Lecture notes on theory of condensed matter. http://www.ilorentz.org/~brink/course/tcm.html, Leiden, 2006. Last accessed 29/05/2007.

[208] VAN DER LAAN, G. Angular momentum sum rules for X-ray absorption. *Phys. Rev. B 57*, 1 (Jan 1998), 112–115.

[209] VAN DER LAAN, G. Relation between the angular dependence of magnetic X-ray dichroism and anisotropic ground-state moments. *Phys. Rev. B 57*, 9 (Mar 1998), 5250–5258.

[210] VAN DER LAAN, G. Magnetic linear X-Ray dichroism as a probe of the magnetocrystalline anisotropy. *Phys. Rev. Lett. 82*, 3 (Jan 1999), 640–643.

[211] VAN DER LAAN, G., ZAANEN, J., SAWATZKY, G. A., KARNATAK, R., AND ESTEVA, J.-M. Comparison of X-ray absorption with x-ray photoemission of nickel dihalides and NiO. *Phys. Rev. B 33*, 6 (Mar 1986), 4253–4263.

[212] VAN ELP, J., AND TANAKA, A. Threshold electronic structure at the oxygen K edge of 3d-transition-metal oxides: A configuration interaction approach. *Phys. Rev. B 60*, 8 (Aug 1999), 5331–5339.

[213] VAN WEZEL, J., VAN DEN BRINK, J., AND ZAANEN, J. An intrinsic limit to quantum coherence due to spontaneous symmetry breaking. *Phys. Rev. Lett. 94*, 23 (2005), 230401.

[214] VAN WEZEL, J., ZAANEN, J., AND VAN DEN BRINK, J. On the relation between decoherence and spontaneous symmetry breaking. 14, arXiv.org:0606140.

[215] VERNAY, F., PENC, K., FAZEKAS, P., AND MILA, F. Orbital degeneracy as a source of frustration in $LiNiO_2$. *Phys. Rev. B 70*, 1 (2004), 014428.

[216] VILLAIN, J., BIDAUX, R., CARTON, J., AND CONTE, R. Order as an effect of disorder. *Journal de Physique (Paris) 41* (1980), 1263.

[217] VON DELFT, J., AND HENLEY, C. L. Destructive quantum interference in spin tunneling problems. *Phys. Rev. Lett. 69*, 22 (Nov 1992), 3236–3239.

[218] WALDTMANN, C., EVERTS, H.-U., BERNU, B., LHUILLIER, C., SINDZINGRE, P., LECHEMINANT, P., AND PIERRE, L. First excitations of the spin 1/2 heisenberg antiferromagnet on the kagomé lattice. *Eur. Phys. J. B 2* (1998), 501–507.

[219] WASINGER, E., DE GROOT, F., HEDMAN, B., HODGSON, K., AND SOLOMON, E. L-edge X-ray absorption spectroscopy of non-heme iron sites: Experimental determination of differential orbital covalency. *J. Am. Chem. Soc. 125*, 42 (Sep 2003), 12894–12906.

[220] WATANABE, H. On the ground level splitting of $Mn^{++}$ and $Fe^{+++}$ in nearly cubic crystalline field. *Progr. Theor. Phys. 18* (October 1957).

[221] WEIDNER, R. T., WEISS, P. R., WHITMER, C. A., AND BLOSSER, D. R. Magnetic resonance absorption of diluted iron ammonium alum. *Phys. Rev. 76*, 11 (Dec 1949), 1727–1728.

[222] WEN, X. G. Mean-field theory of spin-liquid states with finite energy gap and topological orders. *Phys. Rev. B 44*, 6 (Aug 1991), 2664–2672.

[223] WILLS, A. *A Study of Experimantal Kagomé Antiferromagnets Based on the Jarosite Series.* PhD thesis, The University of Edinburgh, 1996.

[224] WILLS, A., HARRISON, A., RITTER, C., AND SMITH, R. Magnetic properties of pure and diamagnetically doped jarosites: Model kagomé antiferromagnets with variable coverage of the magnetic lattice. *Phys. Rev. B 61* (2000), 6156.

[225] WILLS, A. S. Long-range ordering and representational analysis of the jarosites. *Phys. Rev. B 63*, 6 (Jan 2001), 064430.

[226] WILLS, A. S. Magnetic excitations in a $S = 1/2$ pyrochlore antiferromagnet. Tech. Rep. RB21001, ISIS, 2005.

[227] WILLS, A. S. Magnetic excitations in a $S = 1/2$ pyrochlore antiferromagnet. Tech. Rep. RB21002, ISIS, 2005.

[228] WILLS, A. S., DUPUIS, V., VINCENT, E., HAMMANN, J., AND CALEMCZUK, R. Aging in a topological spin glass. *Phys. Rev. B 62*, 14 (Oct 2000), R9264–R9267.

[229] WILLS, A. S., AND HARRISON, A. Structure and magnetism of hydronium jarosite, a model kagomé antiferromagnet. *J Chem Soc, Faraday Frans. 92* (1996), 2161–2166.

[230] WILLS, A. S., HARRISON, A., MENTINK, S. A. M., MASON, T. E., AND TUN, Z. Magnetic correlations in deuteronium jarosite, a model $S = 5/2$ Kagomé antiferromagnet. *Europhysics Letters 42* (May 1998), 325–330.

[231] WILLS, A. S., OAKLEY, G. S., VISSER, D., FRUNZKE, J., HARRISON, A., AND ANDERSEN, K. H. Short-range order in the topological spin glass $(D_3O)Fe_3(SO_4)_2(OD)_6$ using xyz polarized neutron diffraction. *Phys. Rev. B 64*, 9 (Aug 2001), 094436.

[232] WOOD, J. H., AND PRATT, G. W. Wave functions and energy levels for Fe as found by the unrestricted hartree-fock method. *Phys. Rev. 107*, 4 (Aug 1957), 995.

[233] WU, M. K., ASHBURN, J. R., TORNG, C. J., HOR, P. H., MENG, R. L., GAO, L., HUANG, Z. J., WANG, Y. Q., AND CHU, C. W. Superconductivity at 93 k in a new mixed-phase Yb-Ba-Cu-O compound system at ambient pressure. *Phys. Rev. Lett. 58*, 9 (Mar 1987), 908–910.

[234] YILDIRIM, T., AND HARRIS, A. B. Magnetic structure and spin waves in the kagomé jarosite compound $KFe_3(SO_4)_2(OH)_6$. *Phys. Rev. B 73*, 21 (2006), 214446.

[235] ZAANEN, J., SAWATZKY, G. A., AND ALLEN, J. W. Band gaps and electronic structure of transition-metal compounds. *Phys. Rev. Lett. 55*, 4 (Jul 1985), 418–421.

[236] ZABEL, H. *Neutron and synchrotron radiation for condensed matter studies*, vol. 1. EDP Sciences, Springer-Verlag, 1993, ch. Interactions of Neutrons with matter; Inelastic case, pp. 285–322.

[237] ZEIGER, H. J., AND PRATT, G. W. *Magnetic interactions in solids.* Clarendon Press, Oxford, 1973.

[238] ZENG, C., AND ELSER, V. Numerical studies of antiferromagnetism on a kagomé net. *Phys. Rev. B 42*, 13 (Nov 1990), 8436–8444.

[239] ZHENG, X. G., KAWAE, T., KASHITANI, Y., LI, C. S., TATEIWA, N., TAKEDA, K., YAMADA, H., XU, C. N., AND REN, Y. Unconventional magnetic transitions in the mineral clinoatacamite $Cu_2Cl(OH)_3$. *Phys. Rev. B 71*, 5 (2005), 052409.

[240] ZHENG, X. G., KUBOZONO, H., NISHIYAMA, K., HIGEMOTO, W., KAWAE, T., KODA, A., AND XU, C. N. Coexistence of long-range order and spin fluctuation in geometrically frustrated clinoatacamite $Cu_2Cl(OH)_3$. *Phys. Rev. Lett. 95*, 5 (2005), 057201.

[241] ZHITOMIRSKY, M. E., AND TSUNETSUGU, H. Exact low-temperature behavior of a kagomé antiferromagnet at high fields. *Phys. Rev. B 70*, 10 (2004), 100403.